PHD DEGREE IN MARINE SCIENCES

Retroflections in the Tropical Atlantic Ocean

IGNASI BERENGUER VALLÈS CASANOVA

SUPERVISED BY
DR. JOSEP LLUÍS PELEGRÍ LLOPART

INSTITUT DE CIÈNCIES DEL MAR, CSIC

Tesis presentada per obtindre el títol de Doctor
per la Universitat Politècnica de Catalunya

Programa de Doctorat en Ciències del Mar
Departament d'Enginyeria Civil i Ambiental

Summary

In the tropical Atlantic, the upper ocean circulation is the area of confluence of two major vertical cells: the large-scale overturning Atlantic Meridional Overturning Circulation (AMOC) and the regional relatively shallow Subtropical Cells (STCs). Both meridional cells interact in a complex system of zonal currents driven by fluctuations of the trade winds. The thermocline waters that subduct in the subtropical South Atlantic join the northward AMOC limb in the western boundary North Brazil Current (NBC). When the NBC crosses the equator it retroflects forced by fluctuations in the easterly winds. These changes in the wind field are part of coupled ocean-atmosphere variations that span across the entire Atlantic and cover a wide range of timescales. The present thesis aims at describing the NBC retroflection in the equatorial band and improving our current knowledge on the upper-ocean circulation in the tropical Atlantic and its interaction with the climate variability.

The NBC system carries warm and highly saline waters from the subtropical gyre to the tropics, for a total of 38.5 Sv and 2.0 PW, in what represents the main AMOC cross-equatorial pathway. This subtropical-tropical transfer accounts for water-mass and heat contributions coming from the eastern subtropical boundary (14.9 Sv, 0.82 PW) and the interior subtropical gyre (7.4 Sv, 0.28 PW). As an opposite path, shallow tropical waters transfer 1.4 Sv and 0.14 PW to the subtropics. Adding interior pathways and tropical recirculation transports, a total of 20.6 Sv and 1.0 PW are effectively exported northward through 5°S.

As the NBC crosses the equator, 11.4±1.3 Sv of South Atlantic waters retroflect into the eastward Equatorial Undercurrent (EUC) at 32°W, which join 2.8±0.4 Sv arriving from the northern hemisphere. The NBC-EUC retroflection takes place at different latitudinal bands. Most of the waters turn eastward south of 3°N (7.2±0.6 Sv) but a substantial amount does so north of this latitude (5.1±0.4 Sv). The variability of the EUC transport at 32°W is characterized by principal spring and secondary fall monthly-mean maximum, with the fall maximum only present in the northern retroflection. At interannual scales the EUC transport shows a weak yet significant correlation with the Atlantic Niño index, and reflects a major increase in the contribution from the South Atlantic tropical waters during 2008-2016 as compared with 1997-2007.

The NBC retroflection occurs within an area where changes in Sea Surface Height (SSH) anomalies (SSHA) respond to the two main modes of Tropical Atlantic Variability (TAV): the Meridional Mode (MM) and Equatorial Mode (EM). During the development of warm (cold) MM events, all North Equatorial Countercurrent (NECC), EUC and north South Equatorial Current (nSEC) intensify (weaken). Conversely, during the decaying phase, anomalous wind curl north of the equator, triggers a downwelling (upwelling) Rossby wave that propagates westward and is reflected at the South American coast. The resultant downwelling (upwelling) Kelvin wave reverses the equatorial zonal gradients in boreal summer, weakening (strengthening) both equatorial nSEC and

EUC.The activation of the RW-reflected mechanisms shifts the zonal SSHA, enhancing (weakeking) the nSEC and favoring the termination of the EM event. Remarkably, the EUC displays a non-linear response probably as a result of external forcings and/or the intrinsic diversity of the EM. The development of warm EM is accompanied by an anomalous reduction (intensification) of equatorial nSEC and NECC during boreal spring.

The diversity of EM has been studied by applying an empirical orthogonal function (EOF) analysis of a sample of 22 time series of warm EM events (referred as Atlantic Niño). This technique reveals four different types of spatio-temporal distributions of SST anomalies (SSTA) in the equatorial Atlantic in the period 1982-2019. Early-terminanting and persistent categories are associated with different dissipation times for the Atlantic Niño. While early-onset and late-onset refers to the diverse Atlantic Niño timings found in the sample. These four different types of Atlantic Niño are associated with different climatic response on the surrounding continents. Interestingly, early-terminating, persistent and early-onset Atlantic Niño seem to be preceded by local (i.e: MM) and remote (i.e: ENSO) forcings in boreal spring. While, late-onset Atlantic Niño is more related with internal variability.

Resum

La circulació oceànica a les capes superiors de l'Atlàntic tropical es caracteritza per la confluència de dos importants sistemes de circulació meridional: la circulació meridional de gran escala de l'Atlàntic (AMOC, per les seves sigles en anglès) i el sistemes regionals de cèl·lules subtropicals (STCs). Ambdues cèl·lules circulatòries interactuen en un complex sistema de corrents zonals governat pel patró de vents alisis. Les aigües que convergeixen al subtròpic de l'Atlàntic Sud per bombament d'Ekman es situen a la termoclina i retornen cap a l'equador, juntament amb la branca de retorn de la AMOC. Les dos aigües conflueixen al marge occidental constituint el sistema de corrents nord del Brasil (NBUC/NBC). Quan la NBC creua l'equador esdevé inestable per l'absència de Coriolis i es sotmesa als gradients d'altura de la superfície del mar (SSH) associats amb el sistema de vents de component est. Part de la NBC es desenganxa del talús per alimentar les diferents corrents zonals esdevenint un important sistema de retroflexió. La variabilitat d'aquesta retroflexió està per tant lligada a les oscil·lacions del camp de vent predominant i les modificacions associades dels gradients de SSH. Aquestes fluctuacions formen part d'un complex sistema acoblat entre l'atmosfera i l'oceà que es presenta a diferents escales temporals i espacials. L'objectiu d'aquesta tesi és descriure el sistema de retroflexió a la banda equatorial i millorar el nostre coneixement sobre la interacció entre aquest sistema de corrents de les capes superficials i termoclina amb diferents modes de variabilitat climàtica.

El sistema NBC/NBUC transporta un total de 38.5 Sv i 2.0 PW d'aigües relativament salines del gir subtropical de l'Atlàntic Sud que representen el principal camí de retorn de la AMOC. Aquesta transferència subtropical-tropical conté aigües del marge meridional (14.9 Sv, 0.82 PW) i aigües interiors de la conca subtropical (7.4 Sv, 0.28 PW). Per altra banda, aigües de capes superficials provinents del gir tropical es traspassen al gir subtropical amb un total de 1.4 Sv i 0.14 PW. Tenint en compte aquest traspàs, i la recirculació tropical, el resultat es un transport net en direcció nord de 20.6 Sv i 1.0 PW a 5°S. Un cop la NBC creua l'equador 11.4 ± 1.3 Sv de l'Atlàntic Sud alimenten la corrent equatorial situada a la capa de la termoclina (EUC) a 32°W. Aquestes aigües es sumen als 2.8 ± 0.4 Sv provinents de l'hemisferi nord. La retroflexió NBC-EUC es dona lloc a diferents bandes latitudinals al voltant de l'equador. La majoria d'aigües giren en direcció est per sota els 3°N (7.2 ± 0.6 Sv) però una important contribució es dona lloc més al nord (5.1 ± 0.4 Sv). La variabilitat de la EUC a 32°W està caracteritzada per dos màxims a la primavera i tardor boreal. Però el màxim de tardor només es troba present en les aigües del gir més septentrional. A escala interanual, el transport de la EUC mostra una correlació negativa dèbil però significativa amb l'índex de l'Atlàntic Niño i curiosament presenta una tendència positiva entre el període 2008 al 2016 en comparació amb el període 1997-2007.

La retroflexió de la NBC es dona lloc en una àrea on canvis anòmals en l'altura de la superfície del mar (SSHA) responen als dos modes principals de variabilitat climàtica interanual de l'Atlàntic

tropical (TAV): el mode meridional (MM) i el mode equatorial (EM), aquest últim conegut també com Atlantic Niño/Niña. Durant el desenvolupament d'un episodi positiu (negatiu) de MM la contracorrent nord equatorial (NECC), EUC i la branca nord de la corrent sud-equatorial (nSEC) s'intensifiquen (es debiliten). Contràriament, durant el decaïment del MM el mecanisme de reflexió d'ona Rossby (RW) al marge occidental esdevé en ona Kelvin que es propaga cap a l'est al llarg de l'equador. Quan arriba al marge oriental de l'Atlàntic tropical la situació es reverteix desenvolupant una zona de convergència o divergència respectivament que equivaldria a EM positiu (negatiu). Tant la corrent superficial nSEC com la NECC es debiliten en situacions de EM positiu, contràriament la EUC no mostra una resposta linear indicant possibles forçaments externs o una alta diversitat dels episodis de EM.

En aquest sentit la diversitat d'episodis positius de EM, anomenats també Atlantic Niño, han estat estudiats aplicant anàlisi de funcions ortogonals en una sèrie temporal de 22 casos. Els resultats mostren quatre tipus de distribució en l'espai-temps d'anomalies de temperatura superficial del mar (SSTA) a l'Atlàntic equatorial. La classificació és en funció del temps en que apareixen i la seva extensió temporal i espacial. Cada un d'aquest quatre tipus d'Atlàntic Niño està associat a una resposta climàtica a les zones continentals del nord-est d'Amèrica del Sud i l'Àfrica Occidental. Curiosament, tres dels quatre tipus s'expliquen per les condicions prèvies locals (i.e: MM) i remotes (i.e: ENSO) durant la primavera anterior.

Contents

List of Figures

List of Tables

List of Abbreviations

AAIW	Antartic Intermediate Water
AC	Agulhas Current
ACC	Antartic Circumpolar Current
AD	Angola Dome
ADCP	Acoustic doppler current profiler
AMO	Atlantic Multidecadal Oscillation
AMOC	Atlantic Meridional Overturning Circulation
BC	Brazil Current
cSEC	central South Equatorial Current
CTD	Conductivity temperature depth
CW	Central Water
EM	Equatorial Mode
ENSO	El-Niño Southern Oscillation
EOF	Empirical Ortogonal Function
ER	Equatorial Retroflection
EUC	Equatorial Undercurrent
GD	Guinea Dome
ITCZ	Intertropical Convergence Zone
KW	Kelvin wave
LADCP	Lowered acoustic doppler current profiler
LSF	Lagrangian stream function
MM	Meridional Mode
NADW	North Atlantic Deep Water
NAO	North Atlantic Oscillation
NBC	North Brazil Current
NBCR	North Brazil Current Retroflection
NBUC	North Brazil Undercurrent
NAW	North Atlantic Water
NEAW	North Eastern Atlantic Water
NEC	North Equatorial Current
NECC	North Equatorial Countercurrent
NER	North Equatorial Retroflection
NEUC	North Equatorial Undercurrent
NICC	North Intermediate Countercurrent
RW	Rossby wave

SAW	South Atlantic Water
SACW	South Atlantic Central Water
SAMW	Subantartic Mode Water
SEAW	South Eastern Atlantic Water
SMW	South Atlantic Mode Water
nSEC	north South Equatorial Current
SEC	South Equatorial Current
sSEC	south South Equatorial Current
SER	South Equatorial Retroflection
SEUC	South Equatorial Undercurrent
SICC	South Intermediate Countercurrent
SSH	Sea surface height
SSHA	Sea surface height anomaly
SST	Sea surface temperature
SSTA	Sea surface temperature anomaly
STC	Subtropical Cell
TAV	Tropical Atlantic Varability
TIWs	Tropical Instability Waves
TSW	Tropical Surface Waters
WB	Western Boundary
WES	Wind evaporation SST

Al pare i la mare

Chapter 1

Introduction

The elementary concept of the Earth's spherical shape is a common principle in many diverse fields of knowledge. Indeed, theories from distinct sciences such as anthropology, ecology or human history itself rely on this spatial constraint. However, climate is the link between the Earth's geometry and, for instance, the biome distribution, the migration of our ancestors or the first circumnavigations around the planet.

Probably the first description of climate variability as a function of latitude can be attributed to Parmenides, referred to in Meteora (Aristotile, year 350 BC; Aristotle & Webster, 2006). They classified the Earth into three geographical zones based on their relative heat and distance from the equator: the torrid, temperate and frigid zones. Nowadays, the torrid zone is the equivalent to the tropics. Considered too hot to be inhabited by the ancient Greek philosopher, at present the tropics not only accommodate about 40% of the planetary population but it also contains more than 80% of the world's biodiversity (Penny et al., 2020).

The tropics is the region bounded by the axial tilt of the Earth, from 23.43°N to 23.43°S, with 76% of its area covered by the ocean. Because of the Earth's curvature, the tropical area receives the solar radiation with a mean angle of incidence higher than the rest of the planet, resulting in the largest annual-mean amount of heat per unit area. The imbalance is addressed by mechanisms of ocean-atmosphere interaction such as evaporation of surface water, rainfall, convection, wind and ocean circulation, which redistribute solar heat from the tropics toward the poles. The different components of this coupled ocean-atmosphere system have therefore important implications on the climate variability from regional to global scale.

In this context, is of particular interest the tropical system of the Atlantic Ocean. Its basin is relatively narrow and surrounded by two large land masses, northern South America and west Africa, where most of the population lives in developing countries. Their climatic conditions are closely tied to the interactions between ocean, atmosphere and land, with important socio-economic implications. Generally, these interactions are translated in meridional excursions of the Intertropical Convergence Zone (ITCZ) and changes in sea surface temperature (SST; Xie & Carton, 2004). The ITCZ is a belt of tropical deep-convection where trade winds of the northern and southern hemispheres converge, producing a zonal band of thunderstorms and heavy precipitation.

The position of the ITCZ is highly influenced by the SST distribution in the tropical Atlantic, with relatively warm SST favouring convective air circulation. Therefore, the rainfall regime is highly sensitive to SST changes in critical regions such as the semi-arid areas of Sahel or Brazil

Nordeste (Foltz et al., 2019; Giannini et al., 2008; Nobre & Shukla, 1996; Rodríguez-Fonseca et al., 2015; Xie & Carton, 2004) Additionally, the tropical Atlantic is involved in teleconnections with other tropical basins that modulate the climate at interannual and multidecadal timescales (e.g., Ham et al., 2013; Kucharski et al., 2008; Rodríguez-Fonseca et al., 2009; Wang et al., 2009). In the same way, fluctuations of the SST distribution in the tropical Atlantic may be forced remotely from the Pacific, Indian Ocean or off-tropical regions from the Atlantic (Alexander & Scott, 2002; García-Serrano et al., 2017; Klein et al., 1999; Latif & Grötzner, 2000; Martín-Rey et al., 2018; Wang et al., 2017). This ensemble of air-sea interactions and teleconnections that can alter the climatology of this region is known as the Tropical Atlantic Variability (TAV).

The uniqueness of the Atlantic circulation in the global ocean is also a fundamental component of the global climate system. The northern North Atlantic is a region of severe surface heat loss during winter, when the intense westerly winds bring dry-cold airs over the subarctic ocean. One consequence is the loss of buoyancy of surface waters, which leads to the formation and sinking of cold and saline waters. The result is a thick and homogeneous North Atlantic Deep Water (NADW) layer that spreads southward at depths between 2000 and 4500 m. The downward and southward mass flux is replaced by the poleward transport of warm water in the upper layers of the ocean (< 1000 m depth), a vertical latitudinal cell denoted as the Atlantic Meridional Overturning Circulation (AMOC).

The AMOC leads to a unique net northward heat transport along the entire Atlantic basin, in contraposition to the asymmetric poleward transport in the Pacific. Consequently, the ocean circulation of the tropical Atlantic interacts with this large-scale meridional circulation connecting the deep southward and shallow northward branches of the AMOC. Concretely, the intensity of the upper-limb of the AMOC depends on the transfer mechanisms from the wind-driven subtropical gyre in the South-Atlantic to the complex current system of the tropical Atlantic.

1.1 From subtropical to tropical pathways

The South Atlantic subtropical gyre is forced by the high-latitude westerlies and the low-latitude south-easterlies. This wind system drives Ekman convergence, increasing the sea surface high (SSH) in the gyre's centre and the downwelling of the isopycnals, this produce the subduction of surface waters that follow a geostrophic-balanced anticyclonic thermocline pathway (Peterson & Stramma, 1991; Stramma & England, 1999). In contrast, the South Atlantic tropical gyre is much shallower, characterized by equatorial Ekman divergence that depletes the SSH and upwells the pycnocline, and leads to a cyclonic circulation with important zonal flows. Both circulation systems meet in the South Equatorial Current (SEC), a north-westward flow which connects the eastern and western boundaries of the South Atlantic.

The SEC is fed by the Benguela Current and transports subtropical waters towards Brazil. Once this current reaches the western margin, it bifurcates near 15ºS into the southward Brazil Current (BC) and the northward North Brazil Current (NBC) and North Brazil Undercurrent (NBUC), representing the western branches of subtropical and tropical gyres respectively (Figure 1.1). Nevertheless, the position of this bifurcation shifts southward with depth with intermediate waters turning poleward further south, as far as near 27°S (Boebel et al., 1999; Legeais et al.,

2013)

The warm and salty thermocline waters from the subduction region in the subtropical South Atlantic can flow northward with the NBC. As this current crosses the equator, an important portion of thermocline waters turn to the east within the NBC retroflection system forming the Equatorial Undercurrent (EUC). Centered at the equator, the EUC constitutes the northern branch of the tropical gyre. Here, because of the changing sign in the Coriolis parameter, the easterlies drive equatorial Ekman divergence and upwelling. As the EUC flows east, it shoals and ventilates the upwelling zones at the center and eastern equatorial Atlantic. The tropical gyre is closed by surface poleward transport driven by Ekman divergence. It reaches the subtropics and subducts to the thermocline level coming back to the western boundary. This three-dimensional perspective of the tropical gyre constitutes a shallow meridional overturning circulation known as Subtropical Tropical Cell (STC; McCreary & Peng Lu, 1994).

The upper limb of AMOC joins the South Atlantic subtropical gyre through two routes: a warm-salty route from the Indian Ocean via the Agulhas Current (AC) and a cold-fresh route entering from the Pacific through Drake's passage as the Antarctic Circumpolar Current (ACC) (Gordon, 1986; Rintoul, 1991; Rühs et al., 2019; Speich et al., 2001). Both routes meet at the Benguela Current where they turn northwest into the SEC. After reaching the western boundary, the AMOC enters the tropical gyre through the western boundary NBC system, doubling or tripling the strength of the southern STC as compared with its northern counterpart(Da Silveira et al., 1994; Hazeleger & Drijfhout, 2006; Stramma et al., 1995; Zhang et al., 2003).

One of the methods used to estimate ocean pathways is to perform Lagrangian analysis by advecting virtual particles on a Eulerian velocity field. A great advantage of Lagrangian modelling is that particles can be advected backwards in time, allowing us to determine the origin of water masses at a certain location (van Sebille et al., 2018). We apply this methodology in **chapter 2** in order to estimate the mean estate of the subtropical and tropical pathways in the South Atlantic and the implications of the AMOC warm route.

1.2 Retroflections in the tropical Atlantic Ocean

Both meridional circulation schemes, AMOC and STCs, interact under the influence of complex zonal flows driven by the trade wind system of the tropical Atlantic Ocean. Forced by the southeasterlies, the SEC is the predominant westward flow in the upper layers (Figure 1.1), with a substantial meridional extension. This current is often defined by three branches: the southern (sSEC, 10°S – 25°S), central (cSEC, 3°S – 5°S) and northern branches (nSEC, 2°N – 4°N) (Stramma & England, 1999, Figure1). The sSEC is the one that brings surface to intermediate waters from the subtropics and Indian ocean, which constitutes the core of the returning limb of the AMOC. The cSEC instead, is a shallower westward flow in the upper 200 m transporting mostly eastern tropical and equatorial waters. Finally, the nSEC is a surface current that connects eastern with northwestern equatorial Atlantic. The northward western boundary NBC continuously increases its transport via input from the sSEC and cSEC branches. After its origin near 15°S, where de sSEC bifurcates, the cSEC contributes to a wider and stronger NBC, in boreal summer incrementing its transport from 21 Sv at 15°S to 36 Sv at 5°S (Da Silveira et al., 1994).

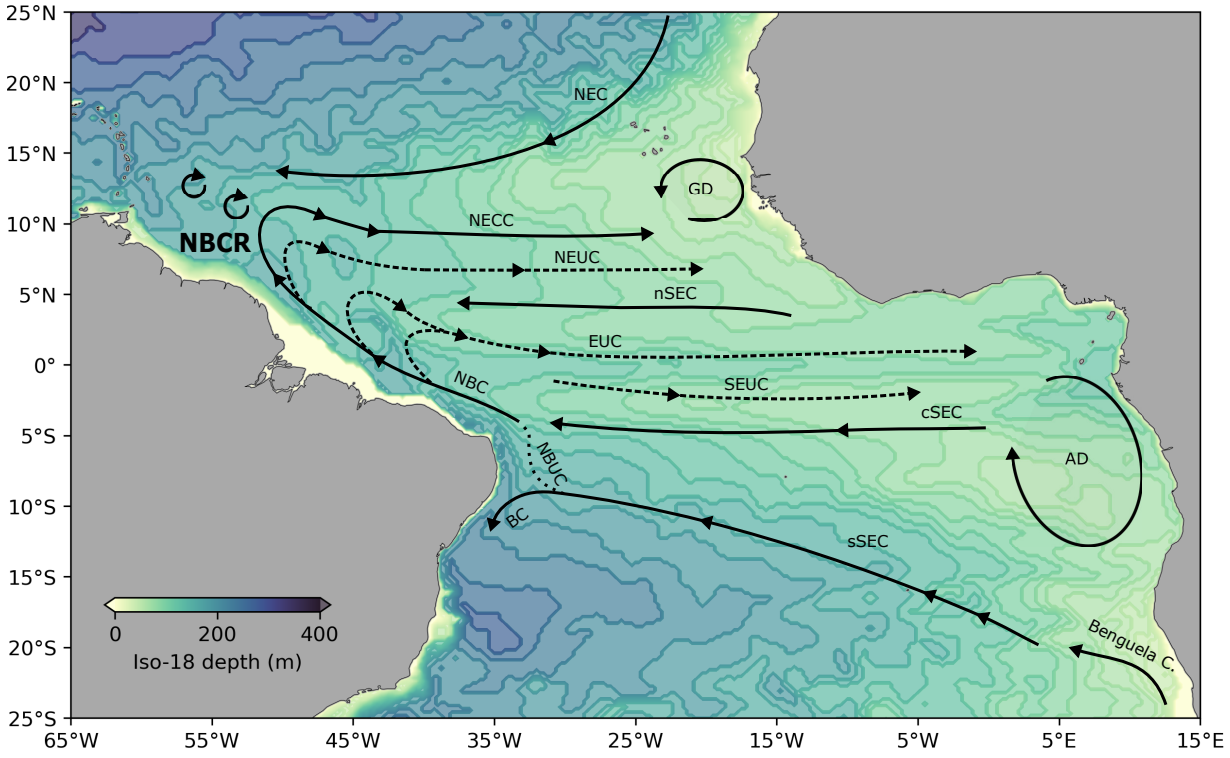

Figure 1.1: Schematic of the tropical Atlantic Ocean upper-circulation system overlaid on the mean 18°C isothermal depth of April 2010 from GLORYS2v4 reanalysis (Garric et al., 2017), which is used as a proxy of the thermocline depth. From north to south, the main surface currents (solid lines) are North Equatorial Current (NEC), North Equatorial Countercurrent (NECC), and South Equatorial Current with northern, central and south branches (nSEC, cSEC, sSEC). In the thermocline, we find the Equatorial Undercurrent (EUC) located between its northern and southern counterpart (NEUC and SEUC) (dashed black lines). The northward western boundary currents are the North Brazil Current (NBC) and the deeper North Brazil Undercurrent (NBUC). Brazil Current (BC) and Buenguela Current constitute the western and eastern branches of the Subtropical gyre. Finally, the Angola and Guinea Domes (GD, AD) are located in the eastern margin of the north and south tropical gyres.

The northward warm NBC mass transport exceeds the required AMOC transport by around 17 Sv (Frajka-Williams et al., 2019). Hence, an important part is distributed through the recirculation pathways of the interior basin, which mostly take place through a complex retroflection system. As the NBC crosses the equator and the Coriolis force turns zero, it is more influenced by wind forcing and pressure gradient fluctuations. Further north, near 7°N, the annual motion of the ITCZ is responsible for piling surface waters and creating a latitudinal pressure-gradient that drives the seasonal appearance of a zonal jet (Rosell-Fieschi et al., 2015). Therefore, an unstable NBC retroflects into the equatorial and tropical ocean at different latitudes and depths. Two major zonal currents arise from the NBC retroflection (NBCR) system in the upper layer (Figure 1.1): the EUC and the North Equatorial Countercurrent (NECC). Moreover, resulting from the 7°N seasonal retroflection process, the NBC switches between times when it flows into the Caribbean essentially unperturbed and periods when anticyclonic rings are shed. In either case, it is an important mechanism of the inter-hemispheric exchange of mass and heat transport and major part of the AMOC returning limb (Garzoli et al., 2004; Jochumsen et al., 2010; Stramma et al., 2005).

The most prominent seasonal variations are found north of the equator, between 4°N and 10°N where the NBCR connects with the NECC, an eastward current closely tied with the seasonal cycle of the trade winds. In boreal spring, when the ITCZ begins to shift northward, the NECC starts to form along 6°-7°N in the eastern Atlantic. The NECC progressively extends to the western margin, until the ITCZ reaches its northernmost position in late summer (Rosell-Fieschi et al., 2015). In late winter, when the ITCZ is back to its southern location, the entire NECC disappears and the flow is dominated by the southward extension of the North Equatorial Current (NEC), the southern branch of the North Atlantic sub-tropical gyre.

South of the NBC-NECC system, the thermocline waters retroflect from the NBC to feed the EUC. The EUC is bounded by two other sub-thermocline currents, the North and South Equatorial Undercurrent (NEUC and SEUC), both also supplied by the retroflection of the NBC waters. In contrast with the NECC, the EUC is a quasi-permanent eastward flow with its core located at the thermocline level. The EUC plays an important role in the equatorial Atlantic ecosystem through vertical mixing and zonal advection, as it provides highly-oxygenated waters to the equatorial and Guinea Gulf upwelling systems (Foltz et al., 2019). Moreover, its recently observed intensification counteracts warming-induced deoxygenation in the upper ocean (Brandt et al., 2021).

Because of its role in the inter-hemispheric exchange of heat and mass transport, the NBC-NECC retroflection has attracted much interest among the oceanographic community during recent decades. In contrast, the water sources and pathways that contribute to the NBC-EUC retroflection, and their interaction with the fluctuations in the trade wind system, still remain poorly understood. In **chapter 3** we use off-line Lagrangian modelling again in order to characterize the EUC formation at the western margin. Our results reveal four main sources, and their water mass transformation, that feed the NBC-EUC retroflection. Moreover, the Lagrangian analysis suggest that the recent EUC intensification is associated with an increment of water mass contribution from south-eastern tropical Atlantic.

1.3 Tropical Atlantic Variability

The tropical Atlantic climatic system is the result of complex local and remote ocean-atmosphere interactions at multiple time scales. The annual cycle is the dominant variability in the tropical Atlantic. In the ocean, it is characterized by the formation of the cold tongue in the central and eastern equatorial Atlantic in boreal summer (June-July-August, JJA). SSTs reach their minimum as a result of the trade winds intensification, which build up a zonal pressure gradient and cause the elevation of the thermocline depth in the eastern side. Cool waters from the intensified coastal upwelling system in Gulf of Guinea also propagate westward along the equator. The consequence is the development of a distinct cold tongue centered slightly south of the equator, reaching its maximum in July and August (Ding et al., 2009).

In the atmosphere, the seasonal pattern is defined by the meridional excursions of the thermal equatorial maximum (ITCZ). The ITCZ is associated with a narrow low-pressure surface band, characterized by cumulus clouds and heavy precipitation due to the convective air circulation. At the surface levels, the north and south trade winds systems converge into the ITCZ. In contrast with the land, where the ITCZ largely follows the seasonal march of the Sun, in the ocean the

ITCZ position is coupled with the SST distribution (Philander et al., 1996). The wind-evaporation-SST (WES) feedback narrows the convective zone to a band of warm SSTs, between 27°C and 29°C (Xie & Philander, 1994). As a consequence, the oceanic ITCZ is tied with the equatorial asymmetric SST distribution and its fluctuations over time. From March to April, the SST is uniformly warm between 10°S and 5°N, the oceanic ITCZ is therefore very near the equator, where the trade winds converge. In June, the equatorial cold-tongue starts to develop and the ITCZ is displaced north in the eastern side of the tropical Atlantic. The ITCZ gradually moves northward from east to west and reaches its northernmost position in September.

Superimposed onto the seasonal fluctuations, two leading modes of interannual variability can disrupt the climatology of the tropical Atlantic (Figure 1.2). These modes are defined by zonal and meridional gradients of anomalous SST (SSTA), respectively, with important climatic implications on the surrounding continents. The first mode of interannual variability is the Equatorial Mode (EM), also known Atlantic Niño/Niña, characterized by intermittent oscillations in the seasonal cold-tongue formation. Typically, the EM is phase-locked with the seasonal cycle as the maximum anomalous SST appears in boreal summer in the central-eastern equatorial Atlantic. The resultant zonal SSTA gradient responds to zonal wind anomalies and is also reflected at thermocline depth. The warm (cold) EM corresponds to a deeper (shallower) thermocline at the cold tongue region in boreal summer, led by anomalous westerly (easterly) wind anomalies at the western equatorial Atlantic in boreal spring (Keenlyside & Latif, 2007). The variability is usually characterized with the ATL3 index that is the averaged SST anomaly over the ATL3 region [20°W-0°E, 3°S-3°N](Figure 1.2).

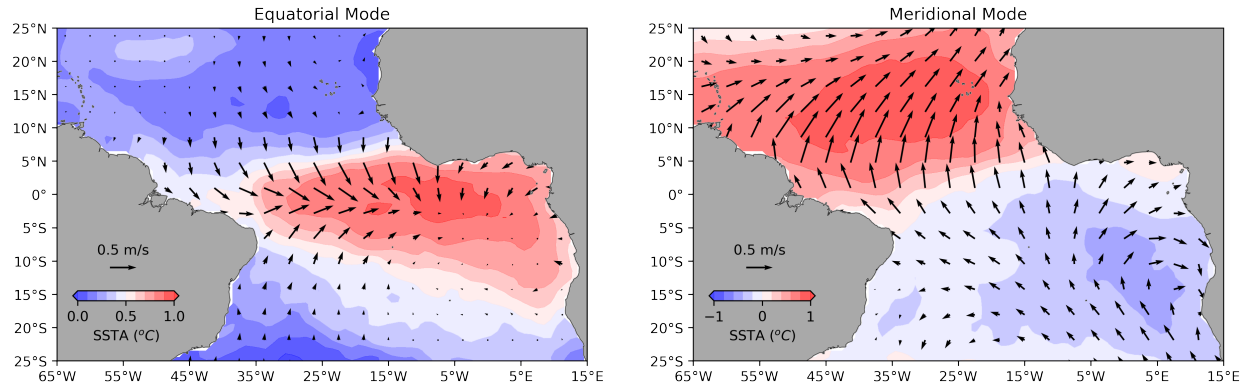

Figure 1.2: SSTA (contours) and wind (vectors) anomalies regressed onto two first Principal Component Analysis (PCA) which corresponds to the EM and MM. PCA is calculated on SSTA in tropical Atlantic derived from HadiSST dataset (Rayner et al., 2003) between 1948 and 2014. Wind anomalies are derived from NCEP/NCAR reanalysis data set for the same time-span (Kalnay et al., 1996).

Because of its similarity with El Niño-Southern Oscillation (ENSO), the warm EM is also known as the Atlantic Niño. It is widely accepted that the same coupled ocean-atmospheric mechanisms in ENSO-like dynamics, known as Bjerknes feedback (Bjerknes, 1969), operate in the Atlantic Niño (Keenlyside & Latif, 2007; Lübbecke & Mcphaden, 2013). This feedback mechanism consists of three components summarized in Figure 1.3: during the development of Atlantic Niño the (1) equatorial easterlies weaken in the western basin, (2) thermocline deepens in the east, which means an increase of the heat content in the mixed layer, which causes (3) a warming of

the eastern basin SST above average. Nevertheless, in the tropical Atlantic the amplitude of these components is weaker than in the Pacific (Keenlyside & Latif, 2007; Zebiak, 1993). For instance, during an Atlantic Niño year the SSTA hardly exceeds 1°C in the ATL3 region, in contrast with 3°C for the Pacific. The timing and spatial distribution also notably differs from its Pacific counterpart. A narrow SSTA distribution placed near the equatorial Atlantic band in JJA contrasts with the extended dipole structure in the tropical Pacific lasting a minimum of five months (Lübbecke et al., 2018).

Despite the prevailing thought of Bjerknes feedback as the main driver for the Atlantic Niño, additional mechanisms have been proposed to generate equatorial Atlantic variability (e.g., Brandt et al., 2011; Foltz & McPhaden, 2010; Lübbecke et al., 2018; Richter et al., 2013). Remarkably, some warm events develop despite the absence of anomalous westerly winds, or even in the presence of intensified easterlies from previous boreal spring. Richter et al. (2013) classified these events as non-canonical, suggesting that they might be driven by meridional advection of anomalous warm sub-surface water from north of the equator. However, other mechanisms might be involved in the development of these atypical Atlantic Niño events. Brandt et al. (2011) revealed the generation of eastern equatorial SST variability as a result of upward energy propagated through vertically alternating equatorial deep-jets. Another relevant and more often mechanism is the wave-induced temperature anomaly through off-equatorial forced Rossby waves boundary-reflected into equatorial Kelvin waves (hereinafter, RW-reflected mechanism) (Burmeister et al., 2016; Foltz & McPhaden, 2010; Lübbecke & McPhaden, 2012, Figure 1.3). In this case, the sea-level anomalies associated with the wind-forced Rossby waves gives relevance to the off-equatorial pre-conditions that may be related to other local and remote climate forcing. Concretely, the RW-reflected mechanism can be forced by an intrinsic Meridional Mode (MM) pattern (Foltz & McPhaden, 2010; Martín-Rey & Lazar, 2019) or the remote ENSO influence (Lübbecke & McPhaden, 2012; Martín-Rey et al., 2018). In chapter 4 we describe the RW-reflected mechanism using a group of ocean reanalysis and model simulation. Moreover, we explore the response of the upper-ocean circulation described in chapter 3 under the emergence of both tropical modes.

Typically, the MM develops in boreal spring when the SST variability in the tropical north Atlantic is strongest and the ITCZ is most sensitive to anomalous meridional SST. Enhanced cross-equatorial winds flow towards the anomalous warm SST region as the ITCZ moves meridionally towards the warmer hemisphere (Chang et al., 1997; Nobre & Shukla, 1996). The MM is also associated with rainfall variability in north-eastern Brazil and Sahel regions (Folland et al., 1986; Kushnir et al., 2006; Nobre & Shukla, 1996), as well as increased atmospheric cyclone activity (Patricola et al., 2014; Vimont & Kossin, 2007). In contrast with the Atlantic Niño, where ocean dynamics has an important role, the MM is more related to thermodynamic mechanisms described in the WES feedback (Amaya et al., 2017; Chang et al., 1997; Xie & Philander, 1994).

Several model studies have shown that both the Atlantic Niño and MM can be excited by large-scale forcing such as variations in the North Atlantic Oscillation (NAO), ENSO and Atlantic Multidecadal Oscillation (AMO) (e.g., Chiang et al., 2002; Czaja et al., 2002; Kerr, 2000; Martín-Rey et al., 2018; Tokinaga et al., 2019; Wang et al., 2004). In particular, the AMO has been considered as the footprint of AMOC on SST variability at decadal and multidecadal time scales. A positive AMO is characterized by warm SSTA in the entire North Atlantic, concurrent with cool SSTAs

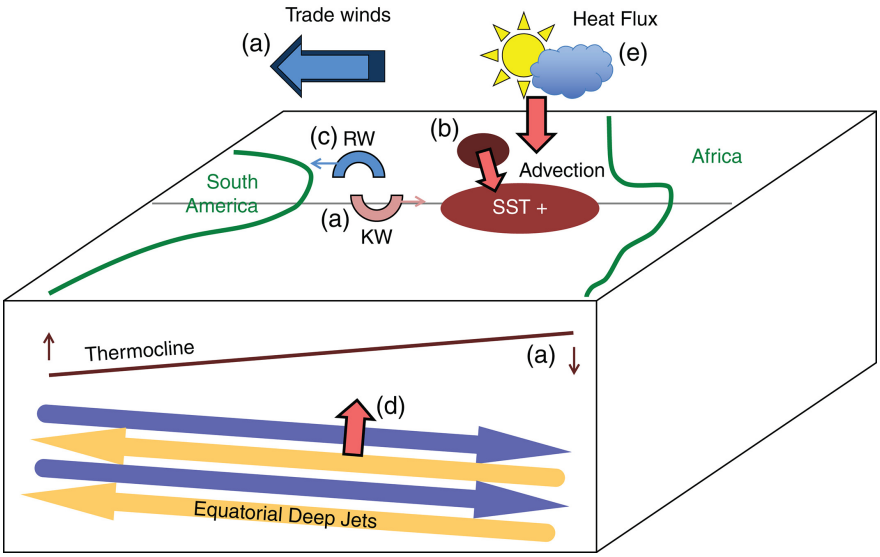

Figure 1.3: Schematic of different mechanisms involved to generate the Atlantic Niño: (a) the Bjerknes feedback is associated with weaker trade winds and the adjustment of the thermocline depth; (b) the meridional advection of temperature anomalies; (c) Rossby wave propagation and reflection as Kelvin waves; (d) zonal propagation of equatorial deep jets; (e) appearance of net surface heat flux anomalies (source: Lübbecke et al., 2018).

in the South Atlantic (Enfield et al., 2001; Knight et al., 2006). This basin-wide anomalous SST appears to be strongly associated with the MM and is manifested in the tropical Atlantic climate (e.g., Vimont & Kossin, 2007). Additionally, Martín-Rey et al. (2018) show that different AMO phases induce changes in the Atlantic subtropical Highs, modulation the tropical Atlantic mean state. They noted that a shallow mean thermocline, associated with negative AMO, is responsible for a higher SST variability in the eastern equatorial Atlantic. Indeed, several model studies suggest that North Atlantic SST responds to multidecadal changes of the AMOC suggesting that a potential weakening of the AMOC may induce negative AMO-like SST distribution, hence impacting SST variability in the tropical Atlantic (Haarsma et al., 2008; Latif et al., 2006; Polo et al., 2013; Svendsen et al., 2014; Wang & Zhang, 2013).

The large-scale and local forcings and their interactions can modulate the emergence, properties and impacts of the Atlantic Niño (Losada & Rodríguez-Fonseca, 2016; Losada et al., 2012a; Losada et al., 2012b; Martín-Rey et al., 2018; Martín-Rey et al., 2014; Rodríguez-Fonseca et al., 2009). In **chapter 5** we explore the diversity of Atlantic Niño by applying an inter-event Empirical Orthogonal Function (EOF; Lee et al., 2014) to different reanalysis data-sets. Our results show four distinct types of Atlantic Niño according to its onset and persistence, also illustrating different zonal distributions along the equatorial band.

1.4 Aims and thesis outline

Although the monitoring of the tropical Atlantic has progressed substantially over the last decade (Bourlès et al., 2008; Foltz et al., 2019), available observational periods are still short and irregular in time and space. he scarcity of in-situ data turns model and reanalysis datasets into an indispensable tool to understand the whole tropical Atlantic system. The main objective of this

thesis is to improve our knowledge of the tropical Atlantic system, from upper-ocean circulation to climatic variability, using a combination of observational, reanalysis and model datasets. Each of the following chapter addresses this need to provide further knowledge about the processes involved in the upper ocean circulation and their connection with basin-scale climate variability modes. Our results allow for achieving a better understanding of the crucial role played by the tropical Atlantic in the global climate system.

In **chapter 2** we situate the tropical Atlantic as an interhemispheric gateway for the Atlantic meridional overturning circulation (AMOC). The AMOC returning limb, which flows from the South Atlantic to the tropical Atlantic Oceans, is the cause that heat transport in the entire Atlantic flows northwards. In particular, it is the main transfer mechanism of mass and heat from the South Atlantic subtropical to tropical gyres. However, the exchange between the subtropical and tropical gyres is bidirectional, with relatively shallow tropical waters reaching the subtropics. In order to investigate the intensity of the AMOC returning limb and the water exchange between the subtropical and tropical South Atlantic gyres, we use the Lagrangian modelling on a velocity field that arises from a global ocean reanalysis dataset. We release particles in the southern and northern boundaries of an area where subtropical and tropical gyre meet in order to estimate the relative southward and northward transfer of mass and heat in the upper 1500 m of the water column.

We plunge into the tropical Atlantic in **chapter 3** where we describe the North Brazil Current (NBC) – Equatorial Undercurrent (EUC) retroflection. Thermocline waters carried by the NBC, partly composed by AMOC waters, turn eastward to ventilate the EUC, which constitutes the northern (southern) branch of the North Atlantic (South Atlantic) tropical gyre. To this end, we start with observations acquired during the MOC2 oceanographic cruise carried out in April 2010 in the west-equatorial region. Lowered Acoustic Doppler Current Profile (LADCP) velocities are used to provide a quasi-synoptic picture of the current system and to quantify the Eulerian water mass balances. These observations, however, do not allow us to investigate the water sources and retroflection pathways. Hence, we use a detailed Lagrangian analysis that help us, on one hand, determine the water sources, water mass transformation and retroflection pathways in the western equatorial Atlantic, and, on the other hand, provides the possibility of examining the temporal variability over an 18-years period.

Chapter 4 is a preliminary study where we search the potential link between the upper-circulation system with the main two modes of interannual variability in the tropical Atlantic, the Meridional Mode (MM) and the Equatorial Mode (EM). Our aim is to characterize the response of the surface and sub-surface currents under the emergence of tropical modes. For such purpose, we quantify how the connectivity between the western and eastern equatorial Atlantic is altered by the propagation of Rossby waves and their western-boundary reflection into eastward equatorially-trapped Kelvin waves. The study uses a set of three oceanic reanalyses, an interannual forced-ocean simulation and Lagrangian simulations have been used.

In **chapter 5** we investigate the complexity of interannual variability in the tropical Atlantic. Concretely, we focus on the intrinsic diversity of the warm EM event, referred as Atlantic Niño. The variability in the onset and dissipation of anomalous sea surface temperatures (SSTs) is captured by four main types of Atlantic Niño through an inter-EOF analysis of monthly-mean SST

anomalies (SSTAs) (Lee et al., 2014). Using different observational and reanalysis datasets, we discuss the mechanisms involved behind each variety of Atlantic Niño and the rainfall response over West-Africa and South America.

The thesis ends with a concluding **chapter 6** where we expose the main results, summarize the most relevant conclusions and point at future lines of research.

Chapter 2

Subtropical-tropical transfer in the South Atlantic Ocean

Here we explore the water transfer between the subtropical and tropical gyres of the South Atlantic Ocean to better understand its unique equatorward heat delivery. A Lagrangian technique is applied to the reanalysis product GLORYS2V4 in order to trace back the western boundary flow in the tropical (North Brazil Undercurrent, NBUC) and subtropical (Brazil Current) gyres. Most of the northward NBUC core transport (14.9 Sv at 8°S) arrives from the eastern boundary subtropical current (Benguela Current) via the zonal South Equatorial Current. This subtropical-tropical transfer represents the core of the returning limb of the Atlantic meridional overturning circulation and accounts for most of the observed increase in heat and salt-volume transports (0.18 PW and 0.19 Sv from 30°S to 8°S, respectively) across the South Atlantic. The NBUC also includes Antarctic Intermediate Water below 400 m (7.4 Sv at 8°S) coming from the interior subtropical gyre, as well as water from the current's surface and peripheral components coming from the tropical gyre (13.3 Sv at 8°S). The Brazil Current (9.9 Sv at 29°S) is mostly composed of subtropical water originating in the upper 800 m west of the eastern boundary current at 30°S (8.5 Sv), with a minor contribution of surface tropical water that transfers to the subtropics (1.4 Sv).

This chapter has been published as: Cabré, A., Pelegrí, J. L., and Vallès-Casanova, I. (2019). Subtropical-tropical transfer in the South Atlantic Ocean. Journal of Geophysical Research: Oceans, 124(7), 4820-4837, https://doi.org/10.1029/2019JC015160.

2.1 Introduction

The South Atlantic plays a crucial role in the returning limb of the Atlantic meridional overturning circulation (AMOC), being the only basin that transfers heat equatorward from the subtropics to the tropics to compensate for the southward transfer of North Atlantic Deep Water (NADW; Ganachaud & Wunsch, 2000; Garzoli et al., 2013; Talley, 2003). However, the exchange pathways between the subtropical and tropical gyres in the South Atlantic are poorly understood, due to both an historical lack of observations and the complex interaction between the upper-thermocline gyres and the AMOC. The South Atlantic subtropical gyre is characterized by an anticyclonic

(anticlockwise) circulation, with the isopycnals (sea surface height) deepening (rising) toward the gyre center located in the western half of the basin (e.g., Garzoli et al., 2013; Schmid, 2014). The western boundary current of this subtropical gyre is the Brazil Current (BC), and its southern limit is the South Atlantic Current, starting at the Brazil- Malvinas Confluence near 39–40°S and flowing east between about 43°S and 47°S, on the northern side of the subantarctic fronts (e.g., Boebel et al., 1999; Garzoli, 1993; Gordon, 1989; Jullion et al., 2010; Orúe-Echevarría et al., 2019). The subtropical water masses continue northward in the eastern side as the Benguela Current (Garzoli & Gordon, 1996) and finally flow back to the western boundary as the South Equatorial Current (SEC).

The tropical gyre meets with the subtropical gyre along the SEC, before turning north along the western boundary as the North Brazil Undercurrent (NBUC). A fraction of this near-surface current recirculates into the equatorial ocean via the Equatorial Undercurrent (EUC) (and its southern and northern branches) and upwells in the central and eastern equatorial ocean. This upwelled water is then carried southward mostly by Ekman surface flows before subducting back toward the northwest, hence joining the SEC and completing what is called the subtropical cell (STC; Hazeleger & Drijfhout, 2006; Schmid, 2014; Schott et al., 2004). The bifurcation latitude between the northward and southward western boundary currents, defining the western end of the tropical-subtropical border, shifts poleward with depth (Stramma & England, 1999). Surface water masses (0–100 m) bifurcate around 14°S (Rodrigues et al., 2007) where the southward BC originates. The South Atlantic Central Water bifurcates around 21°S and the Antarctic Intermediate Water (AAIW) near 28°S (Stramma & England, 1999). This results both in the downstream deepening of the BC towards the Brazil-Malvinas Confiuence (Rocha et al., 2014) and the shoaling of the NBUC toward the tropics (see schematics in Soutelino et al., 2013).

The presence of the AMOC modiies the picture of two semi-isolated wind-driven gyres, accounting for the transfer of water masses from the subtropical to the tropical gyre mostly along the SEC (Lazar et al., 2001)(Garzoli Matano, 2011;. Another consequence of the AMOC is that a portion of subtropical water masses originates or recirculates into other basins as part of a Southern Hemisphere supergyre (Fratantoni et al., 2000; Laurian & Drijfhout, 2011; Speich et al., 2007). According to Gordon et al. (1992) and most recent literature (e.g., Speich et al., 2007), a major proportion of the surface and central water masses that end up in the Benguela Current and SEC are irst carried to the Indian Ocean through the South Atlantic Current and then recirculate back via the Agulhas Current past South Africa. Some of the deeper AAIW that eventually becomes part of the AMOC recirculates even further east into the Pacific basin (Speich et al., 2007).

Our goal is to expand our knowledge on the interconnections between the subtropical and tropical gyres in the South Atlantic down to a depth of 1500 m, which includes all surface, central, and intermediate water masses. For this purpose, we use the hydrographic and velocity fields from GLORYS2V4, an eddy-permitting reanalysis model. From the release of particles along selected sections, we infer the predominant pathways and ages for water parcels transferring between the subtropical and tropical gyres as well as for water parcels recirculating within each gyre. In particular, we focus on the pathways followed by the subtropical water masses that reach the NBUC—what may be considered as the returning branch of the AMOC in the South Atlantic and investigate the mechanisms responsible for the associated changes in heat and freshwater

transports. The structure of the chapter is as follows. In section 2 we introduce the data and methods, and in section 3 we present the pathways and the heat and salt transports associated with the different water masses. We conclude in section 4 with a discussion of the new perspectives brought about by the Lagrangian approach and of the mechanisms necessary to produce the observed changes in heat and salt transport.

2.2 Materials and methods

2.2.1 Reanalysis model GLORYS2v4

The Mercator Ocean team computed and provided monthly-averaged values from the reanalysis model GLORYS2V4, an eddy-permitting model with $\approx 0.25°$ resolution (Garric et al., 2017, herafter GLORYS). The monthly climatology includes values of salinity, temperature, and the three-dimensional velocity field, as calculated using the 23-year data set (1993 to 2015). Our region of study is the South Atlantic Ocean between 30°S and 5°S and down to 1500 m. The position of the northern and southern boundaries ensures that the entire subtropical-tropical boundary is contained in the domain and further warrants that the particles circulate only once through either the subtropical or the tropical gyre before leaving the domain. Mignac et al. (2018) have recently performed an exhaustive comparison between current data assimilation products (including GLORYS), free-running models, and observations. This comparison shows that the reanalysis products are more accurate than the free-running models at representing the AMOC's strength and meridional heat transport at 35°S and the NBUC volume transport at 11°S. Although the heat and volume transports are systematically underestimated across models, GLORYS is the one that shows the highest agreement with observations (Mignac et al., 2018). Drijfhout et al. (2003) have also found that eddy-permitting models are essential to correctly represent the Lagrangian pathways in the thermocline. These results endorse the idea that GLORYS will be a very valuable tool for examining the exchange of subtropical and tropical waters in the South Atlantic Ocean; further information on the model's performance can be found in von Schuckmann et al. (2016).

2.2.2 Lagrangian experiments

We use the Connectivity Modeling System code v2.0 (Paris et al., 2013) (Paris et al., 2013) to track 10000 particles pathways offline. The inputs for this code are the time-varying horizontal (u, v) and vertical w velocity component fields and fixed values for the horizontal (k_h) and vertical (k_v) diffusion coefficients. We choose two latitudinal sections near the western boundary (black lines in Figure 2.1a) where we release the particles and trace their trajectories back in time to study the transport between the subtropical and tropical gyres.

1. Section 8°S experiment traces back the northward flow at 8°S in the upper 1400 m layer, between the South American coast and 15°W (Figure 2.1d). This experiment is designed to include both the NBUC, which is located between the continental slope and about 32.5°W, and the northward thermocline transport ($\approx$ 50–200 m) found in the interior ocean as far as 15°W.

2. Section 29°S experiment traces back the southward flow at 29°S in the upper 1000 m layer, between the coastline of South America and 46°W (Figure 2.1f). This experiment is designed to

track the BC, isolated from the deeper northward countercurrent and from the deeper southward deep western boundary current.

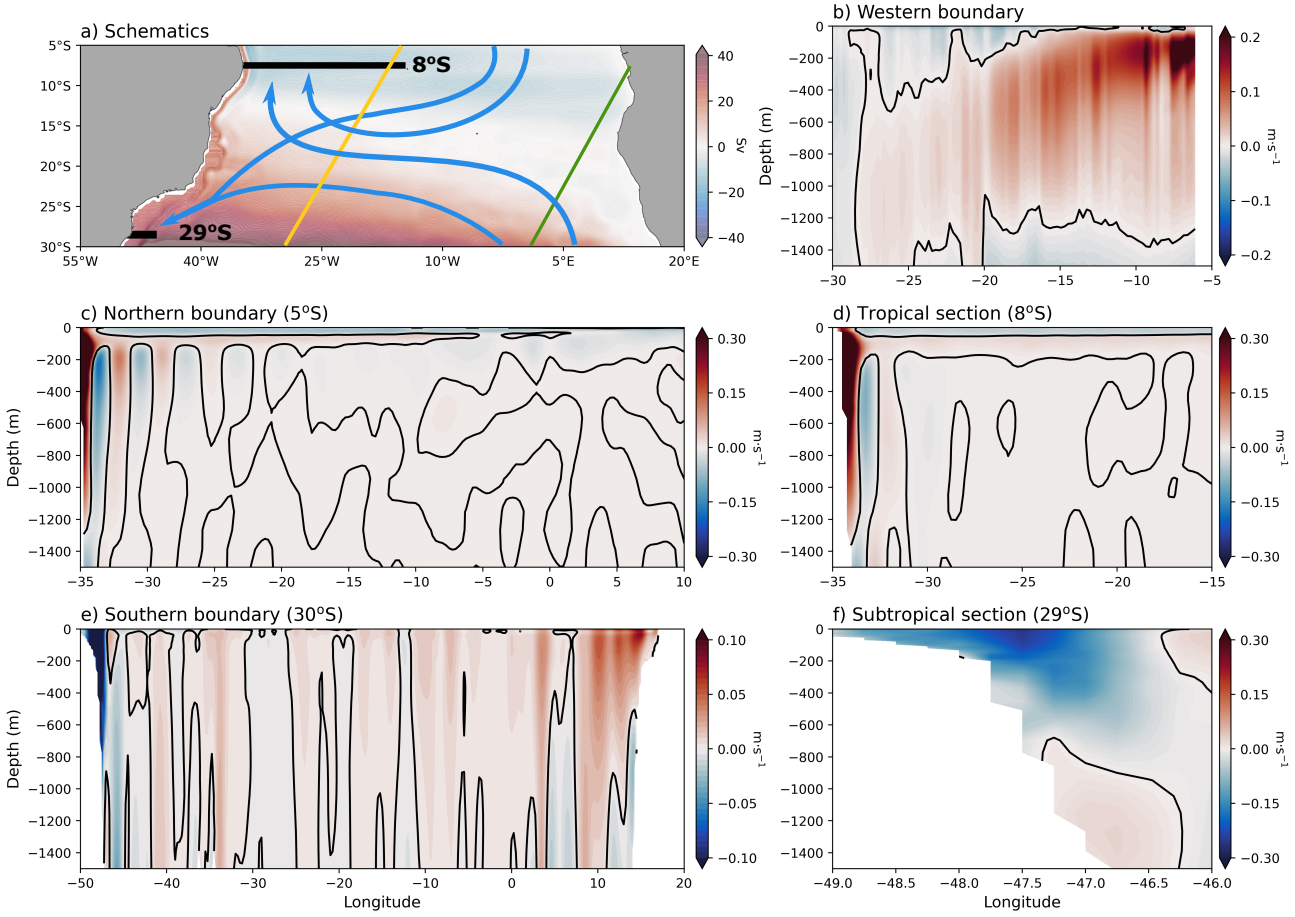

Figure 2.1: (a) Meridional transport (Sv) in the top 1500 m, accumulated from the eastern boundary, as obtained from climatological averaged meridional velocities. The experiment release sections are shown in black, the northern and southern boundary sections in gray, and the schematic representations of the four possible trajectories in blue. Two sections approximately perpendicular to the main flow are shown in yellow (western) and green (eastern). (b) Western-boundary meridional velocity, averaged within a 2.5° band off the coast (m s^{-1}) as a function of depth (m) and latitude. Meridional velocity (m s^{-1}) depth-longitude profile at (c) the northern boundary (5°S), (d) the 8°S release section, (e) the southern boundary (30°S), and (f) the 29°S release section.

The number of particles N released at each pixel (lon, depth) is set to be proportional to the meridional transport at that location, vA (where v is the meridional velocity and A is the vertical area of the pixel, Δlon Δdepth), that is, more particles are released wherever and whenever the meridional transport is higher. This way, each particle carries the same water transport (vA/N), which optimizes the sampling and facilitates the calculation of Lagrangian streamlines (Blanke et al., 1999; Peña-Izquierdo et al., 2015; van Sebille et al., 2018). Our focus is on the climatological and year-averaged velocities, hence leaving aside the impact of interannual variations. The difference between both cases will reveal the role of seasonality on the net transfer of water between the tropical and subtropical gyres. We use the monthly-averaged velocity and density data interpolated every 3 days, as several tests show that the trajectories are fairly insensitive to a higher temporal resolution while a lower resolution causes some significant differences in the fast-current regions

(not shown). The model is eddy-permitting but not entirely resolved, so the level of diffusion is probably underestimated (see a more detailed analysis of diffusion parameters in Peña-Izquierdo et al., 2015). We have studied the sensitivity of our results when the following diffusion parameters are added to the Lagrangian experiments: k_h = 0, 100, 500, 1000 m^2 s, and k_v = 0, 10^5, 10^6, 10^7 m^2 s^{-1}. We find that a value of 100 m^2 s^{-1} for horizontal diffusivity minimizes the number of particles that are lost near coastal regions or near the surface due to methodological limitations. This is also the preferred value in Peña-Izquierdo et al. (2015), who analyzed in detail the differences between horizontal diffusivity coefficients in the ECCO2 model, with the same horizontal resolution as GLORYS. Changes in vertical diffusion do not affect our results significantly, so we set it to 0 for the final experiments. Importantly, our general conclusions remain the same when using a different set of diffusion parameters (see the sensitivity of the Lagrangian transports to a selected set of diffusion parameters in Table 2.1).

2.2.3 Lagrangian stream-function

The Lagrangian stream-function differs from the traditional Eulerian stream-function because it only shows the transports associated to pathways that end up at the release section (Blanke et al., 1999, and references therein). The calculation is straightforward if we assume conservation of volume transport, which holds true if particles leave the studied domain. This is the case for our experiments, where nearly all released particles (> 97%) leave the domain in less than 50 years. To calculate the Lagrangian stream function in the South Atlantic, we first define an output grid (0.5° resolution) and evaluate, at each time step (backward in time) and for each particle, whether the particle has moved meridionally to a different output grid cell. If so, the initial meridional transport (vA/N), positive for the 8°S experiment and negative for the 29°S experiment, is added to the intersection between cells (multiplied by -1 if northward, +1 if southward to account for backtracking of the particle trajectory). If more than one cell is crossed in a single time step, transport is added to each crossed intersection. Eventually, the particles leave the domain either through the northern or southern borders (Figures 2.1c and 2.1e). The meridional transport is cumulatively integrated with longitude (from the eastern side of the Atlantic) and results in our final Lagrangian stream function.

2.2.4 Mass, heat, and salt transport calculation

The total volume V and mass M transports (m^3 s and kg s) are calculated as

$$V = \sum_{i=1}^{N} V_i, \; M = \sum_{i=1}^{N} \rho_i V_i \tag{2.1}$$

where V_i is the i particle volume transport (m^3 s^{-1}) and ρ_i the water density at the i location. Volume transport is conserved by construction in our experiments, and mass transport is almost conserved because particles approximately follow constant density lines. The total heat transport H (in watts) across a section at any fixed latitude is calculated as

Table 2.1 Sensitivity of experiments to a selection of horizontal and vertical diffusion parameters ($m^2\ s^{-1}$) and to the use of different velocity fields (Climatological CLIM Versus Year-Averaged YR-AV)

Section	Pathway	CLIM $k_h = 0$ $k_v = 0$	CLIM $k_h = 100$ $k_v = 0$	CLIM $k_h = 100$ $k_v = 10^{-5}$	CLIM $k_h = 500$ $k_v = 0$	YR-AV $k_h = 100$ $k_v = 0$	YR-AV $k_h = 500$ $k_v = 0$
8°S	5°→ 8S	12.9	13.3	13.1	14.0	13.1	13.6
(38.5 Sv)	30°→ 8S	21.9	22.3	22.4	23.1	22.4	23.4
	z >1500 m→ 8S	3.6	2.9	3.0	1.4	3.0	1.5
29°S	5°→ 29S	-1.5	-1.4	-1.5	-1.6	-1.6	-1.6
(-9.9 Sv)	30°→ 29S	-8.4	-8.5	-8.4	-8.3	-8.3	-8.3

Note. The table shows the water volume transport (Sv) associated to each Lagrangian experiment. The first column shows the collecting section (the meridional water transport is shown in parenthesis, with positive/negative values indicating northward/southward transports), the second column indicates the pathway, and the remaining columns quantify the associated northward/southward (positive/negative) transports.

$$H = c_p \sum_{i=1}^{N} \rho_i V_i (T_i - T_r) \tag{2.2}$$

where T_i is the particle potential temperature, T_r is the reference temperature (set as 0°C), and c_p is the sea water heat capacity ($c_p = 3985$ J kg^1 K^1). The salt transport S (kg s^{-1}) is calculated as

$$S = \sum_{i=1}^{N} \rho_i S_i V_i \tag{2.3}$$

where S_i is the particle salinity. In this paper, the salt transport is also expressed in mass transport units (Sv), following Talley (2008) and using 35 as the average salinity,

$$S = \sum_{i=1}^{N} \frac{S_i}{35} V_i \tag{2.4}$$

2.2.5 Trajectory clustering

We also average the spatial trajectories (longitude, latitude, and depth) and properties (temperature, salinity, and density) for all the particles that belong to one same group. For example, in section 2.4 we consider all particles that belong to the same density bin (group) and combine the individual trajectories based on the fraction of distance traveled from the origin to the end section (after normalizing the traveled distance for each particle from 0 to 1). These results are not an exact representation of the real averaged trajectories but help visualize the differences between groups.

2.3 Transfer of water masses between the tropical and subtropical gyres

We can use the velocity fields at any time to calculate the instantaneous depth-integrated (0 – 1500 m) Eulerian stream function. As for the Lagrangian streamlines, we do so by accumulating the meridional transport from the eastern side of the basin. Since we are not integrating the full water column, and there is a small fraction of water particles that upwells from deeper layers, the

Eulerian transport is not strictly conserved. However, the non-conservative fraction is small so that the Eulerian stream function becomes a useful complementary tool.

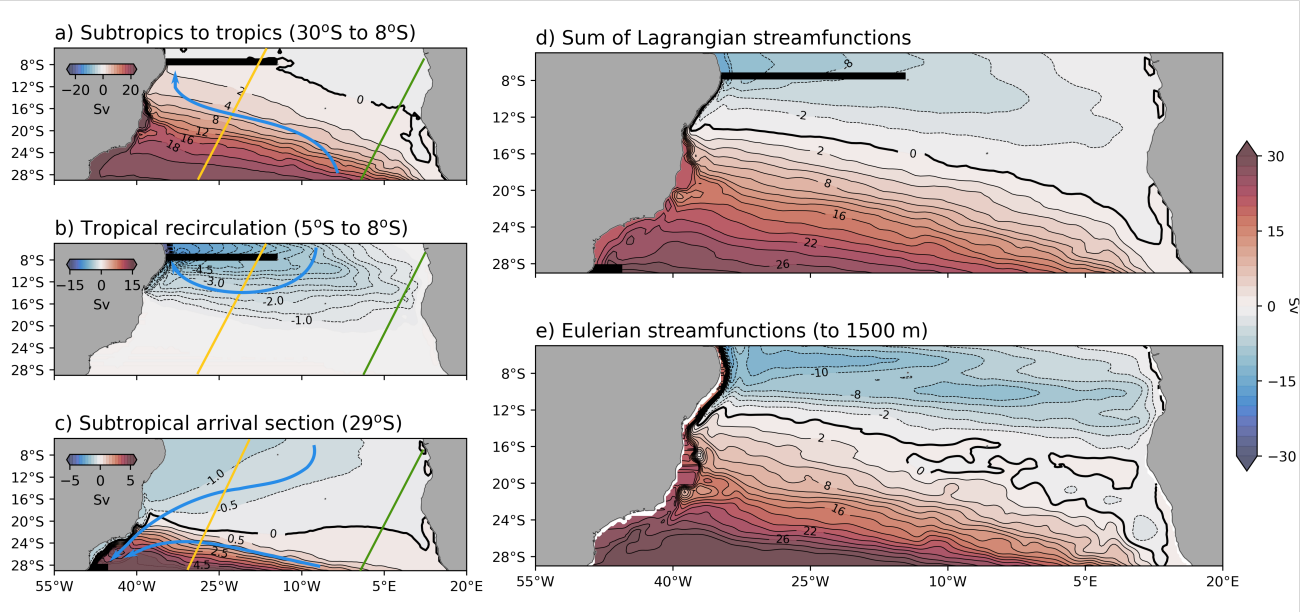

Figure 2.2: Lagrangian streamlines (Sv) for particles that (a) transfer from 30°S to 8°S, (b) transfer from 5°S to 8°S, and (c) end at the subtropical 29°S section. The release sections are shown in black, the two sections perpendicular to the main flow are shown in yellow and green as in Figure 2.1a, and the schematic of the trajectories are shown in blue. The sum of the four Lagrangian streamlines is shown in (d). The Eulerian stream function down to a depth of 1500 m is shown in (e) for comparison.

The mean velocity fields (Figures 1.1b – 1.1f), and the Eulerian (Figure 1.2e) and Lagrangian streamlines (Figures 1.2a – 1.2d) reflect the existence of the western and eastern boundary currents. These boundary currents are identified as a connected region, adjacent to the continental slope, where the flow has one predominant direction. At the reference sections, they are located as follows: The NBUC is found west of 33°W at 5°S (Figure 1.1c) and west of 32.5°W at 8°S (Figure 1.1d), the BC is placed west of 46.2°W at 29°S (Figure 1.1f) and west of 47°W at 30°S (Figure 1.1e), and the Benguela Current is located east of 8°E at 30°S (Figure 1.1e).

For our analysis we follow Ganachaud and Wunsch (2000) and Talley (2003) and split the particles among surface and near-surface, central, and intermediate layers, considering their initial or final vertical location; along their trajectory, particles often change greatly their location in the water column (Table 2.2). The surface particles occupy roughly the upper 60 m of the water column (potential density σ_0 less than about 25.0/25.5 kg m^{-3} in the western/eastern basins), and the near-surface particles are found immediately below, down to some 100–200 m (σ_0 up to 26.0 kg m^{-3}). The central layers correspond to the Subtropical Mode Waters, corresponding to thermocline waters reaching down to less than 600 m (σ_0 from 26.0 to 26.8 kg m^{-3}). The intermediate layers travel at depths of roughly 500 – 1500 m, including both Subantarctic Mode Water (SAMW, with σ_0 from 26.8 to 27.2 kg m^{-3}) and AAIW (σ_0 from 26.8 to 27.55 kg m^{-3}).

The main objective of the forthcoming discussion is to understand and quantify the four possible pathways for water departing in the tropical/subtropical gyres and ending at the NBUC and

Table 2.2 The average depths at which the given water masses (left column) reach their maximal potential density value σ_0 for the Different Latitudinal Sections; This also includes the dependence with longitude

Water mass	σ_0 max kg m^{-3}	Depth (m)					
		8°S section	29°S section	5°S west of 0°E	5°S east of 0°E	30°S west of 8°E	30°S east of 8°E
Surface	25	104	13	82	35	25	–
Near surface	26	148	203	111	79	162	103
Central	26.8	306	578	339	364	590	456
Intermediate	27.2	848	1080	837	831	1096	906
	27.55	1390	1765	1371	1372	1712	1510

BC: the subtropical and tropical recirculations and the exchange between the tropical and subtropical gyres (blue trajectories in Figure 1.1a). Throughout this paper, we will refer to those water masses transferred from the subtropical to the tropical gyre as AMOC water masses.

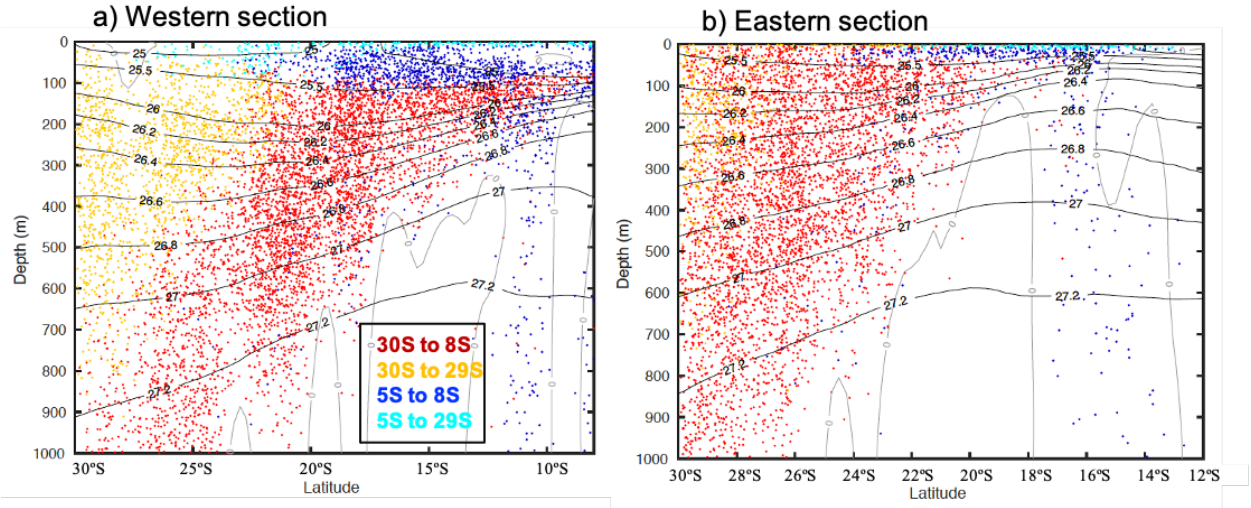

Figure 2.3: Depth-latitude distribution of particles flowing west in the (a) western and (b) eastern cross sections of Figure **??**a, colored by the water route as labeled. The black lines show the potential density contours (σ_0), and the gray line shows the zero zonal velocity contour

2.3.1 Velocity fields and water masses

The boundary current system off the eastern coast of South America (Figure 2.1b) is similar to the one simulated by Rodrigues et al. (2007), who studied in detail the bifurcation between northward and southward currents at the western boundary. The western boundary currents at 5°S and 11°S are consistent with Hummels et al. (2015) and Schott et al. (2005) observations, both in terms of depth structure and volume transports. Further, the southward deepening and strengthening of the BC in GLORYS approximately coincides with real estimates obtained from moorings in Rocha et al. (2014). They find 5.7 Sv at 25°S (mooring C3, July and August) and 10.0 Sv at 28°S (mooring W333, December and January), while we respectively find 5.1 and 10.4 Sv when considering the same sampling periods.

Figure 2.3 shows the spatial distribution of the different water masses when crossing the South Atlantic westward through oblique sections centered at 25°W and 5°E (hereafter western and eastern sections; yellow and green lines in Figure 2.1a, respectively). Consider first the eastern section, which is clearly dominated by the subtropical pathways to the tropics (30°S to 8°S, AMOC water; Figure 2.2a and red dots in Figure 2.3b); these water masses account for most of the transport to the northwest (18 Sv), while subtropical recirculating water masses represent only 1.5 Sv. The subtropical recirculation takes place further south and shallower than the AMOC water, its surface layers reaching only as far north as about 20°S (orange dots in Figure 2.3b). We find that the direction of the velocity at 30°S determines whether the particle will continue to the north or will recirculate within the subtropical gyre: The more northward the velocity at 30°S, the more likely it will leave the subtropical gyre and reach 8°S (not shown).

Only a small fraction of tropical recirculating water masses (1.1 Sv) reach the eastern section (blue dots in Figure 2.3b). These water masses flow either (a) within the surface (upper 50 m), on top of AMOC water masses (0.3 Sv) and interacting with surface recirculating subtropical water masses from 24°S to 21°S, (b) at similar depths as AMOC water (0.2 Sv), or (c) through deep zonal jets at $\tilde{1}$5–17°S that do not interact with AMOC water (0.6 Sv).

Consider now the western section where all four pathways are clearly separated (Figure 2.3a). The Vitória-Trindade Ridge, which along this section is located at 21°S, defines the near-surface bifurcation latitude between the subtropical gyre (5.5 Sv) and the AMOC water mass (21.8 Sv), in agreement with Soutelino et al. (2013). The bifurcation latitude shifts south with depth (see also black line in Figure 2.1b). Note that the subtropical gyre penetrates to the intermediate layers (Figure 2.3a), in agreement with results by Schmid et al. (2000). Moreover, this western section clearly illustrates that the entire AMOC transfer, from the subtropics (30°S) to the tropics (8°S), occurs mainly within central and intermediate layers.

The transport of recirculating tropical water masses that reach the western section equals 3.9 Sv, with about half arriving directly from 5°S and the other half after having transited southeast into the Angola Dome (Figure 2.2b), returning west partly as deep zonal jets along 10–12°S (1.0 Sv; blue dots in Figure 2.3a). The tropical water masses that are transferred to the subtropics (1.4 Sv) flow on top of the recirculating tropical water masses (cyan dots in Figure 2.3a) and eventually fill the surface part of the southward flow in the western boundary (Figure 2.1b).

2.3.2 Transport at the tropical 8°S section

A total of 38.5 Sv follow north through the 8°S section, with most of it (35.0 Sv) occurring at all depths within the NBUC and a small fraction (3.5 Sv) flowing through the interior thermocline near the surface (50–150 m). The origins of this northward current are shown in Figure 2.4a. Most of it, 22.3 Sv (58% of the total volume transport), enter the domain in the subtropics (30°S, black dots and contours in Figure 2.4a). These subtropical water masses feed the core of the NBUC (21.4 Sv at depths 100 to 1200 m) and the near-surface interior layers (0.9 Sv at depths 50 to 150 m). The 8°S current also transports 13.3 Sv of tropical origin (34.5% of the total volume transport), feeding the surface (3.8 Sv) and eastern edge (6.2 Sv) layers of the NBUC, the central and intermediate layers near 32°W (1 Sv at depths 200 to 1,000 m), and the near-surface (50–150 m) interior flow as

far as 15°W (1.8 Sv; red dots and contours in Figure 2.4a). The remaining fraction of the NBUC (2.8 Sv, 7%) originates below 1500 m in the subtropics (green dots in Figure 2.4a).

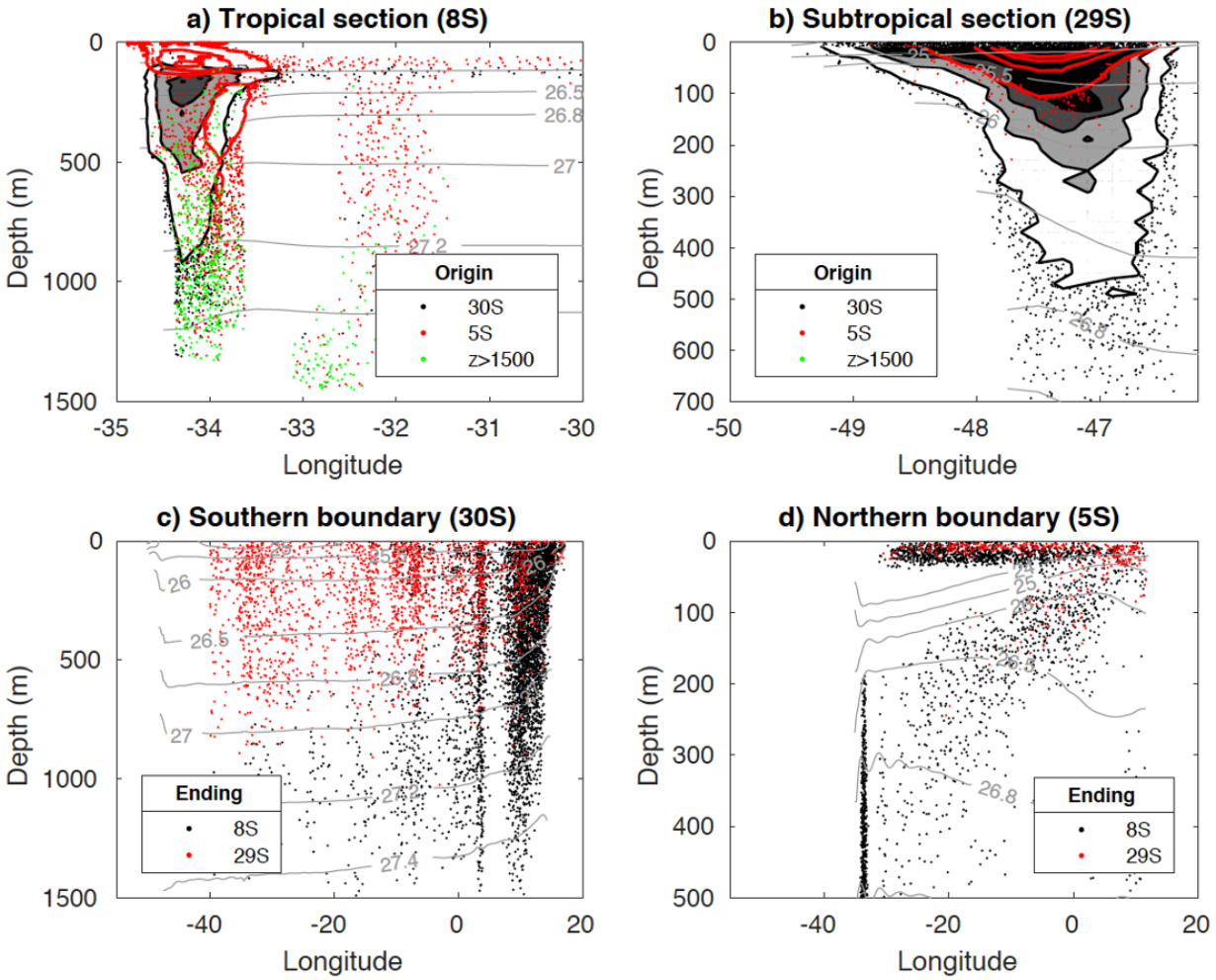

Figure 2.4: Spatial distribution of particles at (a) the tropical section (8°S), (b) the subtropical section (29°S), (c) the southern boundary (30°S), and (d) the northern boundary (5°S), colored depending on the origin and ending as labeled. In (a) and (b), for the sake of clarity, the colored dots are replaced by contour lines wherever the number of particles is large (>10, 25, 60, and 80 particles in pixels of size 0.2° × 20 m). The potential density lines (s0) are shown in gray.

As noted in the methods section, the results are qualitatively similar when using different diffusivities (Table 2.1). However, as the horizontal diffusivity increases, the border between the tropical and subtropical Lagrangian streamlines diffuses and the number of particles originating deeper than 1500 m decreases (not shown).

2.3.2.1 Subtropical to tropical transfer (30°S to 8°S)

Most of the water of subtropical origin (originating at 30°S) that ends in the NBUC at 8°S comes from the deep flow (down to ≈ 1500 m) in the eastern basin (east of 8°E) at 30°S (14.9 Sv; black dots in Figure 2.4c). This flow constitutes the core of the returning limb of the AMOC, arriving mainly from the Indian Ocean via Agulhas rings and filaments (e.g., Donners & Drijfhout, 2004; Gordon et al., 1992; Speich et al., 2007). Finding the exact origin of this northward flow at 30°S

would require running the Lagrangian experiments over a much larger domain, which is beyond the scope of this paper.

Interior water masses (departing west of 8°E at 30°S) also reach 8°S along the intermediate layers, carrying a total of 7.4 Sv. In particular, we find that 6 Sv of these intermediate water masses are transported at $\sigma_0 > 27$ kg m^{-3}, comparable to the 4 Sv reported by Boebel et al. (1999) or the 5 Sv by Schmid et al. (2000) at the same densities. These water masses bifurcate around 28°S in the western boundary, at a location known as the Santos bifurcation (Boebel et al., 1999; Stramma & England, 1999).

Figure 2.2a shows the Lagrangian streamlines for water masses that transfer from 30°S to 8°S. In general, these water masses flow northwestward along a wide band from the eastern side at 30°S to the western boundary where they feed into the northward boundary current. Those water masses that reach the western boundary at the northern latitudes cross the South Atlantic more to the north (Figure 2.2a) and come from the subsurface eastern boundary at 30°S ($25.5 < \sigma_0 < 26.5$ kg m^{-3}; blue and green dots in Figure 2.5a), while water masses originating more to the west and deeper at 30°S flow more directly westward and arrive to the western boundary further south (Figure 2.5a). Another way of understanding the large spatial range of the South Atlantic northwestward subtropical-to-tropical transfer is through a latitude-depth distribution of particles through the western-basin section (which is roughly perpendicular to the main flow, yellow line in Figure 2.1a), illustrating the departing longitude at 30°S (Figure 2.5b). The deeper the transfer, the further south it occurs, in agreement with Stramma and England (1999). At any depth, the westward transfer occurs over a latitudinal band about 10° wide, the latitude of transfer varying both with depth and with the original longitude at 30°S.

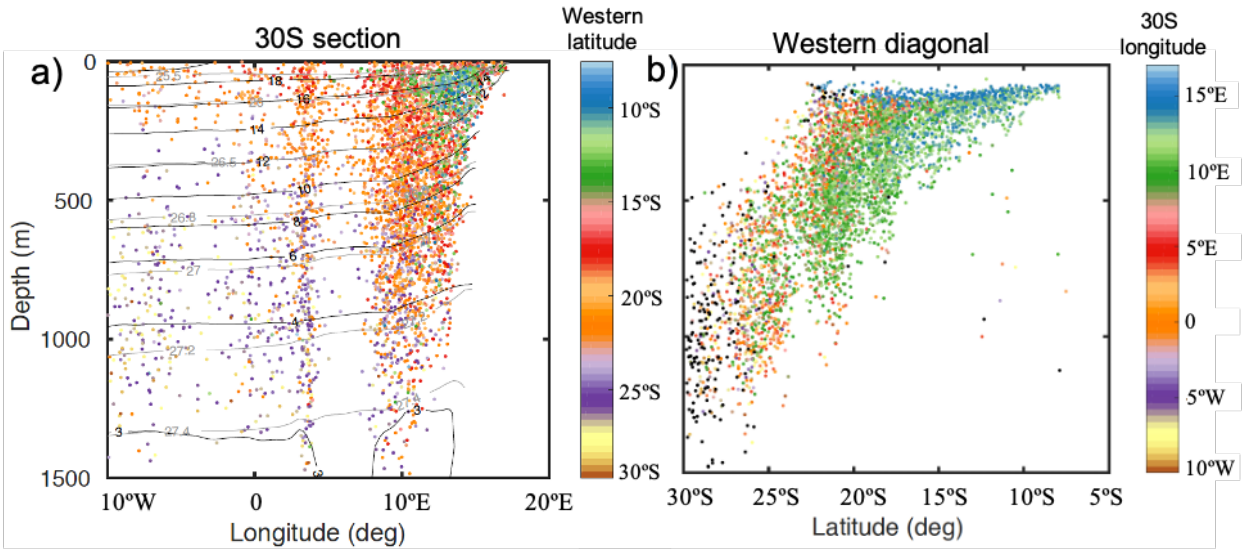

Figure 2.5: (a) Depth-longitude distribution in the eastern margin of 30°S for AMOC particles transferred from 30°S to 8°S, colored by the latitude crossing the western section (yellow line in Figure 2.1a), with density and temperature contours overplotted in gray and black, respectively. (b) Depth-latitude distribution along the western section for AMOC particles, colored by their longitude at the southern boundary (30°S). In both panels, black colored dots show data outside the longitudes or latitudes in the color bars.

Crossing the South Atlantic from 30°S to 8°S takes 8.9 years on average, with a long tail in the distribution and the 20% slowest particles taking over 21.2 years to cross (dark red line in

Figure 2.6a). On average it takes 4.7 years for the surface and near-surface particles, 6.2 years for the central water masses, and 12.8 years for the intermediate water masses (Figure 2.6b). Lazar et al. (2001) found timescales of 5–6 years for anomalies propagating through the thermocline from 30°S to the equator, in good agreement with our results.

2.3.2.2 Tropical recirculation (5°S to 8°S)

The tropical water masses (originating at 5°S, Figure 2.1c) that end up northward at 8°S (red dots in Figure 2.4a) come either from the surface (20–60 m) throughout the entire 5°S section (4.6 Sv), from the near-surface and upper-thermocline layers (4.0 Sv east of 32°W) or from the intermediate western boundary layers (4.6 Sv west of 32°W; black dots in Figure 2.4d).

At 5°S, the surface waters (4.6 Sv) flow southwest before turning north along the western boundary (Figure 2.2b), on average taking 2.6 years to get to 8°S (yellow line in Figure 2.6c). Of these, many particles (40%, 1.9 Sv) recirculate along the surface but 60% (2.7 Sv) escape from the surface winter mixed layer depth, constituting the STC. About 1.1 Sv of these STC subsurface water masses flow along the upper-thermocline, and the remaining 0.7 Sv reach much deeper, in the intermediate levels. We observe that the STC water remains largely separated from the AMOC water masses, in agreement with Hazeleger and Drijfhout (2006), who found that STC water masses feed the surface part of the northward current at 6° and 10°S while AMOC water masses feed the subsurface part of the current (>100 m).

The water masses that originate below the thermocline at 5°S (4.0 Sv) move preferentially toward the southeast before winding west and northwest along the western boundary (Figure 2.2b), in agreement with Hazeleger and Drijfhout (2006). These water masses end up at surface and near surface at 8°S (red dots in Figure 2.4a), mostly above AMOC water masses (black dots in Figure 2.4a), taking on average 14.1 years to flow from 5°S to 8°S, the traveling time increasing with depth (purple line in Figure 2.6c).

Finally, there is a tight recirculation of deep central and intermediate water near the western boundary (western black dots in Figure 2.4d), with 4.6 Sv of water flowing south off the boundary current and recirculating northward at 8°S (red dots and contours east of the core NBUC in Figure 2.4a). These water masses take on average 5.1 years to flow from 5°S to 8°S, the longer, the deeper in the water column they are (orange line in Figure 2.6c).

2.3.2.3 Comparison with literature

Hazeleger and Drijfhout (2006) found 16 Sv of AMOC transport using a simulation with the same horizontal resolution as ours (0.25°). They found that around one third of the AMOC water upwells in the tropics and part of it (2 Sv) recirculates into the STCs before continuing northward. We find a similar amount of STC water masses (2.7 Sv) in our experiments.

Blanke et al. (1999) studied the transport of water from 10°S to 10°N, down to a depth of 1200 m, with a low-resolution simulation (2° zonal and 0.5–1.5° meridional). They found 37.3 Sv of volume transport flowing northward at 10°S, mostly through the western boundary, similar to our 38.5 Sv at 8°S (down to 1500 m), with 17.4 Sv reaching all the way to 10°N. This interhemispheric handover, which is mainly associated to the AMOC, is comparable but less than the transfer we

find from 30°S to 8°S: 14.9 Sv through the eastern boundary (east of 8°E at 30°S, z = 0–1500 m) and 7.4 Sv from intermediate layers (west of 8°E at 30°S, z > 700 m).

The AMOC water masses continue into the North Atlantic subtropical gyre (out of our domain), either directly along the western boundary for the deep water masses (7°C; Blanke et al., 1999) or after meandering around the tropics multiple times for warmer particles (Blanke et al., 1999; Hazeleger & Drijfhout, 2006). In particular, Blanke et al. (1999) found that 19.9 Sv (out of the 37.3 Sv northward transport at 10°S) recirculate in the tropics and return back to 10°S without contributing to the interhemispheric transfer of heat. When comparing their results with ours, we deduce that their recirculating surface and upper-thermocline water coincides roughly with our southward surface tropical water at 5°S. Blanke et al. (1999) also show that intermediate tropical water masses recirculate close to the western boundary, similarly to Schott et al. (2005) who observed this deep tight counterflow at 5–11°S with an associated transport (5 Sv) similar to our result (4.6 Sv).

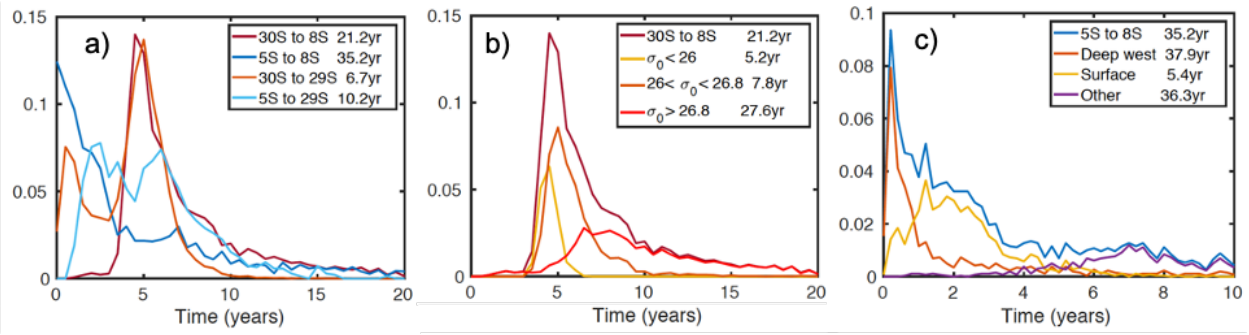

Figure 2.6: (a) Histograms showing the transfer time for the four different routes (arbitrarily normalized to a unit area), as labeled (bin width is 0.5 years). (b) Contributions of different density bins in the 30°S to 8°S course, as labeled. (c) Contributions of the different depth levels in the 5°S to 8°S course, as labeled (bin width is 0.2 years). The legend also shows the time that divides the 80% quickest particles from the 20% slowest particles.

2.3.3 Transport at the subtropical 29°S section

The southward western boundary BC carries a total of 9.9 Sv at 29°S, split between 1.4 Sv at the surface and near-surface layers coming from the tropics (red dots and contours in Figure 2.4b), and 8.5 Sv at the upper-thermocline layers coming from the subtropics (black dots and contours in Figure 2.4b). The subtropical water masses reaching 29°S originate mostly west of 8°E at 30°S (west of the AMOC eastern boundary flow) in the surface and central layers (red dots in Figure 2.4c), taking an average of 4.4 years (orange line in Figure 2.6a). The tropical water masses transferring to 29°S come mainly from the surface (1.0 Sv) and near-surface (0.4 Sv) layers at 5°S (red dots in Figure 2.4d); these water parcels on average take 5.8 years, the further west they start, the quicker the transfer (cyan in Figure 2.6a).

These results indicate that the timescale needed for thermocline particles to cross the South Atlantic is typically 5–10 years. This applies to the water parcels recirculating the tropical gyre (dark blue in Figure 2.6a), to those beginning at 30°S as part of the AMOC and arriving to 8°S (red in Figure 2.6a), and to the particles recirculating within the subtropics (orange in Figure 2.6a).

2.3.4 Heat and freshwater transfer

2.3.4.1 AMOC returning water

We first focus our analysis on the AMOC water (e.g., transfer from 30°S to 8°S in our experiment). The total heat transport at any latitude and longitude (cumulative with respect to the western boundary) is the sum of the conserved heat transport—calculated considering that the water particles maintain their 30°S original temperature along their trajectory (contour lines in Figure 2.7) and the heat gain at any latitude as compared with 30°S (color shading in Figure 2.7). Water masses flowing from 30°S to 8°S transport 0.90 PW of heat at 30°S and gain an additional 0.20 PW along the South Atlantic, most of it (0.15 PW) occurring gradually from 30°S to 18°S. Water masses departing 30°S west of 8°E originally transport 0.64 PW and only warm by 0.02 PW (Table 2.3); in contrast, water masses departing east of this latitude initially only carry 0.26 PW and warm by 0.18 PW (Table 2.3). After their incorporation into the western boundary, water masses actually cool slightly (0.01 PW). See Table 2.3 for a comparison among water masses.

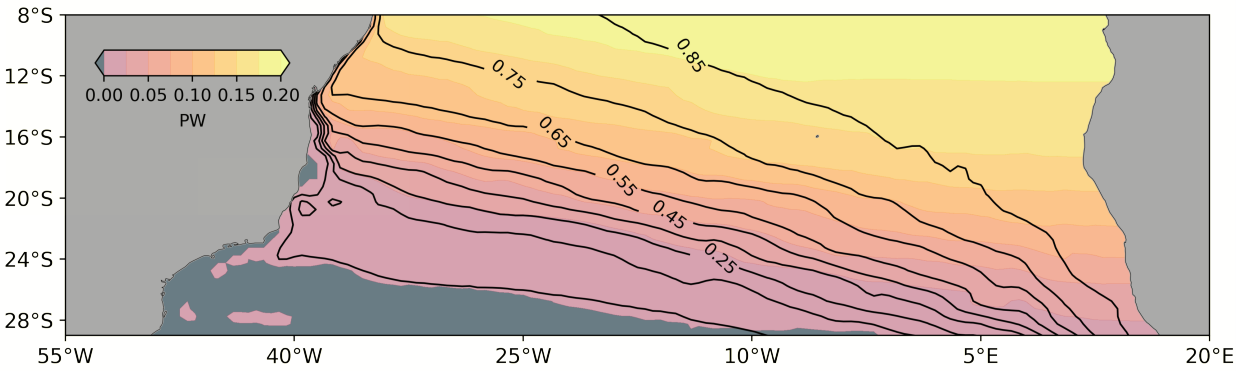

Figure 2.7: The color-filled contours show the northward heat transport (PW) that is gradually accumulated from the western and southern boundaries as particles increase their temperature while moving from 30°S to 8°S. In contrast, the black solid contours show the conservative northward heat transport accumulated from the western boundary, calculated considering that the water particles maintain their 30°S original temperature along their trajectory.

Temperature and salinity increase toward the tropics up to 8°S along isopycnals and also toward the west for light water masses (σ_0 < 26 kg m^{-3}; not shown). Hence, as particles cross the South Atlantic approximately along isopycnals, we expect them to gain not only heat but also salt. In particular, subtropical (30°S) water reaching 8°S gains 0.22 Sv of salt-volume transport (Table 2.3).

Within the central water stratum, temperature and salinity bear a linear relation, with both properties increasing toward the sea surface (light blue and green dots in Figure 2.8a; Poole & Tomczak, 1999). A scatter plot of temperature and salinity changes between 30°S and 8°S displays an approximate linear relation (Figure 2.8b). Since the slope of the central-water T-S relation is greater than the slope of the isopycnals (Figure 2.8a), we expect the particles to move toward lighter isopycnals to match the observed temperature and salinity increase (Figure 2.8b). Indeed, as particles flow north, the temperature increase overcompensates the salinity changes

Table 2.3 The 30°S-to-8°S volume transport, total heat gain and total salinity gain.

Volume transport		Heat gain	Salt gain
Total	22.3 Sv	0.20 PW	7.8×10^{-6}kg s^{-1} (0.22 Sv)
Eastern boundary water (East of 8°E at 30°S)	66.9%	88.8%	86.7%
Intermediate water ($\sigma_0 > 26.8$)	45.2% (25.6)	36.6% (30.1)	19.5% (16)
Central water ($26 < \sigma_0$ 26.8)	39.8% (31.0)	41.6% (41.0)	41.3% (40)
Surface and near surface ($\sigma_0 < 26$)	15.0% (10.2)	21.8% (17.7)	39.2% (30.7)
Water masses that downwell (from 30°S to western section)	54.7% (36.2)	43.9% (39)	63.9% (53.2)
Water that warms the most ($\Delta T > 5$°C)	13.5% (13.2)	50.4% (49.5)	47.2% (46.5)
Interior arriving water (East of 33°W at 8°S)	4.6%	16.8%	15.3%

Note. The following rows show the percentage of the total for the different water masses (defined in the first column). In parentheses are percentage values of the total contributed by the eastern boundary current (east of 8°E at 30°S).

so that water masses gain some buoyancy (Figure 2.8c). However, we find that changes in density are relatively small when compared to changes in spiciness (Flament, 2002), showing that most of the diffusive and advective motions occur along quasi-isopycnals. We also find that, for the same change in temperature, surface particles increase their salinity more than deep particles (Figure 2.8b and Table 2.3). This means that, for a similar increase in spiciness, the surface particles decrease their density less than the deep particles, essentially indicating the more stable character of the highly stratified near-surface waters (Figure 2.8c).

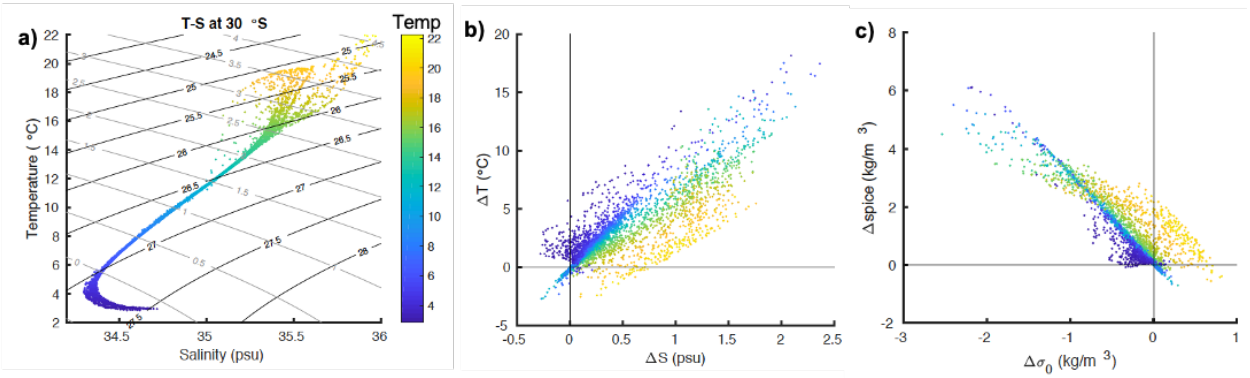

Figure 2.8: (a) Temperature-salinity scatter plots at 30°S for AMOC water masses transferring from 30°S to 8°S. (b) Scatter plot of the change in temperature and salinity for particles starting at 30°S near the eastern boundary (longitude > 8°E; colored by initial temperature). (c) Scatter plot of the change in density and spiciness for particles, as in (b).

Where and how are particles warming? The majority of the AMOC particles crossing the ocean gain heat, apart for a small fraction that cool (Figures 2.8b and 2.9a) once inside the western boundary. As we have already said, most of the heat gain (88.8%) occurs for 30°S particles departing east of 8°E (Table 2.3 and green and yellow dots in Figure 2.9a). This heat gain occurs through

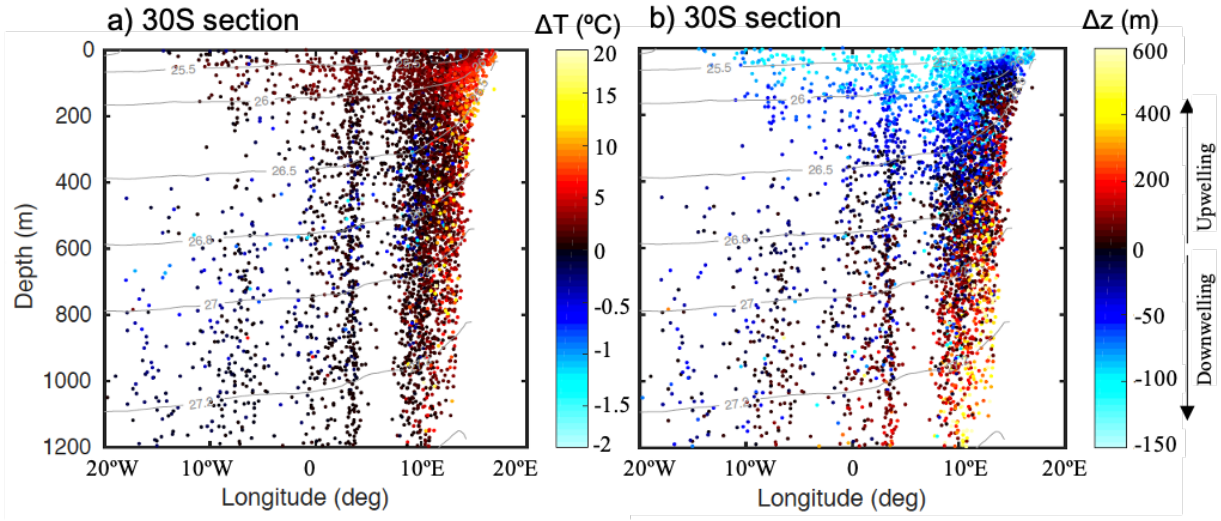

Figure 2.9: Depth-longitude distribution of the Atlantic meridional overturning circulation particles (30°S to 8°S) in the eastern side of 30°S, colored by (a) temperature increase from 30°S to the western cross section and (b) depth change (m), positive if particles upwell and negative if particles downwell. Note that the color tables are linear, but the stretch depends on the sign of the data points. Potential density lines (σ_0) are overplotted in gray.

the full depth of the water column, in central (41.6%), intermediate (36.6%), and surface/near-surface layers (21.8%; Table 2.3). About 50% of the heat gain occurs through particles that warm over 5°C (Table 2.3) mostly in the central and intermediate layers (green and blue in Figure 2.8b). In order to identify how these particles gain so much heat, we group together the particle trajectories based on the total temperature change from 30°S to 8°S, as explained in section 2.5. The average trajectories show again that the eastern particles warm most and travel further north (red lines in Figure 2.10d). They warm by upwelling several hundred meters when crossing the South Atlantic (especially from 30°S to 22°S, red lines in Figures 2.10e and 2.10f; see also upwelling in Figure 2.9b) and mixing with surface warm water masses. Such large upwelling is associated with the rising of the isopycnals at the boundary between the subtropical and tropical gyres, with most warming occurring in the easternmost central and intermediate layers (Figure 2.9a). On the other hand, surface and near-surface layers downwell along isopycnals and experience small or moderate warming (Figure 2.9).

2.3.5 Other pathways

We next repeat the procedure of last section and explore the heat and salt gain in the other three pathways: recirculations within the subtropical and tropical gyres and transfer from the tropics to the subtropics. In particular, following section 2.5, we group the particle trajectories based on their total temperature and salt changes and summarize here the main findings.

Subtropical recirculating water masses (30°S to 29°S) transfer northward 0.51 PW of heat at 30°S and gain 0.04 PW on their way to 29°S (salmon pink trajectory in Figure 2.11). While crossing the Atlantic, these particles in average downwell without much warming except for the easternmost water masses, which initially upwell and warm (similar to the eastern AMOC water masses)

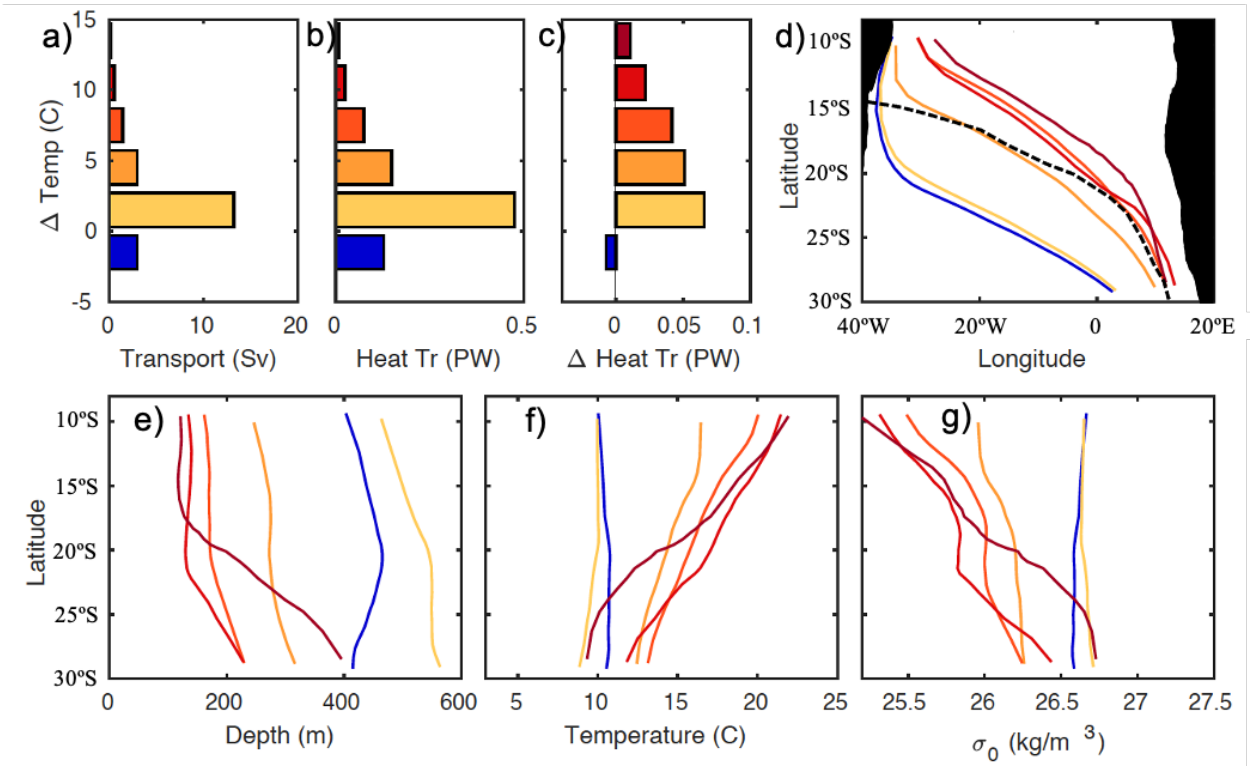

Figure 2.10: Histograms of (a) volume transport and (b) heat transport at 30°S and (c) heat gain for these particles after reaching 8°S, binned as a function of the total temperature change. We present, for each temperature bin, (d) the mean trajectories (longitude and latitude) as well as the (e) average depth, (f) temperature, and (g) density (as a function of latitude) along these pathways; the curves are color-coded as in panels (a-c). The zero Lagrangian streamline in Figure 2.2d is shown as a dashed line in panel (d).

before submerging back to the west. However, water masses that cross 30°S west of 10°W warm only once inside the western boundary.

Tropical recirculating water masses warm and get saltier when circulating around the tropical gyre from 5°S to 8°S (three darkest blue trajectories in Figure 2.11). The warming (0.08 PW) occurs only for water masses below the surface mixed layer, which first flow southeast and then warm as they move toward the western boundary (not shown). In the process, these waters also increase their salinity by 0.08 Sv. Surface water masses that subduct in the STC (into the saltier near-surface layers) also increase their salinity by 0.10 Sv.

Tropical water masses that feed into the subtropical southward flow do not experience any significant change in either heat or salinity (light blue trajectory in Figure 2.11).

2.4 Discussion and concluding remarks

We have combined the Connectivity Modeling System code v2.0 offline tracking software (Paris et al., 2013) and the GLORYS velocity fields (Ferry et al., 2012) to backtrack particles released in the western boundary region of the tropical (8°S) and subtropical (29°S) South Atlantic gyres. For our analyses, we have explored four paths of propagation down to 1500 m within the subtropical and tropical gyres and the exchange between both gyres. The water masses are split among surface, near-surface, upper-thermocline (central), and intermediate strata (Table 2.2).

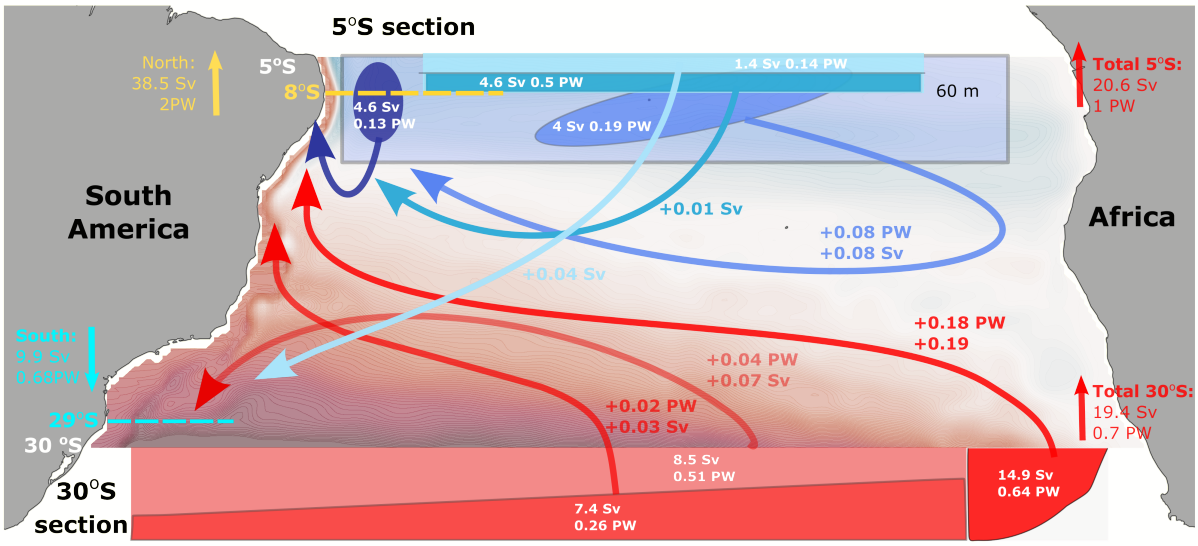

Figure 2.11: Schematics showing the average transfer between tropical and subtropical gyres on top of the Eulerian streamlines in Figure 2.1a. In red, water masses coming from the subtropical 30°S section (darker red if deeper). In blue, water masses coming from the tropical 5°S section (darker blue if deeper). The initial water-volume (Sv) and heat (PW) transports are labeled in white; the heat gain (PW) and salt transport gain (Sv) are labeled along the pathway if higher than 0.01. The collecting sections are shown as dashed lines.

Figure 2.11 and Table 2.3 summarize the main pathways of transfer, and the volume and heat transport associated to each of these, when using mean-seasonal-cycle velocity fields and fixed diffusivities (k_h = 100 m^2 s^{-1}, and k_v = 0 m^2 s^{-1}). We find that the results are qualitatively similar when adopting different diffusivities (Table 2.1). The conclusions are also similar when using yearly averaged velocity fields instead of climatological ones (Table 2.1), which suggests that seasonality does not play a significant role in the mean transfer between gyres. However, there are substantial differences across seasons, which need to be considered in order to avoid biases when looking at any particular set of field observations not averaged throughout the whole year.

The tropical gyre represents the pathway from the transoceanic 5°S section to the 8°S western boundary section, while the tropical-subtropical transfer corresponds to the transfer from the transoceanic 5°S section to the 29°S western boundary section. All the pathways starting at 5°S are shown in blue in Figure 2.11. The initial water-volume (Sv) and heat (PW) transports are labeled in white at 5°S, and the heat gain (PW) and salt transport gain (Sv) are labeled along the pathways when higher than 0.01. Most subsurface tropical water masses starting at 5°S end up recirculating into the tropical gyres and become warmer (0.08 PW) and saltier (0.18 Sv) on their way to 8°S. In contrast, most surface tropical water masses end up transferred to the subtropical gyre, carrying 1.4 Sv and 0.14 PW southward.

The subtropical gyre is assessed as the route from the transoceanic 30°S section to the 29°S western boundary section. This pathway is formed by surface, near-surface, and central water masses that depart 30°S at longitudes mostly west of 8°E (red dots in Figure 2.4a). We find that

the subtropical recirculating water masses warm by 0.04 PW from 30°S to the western boundary at 29°S where they flow southward, hence being responsible for a small net southward heat transport. Talley (2003) estimated a net southward warming of ≈ 0.1 PW at 32°S when excluding AMOC water masses. She defined the subtropical gyre as the region with $\sigma_0 < 26.2$ kg m^{-3} starting from the western side until the longitude where the interior northward volume transport equals the southward western boundary transport, hence leaving out the easternmost water masses with net northward transport as AMOC. To compare this value to our results, we must add the heat transport from the tropical gyre to the subtropical gyre (0.14 PW) to the net subtropical warming (0.04 PW). Hence, we effectively find a southward warming of 0.18 PW at 29°S, higher but comparable to the ≈ 0.1 PW estimated by Talley (2003) at 32°S. Talley's method is different from ours, which grants confidence to our results.

The return branch of the AMOC the subtropical-tropical transfer—responds to the pathway from the transoceanic 30°S section to the 8°S western boundary section. It is attained through parcels in the Benguela Current spanning the entire water column (14.9 Sv), from the surface down to intermediate layer, and through intermediate water flowing across the entire subtropical basin (7.4 Sv). All this water ends up in the NBUC and is transferred to the tropical gyre (Figure 2.2a), after gaining 0.20 PW and becoming saltier by 0.22 Sv. Most of the heat and salt gain occurs for water masses of eastern origin (0.18 PW and 0.19 Sv; Table 2.3), while the rest of heat and salt is added by interior intermediate water masses (0.02 PW and 0.03 Sv). This heat gain is mostly explained by the upwelling of water masses in the easternmost central and intermediate layers that mix with more buoyant water masses along the Benguela Current and, to a lesser degree, by surface and near-surface water masses that head generally north as they depart from 30°S and gradually experience moderate warming and downwelling. According to Hazeleger and Drijfhout (2006), AMOC water masses gain an additional ≈ 0.22 PW of heat when crossing from 10°S to 10°N but freshen by 0.16 Sv due to intense precipitation in the tropics.

The classical Eulerian view on the meridional extent of the subtropical gyre (zero Eulerian streamline, located near 12°S in the western boundary in Figure 2.2e) is flawed as the central Atlantic includes both particles that recirculate in the subtropical gyre (orange dots in Figure 2.3a) and AMOC particles that flow into the tropical region (red dots in Figure 2.3a). Using the Lagrangian perspective allows identifying that the northern flank of the Eulerian subtropical gyre is filled with water parcels that continue north, constituting the returning limb of the AMOC, and that the bifurcation latitude between the subtropical flow and the AMOC flow shifts southward with depth (black line in Figure 2.1b, also see Figure 2.3a). The western-boundary bifurcation between the tropical and subtropical gyres is located near 21°S, further south than expected from the Eulerian perspective (border between orange and dark blue dots in Figure 2.3a). Note that north of $\approx$ 21°S, the surface southward transport in the western boundary (Figure 2.1b) is explained entirely by the water masses of tropical origin that transfer into the subtropical gyre (cyan dots in Figure 2.3a).

Baringer and Garzoli (2007) and Majumder et al. (2016) have shown that the full-column northward heat transport at 30°S is 1.5 PW when excluding the southward western boundary. Further, Mignac et al. (2018) used several reanalysis models to show that the full-column integrated net heat transport at 30°S is around 0.5 PW. Both results together imply that there is a southward

transport of 1.0 PW through the western boundary. Our results down to 1500 m show northward transports of 0.90 PW for AMOC particles and 0.51 PW for the interior branch of the subtropical gyre, which together account for most of the full-column 1.5 PW of northward interior transport (excluding the western boundary). In the western boundary, our results show southward transports of 0.55 PW for subtropical particles and 0.14 PW for tropical particles (a total of 0.69 PW) down to 1500 m, which means that the remaining southward 0.31 PW needed to account for the full-column southward 1.0 PW are transferred at depths greater than 1500 m.

Finally, a comparison of the western boundary transports with the total transports through the southern (30°S) and the northern (5°S) boundaries of the study area shows that the Lagrangian experiments account for most of the total transport in the South Atlantic (Figures 2.2d and 2.2e), which means that nearly all water masses in the central South Atlantic eventually channel through the western boundary. At 5°S, we find 20.6 Sv of water flowing north, which are mostly explained by the 22.3 Sv coming from 30°S (and captured at 8°S) minus the 1.4 Sv of tropical origin that escape to the subtropics (for a total of 20.9 Sv); the northward heat transport at 5°S (1.0 PW) is essentially due to the heat carried by AMOC water masses (1.10 PW at 8°S), plus the heat gained along the tropical gyre (0.08 PW) and minus the heat that is transferred from the tropics to the subtropics (0.14 PW), for a total of 1.04 PW. At 30°S, the total integrated northward transport is 19.4 Sv, roughly due to AMOC water masses (14.9 Sv along the eastern boundary and 7.4 Sv in the interior ocean for a total of 22.3 Sv) minus tropical water masses transferred southward (1.4 Sv), a total of 20.9 Sv; the associated northward heat transport at 30°S is equal to 0.70 PW, mostly due to the heat carried by AMOC water (0.90 PW northward) minus the heat gained along the subtropical gyre (0.04 PW southward) and minus the heat transferred from the tropics to the subtropics (0.14 PW southward), a total of 0.72 PW. This means that only about 1.5 Sv and 0.02 PW of the 30°S flow circulate off the western boundary.

Our study has shown that numerical models are a useful tool to assess the actual changes in heat and salt content of water particles as they experience both along-isopycnal and diapycnal transformations. In particular, our results provide a good foundation for developing a future observational strategy of cross-gyre exchange. Past observations aimed at determining AMOC properties have focused mainly on the boundary transports by means of zonal arrays. However, we have shown that the zonal component of the AMOC plays a major role in the subtropical and tropical South Atlantic. Therefore, in order to best quantify the AMOC and to understand its interaction with the tropical and subtropical gyres, it would be convenient to set up meridional arrays that can monitor the zonal flows across the South Atlantic.

Chapter 3

Water mass transports and pathways in the NBC-EUC retroflection

The North Brazil Current (NBC) retroflect into the Equatorial Undercurrent (EUC) and its posterior tropical recirculation is a major regulator for the returning limb of the Atlantic Meridional Overturning Circulation (AMOC). Indeed, most surface and thermocline NBC waters retroflect at the equator all the way into the central and eastern ocean, before they recirculate back through the tropics to the western boundary (WB). Here we use cruise data in the western equatorial Atlantic and reanalysis time series for the equatorial and tropical waters in both hemispheres to explore the recirculation pathways, with special emphasis on the WB equatorial retroflection and its variability. During the 1998-2016 period, the annual-mean EUC transports 15.1 ± 1.3 Sv at 32°W, with 2.8 ± 0.4 Sv from the north and 11.4 ± 1.3 Sv from the south. Most of these waters reach the EUC via a WB retroflection south of 3°N (7.2 ± 0.6 Sv) but a substantial fraction does so north of this latitude (5.1 ± 0.4 Sv), and another 0.5 ± 0.1 Sv come from the North Atlantic subtropics. The southern subtropical waters feed the EUC at all thermocline depths while tropical waters do so at the surface and upper-thermocline levels. The EUC has a major seasonality, with principal spring and secondary fall monthly-mean maxima and a range of 8.8 Sv. The 18 years of monthly- and annual-mean EUC transports at 32°W show a weak yet significant correlation with an Atlantic Niño index, and also reflect a major increase in the contribution from the South Atlantic tropical waters during 2008-2016 as compared with 1997-2007. This variability in total transport, water sources and pathways turns the NBC-EUC retroflection as a major source of uncertainty in the AMOC intensity.

This chapter has been submitted as: Vallès-Casanova, I., Fraile-Nuez, E., Martín-Rey, M., van Sebille,E., Cabré, A., Olivé-Abelló, A., Pelegrí, J. L. Water mass transports and pathways in the North Brazil - Equatorial Undercurrent retroflection. Journal of Geophysical Research: Oceans. (*Under review*).

3.1 Introduction

The cross-equatorial northward flow in the western tropical Atlantic Ocean is carried out mainly by western boundary currents flowing at surface and intermediate levels: the North Brazil Current (NBC), typified by relatively salty thermocline South Atlantic Central Water (SACW), and the North Brazil Undercurrent (NBUC), mostly characterized by the low-salinity Antarctic Intermediate Waters (AAIW) (Figure 3.1). These western boundary currents not only drive an interhemispheric water transport, which is associated with the returning branch of the Atlantic Meridional Overturning Circulation (AMOC), but also distribute South Atlantic and intermediate waters into the equatorial ocean through a complex system of zonal currents (Hüttl-Kabus & Böning, 2008; Rosell-Fieschi et al., 2015). This zonal distribution arises at several locations along the western boundary pathway, with the northernmost position near 7-8°N, as the NBC turns east seasonally into the North Equatorial Counter Current (NECC), associated with the seasonal migration of the Intertropical Convergence Zone (ITCZ) (Castellanos et al., 2015; Garzoli et al., 2004; Garzoli & Katz, 1983; Katz, 1987; Lumpkin & Garzoli, 2005; Polonsky & Artamonov, 1997; Rosell-Fieschi et al., 2015).

The NBUC feeds several eastward south and north intermediate countercurrents (SICC, NICC), located on both sides and within about 5° of the equator (Ollitrault et al., 2006; Rosell-Fieschi et al., 2015; Schott et al., 2003). Similarly, within about 3-4° from the equator, the NBC upper-thermocline waters also turn eastward feeding a zonal system of equatorial near-surface currents. This system is composed by the Equatorial Undercurrent (EUC) along the equator, flanked by its northern and southern branches (NEUC and SEUC) at latitudes between 3° and 4°, north and south, respectively (Castellanos et al., 2015; Hüttl-Kabus & Böning, 2008; Lumpkin & Garzoli, 2005; Rosell-Fieschi et al., 2015; Schott et al., 2003; Schott et al., 2004; Stramma & England, 1999; Urbano et al., 2008, Figure 3.1).

The EUC is a quasi-permanent zonal current that carries salty and highly oxygenated waters across the entire equatorial Atlantic, whose dynamics responds largely to the along-equator wind-drive pressure gradient (Brandt et al., 2008; Metcalf & Stalcup, 1967; Stramma & England, 1999). The origin of the EUC was first described by Metcalf and Stalcup (1967), who concluded that the saltier and highly-oxygenated EUC waters come mostly from the South Atlantic, with a minor contribution of North Atlantic waters (NAW). A few Lagrangian studies have further assessed the contribution of the southern and northern masses to the EUC. Hazeleger et al. (2003), using a high resolution simulation with particles released along 20°W, concluded that the major EUC contributions come from the tropical (southeast and central) South Atlantic while less than one-tenth of the EUC waters come from the North Hemisphere, after subducting near the North Equatorial Current (NEC). White (2015) further confirmed that the EUC upwelled waters in the central equatorial region, in what constitutes the Atlantic cold tongue, originate at the western boundary of the subtropical South Atlantic through the NBUC.

The equatorial undercurrents (NEUC, EUC and SEUC) combine with the tropical cyclonic upper-thermocline gyres, known as the subtropical cells (STC), to ventilate the tropical basin: westward interior thermocline flow connects to the western boundary and recirculates east as the zonal undercurrent, drawing a gyre that includes upwelling at the equator and near-surface

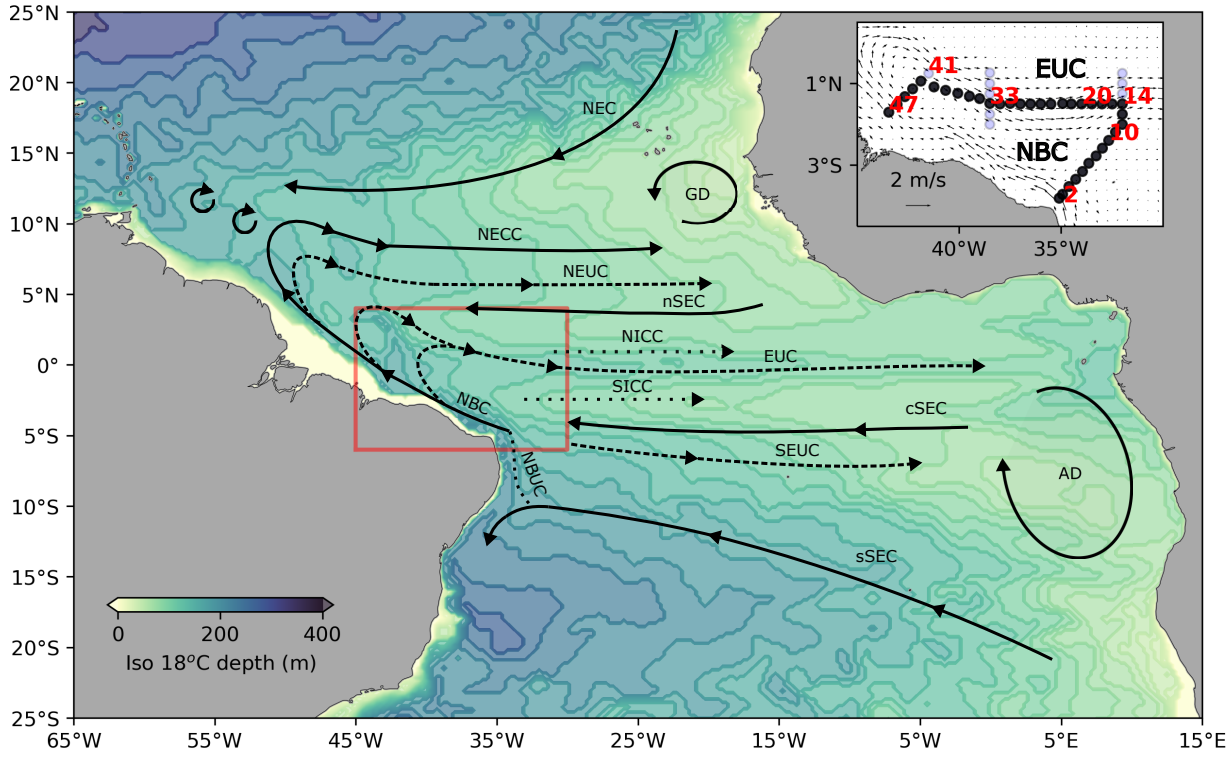

Figure 3.1: Schematics of the tropical Atlantic Ocean circulation system, overlaid onto the GLORYS distribution of the 18°C isothermal depth in April 2010, which is used as a proxy of thermocline depth. From north to south, the main surface currents (continuous lines) are North Equatorial Current (NEC), North Equatorial Countercurrent (NECC), and South Equatorial Current with northern, central and south branches (nSEC, cSEC, sSEC). At the thermocline layer (dashed lines), we find the Equatorial Undercurrent (EUC) located between its northern and southern counterparts (NEUC and SEUC). The Intermediate North and South Countercurrent (NICC and SICC) are also sketched (dotted lines), located between about 400 m and 1100 m. Northward western boundary currents are the North Brazil Current (NBC) and the Brazil Undercurrent (NBUC). The Angola and Guinea domes (GD, AD) are outlined at the eastern margin. The MOC2 cruise area is shown as a red rectangle and in the upper-right inset, with the locations of the hydrographic stations (dots) and the velocity vectors over the 18C isothermal-surface in April 2010; those stations that draw a closed box with the Brazilian coast are shown as black dots.

wind-driven poleward flow (Blanke et al., 1999; Hazeleger & Drijfhout, 2006; McCreary & Peng Lu, 1994; Schott et al., 2004). The complex interaction between this tropical recirculation and the net northward transport, which represents the returning limb of the AMOC, not only affects the heat and salt surface budget in the central and eastern equatorial upwelling regions (Claret et al., 2012; Jouanno et al., 2011; Kolodziejczyk et al., 2014; Schlundt et al., 2014) but also defines the exchange of mass and heat between both hemispheres and across the basin (Hazeleger & Drijfhout, 2006). In particular, Hazeleger and Drijfhout (2006) estimated that 6 Sv of AMOC waters are carried into the equatorial ocean by the EUC, with some 2 Sv recirculating back to the southern tropical hemisphere through the southern STC.

The temporal variability of the thermocline shape and the EUC intensity is associated with ocean-atmosphere feedbacks of the tropical Atlantic climate system (Brandt et al., 2011; Brandt et al., 2012; Brandt et al., 2021; Brandt et al., 2006; Foltz et al., 2019). The nonlinear contribution of remote and local forcing makes it difficult to identify the dominant mechanisms behind the EUC changes. Recent monitoring efforts (Bourlès et al., 2008; Johns et al., 2014) and numerous

model analyses (Arhan et al., 2006; Hazeleger et al., 2003; Hormann & Brandt, 2007; Philander, 1986; Schott & Böning, 1991) indicate the presence of a semiannual cycle, with peak transports in boreal spring and a secondary fall maximum in the western margin. This seasonality weakens and shifts in time from west to east, although the results are not conclusive (Arhan et al., 2006; Hormann & Brandt, 2007). One inconvenient to establish the EUC seasonality is that climate models generally underestimate the EUC intensity as a consequence of important biases in wind stress and ocean stratification (Richter & Tokinaga, 2020; Richter & Xie, 2008). Another main difficulty comes from the unresolved influence of the inter-annual tropical Atlantic variability (TAV), caused by the scarcity of long time series of in situ tropical data(Foltz et al., 2019).

One main mode of inter-annual TAV is associated with the development of anomalous SST in the eastern equatorial Atlantic during boreal summer, which is denoted as the Atlantic Niño or the Equatorial Mode (EM Zebiak, 1993)(EM; Zebiak et al. 1993). The relation between EUC and EM has attracted the attention of the scientific community and is an active line of research. The EUC is expected to strengthen during cool EM events and to weaken during warm ones (Brandt et al., 2014). Such strengthening is particularly important as it could drive a weakening in the inter-hemispheric western-boundary exchange. Nevertheless, the diversity of Atlantic Niño events (Richter et al., 2013; Vallès-Casanova et al., 2020) together with the impact of local and remote forcing (Martín-Rey et al., 2018) makes the interannual variability of the EUC difficult to predict. In addition, fluctuations in EUC transport may be largely influenced by intense wave activity and tropical instabilities (Illig et al., 2004; Illig & Bachèlery, 2019; Perez et al., 2012; Polo et al., 2008; Tuchen et al., 2020; von Schuckmann et al., 2008).

This chapter aims at providing new insights on the EUC origin through in-situ data and outputs from an ocean-model numerical reanalysis. Our objective is to present a detailed description of the mean water masses and their variability into the westernmost EUC, an on the pathways followed by these water masses. The paper is organized as follows. The data and methodology are explained in Section 3.2. Section 3.3 presents observations taken during the oceanographic campaign MOC2, carried out in April 2010 along the western tropical Atlantic (Figure 3.1). These data not only provide an Eulerian view of the velocity fields during the cruise but is also used to validate the model reanalysis. In section 3.4 we offer the Lagrangian perspective, gauging the transports, pathways and transformations associated with waters from different sources (sections 3.4.1 and 3.4.2) and assessing the spatiotemporal variations (sections 3.4.2 through 3.4.5). Finally, section 3.5 closes with the summary and main conclusions.

3.2 Data and methods

3.2.1 Ship-board data

The MOC2 cruise was carried out onboard the R/V Hespérides in two phases, the first one taking place in the western boundary of the equatorial Atlantic Ocean between 7 and 18 April 2010 (Figure 3.1) and the second one representing a transoceanic section along 7°N (()De La Fuente et al., 2014; Hernández-Guerra et al., 2014). In the first phase, a total of 47 hydrographic stations

were occupied, sampling from the sea surface down to 1500 m (or the seafloor if shallower) (Figure 3.2). At each station, vertical casts of temperature, conductivity and oxygen were obtained with a SeaBird 911-Plus multi-probe system mounted on a 24 Niskin-bottle rosette that collected water samples at standard depths, which were used to calibrate the conductivity and oxygen data (De La Fuente et al., 2014; Hernández-Guerra et al., 2014). The temperature and conductivity sensors were duplicated, as an additional measure for quality control. A reference box for the NBC retroflection region can be drawn using 39 out of the 47 field stations, which closes to the southwest with the Brazilian coastline (Figure 3.2).

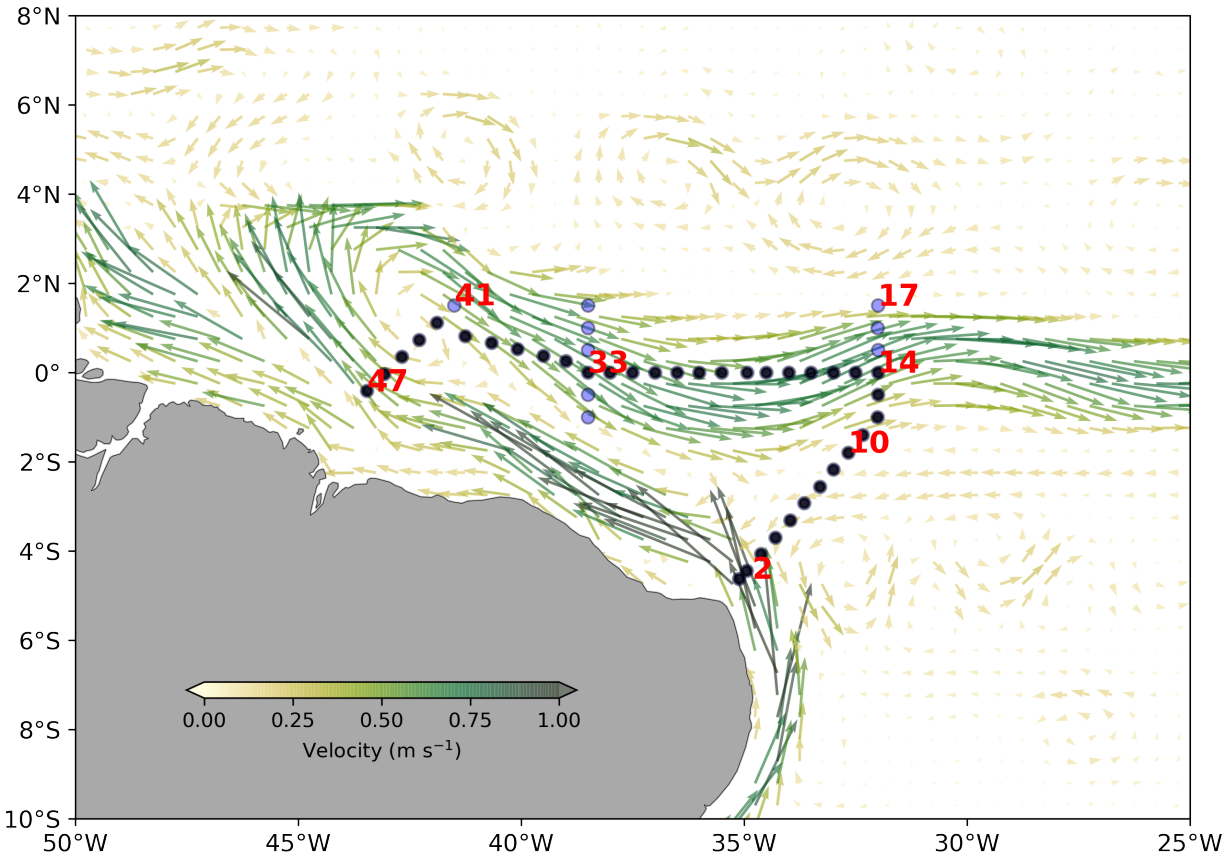

Figure 3.2: Mean ocean currents (vectors) on the 18oC isothermal during April 2010 as predicted by GLY together with the sampling stations during the MOC2 cruise.

A lowered acoustic Doppler current profiler (LADCP) was mounted on the rosette and deployed at each station. The LADCP consisted of two RDI 300 kHz Workhorse Monitor instruments used in synchronized master-slave mode. The system was set to a ping-rate of 1 ping s^{-1} and a bin length of 10 m. An inverse method was applied for the post-processing of the raw data (IFM-GEOMAR LADCP software, Version 10.8, 07 February 2009) (Visbeck, 2002). This resulted in high-quality velocity profiles, even in cases of very weak currents (< 0.05 m s^1). The LADCP velocity data were de-tided using the TPXO.3 global model of ocean tides (Egbert et al., 1994), and rotated to obtain the flow normal to the different segments of the box. Due to technical problems, LADCP profiles were not available at the first and last stations of the box (stations 1 and 47). As the depth at these stations was only about 200 m, data from a ship-mounted ADCP were used to fill these gaps.

A Monte Carlo method was applied to estimate the statistical uncertainty in mass transport for the entire box (Fraile-Nuez & Hernández-Guerra, 2006; Ham et al., 2013). The analysis is performed 2000 times for the matrix $u(u_i, i = 1, 2000)$, simulated in the range $u - \delta u < u < u + \delta u$, where u is either velocity component as obtained from the LADCP for each water depth and station and δu is the standard deviation. With these new velocities, a sample of 2000 mass transports are calculated and used to estimate the statistical uncertainty for each transect and layer.

3.2.2 Ocean reanalysis data

In this study, we use the three-dimensional fields of potential temperature (θ), salinity (S) and velocity components (u, v, w) from the ocean-model numerical reanalysis GLORYS2v4 (hereafter GLORYS), as provided by Mercator Ocean (Garric & Parent, 2018). The GLORYS reanalysis is obtained with the version 3.1 of the ocean NEMO model (Madec & the NEMO Team, 2016) that uses a tripolar ORCA grid with 0.25° horizontal resolution. The vertical grid has 75 levels, with 24 of them in the upper 100 m. The GLORYS reanalysis covers a time period of 23 years, between 1993 and 2016, on a daily basis. The reanalysis assimilates tracked satellite sea level anomaly, sea ice concentrations and sea surface temperature (SST), and salinity profiles from the CORA4.1 in situ database (for further details, see von Schuckmann et al., 2016)). Mignac et al. (2018) shows that GLORYS represents the AMOC strength and meridional heat transport at 35°S better than other models and reanalysis. Here we assess the model accuracy for our study region by comparing the modeled velocity, temperature and salinity with the observations along the sampling sections during the MOC2 survey. For this purpose, we use the daily outputs from GLORYS for the 14 days that lasted the oceanographic survey, extracting the modeled data at the profile locations through linear interpolation.

3.2.3 Lagrangian approach

We analyze the three dimensional GLORYS velocity using the stochastic Lagrangian framework OceanParcels (Delandmeter & Van Sebille, 2019). OceanParcels is an off-line open-source tool for tracking particles in the ocean and inferring the predominant water-mass pathways. This Lagrangian tool uses a new interpolation scheme with the tracer computed as a constant value all over the cell, in accordance with the mass conservation schemes of C-grids (Delandmeter & Van Sebille, 2019). In our simulations, since we are only interested in the average water mass pathways and not in tracer dispersion, particles are advected deterministically by the model velocity fields without adding sub-scale diffusion parameters. In order to fully capture the retroflection waters that feed the EUC, we select the release section for our simulations along 32°W, between 2.5°S and 2.5°N. The vertical limits of the EUC are usually defined by the eastward flow taking place in thermocline layers with potential densities $24.5 < \sigma < 26.8$ kg m^{-3} (Brandt et al., 2006; Johns et al., 2014; Kolodziejczyk et al., 2009; Schott et al., 2005). Brandt et al. (2006) and Johns et al. (2014) have shown that the EUC transport decreases from 20 Sv at 35°W to 14 Sv at 23°W, with most of the transport taking place in the upper ($24.5 < \sigma < 25.5$ kg m^{-3}) and lower-thermocline ($25.5 < \sigma <$ 26.4 kg m^{-3}) layers. At 35°W and 23°W, only 5.4 Sv and 3.0 Sv take place in the surface layers (σ

< 24.5 kg m^{-3}), respectively, while at 23°W only 1.1 Sv occurs in the deep-thermocline layer (26.4 < σ < 26.8 kg m^{-3}). Therefore, for our study, we define the EUC water parcels as those flowing east from the surface to the lower-thermocline layers, i.e. particles are released backwards at each grid cell where the water flows east ($u > 0$) and σ < 26.4 kg m^{-3}. The particles are injected as a function of the magnitude of the normal-to-section velocity at each grid point of the vertical section. Each seeded particle corresponds to an infinitesimal transport and the sum of all transports amounts to the total water transports through the release section (Blanke et al., 1999). With this criterion, we are able to obtain the horizontal streamlines for water parcels reaching or departing some geographical region – the Lagrangian stream functions (LSFs) – hence providing a view of the predominant water pathways. This can be done either using the mean velocity fields or the actual (e.g. daily) velocity values during a certain time interval. The LSF is derived by integrating meridionally the recorded particle transports at each grid wall. Note that for a proper computation of a stream function the flow should be non-divergent, which implies that we have to ensure that all particles start or end out of the domain (Blanke et al., 1999; Döös et al., 2008; Peña-Izquierdo et al., 2015). In our case, to cover the entire tropical Atlantic the release section is left in the middle of the basin assuming a discontinuity from 32°W until the African coast within the band 2°N - 2°S. The temperature and salinity values along the particle trajectories also come from the model, interpolated through the same C-interpolation scheme as the velocity components. Therefore, water mass transformations, including salt and heat fluxes, can be quantified as the particles cross the temperature and salinity gradients. Our study is first situated in the framework of the MOC2 cruise. Thus, we first estimate the different water mass sources and their transformation as they reach the release section in April 2010. Further on, we expand our analysis for the entire GLORYS time span in order to capture the temporal variability of each water source.

3.3 Water mass transports during April 2010

3.3.1 Cruise observations

We quantify the mass transports during the cruise through a combination of LADCP and hydrographic data. To this end, the water column is divided into surface plus upper and lower-thermocline waters (essentially the STC waters, isopycnals less than 26.4 kg m^{-3}), mode waters (central waters of subtropical and subantarctic origin with potential densities between 26.4 and 27.1 kg m^{-3}) and intermediate waters (subantarctic waters with isopycnals between 27.1 and 27.6 kg m^{-3}) (Figure 3.3). Vertical sections of potential temperature and salinity show a warm and salty layer, extending from about the sea surface down to about 200 m (Figure 3.4a,b). This layer corresponds to Salinity Maximum Water (SMW), which is formed by excess of evaporation over precipitation in the subtropics (Mémery et al., 2000). Below the SMW and down to about 400 m, we find the linear -S relationship that characterizes the central mode waters (Figure 3.6). Antarctic Intermediate Water (AAIW) occupies the 400 to 1100 m layer, with potential temperature and salinity ranges of 4.5 - 10°C and 34.6 - 34.8 psu, respectively (Figure 3.4).

A northwestward penetration of the alongshore-flowing NBC shows up in the SMW and CW layers, between stations 1 and 4 (Figure 3.3. The ADCP data show an intense boundary current

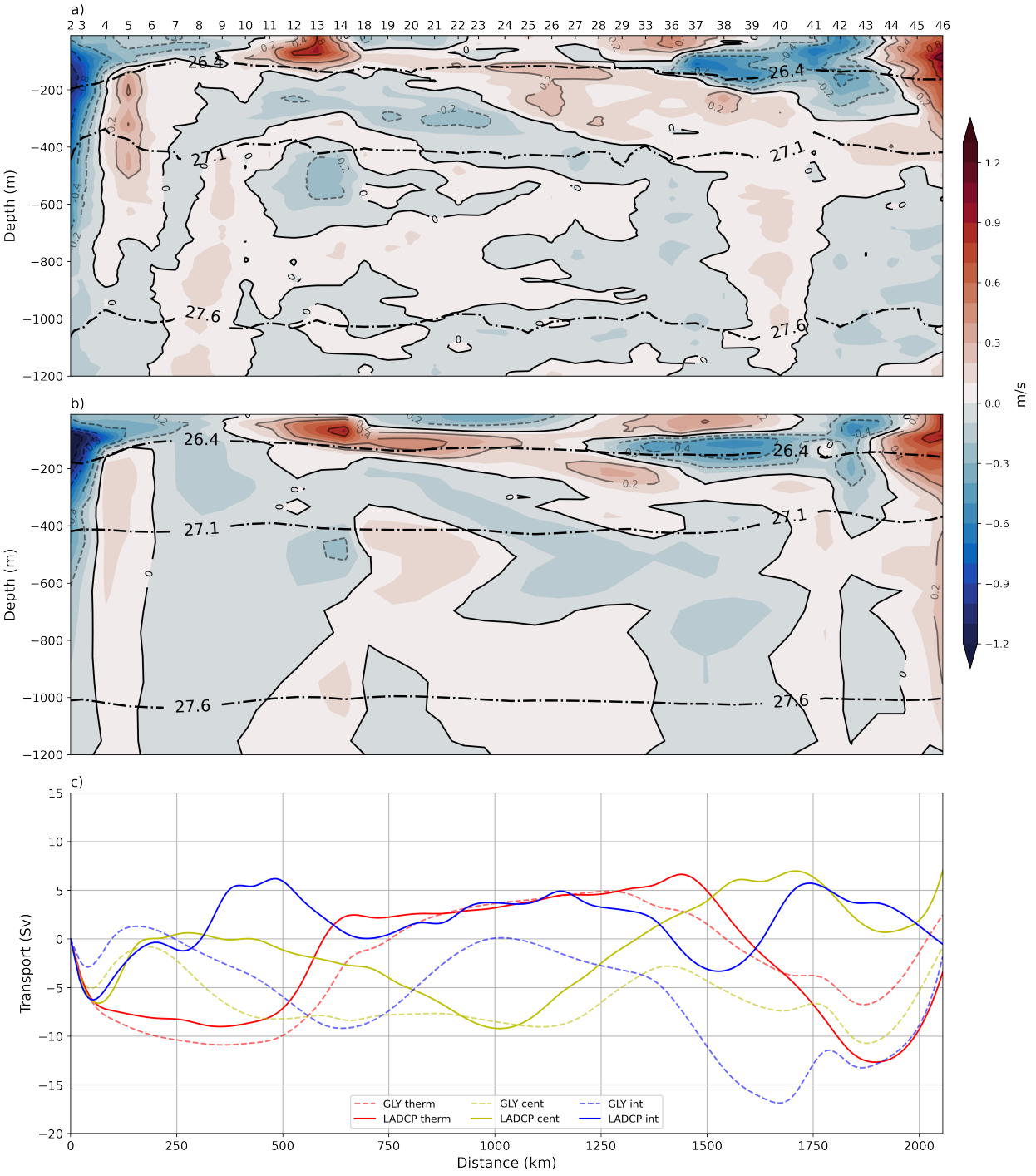

Figure 3.3: (a) Distribution of the normal-to section ADCP velocity, between the sea surface and 1100 m, along the perimeter of the reference section in Figure 1, as if seen from outside the reference box; negative and positive values represent flow into and out of the reference box. The potential density surfaces 26.4, 27.1 and 27.6 kg m^{-3} are drawn as black dashed-dot contours. (b) Same as panel (a) but using the interpolated values from GLORYS. (c) Accumulated mass transport for the surface-thermocline (red), central (yellow) and intermediate (blue) waters; the solid lines represent the observed transports while the dashed lines denote the transports as deduced from GLORYS.

(with velocities up to 1 m s^1) that transports 14.4 ± 0.3 Sv into the box in the southwestern end and 16.6 ± 0.4 Sv out of the box in the northwestern end, in good agreement with estimates by Garzoli et al. (2004) (12.1 to 18.0 Sv) and Schott et al. (2005) (14.2 ± 2.4 Sv). The 2.2 Sv transport increase

between 5°S and 1°S is explained by surface inflow near to the northwestern corner in excess of the NBC surface retroflection: a portion of this flow turns back clockwise towards the coast to rejoin the NBC, thereby supplementing the NBC transport. The main NBC retroflection continues eastwards as the EUC in the subsurface layer, meandering around the equator. The LADCP-inferred EUC transport leaving the box in the eastern margin, between stations 10 and 14, amounts

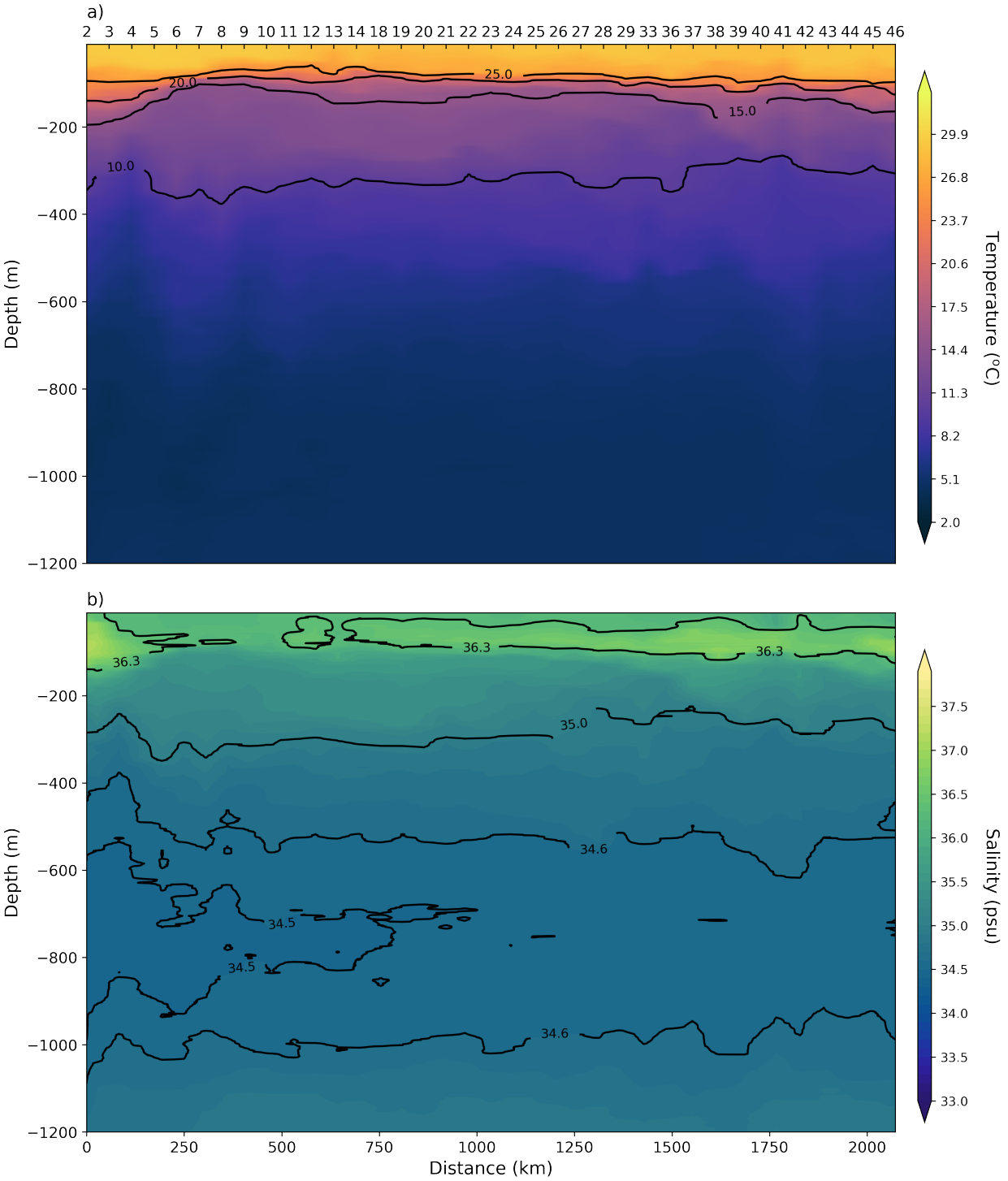

Figure 3.4: (Temperature (a) and salinity (b) distribution derived from CTD observations between sea surface and 1200 m, along the box perimeter drawn by sampling stations marked in black dots in 3.1

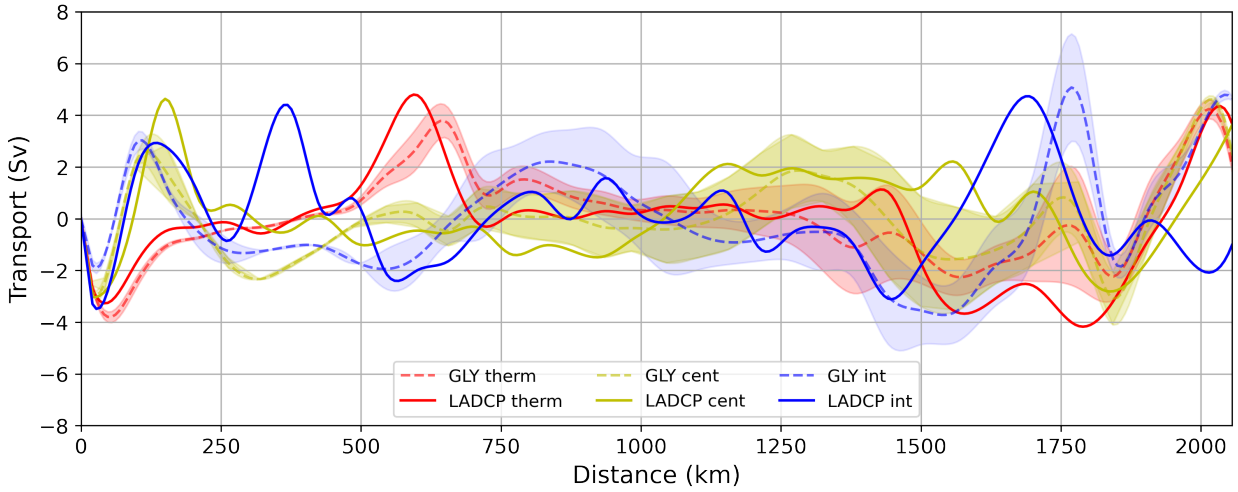

Figure 3.5: Accumulated mass transport along vertical profiles for the surface-thermocline (red), central (yellow) and intermediate (blue) waters; the solid lines represent the observed transports while the dashed lines denote the transports as deduced from GLORYS.

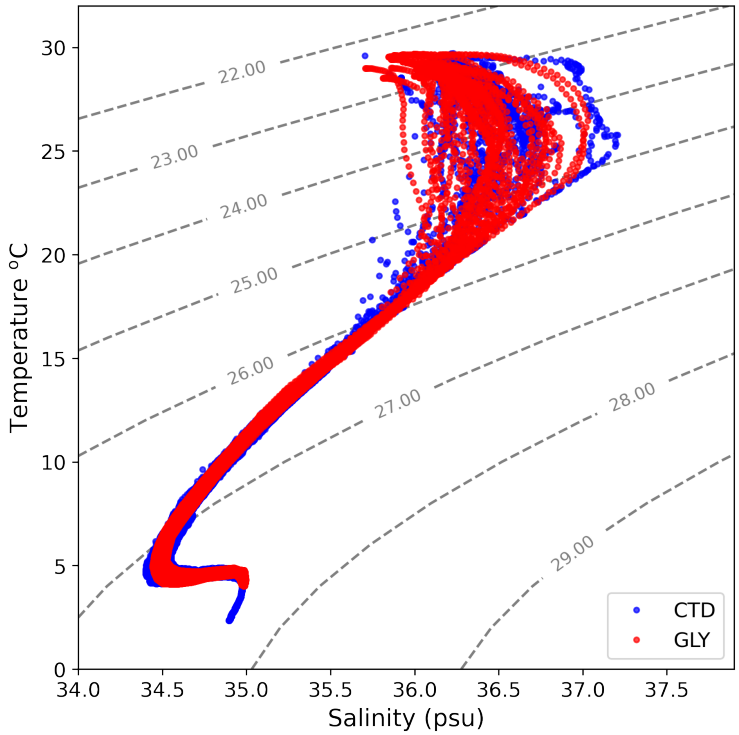

Figure 3.6: Salinity versus potential-temperature diagram derived from observations (blue dots) and GLORYS reanalysis (red dots). Dashed contour lines in grey represent the potential density levels in kg m^{-3}

to 9.5 ± 0.4 Sv; when accounting for the entire eastward flow along 32°W, between 2°S and 1.5°N, the EUC transport increases to 15.4 ± 0.4 Sv. In the intermediate layers, only the NBUC between stations 1 and 3 flows with the same northward orientation as the subsurface-central water (NBC). The NBUC flows into the box with a mean transport of 8.4 ± 0.3 Sv, in good agreement with earlier estimates of 8.9 ± 1.5 Sv by Schott et al. (2005). Moreover, this current presents a salinity minimum of 34.45 psu, which is indicative of a purer source of AAIW (Figure 3.5). This undercurrent rapidly

changes its orientation and flows southeastward out of the box through stations 4-10 into the SICC, with an even larger mass transport: 11.4 ± 0.4 Sv. Between stations 10 and 14, just under the EUC, we observe a westward current into the box, with a transport of 6 ± 0.5 Sv, comparable to the 5.2 ± 4.9 Sv reported by Schott et al. (2005). This flow splits into three branches. The first branch transports about 3 Sv southeastward, feeding the retroflection of the SEIC and explaining its increase as compared with the NBUC. The second branch drives 1.3 Sv northward across the equator and the third branch mass continues northwestward with about 1.7 Sv, apparently into the NICC.

The NICC exits the reference box between stations 38 and 41 with 10.4 ± 0.7 Sv, seemingly fed by the combination of the above westward third branch, a southward flow between stations 27 and 33 (6.5 ± 0.7 Sv), and a western boundary contribution between stations 41 and 47 (2.3 ± 0.5 Sv). The net imbalance of the intermediate water layer is estimated to be -0.1 ± 0.5 Sv.

3.3.2 Model validation

In this section we compare the GLORYS outputs with the cruise data. Specifically, we compare the hydrographic and ADCP data with the modeled current velocity, temperature and salinity, interpolated linearly at the cast positions. Following the previous section, we determine the mass transport balance by integrating along the closed box for subsurface, central and intermediate layers (Figure 3.3c). Note that these cumulative transports aggregate errors, so that the comparison of the observed and modeled values is very good at the surface and thermocline layers but fails in the central and intermediate waters; an alternative comparison of the vertically integrated mass transports per unit length is shown in Figure 3.5.

The comparison shows that GLORYS captures well the surface and thermocline flows (Figure 3.3b). Furthermore, the reanalysis currents of the NBC-EUC have similar magnitudes in the observations and reanalysis. Between stations 29 and 44, the EUC inflow differs moderately between observations and reanalysis, possibly because of the zonal orientation of this section. As the EUC outflows through the meridional section defined by stations 10 to 17, the core is weaker and located further north in GLORYS than in the observations, reflecting a less pronounced modeled EUC meander.

In the central waters, the model also underestimates the abrupt NBC southeast turn between stations 4 to 7 (Figure 3.3b). Further, the outflow between stations 36 and 42 is less intense and shifted north as compared with the observations. Within the intermediate layer, the flow differences are even more significant. While the vertical resolution of the LADCP data is high and constant along the profile, the model resolution decreases with depth. Thus, we already expect discrepancies between model and observations as we reach greater depths. The most remarkable difference is at the northwestern corner of the reference box, with the model showing the NBUC outflowing north while the observations indicate that the NBUC retroflects to feed the SICC and NICC. GLORYS actually underestimates the retroflection of the SICC (stations 8 to 14) and the outflow of the NICC (it only appears in stations 40-41). Despite the differences, the integrated mass transports are close to zero for both the model and the observations (Figure 3.3c).

To evaluate the model accuracy in terms of temperature and salinity, we cluster the values at different depths and plot them against the observations (Figure 3.7; an alternative view is provided in Figure 3.6, which presents a salinity-temperature diagram for both observations and reanalysis). Overall, the model represents well the thermohaline structure of the study region. The maximum discrepancies are found in the sub-surface and thermocline layer (50-150 m), which are also the regions of higher variability. At deeper levels (400-1000 m), GLORYS also reproduces fairly well the temperature and salinity observations.

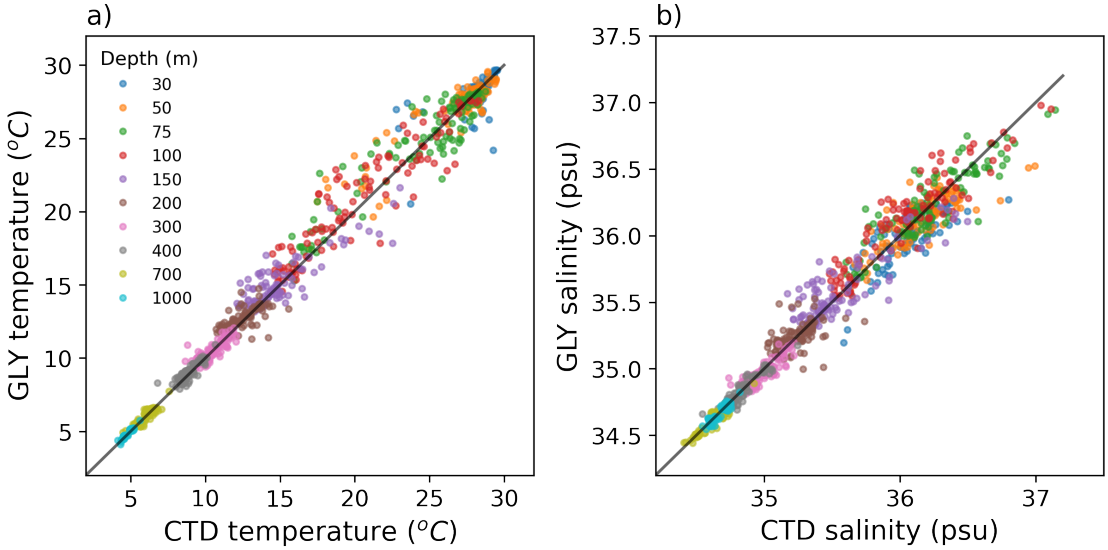

Figure 3.7: Scattered plots of in-situ observations versus the GLORYS reanalysis values interpolated at the stations: (a) temperature and (b) salinity. The variables are clustered by different depth levels (30, 50, 75, 100, 150, 200, 300, 400, 700 and 1000 m), color-coded as indicated.

3.4 Sources and pathways of the NBC-EUC retroflection

3.4.1 Pathways and water mass transformations

The LSFs (Figure 3.8) summarize the main pathways feeding the EUC at 32°W during April 2010. Most of the EUC water sources are South Atlantic tropical and subtropical waters (Figure 3.8). Subtropical southern waters come via the sSEC (Figure 3.1), following the northern margin of the subtropical gyre. On the other hand, the recirculation of the tropical waters may follow either short or long routes. The short route takes place in the western and central gyre, a STC at latitudes less than 5S that returns westward as the cSEC (Figure 3.1). The long path reaches the Gulf of Guinea, following south and turning westward at about 10-15°S, joining with the SEC subtropical waters. North of the equator, the EUC water comes mainly from the eastern tropical Atlantic. These eastern tropical waters are fed by the eastward NECC, turning westward to join the northern SEC (nSEC). There is also a small contribution of subtropical northern waters, originating at the NEC before joining in the NECC-nSEC-EUC connection (Figure 3.8).

The sub-tropical South Atlantic is therefore the major water source into the EUC. With the help of the LSF trajectories, we can identify the relative contribution of each region, and explore the

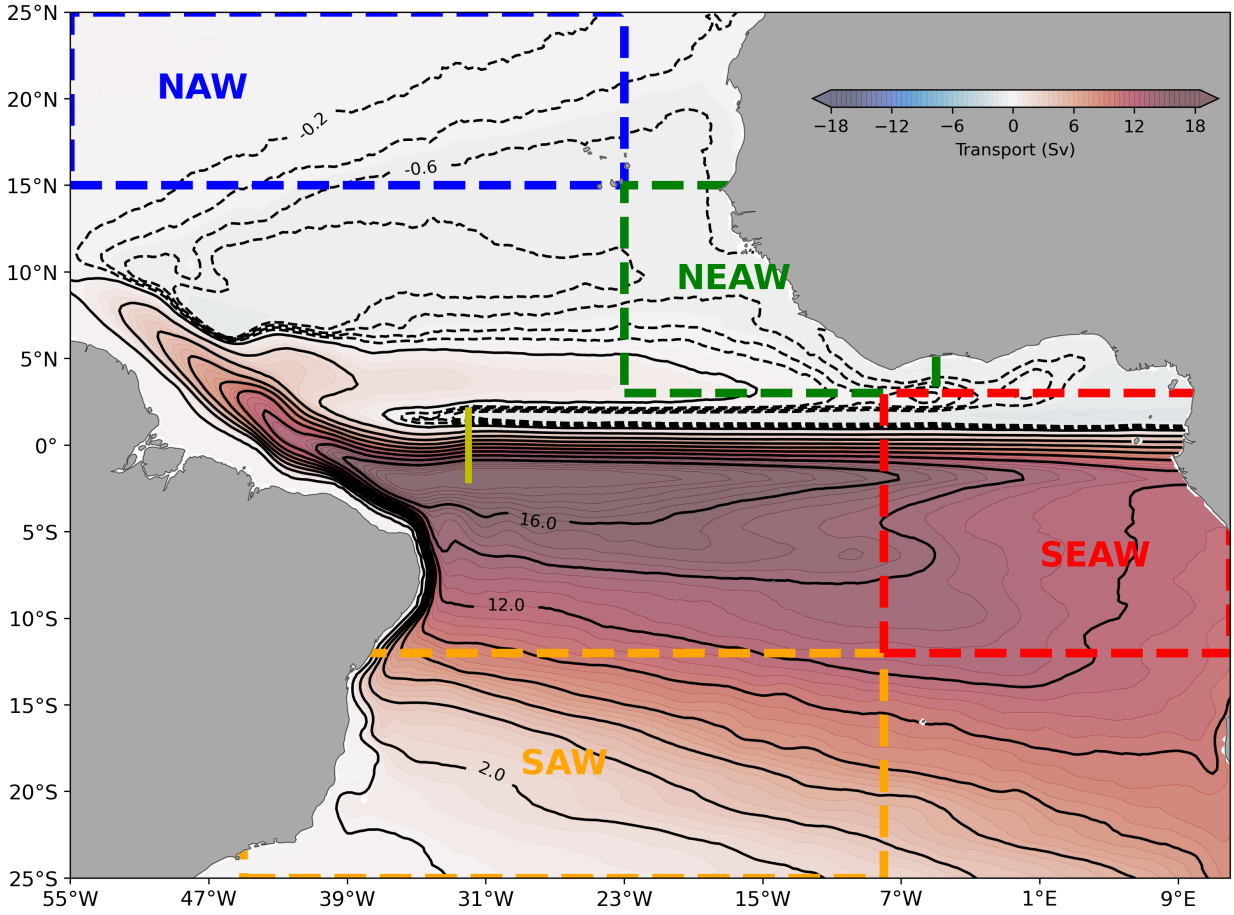

Figure 3.8: Lagrangian stream functions derived from particles released at the 32°W section (yellow solid line). Note the different contour intervals between negative and positive values: while the former are dashed lines drawn every 0.2 Sv the latter are thick lines every 2 Sv. The closed boxes in bold-dashed lines define the regions of different water sources that ventilate the thermocline at the 32°W section: North Atlantic Waters (NAW, dashed blue), Northeast Atlantic Waters (NEAW, dashed green), Southeast Atlantic Waters (SEAW, dashed red) and South Atlantic Waters (SAW, dashed orange).

possible exchange of tropical waters between both hemispheres. For this purpose, we choose three different water sources similar to the ones proposed by Urbano et al. (2008): South Atlantic Waters (SAW; 30°W, 15-25°S), North Atlantic waters (NAW; 35°W, 15-25°N), and North Eastern Atlantic waters (NEAW; 23°W, 3-15°N); additionally, we add a fourth region covering the southeastern tropical Atlantic (SEAW; 8°W-12°E, 15-3°W) (Figure 3.8).

We investigate the contribution of these four sources (SAW, SEAW, NAW, NEAW) to the EUC transport within the $22.0 < \sigma < 26.4$ kg m^{-3} density range, clustered in density bins of 0.1 kg m^{-3} (Figure 3.9). We start with the density distribution at origin (Figure 3.9a). The SEAW has a substantial contribution at all densities, with a major contribution in the surface layer ($\sigma < 24$ kg m^{-3}) (Figure 3.9a). The SAW dominates in the lower-thermocline ($25.5 < \sigma < 26.4$ kg m^{-3}), which corresponds to SMW subducted in the subtropics. Most water originating from the NEAW is relatively fresh and warm Tropical Surface Water (TSW, $\sigma < 24.5$ kg m^{-3}), but there is some contribution from the lower-thermocline. Further north, the small contribution of NAW comes mostly from densities greater than 24.5 kg m^{-3} (Figure 3.9a).

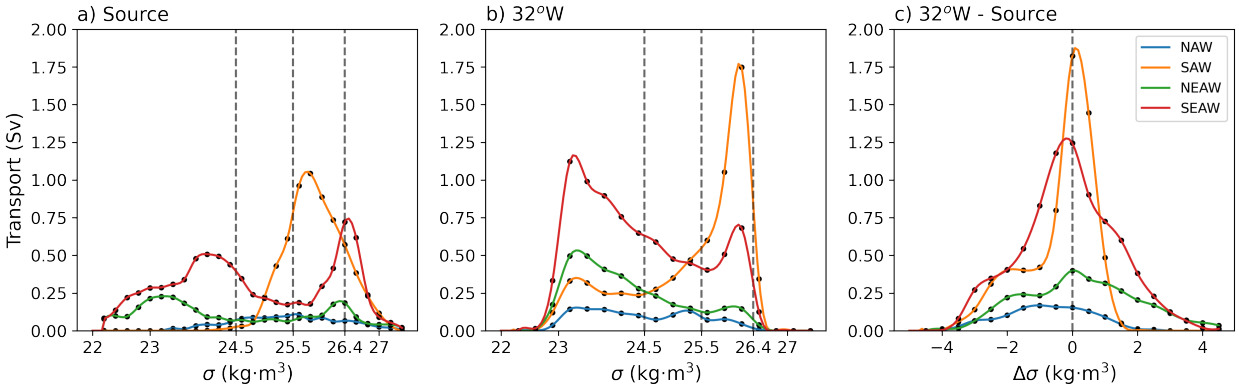

Figure 3.9: Lagrangian transports for 0.1 kg m^{-3} bins (a) at the source region and (b) at the release section; the dashed vertical lines define the lower limits of surface, upper-thermocline and lower-thermocline (24.5, 25.5 and 26.4 kg m^{-3}). (c) Transports as a function of the density change between the source region and release section; the vertical dashed line represents no density change and negative (positive) values indicate that waters at 32°W have become less (more) dense.

Table 3.1 Transport contribution (Sv) to the EUC from the different source regions classified in different density classes at the initial (i) and final (32°W) location.

	SAW		SEAW		NAW		NEAW	
kg m^{-3}	i	32°W	i	32°W	i	32°W	i	32°W
$\sigma < 24.5$	0.04	1.59	4.19	4.98	0.24	0.71	2.04	2.32
$24.5 < \sigma < 25.5$	1.85	1.34	1.06	1.57	0.47	0.33	0.35	0.55
$25.5 < \sigma < 26.4$	3.69	3.42	1.71	1.45	0.34	0.16	0.60	0.37
$26.4 < \sigma < 26.8$	0.77	-	1.02	-	0.15	-	0.25	-

Considering now the density distribution at the target section, we observe that the southern-origin waters dominate in all layers, with a predominance of SEAW and SAW in the surface and lower-thermocline layers, respectively. The NEAW appears as the next most frequent surface contribution and the NAW is the less common although equally distributed in all layers (Figure 5b). In terms of density change, all water sources have their maximum close to $\Delta\sigma = 0$ kg m^{-3} and display a symmetric curve around this maximum, indicating that there is no preferential net diapycnal transformation; the only exception is NAW, with a net tendency to becoming lighter (Figure 3.9c). The source and 32°W transports are summarized in Table 3.1.

For a better understanding of the density changes, we visualize the Lagrangian transports from each source region in thermohaline coordinates (Figure 3.10). This picture helps identify the existence of diapycnal and isopycnal mixing, the later displaying density-compensating changes in temperature and salinity (Döös et al., 2012; Tamsitt et al., 2018). Consistent with Figure 3.9c, the largest water transformations appear in the upper-thermocline layers of the NAW (Figure 3.10a) and the SAW (Figure 3.10b). These subtropical waters mix with the relatively warm and fresh TSW (formed in regions of high insolation and where precipitation exceeds evaporation) and turn lighter during their course into the EUC. In contrast, surface NEAW and SEAW get saltier and warmer as they reach the EUC (Figure 3.10c,d) but remaining in the same density layer. Finally, at the lower thermocline the linear T-S relationship in SAW and, to lesser extent, SEAW remains practically equal, showing similar transport values (Table 3.1).

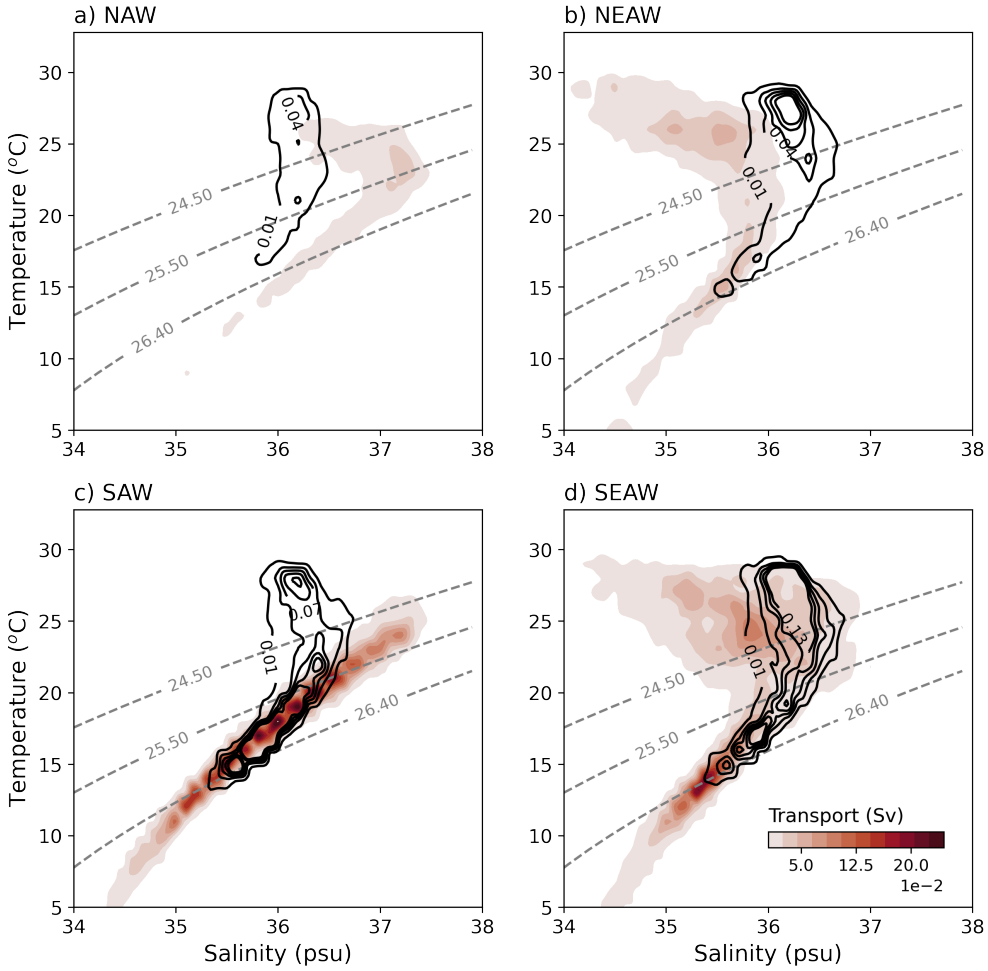

Figure 3.10: Transport in T-S space, calculated for (temperature, salinity) bins of (0.2°C, 0.02 psu). Colors represent the distribution at the source locations, while solid contours refer to particles reaching the 32°W release section for (a) North Atlantic Water NAW, (b) South Atlantic Water SAW, (c) North Eastern Atlantic Water NEAW, and (d) South Atlantic Water SEAW. The dashed gray lines are the lower isopycnals that delimit the surface, upper-thermocline and lower-thermocline layers.

3.4.2 Retroflection pathways

Particles reaching the NBC retroflection zone turn eastward from the western boundary at different latitudinal levels, between 3°S and 12°N, to feed the EUC at 32°W (Figure 3.11a). Here, we classify the trajectories in three different latitudinal retroflection pathways: the south-equatorial retroflection (SER) refers to waters that turn east before reaching 0°S, the equatorial-retroflection (ER) relates to waters retroflecting between 0°S and 3°N, and the north-equatorial retroflection (NER) identifies waters that turn eastward north from 3°N (Figure 3.11a). Additionally, we also account for particles that come directly from the North Atlantic Ocean (NR). The major retroflection corresponds to the NER, with 6.4 Sv in April 2010 that represent over 40% of the total EUC. The SER transport is 3.1 Sv while the ER is about 5.3 Sv. The water turning from the North Atlantic accounts for 1.2 Sv.

The contribution of the different retroflection pathways reaching 32°W in April 2010 is shown in Figure 3.11c. The ER alone would produce a double EUC core, with a peak value at about 60 m and a second maximum at about 80 m, but it is the NER that reinforces the deep core so as

to produce the image of a single nucleus somehow stretching between the equator at about 60 m and 1°N around 100 m (Figure 3.11c). In contrast, the predominant inflow from the SER and NR routes are located in the surface and upper-thermocline layers, between 60 and 80 m and changing in latitude between about 1°S (SER) and 0.7°N (NR) (Figure 3.11b,c).

Figure 3.12 shows again the contribution of the several retroflection pathways at 32°W but now split among source regions. Southern waters (SAW and SEAW) are present in all retroflection routes that depart from the NBC (Figure 3.12c,d). The lower-thermocline waters from SAW dominate the deep core, at 0° for the ER and at 0.5°N for the NER, while the SEAW is associated

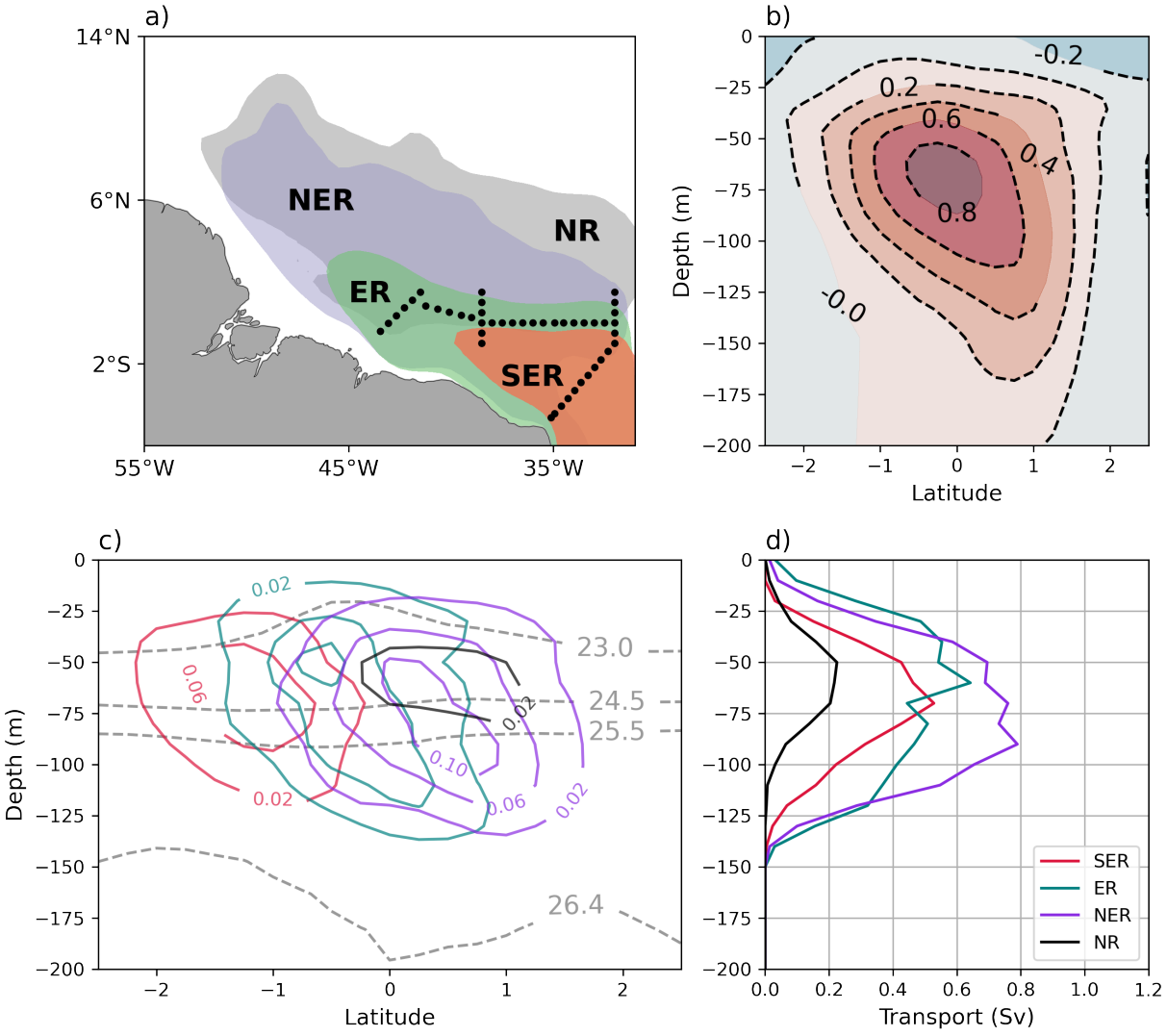

Figure 3.11: The NBC-EUC retroflection is divided in four main pathways relative to the equator: south-equatorial retroflection (SER, red color), equatorial-retroflection (ER, green color), north-equatorial retroflection (NER, violet color) and waters from the North Atlantic (NR, gray color). (a) Retroflection areas shaded by their respective colors, representing >75% of particles grouped per retroflection pathway. The black dots denote the locations of the hydrographic stations during the MOC2 cruise. (b) Latitude-depth distribution of zonal velocity at the 32°W section. (c) Latitude-depth transport distribution of the four pathways (solid colored lines) plotted together with the density levels (gray-dashed contours); transports correspond to depth and latitude bins of 10 m and 0.25°, respectively. (d) Latitudinal-integrated transports along 32°W for all retroflection pathways.

with the shallow core between 1.5°S and 1.5°N, with ER and NER mainly contributing south and north of the equator (Figure 3.12d). The NAW and NEAW reach the shallow EUC core, with the NAW arriving along the NR and NER routes, and the NEAW including all NR, NER and ER pathways (Figure 3.12a,c). Because of its latitudinal position, the NR appears closely tied to the NECC flow, looping through the interior basin of the tropical Atlantic and therefore dragging eastern waters carried through the nSEC (Figure 3.8).

3.4.3 Water source and pathway variability

In the previous sections we have focused our analysis on particles arriving to 32°W on April 2010, providing a Lagrangian perspective to the EUC observations during the MOC2 cruise. We may pursue the Lagrangian approach to explore the NBC-EUC pathways and transports during the entire GLORYS time series (1993-2016). For this objective, we take into account the travelling time between the source regions and the 32°W release section, what is named the ramp-up period (Van Sebille et al., 2014). These times are determined by comparing the time series of the Eulerian transport at the 32°W section with the Lagrangian transports from all source regions (Figure 3.13a).

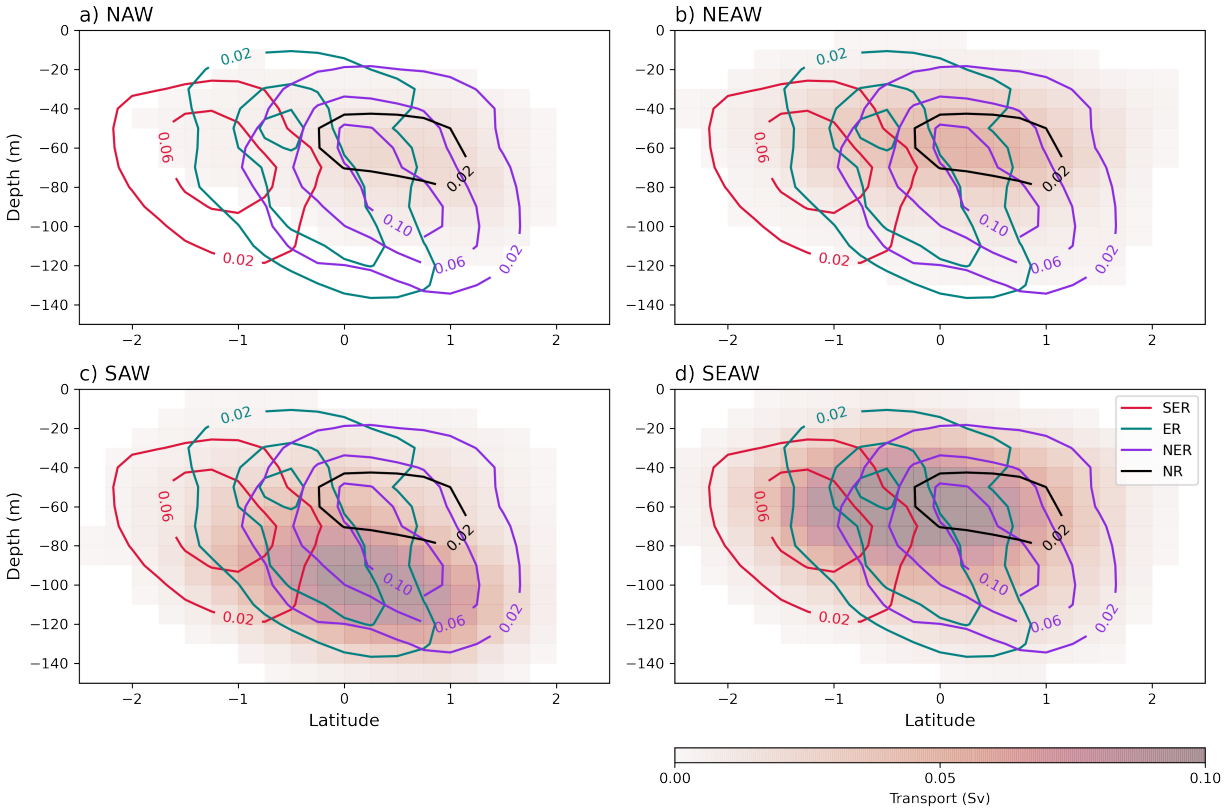

Figure 3.12: Latitude-depth transport distribution at the meridional section 32°W associated with each source region (shading): (a) North Atlantic Waters (NAW), (b) South Atlantic Waters (SAW), (c) North-eastern Atlantic Waters (NEAW), and (d) South-eastern Atlantic Waters (SEAW). Transports correspond to depth and latitude bins of 10 m and 0.25, respectively. In order to illustrate the coincidence of source region and pathway, the contributions of the different equatorial pathways is overlaid: south-equatorial retroflection (SER, solid red line), equatorial retroflection (ER, solid green line), north-equatorial retroflection (NER, solid violet line) and North Atlantic retroflection (NR, solid black line).

It turns out that, starting on 1997, the sum of all Lagrangian transports is similar to the Eulerian transport with a correlation coefficient of 0.71 ($P < 0.05$). The SAW stabilizes earlier than the other sources with a ramp-up of about 3 years, while all other regions take from 4 to 5 years. After removing these initial years, the result is a time series of about 18 years (1998-2016) that allows us to characterize the year-to-year transport variability (Figure 3.13).

The major contributions to the EUC transport come from the SAW and SEAW regions at all times (Figure 3.13b). From these two regions, the fraction of sub-tropical waters is higher than the tropical contribution until 2008. Remarkably, the SEAW contribution increases in 2008, becoming comparable to the SAW contribution (Figure 3.13). Similarly, the NEAW transport also experiences a slight increase in mean transport and variance from 2008 onwards (Figure 3.13b).

The transports associated to the different equatorial retroflection pathways are illustrated in

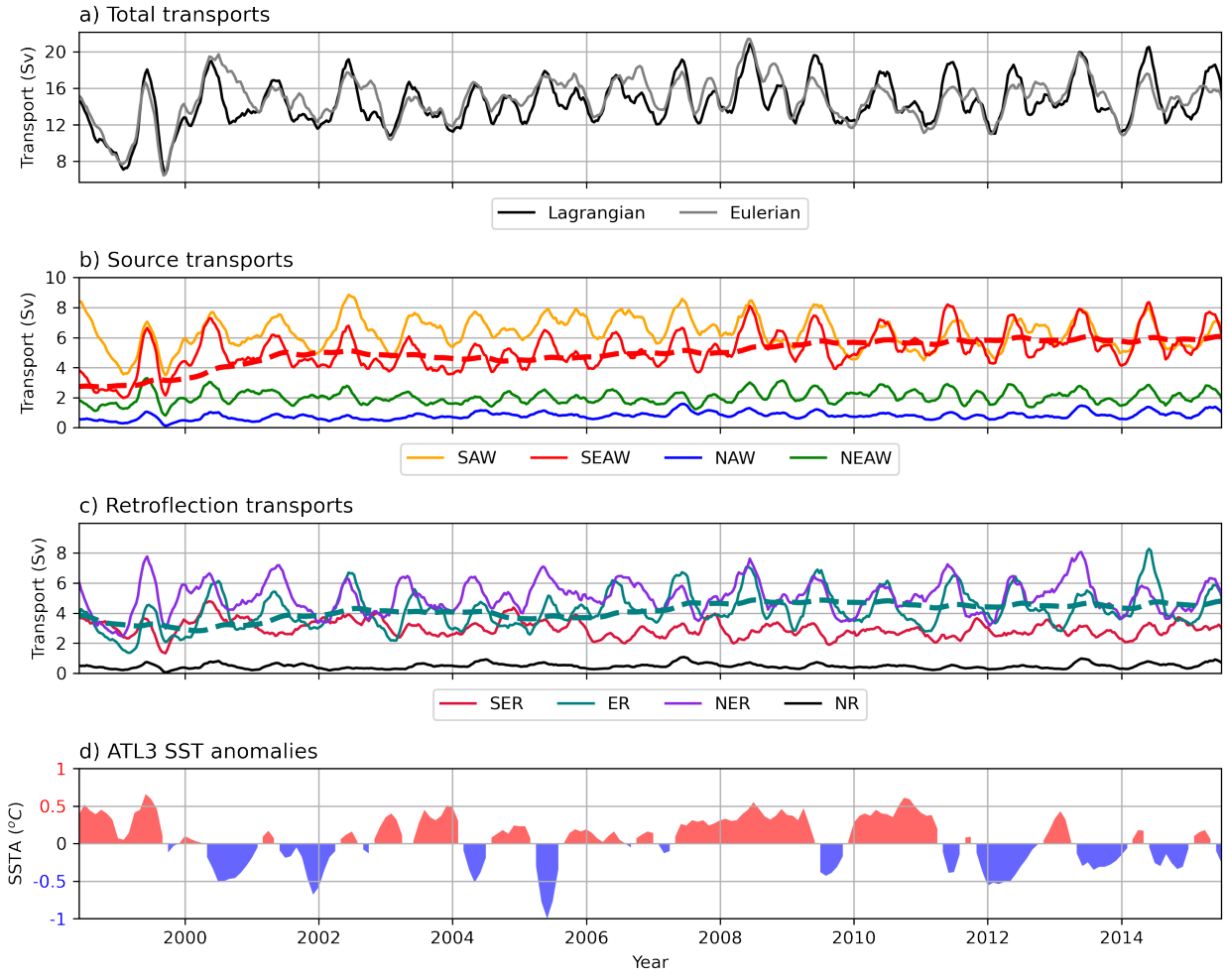

Figure 3.13: Time series of water transports, smoothed with a 6-month running-average. (a) Total Lagrangian (black line) and Eulerian (gray line) EUC transports at 32°W. (b) Lagrangian contributions from South Atlantic Waters (SAW, orange line), South-eastern Atlantic Waters (SEAW, red line), North Atlantic Waters (NAW, blue line) and North-eastern Atlantic Waters (NEAW, green line); the dashed red line is a 4-year running average of SEAW transport. (c) Lagrangian transports for each retroflection pathway: south-equatorial retroflection (SER, red), equatorial retroflection (ER, green), north-equatorial retroflection (NER, violet) and north-retroflection (NR, black); the dashed green line is a 4-year running average of ER transport. (d) ATL3 index anomalies as derived from the ERSSTv5 dataset (Huang et al., 2017).

Figure 3.13c. At a first glance, by only considering the level of water transports, it would appear as if there may be a relation between water source and retroflection pathway as follows: NAW with NR, NEAW with SER, and the two southern waters (SAW and SEAW) with ER and NER. However, our previous analyses on the relation between source and pathway warn us that this relation will only hold for the northern subtropical waters (NAW) through the northern retroflection (NR). All other source waters (SAW, SEAW and NEAW) appear to weave in the NBC-EUC retroflection region, following all three SER, ER and NER pathways.

Table 3.2 Annual-mean values and standard deviations (in Sv) for the total, source and retroflection equatorial transports at 32°W, for both the 1998-2016 period and 2010.

	1998-2016	2010
Eulerian	15.1±1.3	14.7±2.1
Total	14.3±1.2	12.2±2.9
NAW	0.8±0.2	0.7±0.2
NEAW	2.0± 0.2	1.9±0.7
SAW	6.3±0.5	5.0±1.0
SEAW	5.1± 0.8	4.7±1.4
NR	0.5± 0.1	0.4±0.1
NER	5.1± 0.4	4.5±0.8
ER	4.2±0.6	3.3±1.4
SER	3.0±0.3	2.5±0.4

Table 3.2 summarizes the annual mean and inter-annual variability in the partial and total transports at 32°W, both considering the water source and water pathway. The EUC Lagrangian transport is 14.3 ± 1.2 Sv while the EUC Eulerian transport is very similar, 15.1±1.3 The northern (NAW and NEAW) and southern (SAW and SEAW) source regions account for 2.8 Sv and 11.4 Sv, respectively. The main retroflection pathway is NER (5.1 ± 0.4 Sv) followed by ER and SER. In 2010 the EUC transport at 32°W is 2 Sv below the average, about half of this reduction arising from a decrease in the SAW source region and the ER pathway. At the time of the cruise, April 2010, the transport through 32W was of 15.4 Sv.

In order to identify if there is a preferential connection between origin and pathway, we have calculated the correlation at zero time-lag between the source and retroflection transports (Table 3.3). All correlations are significant ($P < 0.01$), indicating that the source variability is carried out to all retroflection pathways. Considering only those correlations above 0.6, we can identify the following major connections: the northern retroflection (NR) accounts mostly for North Atlantic waters (NAW), the north equatorial retroflection accommodates North Eastern (NEAW) and southern (SAW and SEAW) waters, and the equatorial retroflection is the dominant pathway for both southern waters (SAW and SEAW); in contrast, the south equatorial retroflection (SER) shows the lowest correlation values (< 0.5) with all water sources.

Although the 1998-2016 time series is not long enough to evaluate multidecadal trends, the behavior of the EUC transport (Figure 3.13b) is consistent with the reported strengthening of the Atlantic STCs during the last decade (Brandt et al., 2014). Besides the zonal pressure gradient, the EUC can be remotely forced by off-equatorial easterly winds and their associated Ekman poleward transports in both hemispheres, linked with the STCs. Brandt et al. (2021) highlight a positive ten-year trend in equatorial Ekman divergence during 2008-2018, which they associated with a strengthening of the northeast trade winds in the Northern Hemisphere. This intensification of the STC leads to an increase of the SEAW and NEAW arriving to the EUC throughout the equatorial retroflection (ER) (Figure 3.13b,c).

Table 3.3 Correlation between source and retroflection equatorial transports at 32°W, calculated at zero time-lag. Correlation values higher than 0.6 are shown in bold.

	NR	NER	ER	SER
NAW	**0.89**	0.58	0.55	0.31
NEAW	0.48	**0.68**	0.52	0.46
SAW	0.46	**0.65**	**0.70**	0.39
SEAW	0.54	**0.74**	**0.69**	0.39

3.4.4 Seasonal cycle

To analyse the seasonal cycle, for each retroflection pathway and source region, we calculate the monthly Lagrangian transports, linearly detrend the time series and obtain the monthly averages (Figure 3.14). A semiannual cycle appears for all water sources, with a principal maxima in April (18.8 Sv) a secondary maximum in September, and minima both in July and December (10.0 Sv) (Figure 3.14a). A rapid increase in water transport occurs during boreal spring for all water sources, especially for the SAW and SEAW transports (Figure 3.14a).

Regarding the seasonal contribution of each retroflection pathway, the most prominent feature is the difference between the equatorial (ER) and northern (NER) retroflections (Figure 3.14b). The NER reproduces the semiannual cycle while the ER has an annual cycle (maximum in boreal spring and minimum in winter) (Figure 10b). The secondary NER fall maximum is associated with the northward migration of the ITCZ: the south-easterlies in the northern equatorial region lead to the spring-fall westward development of the NECC, from the eastern Atlantic until connecting with the western boundary (Rosell-Fieschi et al., 2015). At this time, the latitudinal pressure gradient intensifies and leads to the NBC retroflection, raising a NEC-NECC cyclonic STC (Figure 4). The eastward NECC waters eventually return westward in the equatorial tropical cell, having a significant yet relatively minor contribution to the surface and lower thermocline layers of the EUC ($\sigma < 26.4$ kg m^{-3}).

The dominant spring maximum coincides with a season of reduced equatorial easterlies, suggesting that the off-equatorial wind variations are driving this NBC-EUC spring supply (Hazeleger et al., 2003).Arhan et al. (2006) concluded that the tropical positive wind stress curl is responsible of western spring intensification, in agreement with the trend reported by Brandt et al. (2021). Eastern observations in the equatorial Atlantic somehow differ from these western-basin results. Johns et al. (2014) found that the main maximum occurs in boreal autumn while the secondary maximum takes place in spring, most prominent at 10°W. They also found that at 23°W the transport remains quite high during boreal spring, with a maximum at the upper and lower-thermocline levels, which is more alike what we find at 32°W.

In 2010, despite the annual mean decrease of 2 Sv (Table 3.2), bimodal transport pattern was reinforced, associated with an increase in the spring and autumn peaks (which lagged about one month after the mean values) and a decrease in the winter values. This took place mostly thanks to the contribution of both eastern tropical waters (SEAW and NEAW), while the SAW fall transport weakened (Figure 3.14). This result is consistent with the 2010 transports observed at 23°W (Johns et al., 2014). When considering the retroflection pathways, the NER was the principal cause

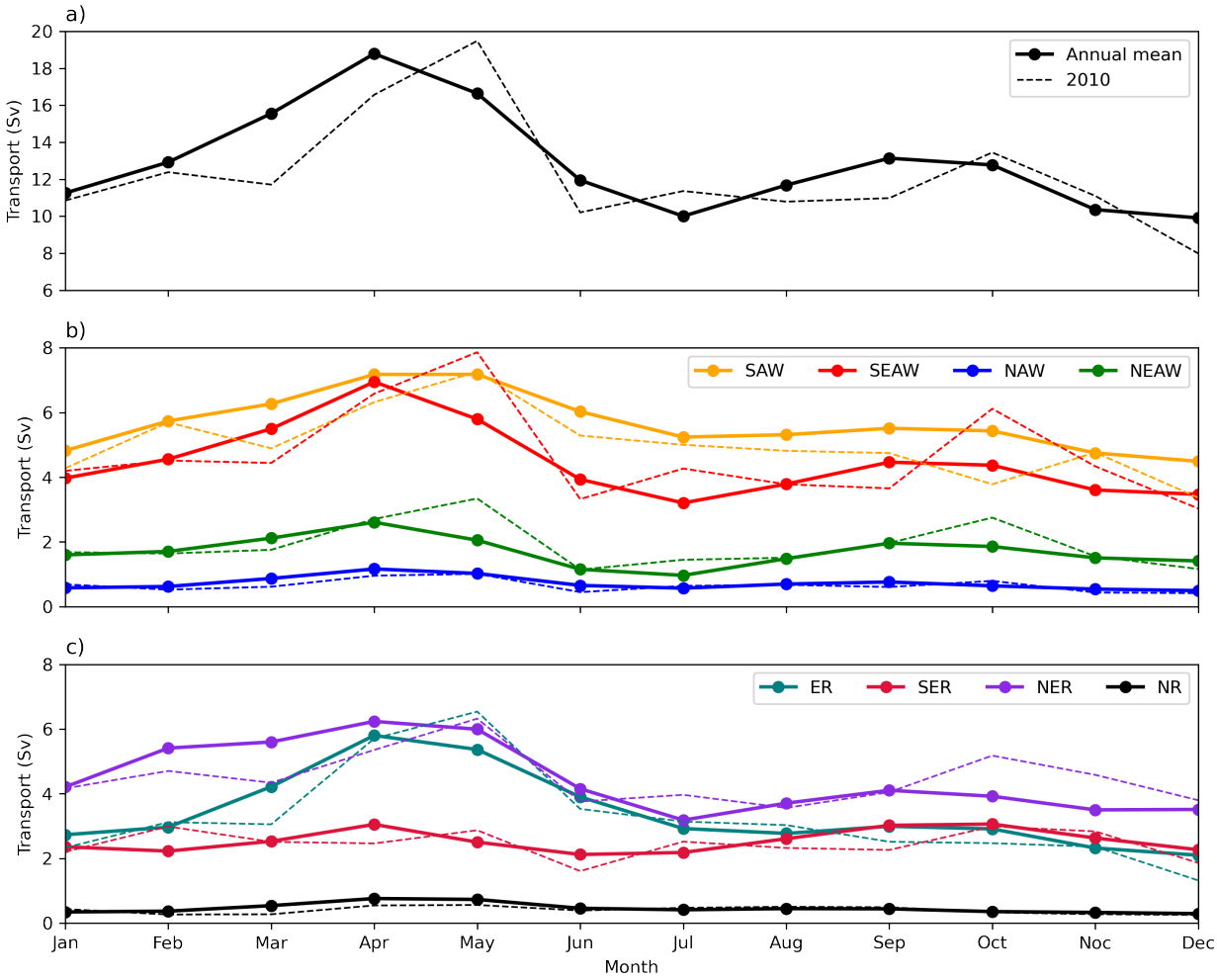

Figure 3.14: Monthly climatological transports at 32°W. (a) Total Lagrangian transports. (b) Transports split per source region: South Atlantic Waters (SAW, orange line), South-eastern Atlantic Waters (SEAW, red line), North Atlantic Waters (NAW, blue line) and North-eastern Atlantic Waters (NEAW, green line). (b) Transports split per equatorial pathway: south-equatorial retroflection (SER, red line), equatorial retroflection (ER, green line), north-equatorial retroflection (NER, violet line) and North Atlantic retroflection (NAR, black line). The dashed lines in both panels correspond to the monthly transports during 2010.

for both the spring and autumn increases while both ER and NER decreased during winter and early spring; the SER transports remain slightly below mean values for the entire year. During 2010, an Atlantic Niño year, the equatorial Atlantic experienced anomalous warm conditions (Figure 3.13d). At this time, the SST anomaly (SSTA) was zonally homogeneous along the equatorial basin (see Figure 5.2 in chapter 5). This result again suggests that extra-equatorial forcing was the principal responsible for the reinforced 2010 bimodal seasonal pattern.

3.4.5 Transport variability and Atlantic Niño

After exploring the EUC remote sources and their western boundary retroflection pathways, we dedicate this section to examine the possible causes for interannual variability. The equatorial band is a key region in the emergence of the Equatorial Mode (EM), which is the main mode of

TAV (Zebiak, 1993). It peaks during boreal summer and is characterized by SSTA values covering the central-eastern equatorial Atlantic and extending along the African coast. The positive (negative) anomalous SSTs are associated with a weakening (strengthening) of trade winds across the equatorial basin, therefore altering the zonal pressure gradient (Lübbecke et al., 2014; Zebiak, 1993). The SSTA in the ATL3 index, a proxy of EM defined as the anomalous SST averaged in the region [3°S–3°N, 20°W–0°] is shown in Figure 3.14. ATL3 is negatively correlated with all Lagrangian transports at 32°W (statistical values from -0.12 to -0.17 for all water sources with P <0.1), with time lags of either 1 month (SEAW, NAW, NEAW) or 2 months (SAW). This means that relatively warm conditions in the surface equatorial Atlantic will be followed by a reduction of the equatorial transport 1-2 months later.

This negative correlation, although weak, is consistent with previous findings (Brandt et al., 2014; Hormann & Brandt, 2007) and can be understood in terms of the large diversity of TAV modes. The emergence of the Meridional Mode (MM) in boreal spring (Nobre & Shukla, 1996), together with the spatiotemporal variability of these modes patterns along the observational record (Martín-Rey et al., 2019; Richter et al., 2013) modulate their impact on the EUC. For instance, some events are characterized by basin-wide SSTA (see Figure 1 in Martín-Rey et al., 2018), as it was in 2010 with less pronounced zonal SSH gradient that lead to a reduced EUC.

The connection between the MM and the EM via ocean tropical instabilities can also affect the mechanisms underlining the EUC variability. A good example is the cool event in 2009, when the EUC was weaker than expected. A negative MM event induces an anomalous north-equatorial wind stress curl during boreal spring that excites upwelling pulses off northwest African. These pulses propagate west as a Rossby wave, which is boundary-reflected in the northeast Brazilian coast and becomes and eastward equatorially-trapped upwelling Kelvin wave (Foltz & McPhaden, 2010). The cause of this atypical 2009 equatorial cooling was the propagation of the Kelvin wave in absence of equatorial easterlies. The variability of the NBC-EUC retroflection and its interaction with climatic modes is therefore complex and deserves further research that is beyond the scope of our study.

3.5 Summary and conclusions

The EUC is the principal conduit diverting the western boundary NBC and recirculating the surface and upper-thermocline waters of the equatorial and tropical Atlantic Ocean. Thus, assessing the water mass contributions and pathways into the EUC is crucial not only to understand the dynamics of the equatorial and tropical oceans but also to predict the intensity and efficiency of the returning limb of the AMOC. In this study, we have examined the NBC-EUC retroflection system combining data obtained in an oceanographic cruise (MOC2 campaign in April 2010) and outputs from the ocean reanalysis GLORYS4v2. In particular, the numerical data has been explored using a combined Eulerian and Lagrangian approach. Previous studies demonstrated that the majority of water that ventilates the thermocline through the NBC retroflection comes from the South Atlantic Ocean subduction region, where tropical and subtropical waters converge (chapter 2). The different contributions from these southern sources, as well as from the North Atlantic, determine the composition of the surface and thermocline equatorial waters.

The April 2010 Eulerian view, either observational or numerical, depicts a NBC that is largely retroflected at the equator into the EUC. The ADCP and numerical data show good agreement in the surface-thermocline ($\sigma < 26.4$ kg m^{-3}) but does less well in the mode ($26.4 < \sigma < 27.1$ kg m^{-3}) and intermediate ($27.1 < \sigma < 27.6$ kg m^{-3}) layers. In particular, within the mode water layers ($26.4 < \sigma < 27.1$ kg m^{-3}) the NBUC depicts a large southward offshore flow that is not visible in the reanalysis. The cruise data down to 27.1 kg m^{-3} depicts a NBC with 14.4 ± 0.3 Sv into the box and 16.6 ± 0.4 Sv out of the box. Most of this outflow feeds back into the EUC, with a transport of 15.4 ± 0.4 Sv at 32°W (9.5 ± 0.4 Sv taking place south of the equator).

In order to obtain the April 2010 Lagrangian perspective, we advected numerical particles with the 3D velocity field of the GLORYS2v4 reanalysis. The Lagrangian transports allow us to quantify the water mass sources and pathways, as well as their final vertical position in density coordinates. We find that the predominant water contribution changes as we shift between density classes. The main water contribution to the EUC occurs within the lower-thermocline layer ($25.5 < \sigma < 26.4$ kg m^{-3}) led by the SAW. In contrast, the waters at the surface ($\sigma < 24.5$ kg m^{-3}) and upper-thermocline ($24.5 < \sigma < 25.5$ kg m^{-3}) layers are mainly from tropical sources, with SEAW as the dominant water mass followed by NEAW (Figure 3.9). Most of the SEAW remains at the surface, reaching the NBC-EUC retroflection via the cSEC; a portion of deeper SEAW moves southward along the eastern boundary (Mercier et al., 2003) and mixes back with warmer SAW, becoming lighter as it reaches the equator. SAW occupy the deeper layers at origin but lose density and upwell as they reach the equator. NAW and NEAW have smaller contributions, with the NAW reaching the EUC through a south-eastward branch of the NECC, which feeds the westward nSEC towards the NBC-EUC retroflection (Figures 3.8 and 3.9).

Additionally, the modeled particle trajectories provide a complete picture of the April 2010 NBC-EUC retroflection pathways in the equatorial region. The dominant pathway is the north equatorial-retroflection (NER, north of 3°N), which feed all layers from the surface to the lower-thermocline, followed by the equatorial-retroflection (ER, between the equator and 3°N; Figure 3.11). In contrast, the south-equatorial and equatorial retroflections feed mainly the surface and upper-thermocline. The major contribution to the EUC lower-thermocline comes from the SAW while both NEAW and NAW are more present in the shallower north-retroflections (Figure 3.12).

The analysis of 18 years of data (1998-2016) shows that the spatiotemporal structure of the retroflection has high seasonal and moderate interannual variability. The Eulerian transports at 32°W show that the annual-mean EUC is 15.1 ± 1.3 Sv, with 11.4 ± 1.3 Sv arriving from the south-eastern tropical (SEAW) and southwestern subtropical (SAW) waters and 2.0 ± 0.2 Sv coming from the eastern North Atlantic tropical waters (NEAW). Western boundary waters retroflecting north of 3°N (NER) represent 5.1 ± 0.4 Sv while those diverting south of this latitude account for 7.2 ± 0.9 Sv.

At seasonal scales, we find a semiannual cycle in the EUC transport at 23°W, with a main peak in April and a secondary one in September and minima in July and December, in agreement with other model analysis (Arhan et al., 2006; Hazeleger et al., 2003; Hormann & Brandt, 2007) and observations (Johns et al., 2014). The variation in the monthly-mean EUC transport is much greater than the inter-annual one, ranging between 10.0 Sv in July and September and

18.8 Sv in April. This semi-annual oscillation results from the combination between the semi-annual shallower northern-retroflection and the annual equatorial-retroflection (Figure 3.14). The autumn maximum, which is only present in the north-retroflection, is linked with the local oceanic linear-response to the equatorial trade winds (Rosell-Fieschi et al., 2015). Conversely, the spring maximum at the upper and lower-thermocline is remotely influenced by the forcing mechanisms of the STCs (Arhan et al., 2006; Johns et al., 2014), leading to a maximum load of SEAW throughout the equatorial-retroflection.

All water sources are present in all the retroflection latitudinal pathways, showing the semi-annual cycle with a maximum transport in boreal spring. However, only the SEAW and NEAW, dominated by the northern retroflection, show a prominent fall maximum. Correlation values between transport time-series of retroflections pathways and water sources confirm the relation between origin and pathway found in 2010. North Atlantic waters are mostly advected by the northern retroflection. However, this northern retroflection is dominated by the tropical and sub-tropical South Atlantic waters, and the equatorial retroflection is highly correlated with the sub-tropical South Atlantic waters.

Additional seasonal-to-interannual transport fluctuations can be associated with the complex TAV interactions, involving a diversity of spatiotemporal mechanisms (Martín-Rey et al., 2018; Vallès-Casanova et al., 2020). Our study does not have a detailed analysis of the inter-annual and decadal variability, yet we have noted a substantial transport increase of SEAW since 2008. This result is in good agreement with the STCs intensification, probably linked with Atlantic multi-decadal variability (Brandt et al., 2021). This trend is leading to a more prominent role of southern tropical waters in the EUC, balancing the contribution of both SEAW and SAW. Its implication in terms of changes in water mass properties carried by the EUC, and the efficiency of the returning limb of the AMOC, remains to be investigated.

Chapter 4

Response of upper-ocean circulation to tropical Atlantic interannual modes

The scarcity of in situ measurements and the variability among individual events has limited our understanding of the drivers and consequences of tropical Atlantic variability (TAV). Here we study the modification of the surface and subsurface ocean circulation as a response of the two main modes of TAV: the Atlantic Meridional Mode (MM) and Equatorial Mode (EM). To quantify the impact of tropical modes on the ocean currents, a set of three oceanic reanalyses and an interannual forced-ocean simulation covering the period 1982-2018 are used. The developing phase of the MM is associated with an intensification of the North Equatorial Countercurrent, the Equatorial Undercurrent (EUC) and the north South Equatorial Current (nSEC) at the eastern equatorial margin. Conversely, the activation of the Rossby-wave reflected mechanism modifies the equatorial gradients, causing a weakening of ocean surface and subsurface transports, accompanied by anomalous warm equatorial conditions in boreal summer. Regarding the EM, the westward surface zonal transport (nSEC) is considerably reduced during boreal spring-summer, with no clear impact at subsurface levels. During the decaying phase, the reflected Kelvin wave, as part of the RW-reflected mechanism, reverses the zonal pressure-gradients at the equator, and, consequently, the westward equatorial nSEC is reinforced. However, the EUC tends to weaken, contrasting with the ocean wave contribution, which suggests the existence of additional off-equatorial forcing. Our results reveal the consistent response of the upper-ocean circulation to the emergence of both MM and EM. Moreover, we demonstrate the key role of ocean wave propagation to modulate the connectivity between tropical and equatorial ocean transports.

This chapter is in preparation as: Martín-Rey, M., Vallès-Casanova, I., Pelegrí, J. L. Response of upper-ocean circulation to tropical Atlantic interannual modes.

4.1 Introduction

The surface winds in the tropical Atlantic Ocean are mainly forced by the latitudinal migration of the Inter-tropical Convergence Zone (ITCZ), with a prominent seasonal cycle between its northernmost position in July-September and its southernmost position in February-April (Schneider

et al., 2014; Waliser & Gautier, 1993). These surface winds not only drive the surface currents but also cause substantial changes in water convergence, which lead to the temporal variability in the off-equatorial geostrophic currents. One major consequence is that the changing circulation of the upper layers in the tropical Atlantic is largely driven by variations in the wind stress field (Castellanos et al., 2015; Rosell-Fieschi et al., 2015; Schott et al., 2004).

The tropical ocean circulation is enclosed by the equatorial branches of the subtropical gyres, the North and South Equatorial Currents (NEC and SEC; Stramma et al., 2003). The North Atlantic tropical gyre has the remarkable seasonal development of the North Equatorial Countercurrent (NECC), which flows eastward with its mean position near 6°N between the NEC and the northern branch of the SEC (Figure 4.1). The NECC exhibits a remarkable seasonal variation, reaching its maximum intensity in boreal spring but vanishing in winter (Fonseca et al., 2004; Garzoli & Richardson, 1989; Rosell-Fieschi et al., 2015). Regarding its zonal distribution, the NECC extends towards the African coast where it bifurcates into the Guinea Dome at the north and joins the Guinea current in the south. Along the western boundary, the upper ocean warm waters flow northward as part of the North Brazil Current (NBC) and North Brazil Undercurrent (NBUC) (Figure 4.1). This poleward flow is embedded in the returning AMOC branch and retroflects permanently at the equator and seasonally near 6°N. This feeds the EUC and the NECC, hence regulating the heat transfer between the subtropical and tropical Atlantic (Hazeleger & Drijfhout, 2006; Lumpkin & Speer, 2003; Stramma et al., 1995).

At the equator, the EUC emerges as a very intense subsurface current (EUC) (Cromwell et al., 1954; Metcalf & Stalcup, 1967), partly supplied by the northward AMOC branch via the NBC (Bourles et al., 1999; Hazeleger et al., 2003; Lumpkin & Speer, 2003; Schott et al., 2004; Zhang et al., 2003). It is generated following the eastward pressure-gradient force that sets up as a response to the easterly winds (Brandt et al., 2006; Provost et al., 2004). The EUC provides relatively cool, salty and oxygen-rich waters to the central-eastern equatorial Atlantic, behaving as the northern-branch of the southern STC and modifying the equatorial upwelling and vertical mixing (Jouanno et al., 2011; Kolodziejczyk et al., 2014). The water transport of the EUC changes along the equator, generally reported to decay eastward but within a high range of uncertainty (Bourlès et al., 2002; Brandt et al., 2006; Kolodziejczyk et al., 2009; Kolodziejczyk et al., 2014; Mercier et al., 2003). Recent observational findings indicate that the strongest EUC transport occurs in fall at the western side (23°W), contrasting with the semiannual cycle in central equatorial Atlantic (10°W) that peaks in boreal spring and fall, and a single EUC maximum at 0°E during boreal spring (Johns et al., 2014). Changes in remote and local winds and in the zonal pressure gradients can drive the zonal variations in the EUC seasonal cycle (Arhan et al., 2006; Giarolla et al., 2005).

At basin scale, the main drivers of TAV are the Meridional Mode (MM) and Equatorial Mode (EM), two air-sea coupled modes peaking in boreal spring and summer respectively (Foltz et al., 2019). The positive phase of the EM displays equatorial warming conditions associated with a reduction of the climatological trades (Zebiak, 1993). The MM is characterized by an interhemispheric sea surface temperature (SST) gradient with anomalous cross-equatorial winds blowing from the cooler to the warmer hemisphere (Nobre & Shukla, 1996). Both tropical modes are tightly linked to changes in the zonal and meridional atmospheric circulation, causing pronounced impacts on the climate of surrounding and remote areas (Ham et al., 2013; Kucharski et al., 2008;

Losada et al., 2012a; Nobre & Shukla, 1996; Polo et al., 2008; Rodríguez-Fonseca et al., 2009; Vimont & Kossin, 2007).

Air-sea processes involved in the generation of TAV modes have been widely investigated. Wind-forced latent heat fluxes are the dominant physical processes responsible for the MM development, through the WES feedback (Amaya et al., 2017; Chang et al., 1997). Strong consensus for the thermodynamic nature of the MM contrasts with an active debate on the mechanisms underlying the EM generation. The prevailing dynamic theory of the EM states that anomalous westerly winds in boreal spring trigger equatorial Kelvin waves (KW) that modify the vertical stratification, activating the thermocline and advective feedbacks (Bjerknes, 1969; Keenlyside & Latif, 2007; Lübbecke et al., 2010; Martín-Rey et al., 2019; Planton et al., 2018; Polo et al., 2015). However, the wave nature of the EM was recently questioned, suggesting the dominant role of air-sea fluxes (Nnamchi et al., 2015, 2016) and subsurface horizontal advection (Richter et al., 2013) in generating equatorial Atlantic SST variability. However, these findings should be interpreted with caution. On the one hand, coupled climate models can overestimate the thermodynamic contribution due to their persistent ocean biases (Dippe et al., 2018; Jouanno et al., 2017). On the other hand, inconsistent results between ocean reanalyses have been found (Nnamchi et al.,

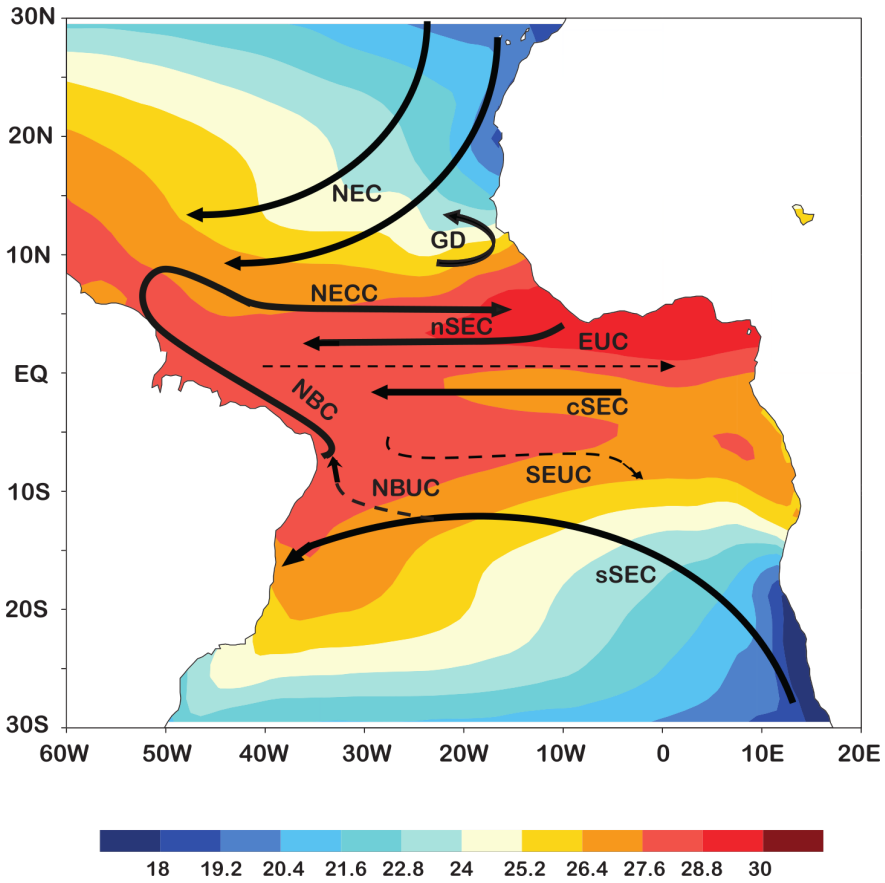

Figure 4.1: Schematic of the ocean circulation in the tropical Atlantic. The main surface (solid lines) and subsurface currents (dashed lines) are presented: North Equatorial Current (NEC), North Equatorial Countercurrent (NECC), the Guinea Dome (GD), South Equatorial Current with northern, central and southern branches (nSEC, cSEC, sSEC), South Equatorial Undercurrent (SEUC), Equatorial Undercurrent (EUC), North Brazil Current (NBC), North Brazil Undercurrent (NBUC). The ocean circulation is overlaid on the climatological SSTs for May, as deduced from the OISST dataset (Reynolds et al. 2002; 2007).

2016), together with further evidence for the wave-induced processes involved in EM generation (Burmeister et al., 2016; Martín-Rey & Lazar, 2019).

Special mention deserves the role played by locally- and remotely-forced ocean waves in shaping the timing and amplitude of the diverse EM patterns (Martín-Rey et al., 2019) and, most outstandingly, in connecting the MM and EM (Foltz & McPhaden, 2010; Martín-Rey & Lazar, 2019). Following the Bjerknes feedback, anomalous westerly winds act as a precursor of equatorial KWs that set up the favorable conditions for the EM development (Bjerknes, 1969; Carton & Huang, 1994; Lübbecke et al., 2010; Martín-Rey et al., 2019). Additionally, oceanic Rossby waves (RW) are excited north of the equator via anomalous wind curl. They propagate westward and are reflected at the western boundary becoming equatorial KWs (Foltz & McPhaden, 2010). These resultant KWs have been suggested to be the decaying mechanism for the traditional EM pattern (Polo et al., 2008) and for the recently defined Horse-Shoe Mode (Martín-Rey et al., 2019). Interestingly, when the RW-reflected mechanism occurs during the MM evolution, it contributes actively to connect, in the same sign, the north tropical and equatorial Atlantic SST variability (Martín-Rey & Lazar, 2019).

In summary, the emergence of MM and EM encompasses wind fluctuations and zonal gradients in sea surface height (SSH), which are the main drivers for surface and subsurface currents. However, the relationship between TAV modes and the changes in the surface tropical Atlantic Ocean have been overlooked. Marked year-to-year variations in the strength and location of the NECC have been reported during a relatively short observational period (1993-2000), associated with SSH and wind curl variability (Arnault et al., 1999; Fonseca et al., 2004). Hormann et al. (2012) have already proposed a linkage between the NECC and the tropical modes, relating the NECC intensification with a negative EM and the northward shift of the NECC with a positive MM. Results from forced-ocean simulations indicated that anomalous warming and positive SSH in the eastern equatorial Atlantic, associated with relaxed easterly winds, are accompanied by a weakening of the EUC (Góes & Wainer, 2003; Hormann & Brandt, 2007). Further studies have suggested that enhanced EUC variability at intra-seasonal to interannual timescales can be associated with the excitation of tropical instability waves (TIWs) and equatorial Kelvin waves (Hormann & Brandt, 2009; Perez et al., 2012). However, most of these studies are based on observations and modelling of observed individual events, which exhibit discrepancies between them (Brandt et al., 2014; Hormann & Brandt, 2009). This, together with the scarce in-situ measurements, has hampered the correct assessment of the impact of TAV modes on ocean transport.

Our study is a first attempt to provide a more accurate characterization of the changes in the upper-ocean circulation under the emergence of MM and EM. For such purpose, we use a set of three oceanic reanalyses and a forced-ocean interannual simulation covering the period 1982-2018. The chapter is organized as follows. Section 4.2 gives an overview of the data and methodology. Section 4.3.1 focuses on the seasonality and variability of tropical ocean currents, section 4.3.2 describes the development of MM and EM, section 4.3.3 investigates the modification of surface and subsurface currents as induced by TAV modes, and section 4.3.4 analyses case studies for cold and warm MM-EM interaction during 2009 and 2010, respectively. Finally, the main conclusions achieved are summarized in section 4.4.

4.2 Data and methods

4.2.1 Observations and ocean reanalyses

The observational SST time series for the 1982-2019 period come from the Optimum Interpolation Sea Surface Temperature (OISST) dataset version 2 (Reynolds et al., 2002; Reynolds et al., 2007), the zonal and meridional wind stress for the 1979-2019 period is extracted from the atmospheric ERA5 reanalysis (Hersbach et al., 2020), and the SSH data for the period 1993-2019 comes from the AVISO website. The multivariate ARMOR3D (Verbrugge et al., 2017) three-dimensional temperature, salinity and geostrophic current ocean data for the 1997-2019 period is also used as an additional observational tool.

To achieve a robust assessment of the ocean transport response to TAV modes, three different forced-ocean reanalyses have been considered. The Ocean Reanalysis System 5 (ORAS5; Zuo et al., 2018) is based on the NEMO ocean model (Madec & the NEMO Team, 2016), version 3.4, with $1° \times 1°$ horizontal resolution and 75 vertical levels. A set of 5 ensemble members, which differ in the initial atmospheric and oceanic conditions, has been performed for the period 1979 to 2018. The ocean model is forced with surface air-sea fluxes from ERA-Interim (Dee et al., 2011) for the period 1979-2014 and the ECMWF operational numerical weather prediction from 2015 onwards. Observations from SST, sea ice concentration, in-situ profiles and sea level anomalies are also assimilated in ORAS5. In the present study, we use the ensemble mean of these 5 members expanding from 1979 to 2018.

The Simple Ocean Data Assimilation version 3 (SODA3; Carton et al., 2018) reanalysis is built onto MOM5, the ocean component of the GFDL CM2.5 coupled model (Delworth et al., 2012), with $1/4° \times 1/4°$ horizontal resolution and 50 vertical levels. The version 3.4.2 considered in the present study, hereinafter SODA342, expands from 1980 to 2018 and uses the atmospheric forcing from ERA-Interim reanalysis.

The Global Ocean and Sea Ice Physics reanalysis version 4 (GLORYS2v4, hereinafter GLORYS) is performed with the version 3.1 of NEMO model, which has $1/4° \times 1/4°$ horizontal resolution and 75 vertical levels (Garric & Parent, 2018). The ERA-interim atmospheric forcing used to force the ocean model, include large-scale correction for radiative and rainfall fluxes. The GLORYS data, which covers the period 1993-2015, assimilates temperature and salinity profiles as well as sea level anomalies, sea ice concentration, SST and mixed layer depth data.

4.2.2 Interannual NEMOINT simulation

To increase the robustness of the results, the forced-ocean NEMOINT simulation has also been used in the present study. NEMOINT uses the tropical Atlantic configuration of the NEMOv3.2 model, with $1/4°$ horizontal resolution in a tripolar grid and 46 vertical levels (Faye et al., 2015). The inter-annual air-sea fluxes from DFS4.4 (Brodeau et al., 2010), which is an improved atmospheric dataset based on ERA40 (Uppala et al., 2005) and ERA-Interim reanalysis, force the ocean model during the period 1960-2011. NEMOINT provides a realistic simulation of the tropical Atlantic seasonal cycle, interannual variability and air-sea mechanisms (Martín-Rey & Lazar, 2019; Martín-Rey et al., 2019).

4.2.3 Methodology

4.2.3.1 Climate anomalies and discriminant analysis

We have selected 1982-2018 as the longer common available period for the observations (OISST) and the two reanalysis (SODA342 and ORAS5), and have used somewhat shorter intervals for the GLORYS reanalysis (1993-2015), ARMOR3D (1997-2019) and the model NEMOINT simulation (1982-2011). Monthly anomalies are computed by subtracting the climatological annual cycle to the entire period. To retain the interannual variability and remove the low-frequency signal and global warming trend, a Butterworth filter with a 7-year cut-off frequency is applied to the monthly anomalies (Butterworth et al., 1930). Seasonal averages are then calculated for each calendar month through averaging over 3-month periods.

The MM and EM modes are calculated as the main modes of SST TAV [70°W-30°E, 30°N-30°S] in boreal spring (March-April-May,MAM) and summer (June-July-August, JJA), respectively. A principal component analysis (PCA; North et al., 1982) provides the empirical orthogonal functions or eigenvectors (EOFs) and the associated time series or principal components (PCs), explaining a percentage of the total variance (von Storch & Zwiers, 1984). The development of MM and EM is analyzed through regression maps of anomalous atmospheric and oceanic variables. The regression maps are calculating by projecting each grid point of an anomalous field over the standardized PCs of the MM and EM. The resultant longitude-latitude maps will represent the change in amplitude of the anomalous variable per 1 standard deviation of the projected index (von Storch & Zwiers, 1984).

Only significant values exceeding 90% and 95% confidence level according to a Monte Carlo test are presented. The response of ocean currents to TAV modes is then assessed through a composite analysis. The composite technique allows for creating a sample of typical anomalous ocean surface and subsurface currents for MM and EM events. We choose those years in which the PC exceeds ± 0.5 std in all datasets. In this sense, the following positive (negative) EM events are identified: 1984 1988 1991 1996 1999 2003 (1992 1997). For the MM, the warm (cold) years are 1983 1998 2005 2010 (1985 1986 1989 1994 1999 2009). The difference of positive minus negative events is represented from January to December, capturing the entire MM and EM evolution. A t-test is applied to estimate whether or not the averages of the positive and negative samples have the same mean (von Storch & Zwiers, 1984).

4.2.3.2 Climate indices for tropical ocean transport

We are interested in the changes experienced by three main zonal currents within the TAV modes region: NECC, EUC and the equatorial nSEC. For both NECC and the equatorial nSEC, we consider the surface zonal velocities. In contrast, for the correct determination of the EUC, we use vertical temperature-salinity (T-S) sections from ocean reanalyses and observations to locate the maximum salinity and oxygen concentration (Figure 4.2); these sections reveal that the 18°C isotherm is a good proxy for the EUC, since it follows perfectly the zonal evolution of the salinity maximum along the equatorial band. Thus, we assess the intensity of the EUC as the zonal velocity along the 18°C isotherm in all numerical datasets, which are also validated with the observational ARMOR3D data.

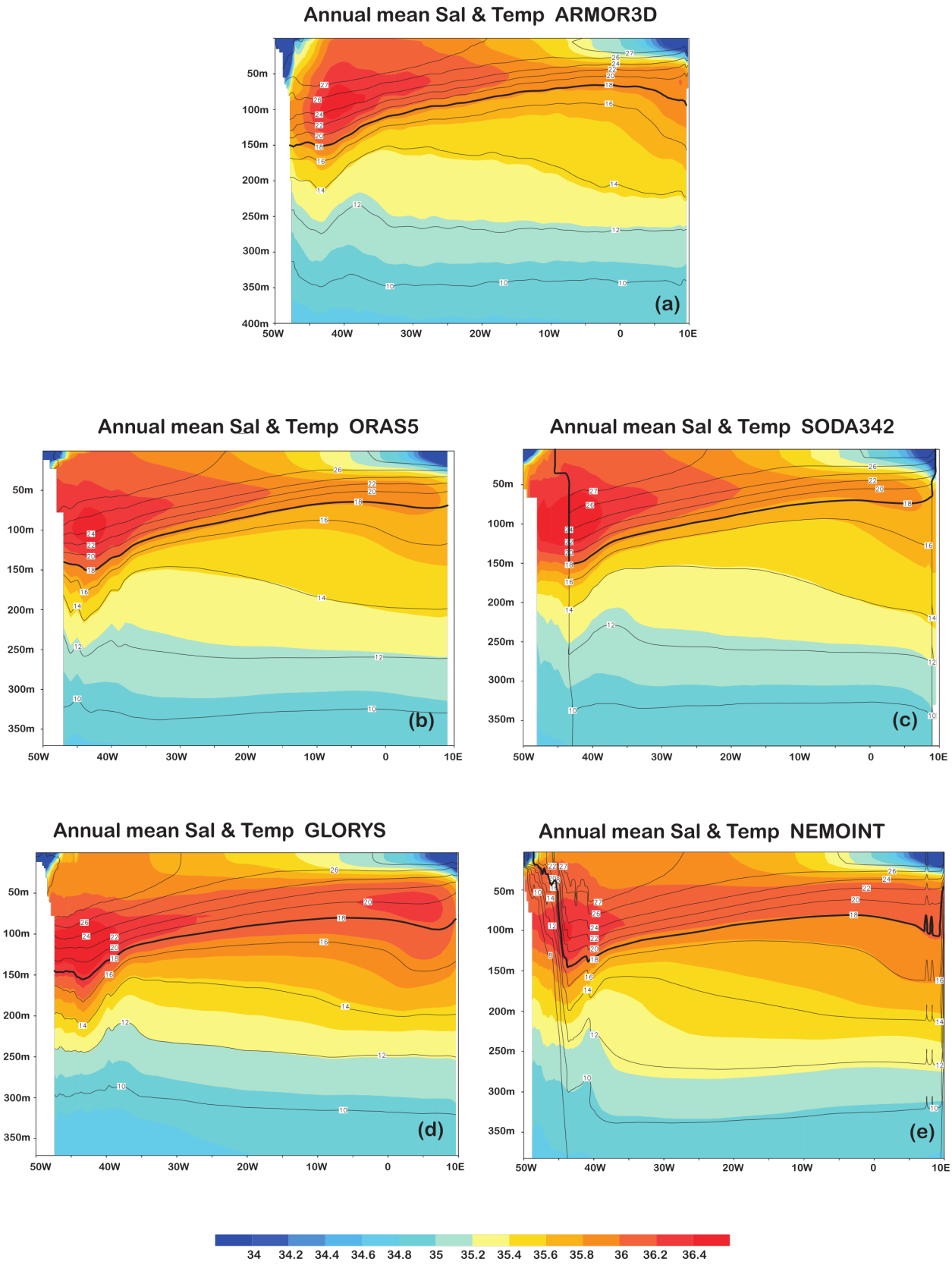

Figure 4.2: Definition of Equatorial Undercurrent (EUC). (a-e) Vertical sections of annual mean temperature (contour, in °C) and salinity (shaded, in psu) along the equator for ARMOR3D, ORAS5, SODA342, GLORYS and NEMOINT. The EUC position is characterized by maximum values of salinity. We choose the isotherm of 18°C (thick black line) as a proxy of EUC since it completely captured the zonal distribution of the current along the entire equatorial band.

To characterize the above-mentioned zonal currents, climate indices are defined in the associated key regions. For NECC, zonal velocities are averaged over the region [50°W-15°W,4°N-10°N].. Regarding the zonally varying distribution of the EUC, two different regions are also considered: in the western equatorial Atlantic [40°W-20°W, 2°N-2°S] (WEUC) and in the eastern side [20°W-10°E, 2°N-2°S] (EEUC) (Figure 4.3). Similarly, at surface levels, the western [40°W-20°W, 2°N-2°S] and eastern [20°W-10°E, 2°N-2°S] equatorial nSEC (Figure 4.3) are analysed separately.

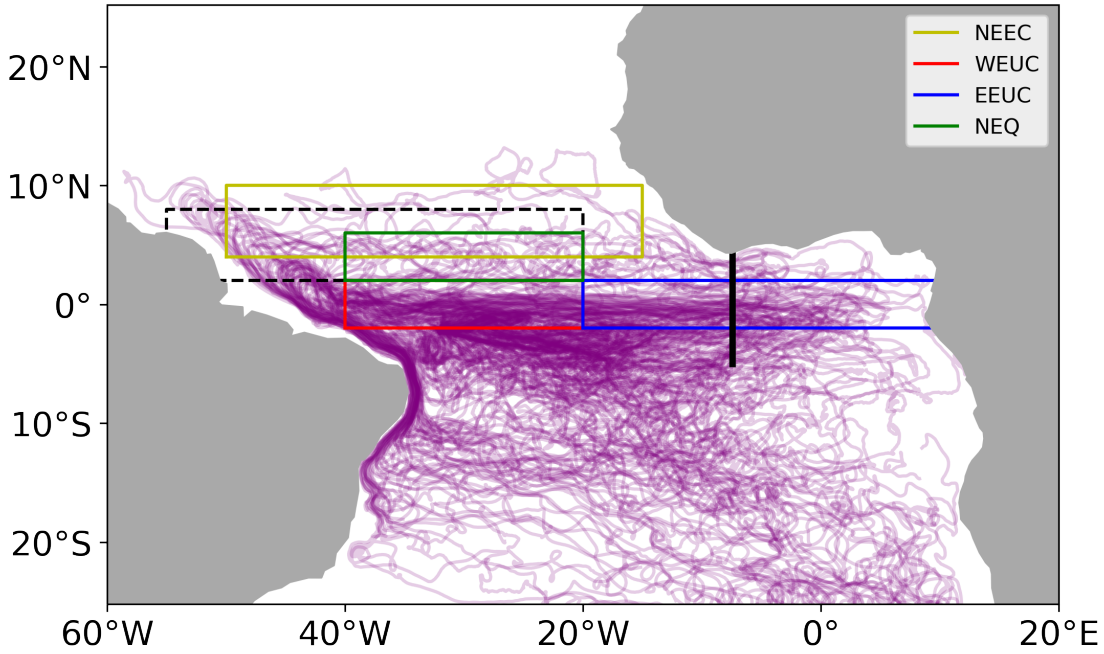

Figure 4.3: Schematic of the Lagrangian particle simulations. Particles are backtracked advected from a release vertical section located at 7.45°W between the African coast and 5°S, from the sea surface to lower thermocline (black line). The equatorial transport is defined as those particles that reach the release section between 2°S -2°N, while the north-equatorial transport considers those particles departing from the area limited between the northeast Brazilian coast to 20°W and 2°N to 8°N (black dashed box). The zonal-current indices are defined as the average of zonal velocities over [50°W- 15°W,4°N-10°N] for NECC (yellow box). Western [40°W-20°W, 2°N-2°S] and eastern [20°W-10°E, 2°N-2°S] indices are considered at surface: WEq-nSEC (red box) and EEq-nSEC (blue box) and subsurface levels: WEUC for (red box) and EEUC for (blue box); The RW-reflected mechanism is assessed through changes in SSH and ocean transport in the north-equatorial Atlantic [40°W-20°W,2°N-6°N] (green box).

4.2.3.3 Lagrangian simulations

Previous studies have brought to light the connection between MM and EM via the RW-reflected mechanism, linking the north tropical and equatorial SST variability (Foltz & McPhaden, 2010; Martín-Rey & Lazar, 2019). Here we investigate the ocean transport connectivity within the tropical Atlantic through Lagrangian simulations that use the three-dimensional velocity fields from NEMOINT. The particles are advected using the Lagrangian tool Ocean Parcels (Delandmeter & Van Sebille, 2019), which supports data discretized on C-grids such as the NEMO-based models. Each particle represents a finite transport from the total amount that flows through a release section at a given time step. By doing so, we are able to determine the water mass reaching and

departing from some predefined geographical zone and how it changes over time (Blanke et al., 1999; van Sebille et al., 2018).

In Figure 4.3 we present the particle trajectories advected backward in time from a meridional section at 7.45°W between the African coast and 5°S, spanning from the sea surface to the lower thermocline ($\sigma < 26.8$ kg m^{-3}) every 10 days. The particles position, temperature and salinity are interpolated every 5 days through the entire NEMOINT model output.

From a near-steady perspective at seasonal scales, waters from the western margin reach the eastern equatorial Atlantic through the NECC near the sea surface, and the EUC at the thermocline (Figure 4.1). The RW-reflected mechanism provides an overlooked transient eastward equatorial pathway, forced by its associated anomalous SSH gradient. We will next investigate how the RW-reflection connects the off-equatorial and equatorial ocean transports. We define the north-equatorial transport as those particles departing from the area limited between northeast Brazilian coast to 20°W and 2°N to 8°N (black dashed box in Figure 4.3). We quantify the equatorial water transport through counting particles that reach the release section between 2°S-2°N (dashed black line, Figure 4.3); for both pathways, we distinguish between thermocline transport (23.5 kg m^{-3} < σ < 26.4 kg m^{-3}) and surface transport ($\sigma < 23.5$ kg m^{-3}).

4.3 Results

4.3.1 Seasonal cycle and variability of tropical Atlantic Ocean currents

We use time-longitude diagrams to assess the skill of the ocean reanalyses and NEMOINT to reproduce the seasonality of the NECC, EUC and the equatorial nSEC, assessed in terms of monthly-mean values and their variance (Figure 4.4).

All datasets show a consistent surface westward flow along the equatorial band during boreal summer (May-August, Figure 4.4a-d), coinciding with the intensification of the easterly winds and the cold tongue development (Lübbecke et al., 2018). The maximum variability of this equatorial nSEC occurs in boreal-spring and summer in the central equatorial Atlantic, reaching as far as the Greenwich meridian (Figure 4.4a-d).

The longitude-time diagrams replicate the zonally varying seasonal cycle of the EUC, as reported in previous studies (Johns et al., 2014). All reanalyses and NEMOINT reproduce a year-long persistent eastward flow in the western equatorial Atlantic [40°W-25°W], with two maxima peaking in boreal spring and autumn (Figure 4.4e-h). Notice that only the fall maximum presents an eastward extension, which coincides with the western EUC (at 23°W) seasonal cycle reported by Johns et al. (2014). East of 20°W, the EUC varies greatly all year long, with the most intense eastward flow in September-October (Figure 4.4e-h).

Finally, the development of the NECC during late summer and fall is well captured in all datasets (Figure 4.4i-l), together with the maximum variability close to the South American coast (Figure 4.4i-l).

The consistent results in the near-surface tropical ocean for all four simulations, in agreement with previous findings (e.g., Brandt et al., 2006; Fonseca et al., 2004; Kolodziejczyk et al., 2009;

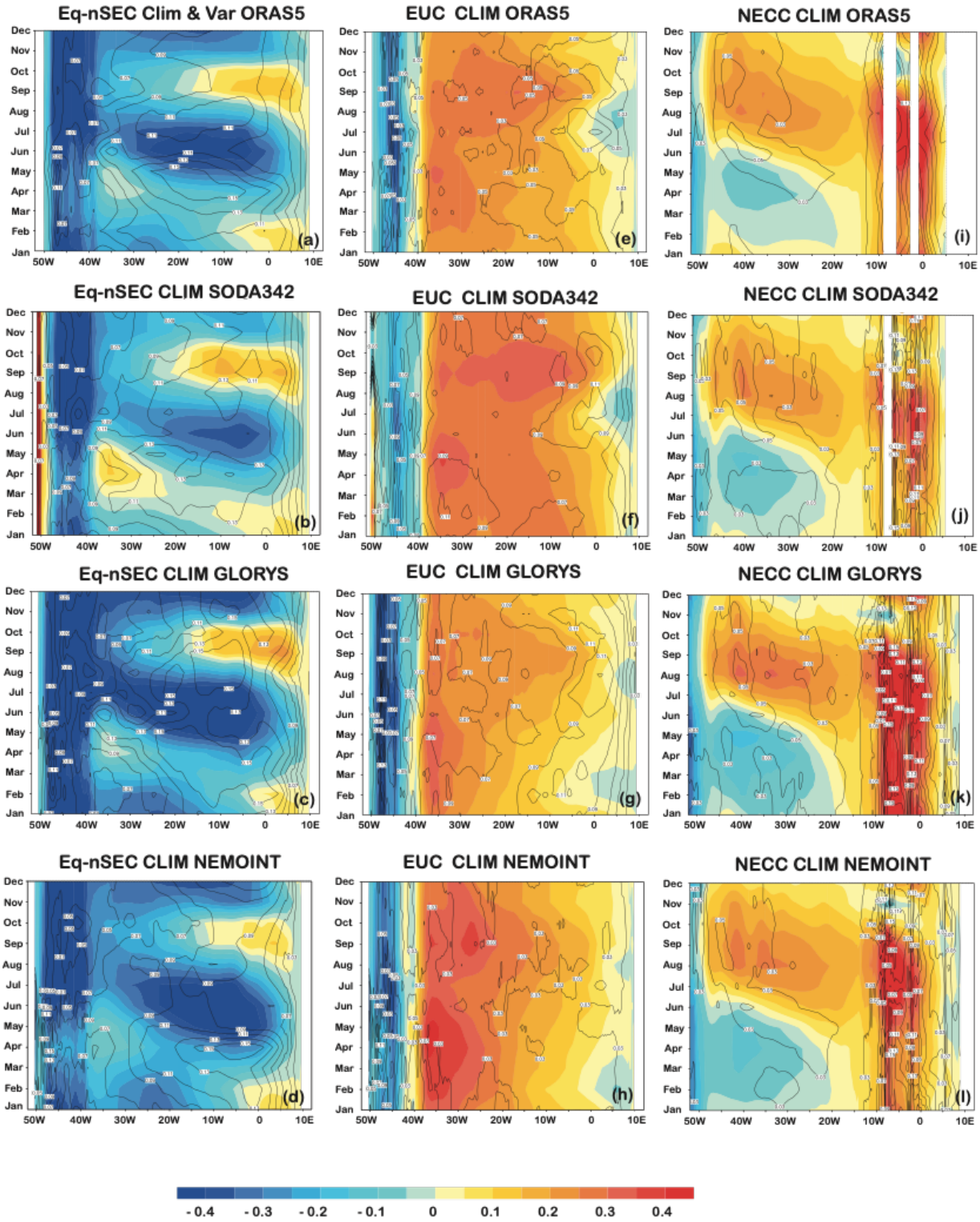

Figure 4.4: Seasonal cycle and variability of surface and subsurface zonal currents. Monthly climatological mean (colours) and standard deviation (contour) of (a-d) the equatorial surface currents Eq-nSEC, (e-h) the eastern Equatorial Undercurrent (EUC), and (i-l) the North Equatorial Countercurrent (NECC), from ORAS5, SODA342, GLORYS and NEMOINT, as labelled.

Rosell-Fieschi et al., 2015), allows us to further explore how ocean currents respond to the TAV modes.

4.3.2 Evolution of Tropical Atlantic Variability modes

MM emerges as the mode leading the SST TAV during boreal spring (March-May) in all datasets, explaining between 32% and 42% of the total variance. While AN appears as either the first (OBS, ORAS5 and NEMOINT) or second (SODA342 and GLORYS) contribution to the SST TAV during boreal summer (June-August), accounting for 21% to 31% of the total variance. The evolution of these patterns and the underlying air-sea mechanisms are described in the next sections.

4.3.2.1 Meridional Mode

The development of the MM starts with an anomalous reduction of climatological north-easterlies in late winter (Figure 4.5a-e), favoring the warming of the surface ocean via latent heat fluxes (Chang et al., 1997). The inter-hemispheric SST gradient produces a see-saw sea level pressure anomaly at both sides of the equator (not shown), giving rise to cross-equatorial winds blowing northward that reinforce the initial SST pattern (Figure 4.5a-j). Consequently, the easterly winds are intensified along the equator, generating weaker and even negative SST anomalies (Figure 4.5f-j). Despite differences in the amplitude and basin-scale structure of the MM, all datasets illustrate this sequence of wind-SST anomalies, in agreement with the thermodynamic mechanisms described in the WES feedback (Amaya et al., 2017; Xie & Philander, 1994). Remarkably, when the MM decays, a pronounced warming emerges in the central-eastern equatorial Atlantic during summer season in all datasets (Figure 4.5k-o). This basin-scale pattern, with persistent warming conditions in north tropical and equatorial Atlantic, resembles the non-canonical EM defined by Richter et al. (2013). Recent findings have identified this configuration with the result of a same-sign interaction between the MM and the EM (Martín-Rey & Lazar, 2019).

To explore the origin of this equatorial warming, we use regression maps of anomalous wind stress curl and SSH over the MM (Figure 4.6) and longitude-time diagrams (Figure 4.7). The MM-induced cross-equatorial winds turn westward in the northern hemisphere (Figure 4.6a-e) and produce anomalous negative wind-stress curl north of the equator during boreal spring (Figure 4.6a-e). This originates an anomalous negative Ekman pumping and downwelling conditions around 30°W, reflected at surface levels as an anomalous SSH elevation (Figure 4.6a-e). The SSH perturbation propagates westwards as a downwelling Rossby wave that is reflected at the South American coast, becoming an equatorial Kelvin wave (KW) (Figure 4.6f-o and Figure 4.7). As the KW moves east, the thermocline flattens, reducing the upwelling and favoring the equatorial warming (Figure 4.6k-o and Figure 4.7).

Notice that the amplitude of equatorial SST anomalies varies among datasets, being stronger in OBS and NEMOINT (Figure 4.6k,o). This can be understood in terms of the local wind forcing. An anomalous wind stress convergence at the equator in OBS and NEMOINT that also contributes to warm the sea surface, amplifying the impact of the downwelling KW (dKW) (Figure 4.6k,o). Conversely, the reinforced easterly winds in GLORYS, ORAS5 and SODA342 (Figure 4.6l-m) tend to cool the surface via equatorial upwelling, and thus counteract the warmer conditions induced by the dKW propagation (Figure 4.6n). Our results corroborate the existence of the RW-reflected mechanism during the MM evolution and confirm its fundamental role in the equal-sign MM-EM connection. Moreover, the varying equatorial SST amplitude among datasets further supports the

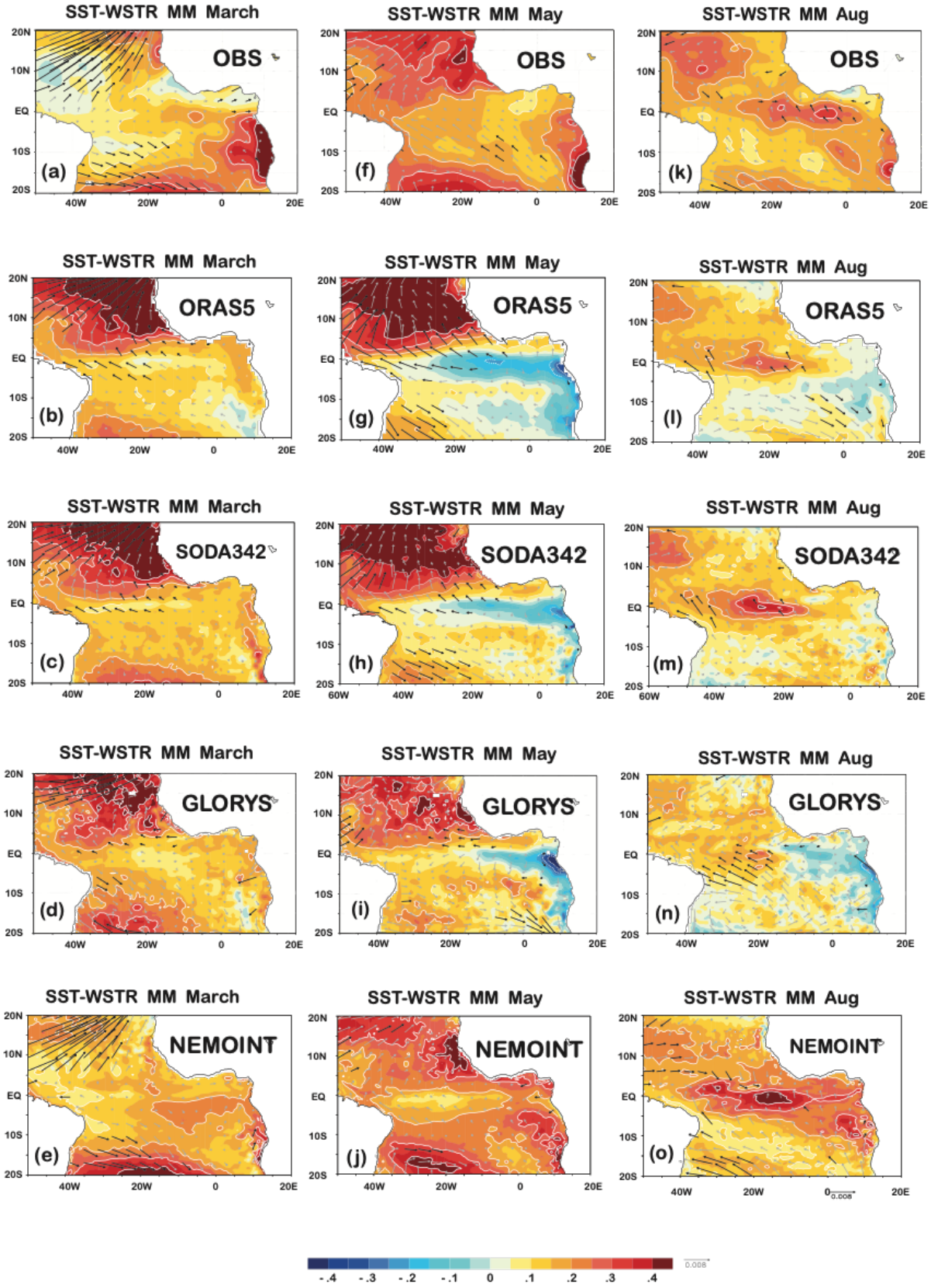

Figure 4.5: Evolution of the Meridional Mode (MM). (a-o) Regression maps of the monthly SST anomalies (coloured, in °C) and wind stress anomalies (vectors, in N m_{-2}) over the MM, from March to August, in (a-c) the observations (OBS), (j-l) GLORYS and (m-o) NEMOINT. For OBS, GLORYS and NEMOINT, the wind stress fields come from DFS4.4, ERA-Interim and ERA5, respectively. Significant values exceeding the 90% confidence level according to a t-test are shown in white contours and black vectors.

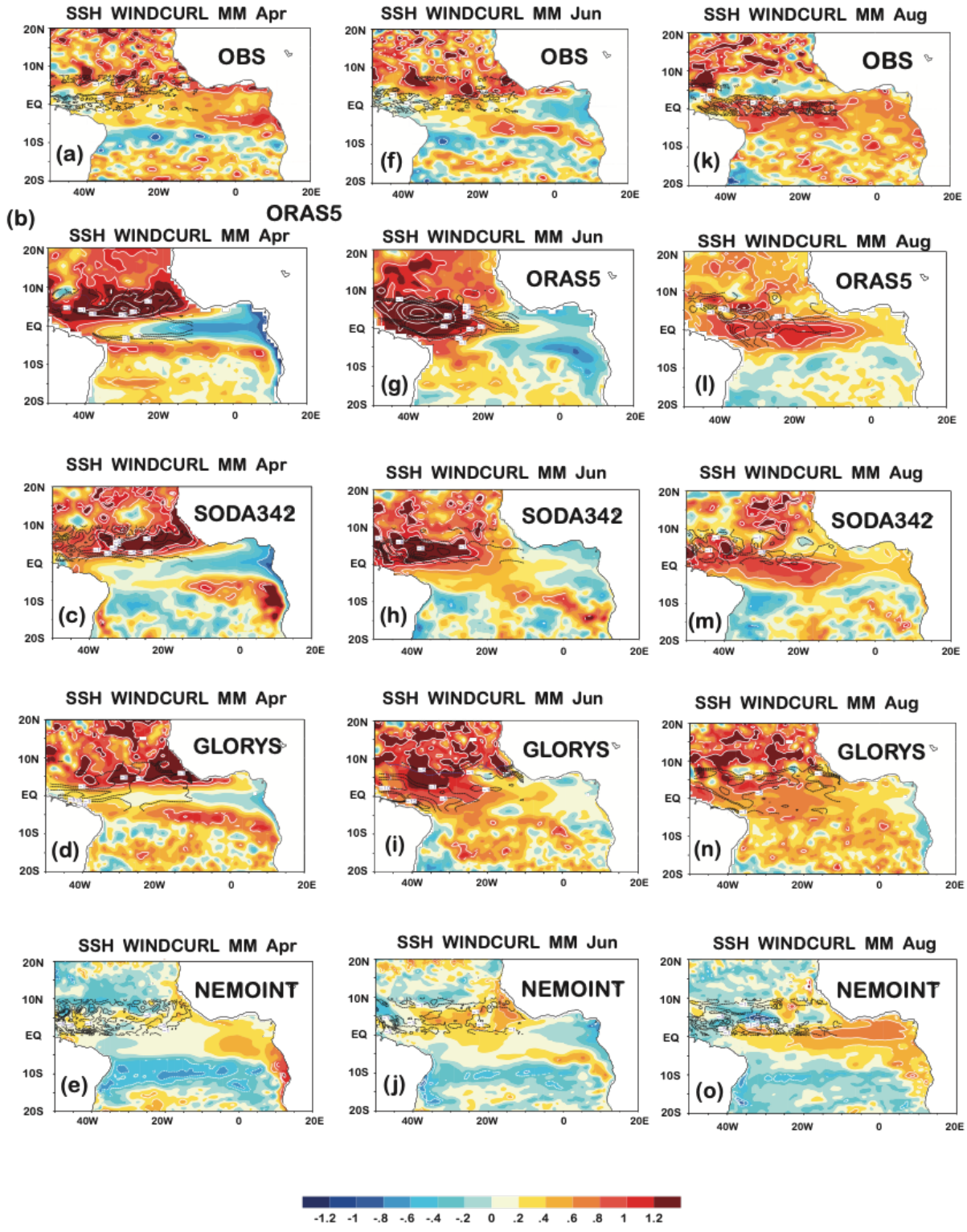

Figure 4.6: Ocean wave propagation associated with the Meridional Mode (MM). (a-p) Regression maps of the monthly SSH anomalies (coloured, in cm) and wind-stress curl anomalies (contours, in 10_{-9} N m_{-3}) north of the equator over the MM, from April to August, in the (a-d) observations (OBS), (e-h) ORAS5, (i-l) SODA342, (m-p) GLORYS, and (q-t) NEMOINT. Notice that negative (positive) wind curl indicates downward (upward) vertical velocities at the base of the mixed layer and the concomitant SSH elevation (reduction). Significant values exceeding the 90% confidence level according to a t-test are shown in white contours.

modulating role of local winds in the effectiveness of the RW-reflected mechanism (Martín-Rey & Lazar, 2019).

4.3.2.2 Equatorial Mode

An anomalous reduction of the climatological south-easterly winds occurs in late winter (Figure 4.8a-j), as part of a weakening of the South Atlantic anticyclone (Lübbecke et al., 2010; Martín-Rey et al., 2019; Polo et al., 2008). These anomalously weak winds cause a reduction of the latent heat loss, warming the south tropical Atlantic (Martín-Rey et al., 2019). At the equator, anomalous westerly winds can cause the thermocline to deepen (Figure 4.8k-o), reducing the equatorial upwelling and activating the dynamic feedbacks responsible for generating the equatorial SST anomalies in summer (Martín-Rey et al., 2019; Polo et al., 2015).

Special mention deserves the different atmospheric forcing and its concomitant SST signal in the north tropical Atlantic among all datasets (Figure 4.8). GLORYS, SODA342 and the observations illustrate an anomalous reinforcement of the climatological trade winds, accompanied by an anomalous surface cooling (Figure 4.8a,f,k; c,h,m; d,i,n). Nevertheless, the opposite behavior is found in ORAS5 and NEMO, with anomalous south-westerly winds leading the warming of the surface ocean (Figure 4.8b,g,l; e,j,o). These two different structures resemble the diverse EM configurations reported along the observational record (Martín-Rey et al., 2018; Vallès-Casanova et al., 2020).

Recent findings suggested the important contribution of the ocean background state for the EM diversity (Martín-Rey et al., 2018). Despite the common period of study, the ocean reanalyses and NEMOINT are performed with different atmospheric forcing, initial conditions and parameterizations, which generate in turn a different tropical Atlantic mean state. Thus, we can hypothesize that the discrepancies among datasets in the simulation of the EM can be understood as the interannual TAV that develops as a response to local and remote atmospheric forcing under different ocean climatologies.

The role of ocean wave activity in the EM evolution is examined in Figures 4.9 and 4.10. An anomalous SSH elevation appears in the central-eastern equatorial Atlantic from April to June (Figures 4.9a-j and 4.10), which sets up the favorable conditions for the warm tongue generation (Figure 4.9k-o). Outstandingly, positive wind curl anomalies appear north-of-the-equator during spring and early summer, which originate anomalous negative SSH anomalies via Ekman induction (Figure 4.9a-j). This triggers an upwelling RW that propagates westward and is reflected at the western boundary in July (Figure 4.10). The resultant upwelling KW (uKW) tends to counteract the previous positive SSH anomalies, contributing to the termination of the EM warm tongue (Figures 4.9k-o and 4.10).

Notice that for ORAS5 and NEMOINT, the positive SST anomalies in the north tropical Atlantic reduce the inter-hemispheric gradient (Figure 4.8b,g,e,j) and thus the associated wind-curl north of the equator (Figure 4.9b,g,e,j). Consequently, the RW-reflected mechanism is weaker and can be masked by the basin-scale low-frequency SSH signal (Figure 4.9k,o). However, the fast decay of the warm tongue elevation in August supports the propagation of the uKW (Figure 4.10i-j). Despite the changes in amplitude, the consistent results among datasets corroborates the contribution of the RW-reflected mechanism for the EM termination, in agreement with previous studies

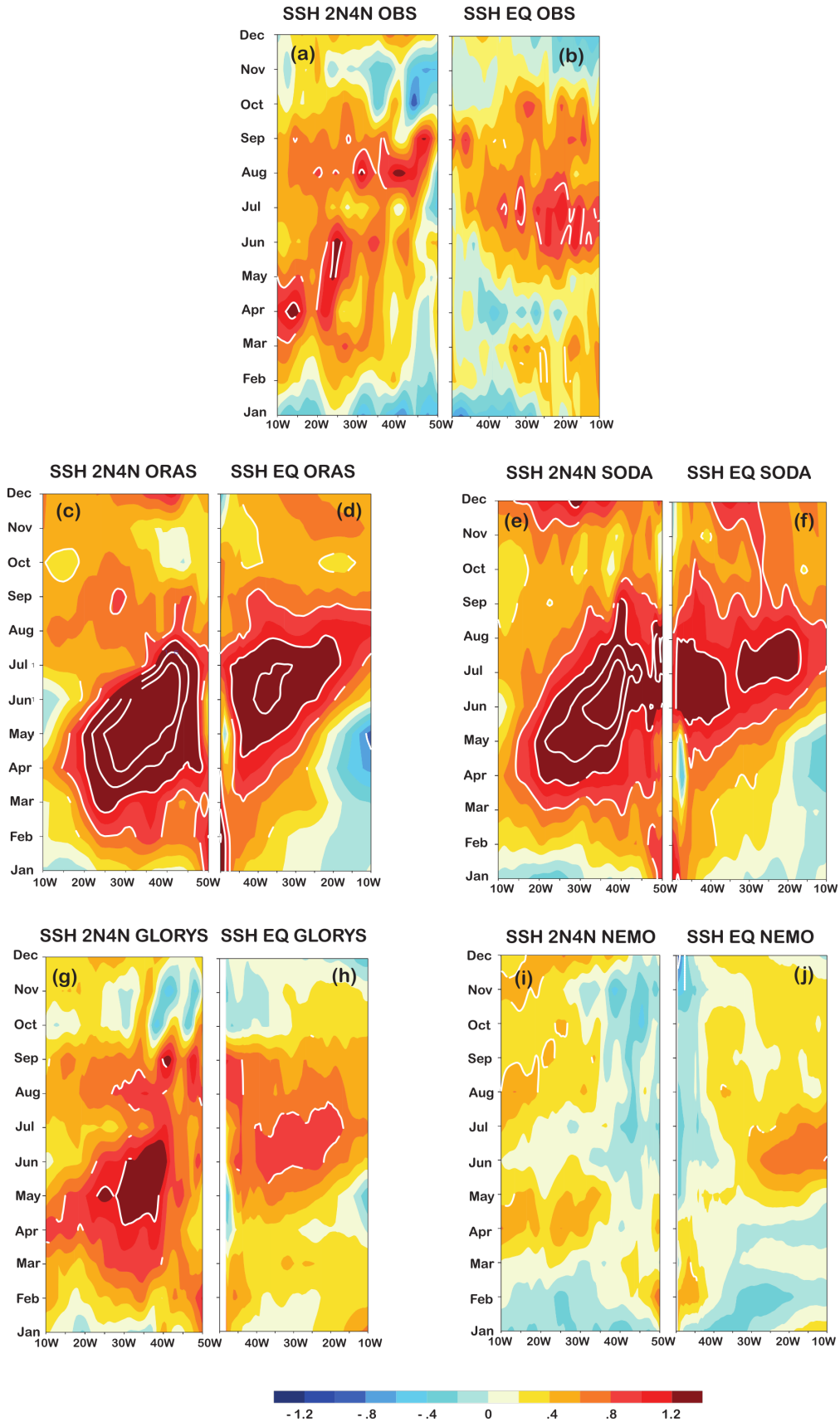

Figure 4.7: Equatorial wave propagation during the evolution of the Meridional Mode (MM). Time-longitude diagrams along 2°N-4°N and along the equator of the regression between the MM and the monthly SSH anomalies (in cm) from January to December for ORAS5, SODA342, GLORYS and NEMOINT. Notice that the x-axis has been reversed along 2°N-4°N to better visualize the boundary-reflection of the downwelling Rossby wave into an equatorial Kelvin wave. Significant values exceeding the 90% confidence level are denoted in white contours.

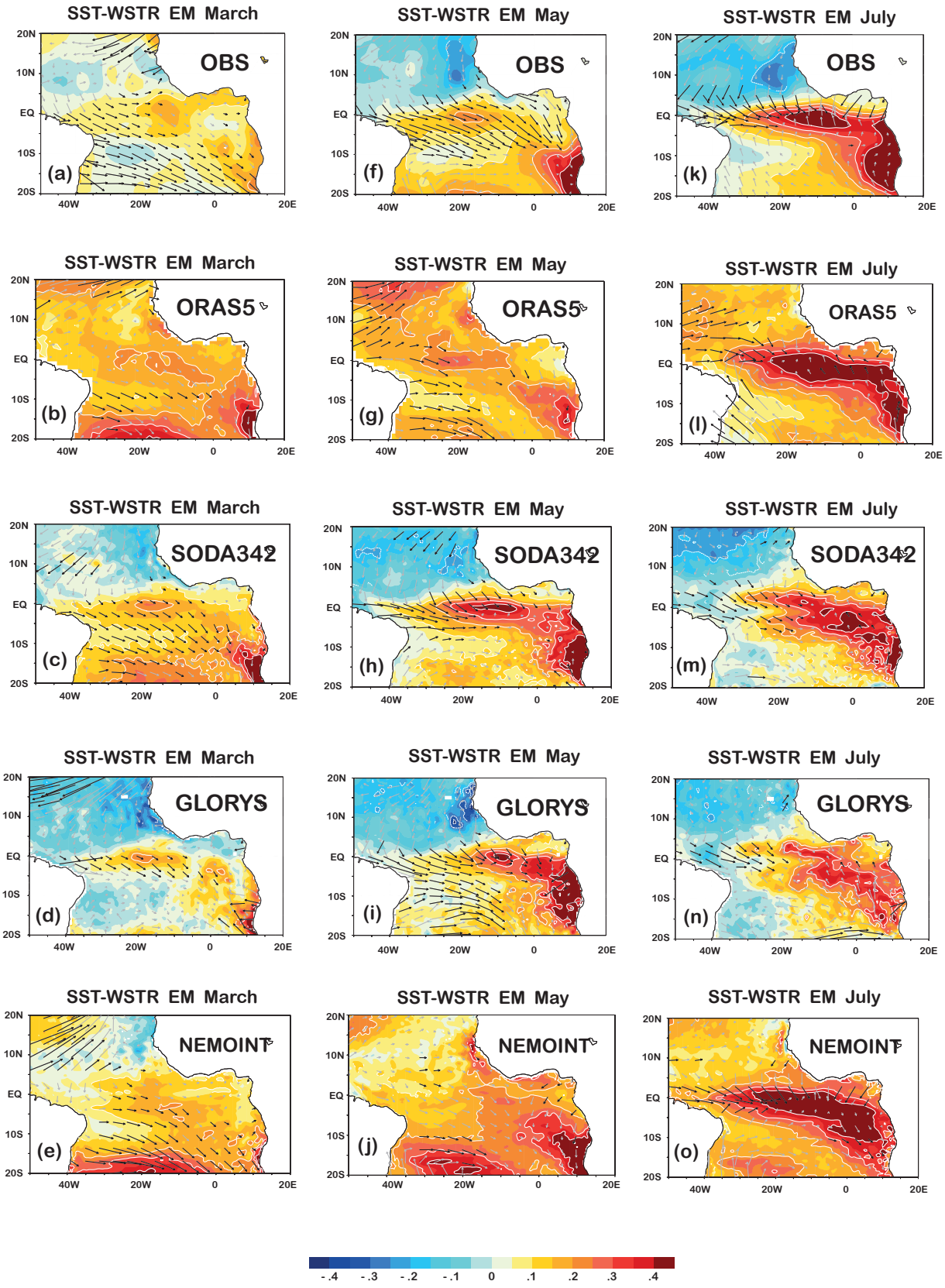

Figure 4.8: Evolution of the Equatorial Mode, as in Figure 4.5

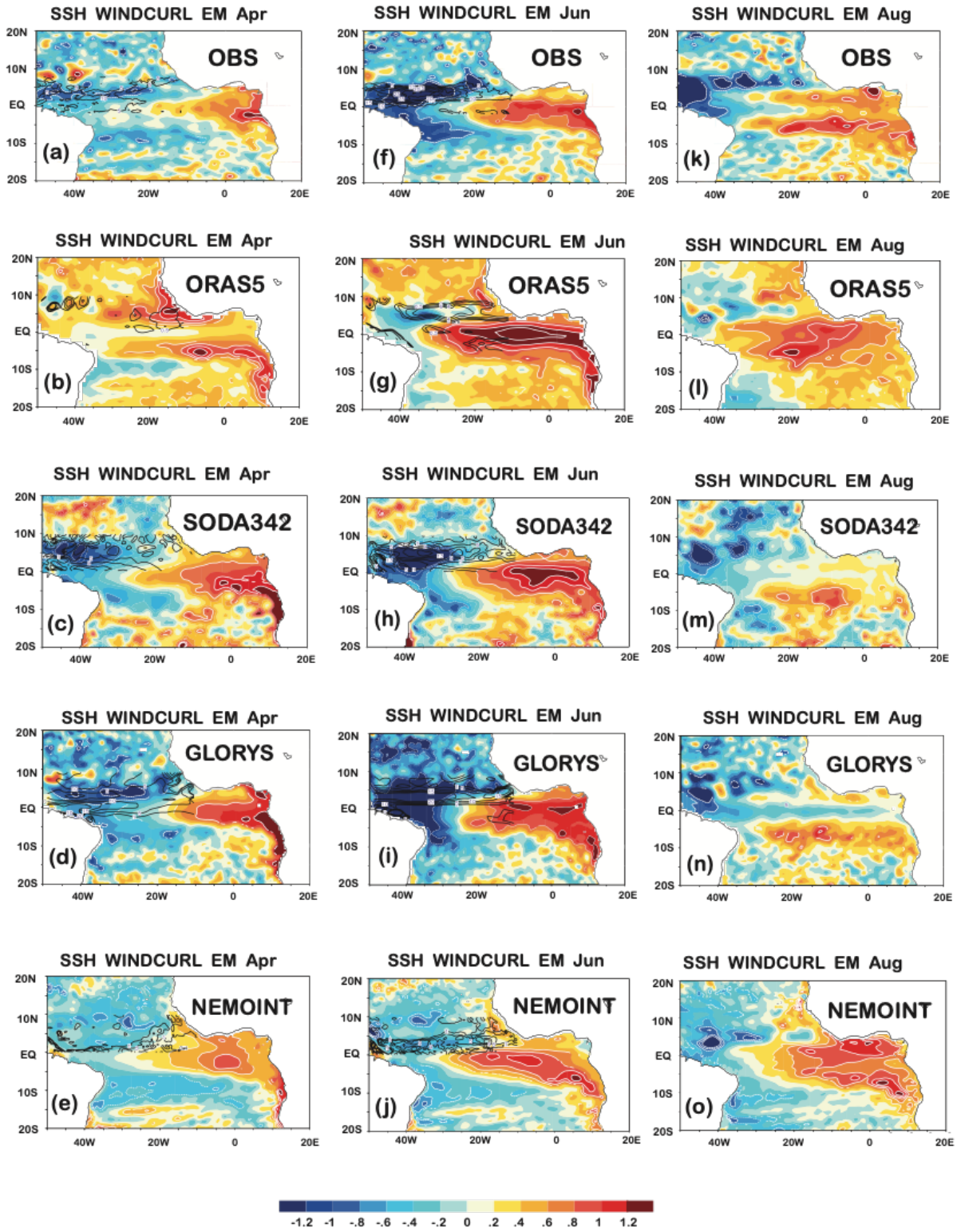

Figure 4.9: Ocean wave propagation associated with the Equatorial Mode, as in Figure 4.6

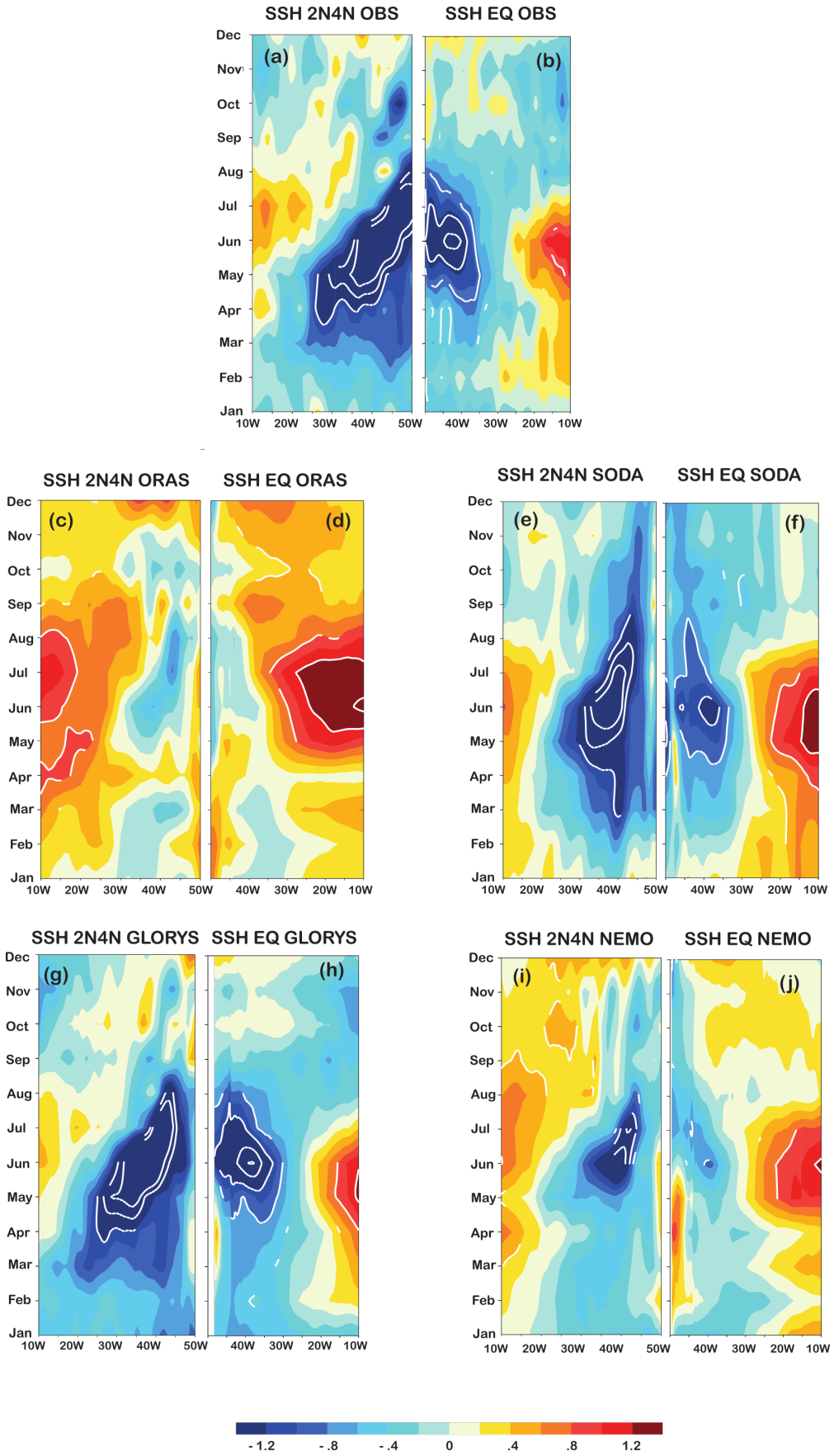

Figure 4.10: Equatorial wave propagation during the evolution of the EM, Figure 4.7

(Martín-Rey et al., 2019; Polo et al., 2008; Vallès-Casanova et al., 2020). Moreover, we provide further evidence on the dynamic nature of the EM and the key role of ocean wave activity for the development and decay of these phenomena.

4.3.3 Ocean currents response to meridional and equatorial modes

In the previous sections, we have demonstrated that the development and decay of MM and EM are intimately linked to surface wind variations and changes in zonal SSH gradients. Under this context, we expect a readjustment of the tropical ocean circulation. Hence, in order to investigate the impact of MM and EM on the NECC, the EUC and the equatorial SEC, we carry out a composite analysis (Figure 4.11).

During the MM, anomalous south-westerly winds north of the equator (Figure 4.5a-j) produce a west-east SSH gradient around 2°N-8°N that reaches its maximum in May and propagates westward afterwards (Figure 4.7), developing high anomalies close to the American coast in June (Figure 4.6f-j). Consequently, the NECC shows anomalous intensification in May-June (Figure 4.11a-d). At the equator, the zonal gradient in SST anomalies reinforces the easterly winds (Figure 4.5a-j and 4.6a-j), which intensifies the anomalous westward equatorial nSEC from February to May (Figure 4.11a-d). The associated increase in the slope of the thermocline enhances the western and eastern EUC in boreal spring (Figure 4.11a-d). This anomalous tropical circulation is drastically reversed in the summer months (Figure 4.11a-d), coinciding with the arrival of the boundary-reflected RW to the equatorial band (Figure 4.7). The eastward propagation of the dKW flattens the thermocline and thus reduce the SST and zonal pressure gradients, which is translated into a weakening of the eastward surface (Figure 4.11a-d) and westward subsurface equatorial currents in boreal fall (Figure 4.11a-d).

Notice that, despite discrepancies in the significance, all datasets reproduce a common response of the tropical ocean currents to the emergence of the MM. Our results reveal that the MM induces a strengthening of the NECC and the equatorial circulation during its developing phase and a weakening during its termination. Furthermore, we demonstrate for the first time that the ocean waves and in particular, the RW-reflected mechanism, have a fundamental contribution in the variability of equatorial upper-ocean ocean circulatation during boreal summer.

The EM develops under a weakening of the climatological trades in the equatorial and south tropical Atlantic (Figure 4.8a-j). At the equator, the ocean adjustment to wind stress variations causes an elevation of the SSH in the eastern side, reducing the zonal SSH and SST gradient associated with a weakening of the westward equatorial nSEC from March to June (Figure 4.11e-h). Noticeably, at subsurface levels the changes in ocean currents during boreal spring are inconclusive, since they differ among datasets and are not significant (Figure 4.11e-h). Despite the discrepancies in the SST signal, all datasets reproduce negative SSH anomalies in the western north-equatorial Atlantic (Figure 4.9a-j), which cause a weakening of the NECC during spring (Figure 4.11e-h). The decaying AN phase is controlled by the RW-reflected mechanism (Figure 4.10). The propagation of the associated uKW shoals the thermocline in the eastern ocean during late summer and autumn (Figure 4.10), reversing the zonal SSH gradient. Consequently, the equatorial nSEC intensifies (Figure 4.11e-h), while the subsurface circulation weakens (Figure 4.11e-h). This uncoupling

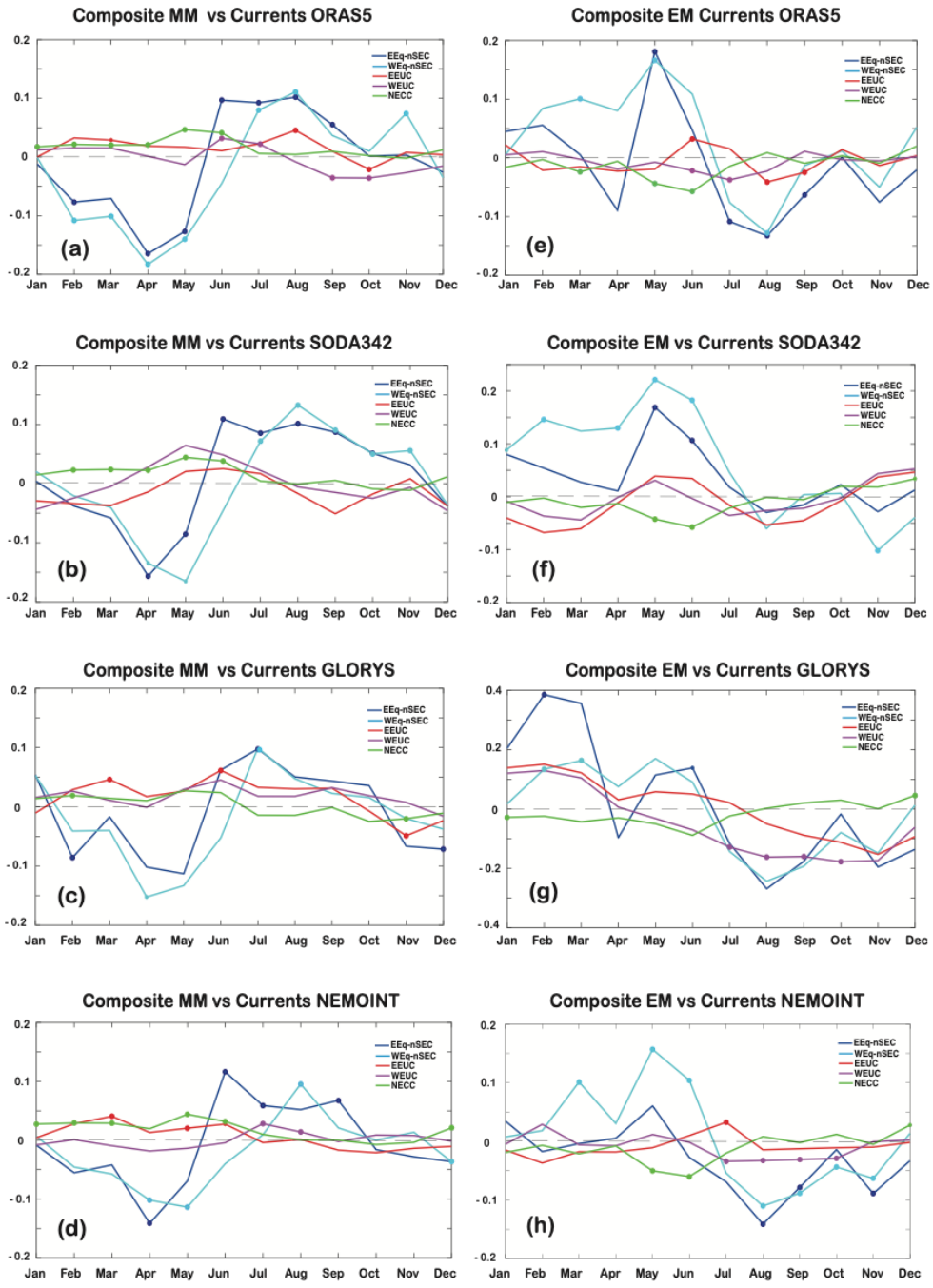

Figure 4.11: Ocean currents (cm s_{-1}) related to the Meridional Mode (MM) and Equatorial Mode (EM). Composite of monthly anomalous (positive minus negative) NECC [50°W-15°W,4°N-10°N], EUC in the eastern Atlantic EEUC [20°W-10°E, 2°N-2°S], EUC in the western Atlantic WEUC [40°W-20°W,2°N-2°S] and equatorial SEC [20°W-10°E, 2°N-2°S] from January to December in (a,e) ORAS5, (b,f) SODA342, (c,g), GLORYS and (d,h) NEMOINT. The events selected for positive (negative) MM are: 1983, 1998, 2005, 2010 (1985, 1986, 1989, 1994, 1999, 2009). Regarding the EM events, years chosen for positive (negative) phases are: 1984, 1988, 1991, 1996, 1999, 2003 (1992, 1997).

between the surface and subsurface circulation suggests that the impact of the RW-reflected mechanism over the EUC can be masked by the influence of other off-equatorial forcing (Brandt et al., 2011; Richter et al., 2013) or the intrinsic AN diversity (Martín-Rey et al., 2018; Vallès-Casanova et al., 2020).

Our results suggest that the ocean currents respond to the emergence of the MM and EM. The robust agreement between datasets reveals that the MM-associated changes in the surface and subsurface equatorial ocean circulation are largely driven by RW and KW propagation. Similarly, the surface ocean currents show a consistent response to the ocean wave propagation during the evolution of the EM. However, the EM-induced subsurface equatorial circulation shows a more complex response, probably due to the contribution of diverse off-equatorial forcings and the intrinsic diversity of the EM.

4.3.4 Case studies of MM-EM interactions: 2009 and 2010 events

A possible interaction between MM and EM has been suggested over the last two decades (Hu et al., 2013; Murtugudde et al., 2001; Servain et al., 1999; Zhu et al., 2012). Recent findings have provided a robust evidence about the MM-EM connection, emphasizing the crucial role played by the RW-reflected mechanism and its interaction with local wind forcing (Foltz & McPhaden, 2010; Martín-Rey & Lazar, 2019).

The existence of the MM-EM linkage suggests a potential interaction between the north tropical and equatorial ocean transport. To further investigate this hypothesis, the 2009 and 2010 events related to same-sign MM-EM connections have been analyzed with NEMOINT dataset. A negative (positive) MM-like pattern develops in boreal spring under the anomalous intensification (reduction) of trade winds in the northern hemisphere and the appearance of cross-equatorial winds blowing to the southern (northern) hemisphere in 2009 (2010) (Figure 4.12a-d). A substantial decrease (increase) of SSH appears in the north-equatorial Atlantic in April that translates to the equatorial band in June-August (Figure 4.12e-h) in agreement with the RW-reflected mechanism (Figure 4.13). Notice that NEMOINT captures in a realistic way the observed RW and KW during the 2009 and 2010 events (Figure 4.13e-f,g-l).

In order to better characterize the connectivity between tropical and equatorial ocean transport, we have performed Lagrangian simulations using the NEMOINT dataset over the full available period. Particles are advected backward in time from a meridional section located at 7.45°W (Figure 4.3), which allows determining the origin of the equatorial ocean currents, and in particular the contribution of the RW-reflected mechanism.

The evolution of surface and subsurface zonal transports along the equatorial band during the 2009 and 2010 events is shown in Figure 4.14b-c. These changes are analyzed together with the modification of the SSH as representative of the RW-reflected mechanism. In 2009, from February to May, an anomalous positive wind curl north of the equator (Figure 4.12e) decreases the SSH (Figure 4.14a) and changes the zonal pressure gradient. Consequently, from March to June, the ocean transport weakens at the subsurface and only slightly at surface levels (Figure 4.14a). According to the RW-reflected mechanism, the uRW is boundary reflected in June becoming an uKW that reaches the African coast in July (Figure 4.13a-b). The modified thermocline slope is reflected

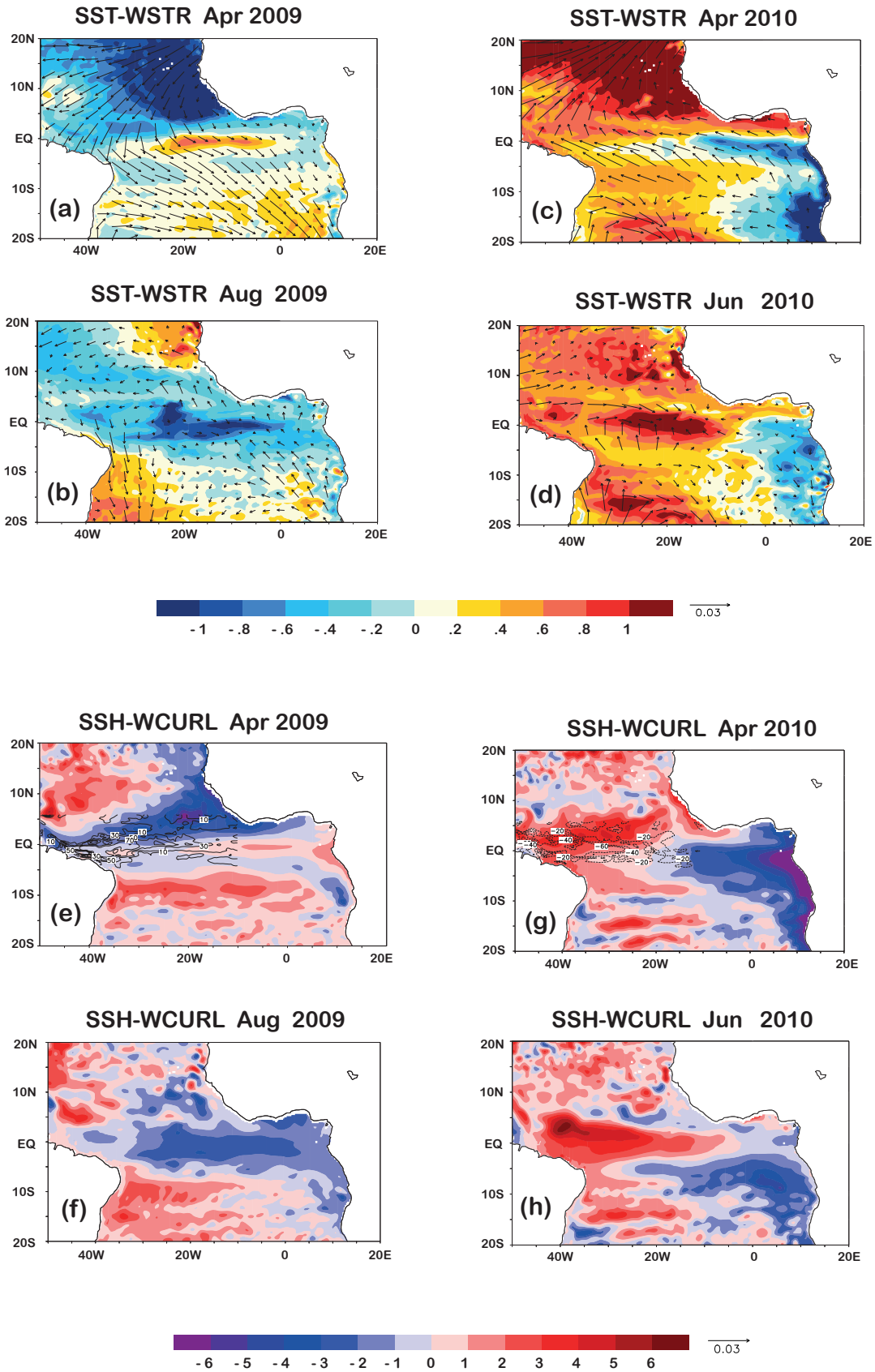

Figure 4.12: Meridional Mode to Equatorial Mode connection during the 2009 and 2010 events. Anomalies in (a-d) SST (shaded, in °C) and wind stress WSTR (vectors, in N m_{-2}) and (e-h) SSH (coloured, in cm) and wind stress curl WCURL (black contours in 10^{-9} N m^{-3}) during April and August, 2009, and during April and June, 2010, from the NEMOINT dataset.

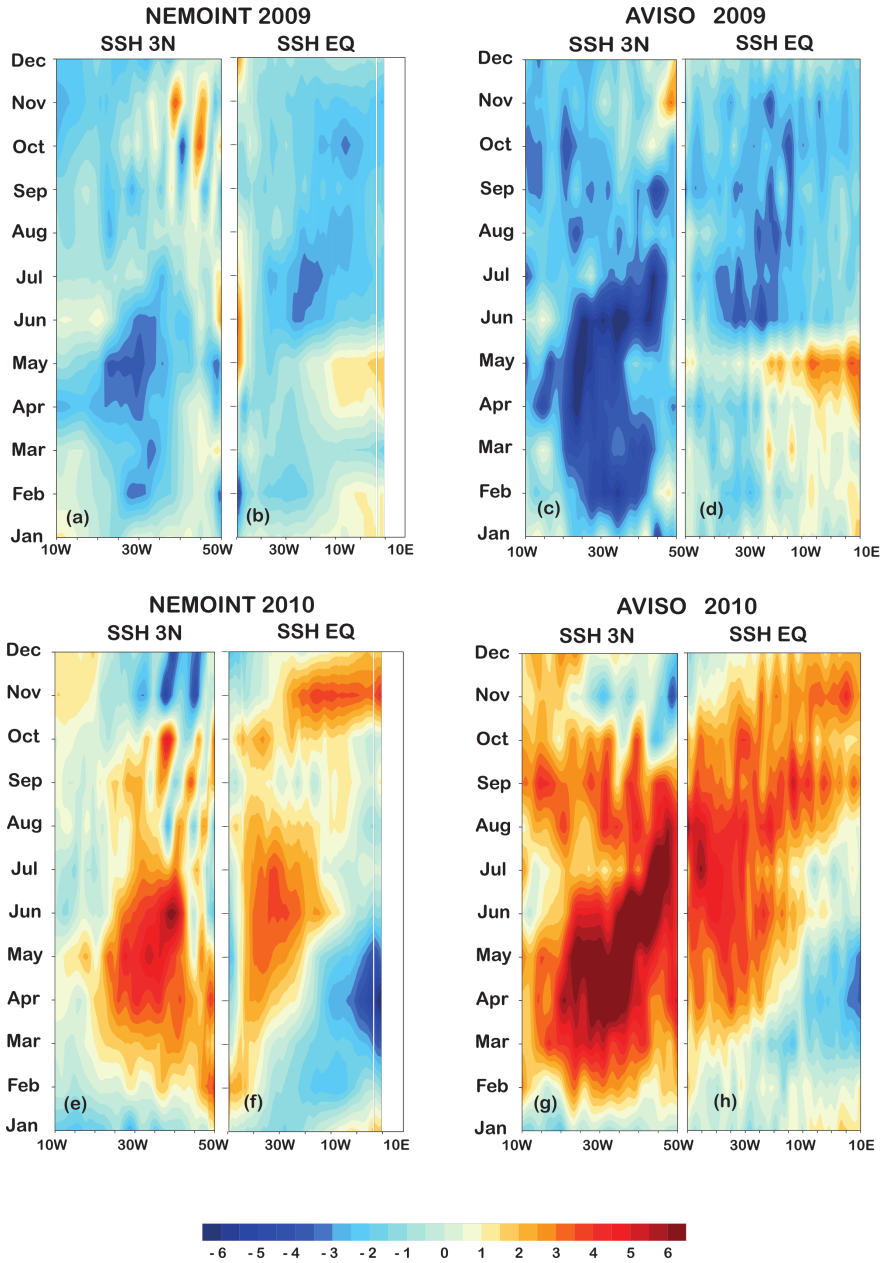

Figure 4.13: Time-longitude plots illustrating the Rossby-wave reflected mechanism during the 2009 and 2010 events. Monthly anomalies in SSH (in cm) along 3°N and along the equator for (a-f) 2009 and (g-l) 2010, from the NEMOINT and AVISO datasets. Notice that the x-axis has been reversed along the 3°N section to better visualize the boundary reflection of Rossby-wave into an equatorial Kelvin wave.

in an east-west SSH gradient, reinforcing the westward subsurface and eastward surface ocean transports (Figure 4.14b).

During boreal spring of 2010, an anomalous Ekman pumping north of the equator raises the SSH (Figure 4.12g and 4.13e,g), which initiates the downwelling RW-reflected mechanism, and enhances the zonal pressure gradient. Similar to 2009, the dRW manifests at the subsurface layers with an intensification of the zonal transport (Figure 4.14a). Following the RW-reflected mechanism, the subsequent dKW crosses the equatorial band (Figure 4.13g-h), raising the eastern SSH from June to December (Figure 4.14c). As a consequence, the zonal SSH gradient is drastically reduced, originating the eastward surface and westward subsurface equatorial transport from summer to fall (Figure 4.14c).

The Lagrangian analysis shows a potential connection between the north-equatorial and equatorial ocean transport variability via the RW-reflected mechanism. The propagation of the baroclinic RW and KW modes modify the east-west pressure gradients, originating the associated redistribution of water masses. Moreover, this connection suggests that the boreal spring variability in the MM can predict the nSEC and EUC variability in the eastern equatorial Atlantic up to 3-4 months in advance.

4.4 Conclusions

Previous studies have reported intraseasonal-to-interannual fluctuations in the zonal ocean currents and their possible connection with tropical and equatorial Atlantic SST variability (Brandt et al., 2014; Hormann & Brandt, 2009; Hormann et al., 2012; Perez et al., 2012). However, the scarcity of in-situ measurements and the discrepancies among individual events have hampered determining the linkages between TAV modes and near-surface ocean transport.

This study has focused on clarifying the response of ocean zonal circulation to the emergence of the Meridional (MM) and Equatorial (EM) modes. For this purpose, a set of three oceanic reanalyses and an interannual forced-ocean simulation covering the period 1982-2018 have been used. All datasets simulate in a realistic way the seasonal cycle and variance of the north tropical and equatorial ocean transport.

A strong westward flow develops at the surface levels during boreal summer in the equatorial Atlantic (nSEC), peaking in June-July, accompanied by enhanced variability in the central-eastern equatorial Atlantic. The eastward North Equatorial Countercurrent (NECC) develops at the sea surface between June until December, stretching from the African coast until South America with maximum variance in the western margin [50°W-30°W]. In the equatorial Atlantic, the subsurface eastward Equatorial Undercurrent (EUC) exhibits substantial changes along the equatorial band. Persistent positive zonal velocities are found in the western side [40°W-25°W], with maxima in boreal spring and fall. However, east of 20°W, the EUC weakens during spring and summer and intensifies in September-October, with the variability peaking in the central-eastern equatorial Atlantic.

The evolution of MM and EM and their associated air-sea mechanisms is well captured by the oceanic reanalyses and the NEMOINT simulation. The MM is characterized by an anomalous reduction of the climatological north-easterlies, which favors the warming of the sea surface

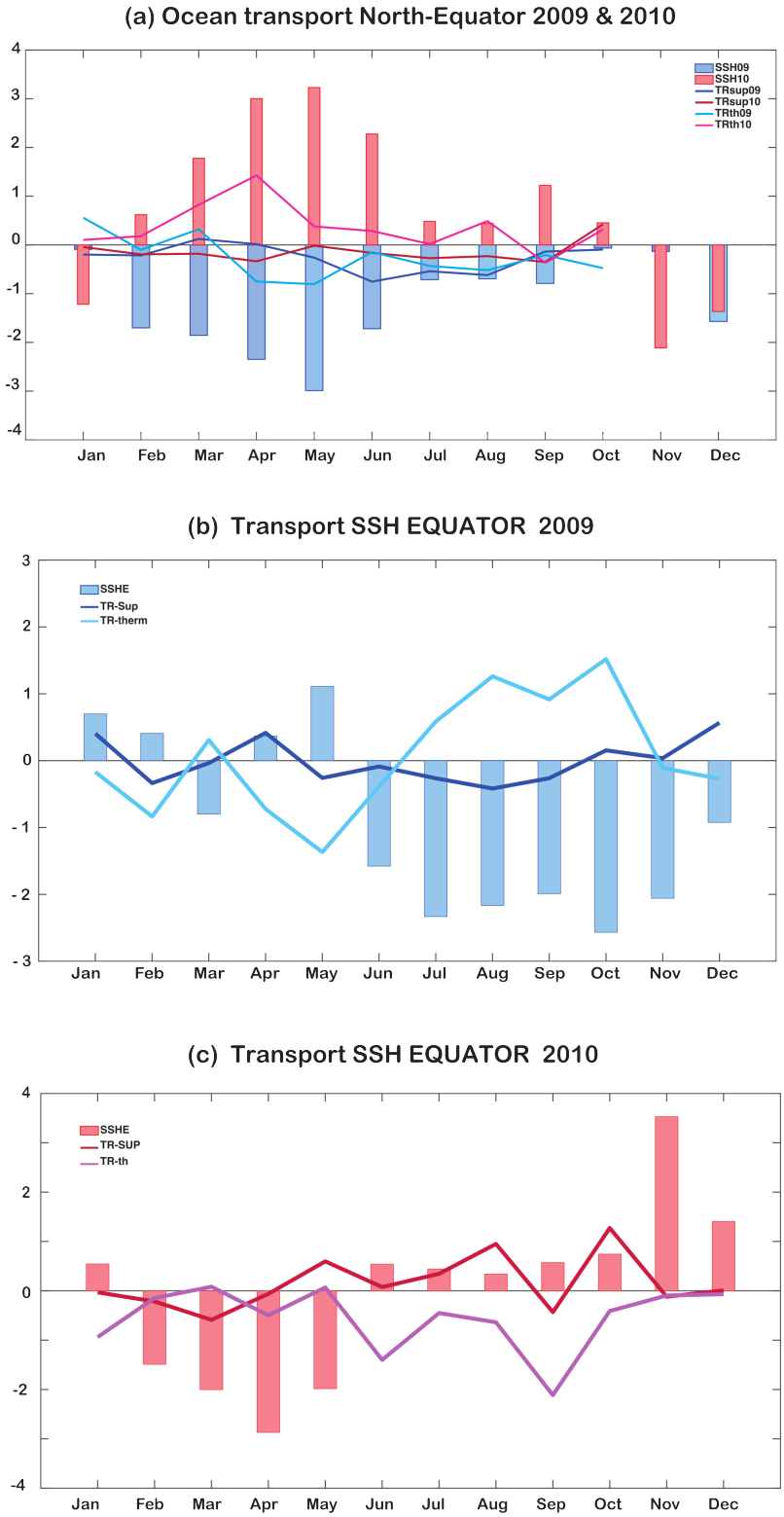

Figure 4.14: Impact of MM-EM linkage on the ocean zonal transports in the 2009 and 2010 events. (a) Anomalous SSH (bars) and surface (dark red and blue lines) and subsurface (pink and light blue lines) ocean transports in the north-equatorial Atlantic [40°W-20°W,2°N-6°N] from January to December in the 2009 and 2010 events. (b) Anomalous SSH (bars) in the eastern equatorial Atlantic [20°W-10°E, 2°N-2°S], and equatorial surface (dark blue) and subsurface (light blue) transports during 2009. (c) Anomalous SSH (bars) in the eastern equatorial Atlantic [20°W-10°E, 2°N-2°S], and equatorial surface (dark red) and subsurface (pink) during 2010. The ocean transports are calculated from the Lagrangian particle trajectories with the NEMOINT simulation.

via reduced latent heat fluxes. The resultant inter-hemispheric SST gradient causes a see-saw in sea level pressure at both sides of the equator, which reinforces the cross-equatorial winds. At the equator, intensified easterlies can favor the surface cooling through vertical mixing. Outstandingly, the positive phase of the MM is followed by an equatorial warming during summer months. An anomalous wind curl north of the equator activates the RW-reflected mechanism coupling the north tropical and equatorial SST variability. Variations in the amplitude of equatorial SST signal among datasets can be understood in terms of the different local wind forcing and its interaction with the ocean waves.

The EM appears as an anomalous weakening of climatological trades in the south tropical Atlantic, reducing equatorial upwelling and leading to the warm equatorial tongue. The anomalous positive wind-curl north-of-the-equator triggers the RW-reflected mechanism that cause the EM termination. The amplitude of the upwelling RWs and KWs and their impact on equatorial SST anomalies differ among datasets, which can be due to different climatologies.

The tropical Atlantic modes illustrate a pronounced impact on the tropical and equatorial ocean currents. During the developing phase of the MM, anomalously intense south-easterly winds in the northern hemisphere progressively increase the SSH in the eastern basin around 2°N-8°N between January and April. This anomaly propagates westwards and causes the summer reinforcement of the NECC. Along the equatorial band, the anomalous easterlies induces an intensification of the westward surface (equatorial nSEC) which causes the thermocline to rise in the east, increasing the east-west SSH gradient. Therefore, the eastward subsurface (EUC) current intensifies. During the decaying phase, in the summer season, the RW-reflected mechanism reverses the equatorial zonal gradients, weakening both the equatorial nSEC and EUC. In the case of the EM, the easterlies weaken along the equatorial band during its developing phase, which cause the SSH to increase in the eastern side. The westward surface ocean currents (equatorial nSEC) weaken from March to July and the west-east SSH gradient diminishes. However, inconclusive results are found at subsurface layers among datasets. Regarding the NECC, a significant weakening is shown in boreal spring, as a response to the eastward zonal SSH gradient. During the decaying phase, the RW-reflected mechanism is activated and contributes to enhance the equatorial vertical stratification. Thus, the thermocline zonal slope increases associated with nSEC intensification. Conversely, the EUC tends to reduce in summer and fall, probably associated with additional equatorial and subtropical forcing.

Lagrangian particle simulations for the 2009 and 2010 events show the associated changes in zonal transports that emerge associated to the interaction between MM and EM. They reveal that the RW-reflected mechanism plays a fundamental role in the connectivity between the tropical and equatorial transports.

In the present chapter, we have provided further evidence for the significant influence of MM and EM in the modification of the tropical upper-ocean circulation. Changes in the wind field, associated with both MM and EM, appear as the main precursor for the NECC interannual variability, while the propagation of both RW and KW are crucial to alter the ocean transport variability at surface and subsurface levels. We have shown that the zonal transport in the eastern equatorial Atlantic may be altered beyond changes in local zonal pressure gradient. Concretely, off-equatorial RW forcing can have a decisive contribution in the ocean connectivity between western

and eastern tropical Atlantic. In particular, the study of the individual 2009 and 2010 events, associated with cold and warm MM-EM interactions demonstrates the predictor role of north-western tropical water transport to the eastern equatorial Atlantic one. Furthermore, the activation of RW-reflected mechanism can provide equatorial transport predictability up to 3-4 months in advance. Hence, water mass properties and oxygen supply in the upwelling system in the eastern equatorial Atlantic may be modified as a result of both Meridional and Equatorial mode events.

Our results represent a step forward towards a better understanding of the connection between north tropical and equatorial Atlantic variability. However, the diversity of TAV modes and changes in the background state caused by natural and anthropogenic forcing can modulate the ocean transport response. Further research using historical and pre-industrial simulations from the Coupled Model Intercomparison Project Phase 6 (CMIP6; Eyring et al., 2016), will help to clarify this issue and will be carried out in future studies.

Chapter 5

On the spatiotemporal diversity of Atlantic Niño and associated rainfall variability over West Africa and South America

The spatiotemporal evolutions of equatorial Atlantic sea surface temperature anomalies (SSTAs) during Atlantic Niño events and the associated climate impacts on the surrounding continents are extremely diverse. In this study, we construct longitude-time maps of equatorial Atlantic SSTAs for each observed AN event during 1948–2019 and perform a spatiotemporal empirical orthogonal function analysis to identify the four most frequently recurring Atlantic Niño varieties. The first two contrast the timing of dissipation (early terminating vs. persistent) and the other two the timing of onset (early onset vs. late onset). Largely consistent with the differences in the timings of onset and dissipation, these four varieties display remarkable differences in rainfall response over West Africa and South America. Most of the varieties are subject to onset mechanisms that involve preconditioning in boreal spring by either the Atlantic meridional mode or Pacific El Niño, while for the late onset variability there is no clear source of external forcing.

This chapter has been published as: Vallès-Casanova, I., Lee, S. K., Foltz, G. R., and Pelegrí, J. L. (2020). On the spatiotemporal diversity of Atlantic Niño and associated rainfall variability over West Africa and South America. Geophysical Research Letters, 47(8), https://doi.org/10.1029/2020GL087108.

5.1 Introduction

Perhaps the most remarkable example of tropical Atlantic atmosphere-ocean variability is the intermittent failure in the seasonal formation of the surface cold tongue, the warm phase of the Equatorial Mode, known as Atlantic Niño, the term referred in this chapter. Closely phase locked with the seasonal cycle, Atlantic Niño usually develops in boreal spring (March–May [MAM]), peaks in the summer (June–August [JJA]), and dissipates in the fall. As summarized in Figure 5.1,

Atlantic Niño is typically characterized by warm sea surface temperature anomalies (SSTAs) and positive sea surface height anomalies (SSHAs) in the eastern equatorial Atlantic and westerly wind anomalies in the western basin (e.g., Carton & Huang, 1994; Philander, 1986; Zebiak, 1993). Some Atlantic Niño events are also responsible for a failure of the West African summer monsoon and increased frequency of flooding in the West African countries bordering the Gulf of Guinea and in northeastern South America (e.g., Folland et al., 2001; Foltz et al., 2019; Giannini et al., 2003; Losada et al., 2010; Lübbecke et al., 2018; Okumura & Xie, 2004; Tschakert et al., 2010). Some studies have also suggested a far-reaching impact on Indian summer monsoon rainfall (e.g., Kucharski et al., 2008; Pottapinjara et al., 2019).

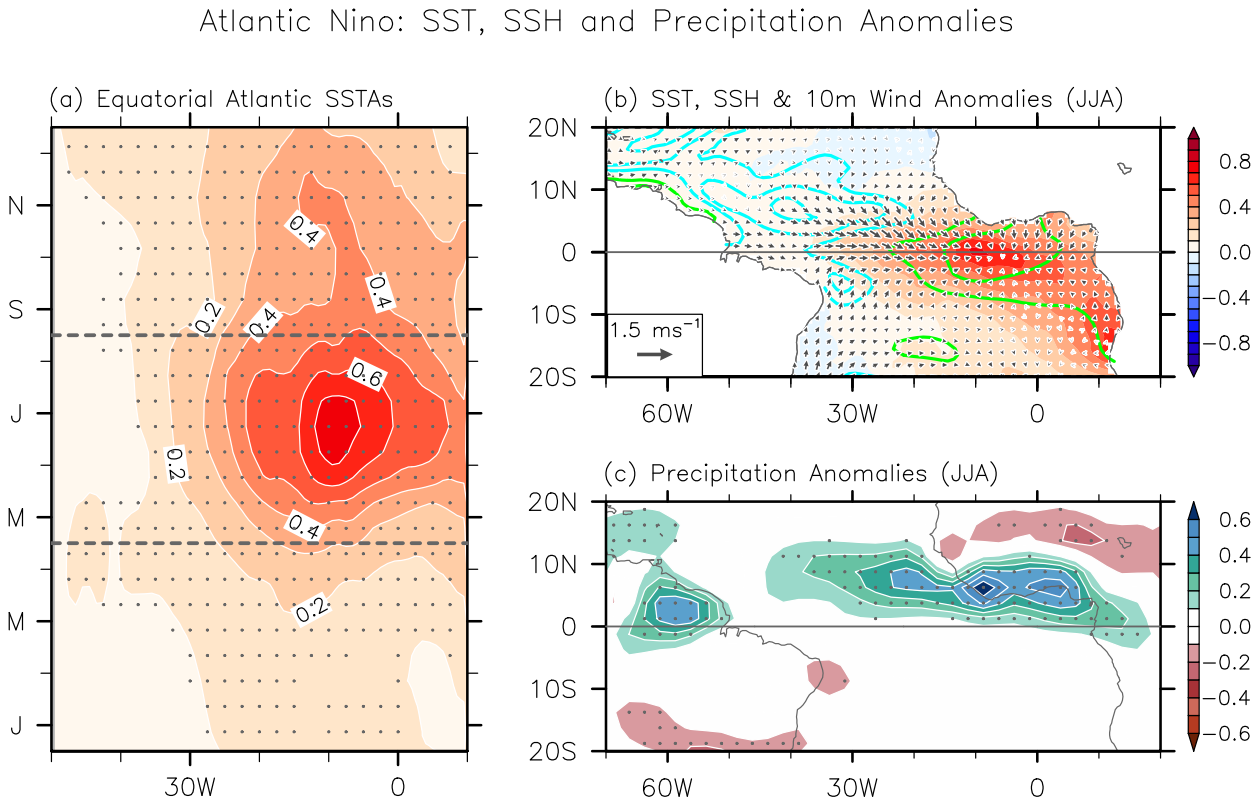

Figure 5.1: (a) Time-longitude plot of composite mean equatorial Atlantic SSTAs, averaged between 3°S and 3°N, from January to December derived from observed Atlantic Niño events. Significant SSTA values at 99% or above based on a Student's t test (two tailed) are indicated by gray dots. (b) Composite mean tropical Atlantic SST (shades), SSH (contours), and 10 m wind (vectors) anomalies; and (c) precipitation anomalies during June–August derived from observed Atlantic Niño events. Positive and negative SSHAs are indicated by green and cyan contour lines, respectively in (b). Significant precipitation anomaly values at 95% or above based on a Student's t test (two tailed) are indicated by gray dots in (c). The units for SST, SSH, winds and precipitation are in °C, cm, m s^{-1}, and mm day^{-1}, respectively. The contour interval for SSH anomalies is 0.5 cm.

In many respects, Atlantic Niño is analogous to El Niño in the Pacific. As such, the leading theory behind it is an atmosphere-ocean positive feedback process known as Bjerknes feedback. Atmospheric teleconnection from the Pacific is thought to cause the westerly wind anomalies in the western basin to initiate the positive feedback (e.g., Carton & Huang, 1994; Chang et al., 2006; Keenlyside & Latif, 2007; Latif & Grötzner, 2000; Lübbecke & Mcphaden, 2013; Martín-Rey et al., 2018; Tokinaga et al., 2019). More specifically, the westerly wind anomalies in the western Atlantic

generate downwelling equatorial Kelvin waves that propagate to the eastern basin, deepening the thermocline and temporarily stalling (or reducing) upwelling-induced SST cooling. As a result, warm SSTAs are produced in the cold tongue region, intensifying the westerly wind anomalies via a Gill-type response (Gill, 1980) to prolong the stalling of the equatorial SST cooling (e.g., Burmeister et al., 2016; Foltz & McPhaden, 2010; Keenlyside & Latif, 2007; Lübbecke & McPhaden, 2012).

However, only a fraction of the observed Atlantic Niño events can be explained by the classical Bjerknes feedback initiated by remote influence from the Pacific (e.g., Brandt et al., 2011; Chang et al., 2006; Lübbecke & McPhaden, 2012; Lübbecke et al., 2018). For instance, some Atlantic Niño events are initiated by oceanic advection of off-equatorial warm anomalies in the absence of westerly wind anomalies in boreal spring (Richter et al., 2013) or are forced by a weakening of the South Atlantic anticyclone and the associated onset of warm SSTAs in the Angola-Benguela region (e.g., Florenchie et al., 2004; Lübbecke et al., 2010; Lübbecke et al., 2014; Nnamchi et al., 2016; Shannon et al., 1986). Such Atlantic Niño events, preconditioned by off-equatorial processes or purely thermodynamic and stochastic processes (Jouanno et al., 2017; Nnamchi et al., 2015), are not governed by El Niño-like dynamics and thus are sometimes referred to as noncanonical events (Richter et al., 2013).

As briefly summarized above, multiple atmosphere-ocean processes are at work to trigger Atlantic Niño events. As such, the dichotomous classification of the observed Atlantic Niño events into canonical and non-canonical events often invoked in recent studies is an oversimplification. The main goal of this study is to objectively identify and explain the differences in the spatiotemporal evolution of equatorial Atlantic SSTAs and the associated rainfall variability over West Africa and South America for the entire lifespans of the events.

5.2 Data and methods

In this study, we combine observational and reanalysis data sets. Monthly SSTAs are derived from three SST data sets for the 1948–2019 period: the Hadley Centre Sea Ice and SST data set version 1 (Rayner et al., 2003), which is used as the primary SST data set; the Centennial in situ Observation-Based Estimates of the variability of SST (Ishii et al., 2005); and the Extended Reconstructed SST version 5 (Huang et al., 2017). Monthly anomalies of surface winds (at 10 m), velocity potential and divergent winds at 200 hPa, and mean sea level pressure are from the National Centers for Atmospheric Prediction-National Center for Atmospheric Research reanalysis (Kalnay et al., 1996) for the same period. Monthly precipitation anomalies are derived from the National Oceanic and Atmospheric Administration gauge observation-based global land precipitation reconstruction (Chen et al., 2002) for the same period. Monthly SSHAs, which are used here as proxies for thermocline depth anomalies, are obtained from European Centre for Medium-Range Weather Forecasts Ocean Reanalysis System 4 (Balmaseda et al., 2013) for 1958–2017.

Since we are mainly interested in interannual variability, a separate 30-year averaged climatology is constructed every 5 years and used to derive SSTAs. For instance, to compute SSTAs for the 1951-1955 period, a 30-year averaged climatology for 1936-1965 is used; to compute SSTAs for 1956-1960, a 30-year averaged climatology for 1941–1970 is used; and so forth. This method

defines Atlantic Niño events by their contemporary climatology. It is also currently being used at National Oceanic and Atmospheric Administration's Climate Prediction Center to define El Niño events.

We identify 22 Atlantic Niño events based on the threshold that the 3-month averaged SSTAs exceed 0.5°C in the ATL3 region [3S°-3°N, 20°W-0°] for at least two consecutive overlapping seasons. Warm events identified based on only one or two SST data sets are excluded to reduce uncertainties in observations. See supporting information in Appendix A1 for an extended discussion of the threshold used to identify the 22 Atlantic Niño events. A longitude-time map of the equatorial Atlantic SSTAs, averaged between 3°S and 3°N, is derived for each of the 22 Atlantic Niño events (Figure 5.2). The time and longitude axes span from January to December and the entire equatorial Atlantic (50°W-10°E), respectively. As shown in Figure 5.2, the spatiotemporal evolution patterns of the 22 events are different in terms of the timing, zonal extent, and amplitude of their onset, peak, and decay (e.g., Martín-Rey et al., 2019; Okumura & Xie, 2006; Richter et al., 2013).

In fact, it is difficult to find any single event that can be described by the composite mean (Figure 5.1a) or any two events that closely resemble each other. For instance, the 1991 event peaked in May-June and dissipated very quickly afterward, followed by the onset of a cold event. In contrast, the 1963 event was very strong and persisted through the end of that year (Figure 5.2).

In order to objectively identify the preferred spatiotemporal modes of the observed Atlantic Niño events, we perform an empirical orthogonal function (EOF) analysis of these 22 longitude-time maps of equatorial Atlantic SSTAs. The resulting principal components (PCs) are associated with each individual Atlantic Niño event, and the EOFs represent a linearly independent set of longitude-time maps. The two leading PCs, which explain 30% and 24% of the inter-event variance, are further rotated by 90° to better align several observed Atlantic Niño events with the PCs. In order to better understand atmosphere-ocean processes associated with the onsets of different Atlantic Niño varieties, spatiotemporal patterns of ocean and atmospheric variables are obtained by linearly regressing the corresponding time series onto these rotated PCs. Note that the same method was previously used to identify the leading spatiotemporal modes of the observed El Niño events in the Pacific (Lee et al., 2014; Lee et al., 2018).

5.3 Four most frequently recurring Atlantic Niño varieties and their climate impacts on the surrounding continents

Each rotated EOF mode represents two contrasting Atlantic Niño varieties or flavors (rotated PC changing from -1 to 1) that correspond to adding and subtracting the rotated EOF SSTA pattern to the composite mean, leading to a total of four main Atlantic Niño varieties (Figure 5.3). The first rotated EOF mode distinguishes two contrasting varieties during the decay phase. As shown in Figure 5.3a, the first variety is characterized by a rapid and complete termination of warm equatorial Atlantic SSTAs shortly after August. It is therefore referred to as an early-terminating variety. Consistent with the early-terminating equatorial Atlantic warm SSTAs, precipitation over the West African sub-Sahel region (averaged over 0°-10°N) is enhanced mainly during July–August, although enhanced precipitation over northeastern South America (averaged over 0°-10°N) tends

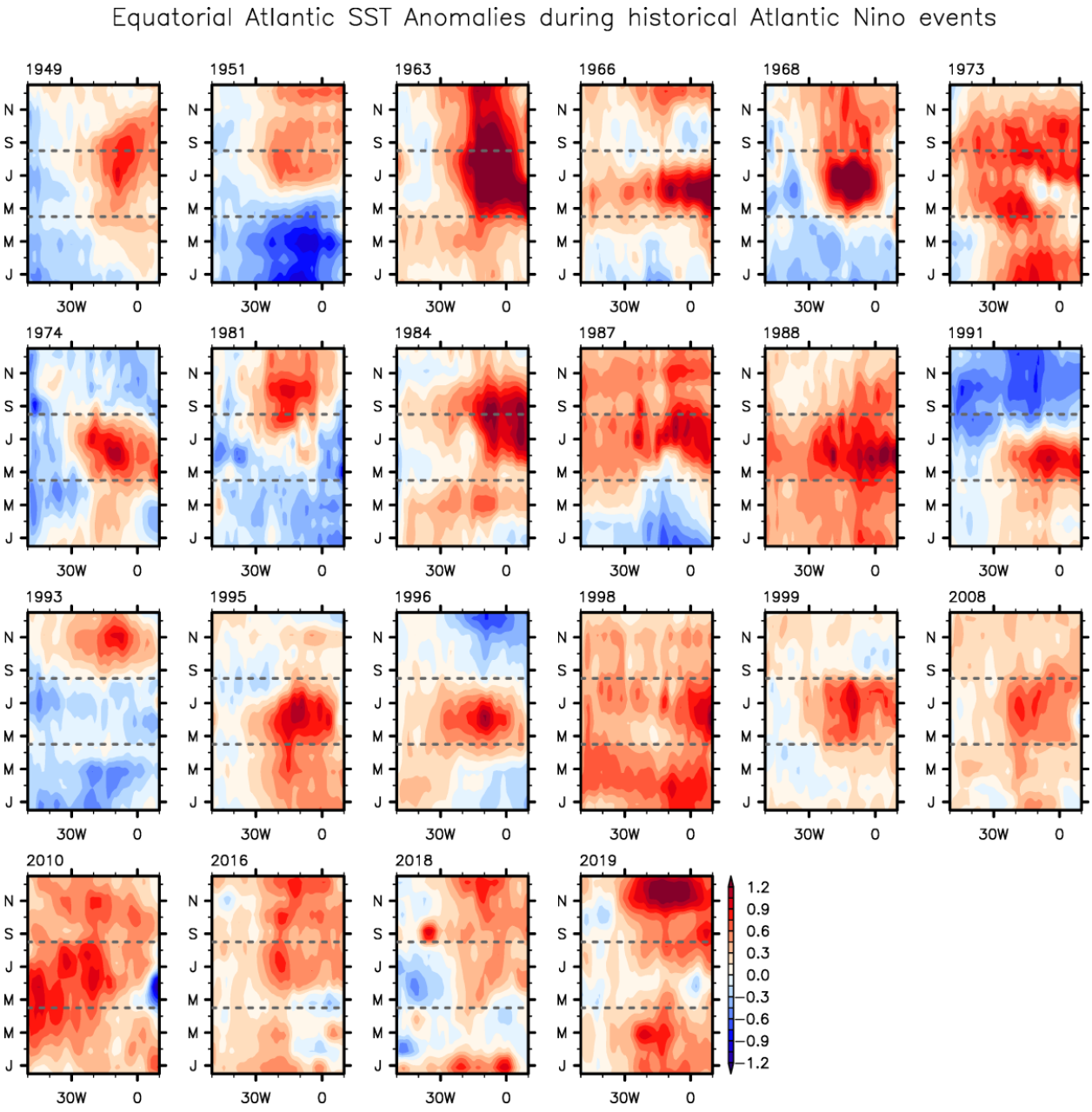

Figure 5.2: Time-longitude plot of equatorial Atlantic SSTAs, averaged between 3°S and 3°N, from January (0) to December (0) for each of 22 observed Atlantic Niño events during 1948-2019. The dashed gray lines indicate May 1 and August 31. The units for SST are in °C.

to persist slightly longer. It is interesting to note that precipitation over northeastern South America is reduced during April and May. Three events (1974, 1991, and 1996) show the characteristics of early-terminating variety (Figure 5.3e).

The second variety is characterized by strong equatorial Atlantic SSTAs that remain until the end of the year and is thus referred to as a persistent variety (Figure 5.3b). Consistent with the strong and persistent equatorial Atlantic SSTAs, precipitation over the West African sub-Sahel region is greatly enhanced for an extended period from July to October. Precipitation over northeastern South America is enhanced during September-December, supported by the persistent equatorial Atlantic SSTAs during those months. However, rainfall is much reduced in January-May, and

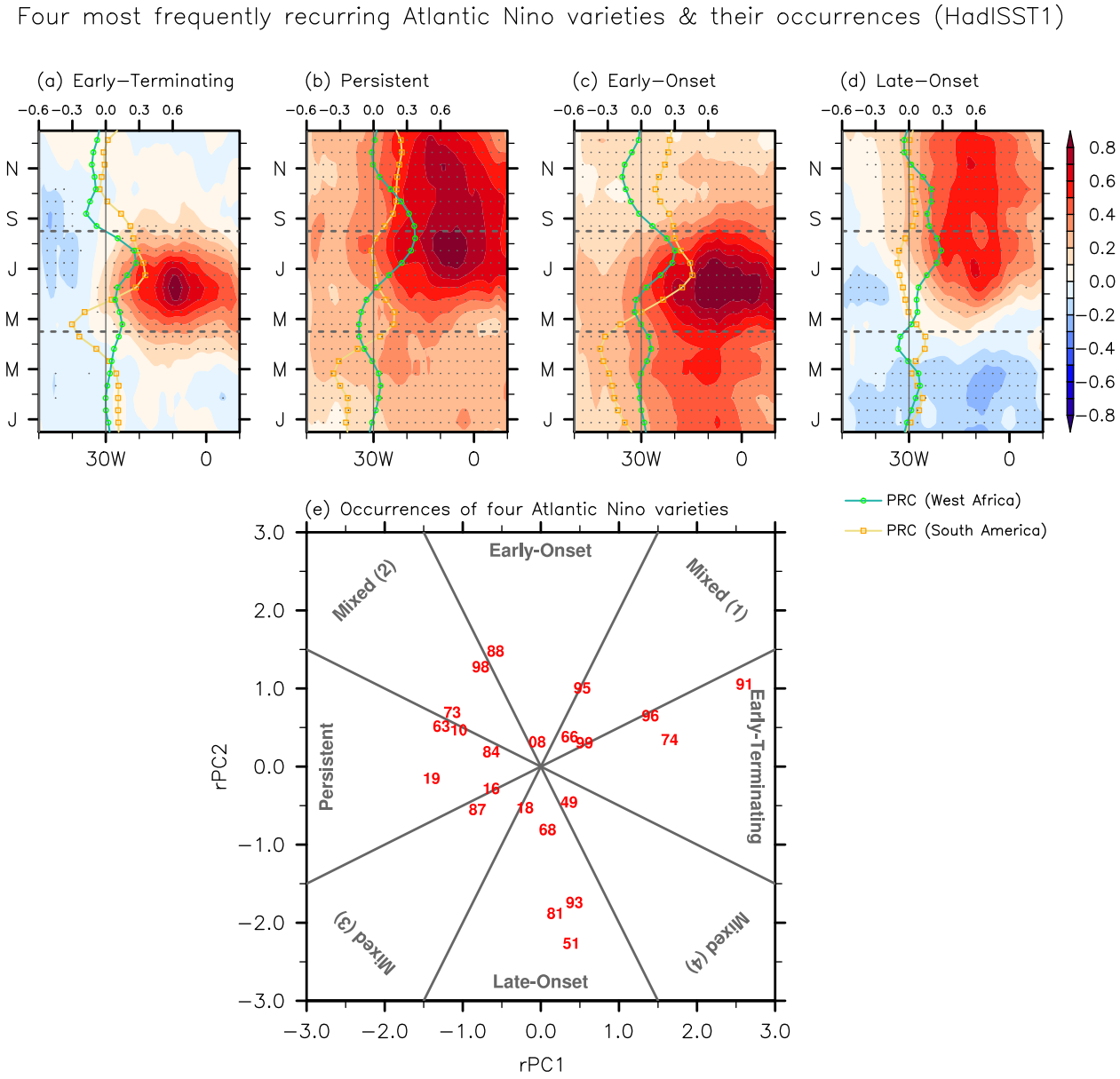

Figure 5.3: (a-d) Time-longitude plots of the tropical Atlantic SSTAs (averaged over 3°S-3°N; shades) illustrate the four most frequently recurring Atlantic Niño varieties during 1948-2019, namely, (a) the early-terminating, (b) persistent, (c) early-onset, and (d) late-onset varieties. Significant SSTA values at 99% or above based on a Student's t test (two tailed) are indicated by gray dots. Land precipitation anomalies over South America (averaged over 0°-10°N and 70°W-50°W; orange lines) and West African sub-Sahel region (averaged over 0°-10°N and 20°W-20°E; green lines) are also shown for each of the four Atlantic Niño varieties. (e) Normalized rotated PC1 versus rotated PC2 values for all 22 events. The two-digit numbers indicate the Atlantic Niño years. The dashed gray lines in (a-c) indicate 1 May and 31 August. The thick gray lines in (e) are the boundaries (i.e., rPC1 = ±2 × rPC2 and rPC2 = ±2 × rPC1) that separate the four varieties from the mixed varieties. The units for SST and precipitation are in °C and mm day$_{-1}$, respectively.

this cannot be explained as a response to the equatorial Atlantic SSTAs. Seven events (1963, 1973, 1984, 1987, 2010, 2016, and 2019) display the characteristics of persistent variety (Figure 5.3e).

The second rotated EOF mode distinguishes two contrasting varieties during the onset phase. Following the two varieties already identified from the first rotated EOF mode, the third variety is characterized by a gradual development of equatorial warm SSTAs starting in January or earlier

and is thus referred to as an early-onset variety (Figure 5.3c). In this case, the equatorial Atlantic warm SSTAs start to dissipate relatively early. Interestingly, the early development of equatorial Atlantic SSTAs does not lead to increased precipitation over the West African sub-Sahel region before July. Thus, West African sub-Sahel precipitation is enhanced for a limited period mainly during July-August for the early-onset variety. Enhanced precipitation over northeastern South America during June-August is consistent with the timing of the maximum equatorial Atlantic SSTAs. However, the reduced precipitation in January-April and the enhanced precipitation in September–December cannot be explained by the equatorial Atlantic SSTAs. Rainfall anomalies over northeastern South America prior to and after the peak seasons for the early terminating, persistent and early-onset varieties are further discussed in section 6. Three events (1988, 1995, and 1998) show the characteristics of early-onset variety (Figure 5.3e).

The fourth variety is characterized by a sudden and late development of warm equatorial Atlantic SSTAs around June and is thus referred to as a late-onset variety (Figure 5.3d). The warm equatorial Atlantic SSTAs tend to persist relatively long compared to the other varieties. Thus, precipitation over the West African sub-Sahel region is much enhanced for an extended period during July-October. Interestingly, however, precipitation over northeastern South America hardly changes during the late-onset variety. Six events (1949, 1951, 1968, 1981, 1993, and 2018) display the characteristics of late-onset variety (Figure 5.3e).

As shown in Figure 5.4, Sahelian rainfall over 10°N–20°N is generally reduced during June-September, thus weakening the West African summer monsoon (e.g., Losada et al., 2010; Vizy & Cook, 2002). The Sahelian rainfall reduction is more robust for the persistent and late-onset varieties but much weaker for the early-onset variety. As shown in Figures A.1 and A.2, the four most frequently recurring Atlantic Niño varieties (Figure 5.3) are very well reproduced when the other two SST data sets are used. See appendix A and Figures A.3- A.4 for additional analysis and discussion on the spatiotemporal diversity of Atlantic Niña.

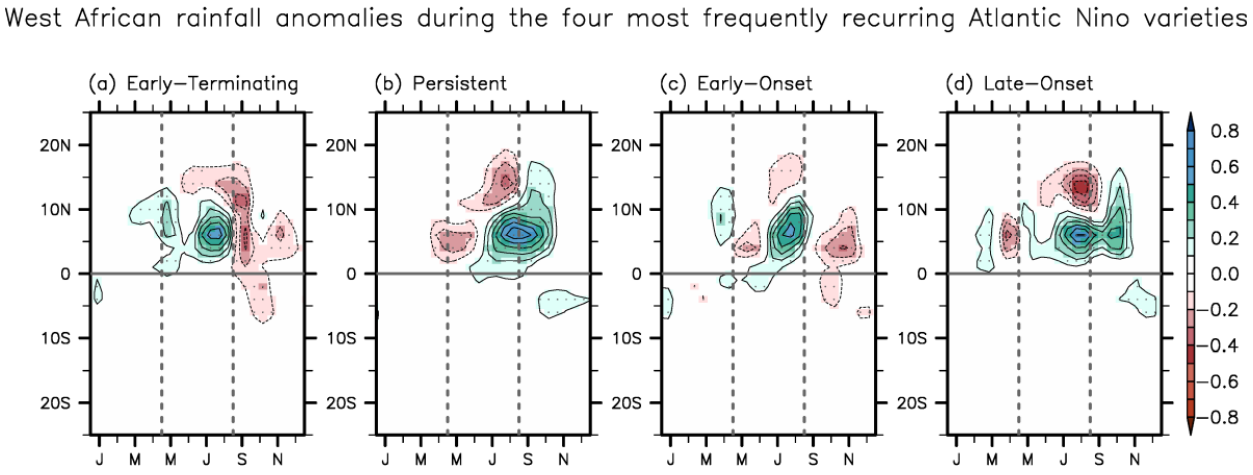

Figure 5.4: Time-latitude plot of West African land precipitation anomalies averaged between 20°W and 20°E, from January (0) to December (0) for the four most frequently recurring Atlantic Niño varieties. Significant values at or above 95% based on a Student's t-test (two tailed) are indicated by gray dots. The units are mm day^{-1}

5.4 Potential onset mechanisms of the four Atlantic Niño varieties

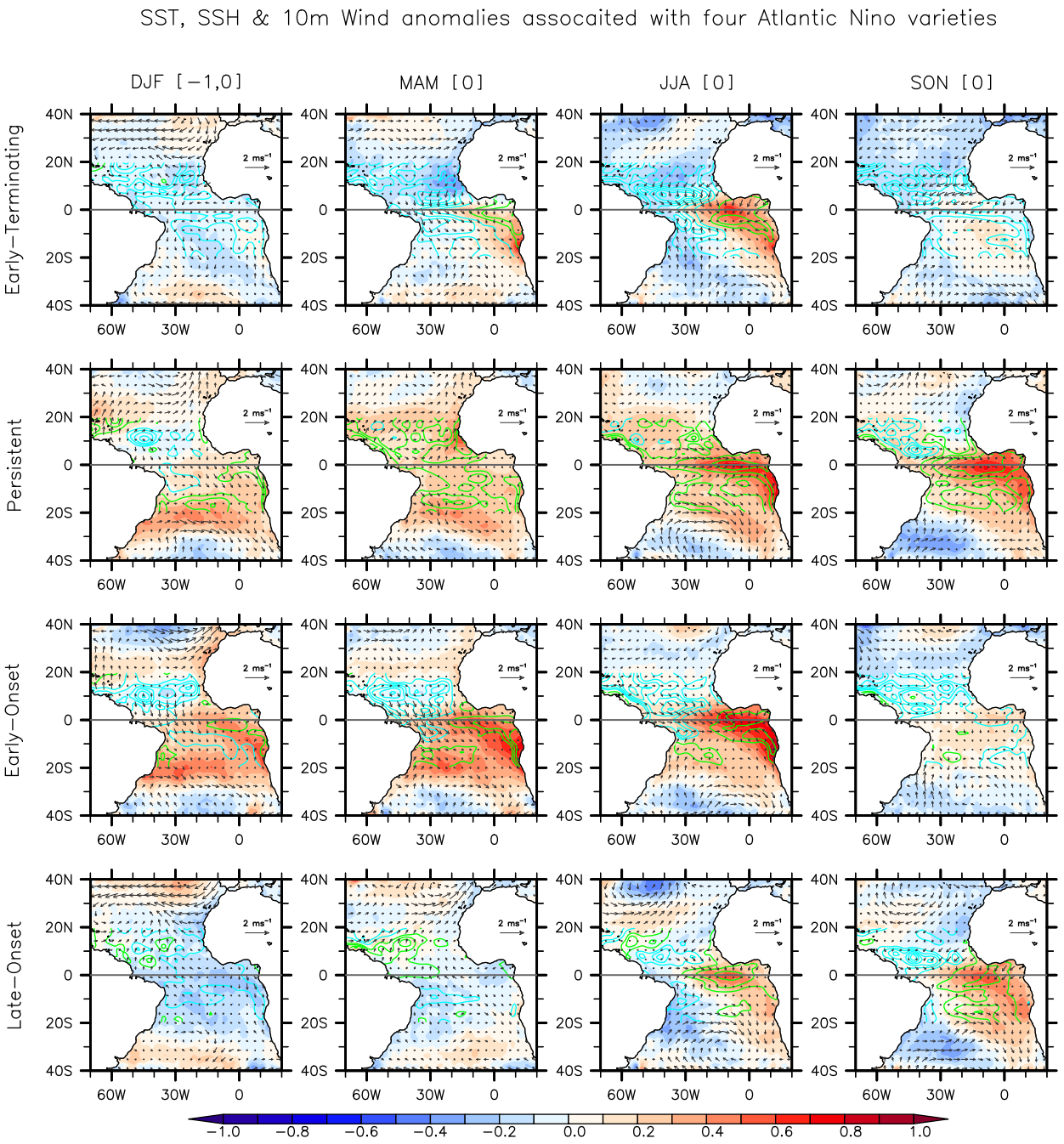

Figure 5.5: SST (shaded), SSH (contours), and 10 m wind (vectors) anomalies regressed onto the four Atlantic Niño varieties for (first row) DJF [-1,0], (second row) MAM [0], (third column) JJA [0], and (fourth row) SON [0]. Positive and negative SSHAs are indicated by green and cyan contour lines, respectively. The units for SST, SSH, and winds are in °C, cm, and m s^1, respectively. The contour interval for SSH anomalies is 0.5 cm.

To better understand atmosphere-ocean dynamic processes linked to the onsets of the four Atlantic Niño varieties, we show maps of surface wind anomalies, SSHAs, and SSTAs regressed onto the four varieties for December-February (DJF [-1,0]), MAM [0], JJA [0], and September-November (SON [0]) (Figure 5.5); any month in the year prior to, during, and after the Atlantic Niño year is

denoted by the suffix (-1), (0), and (+1), respectively. For the early-terminating variety, a negative phase of Atlantic Meridional Mode (MM) develops in DJF (-1,0) and MAM (0) with cold and warm SSTAs in the tropical North Atlantic (TNA) and tropical South Atlantic (TSA), respectively. The resulting cross-equatorial gradient of SSTAs drives interhemispheric wind anomalies (i.e., northeasterly in TNA and northwesterly in TSA) in MAM (0), which lead to a robust development of positive SSHAs and warm SSTAs in the eastern equatorial Atlantic in MAM (0) and JJA (0). Therefore, it appears that the early-terminating variety is driven by a negative phase of the MM in boreal spring. This onset mechanism of AN was previously suggested by Foltz and McPhaden (2010). Additionally, the early-terminating variety appears to be similar to the so-called horseshoe mode, for which upwelling Kelvin waves generated by Rossby wave reflection serve as the dissipation mechanism (Martín-Rey et al., 2019).

For the persistent variety, equatorial wind anomalies and SSHAs are very weak in DJF (-1,0) and MAM (0) and are thus likely to contribute little to the onset. Instead, this mode is preconditioned by a robust weakening of the off-equatorial trade winds in both hemispheres during DJF (-1,0) and MAM (0), which leads to reduced evaporative cooling and warm SSTAs in the TNA and TSA regions in MAM (0). In addition, southwesterly wind anomalies off the coast of West Africa weaken coastal upwelling (evidenced by positive SSHAs), contributing to the gradual build-up of strong warm SSTAs in that area, known as Dakar Niño (Oettli et al., 2016). Richter et al. (2013) suggested that the anomalous warm surface water off the coast of West Africa could be advected to the equatorial Atlantic region to trigger and sustain this Atlantic Niño variety, which they referred to as the non-canonical Atlantic Niño.

The early-onset variety is characterized by an early development of warm SSTAs along the coast of Southwest Africa and the interior TSA (across 20°S) in DJF (-1,0). But, more importantly, it is preconditioned by persistent interhemispheric wind anomalies during DJF (-1,0) and MAM(0). It appears that these wind anomalies are directly responsible for a gradual and early development of warm equatorial Atlantic SSTAs. Therefore, both the early-onset and early-terminating varieties seem to be initiated by interhemispheric wind anomalies. Unlike the early-terminating variety, however, the TNA SSTAs during DJF (-1,0) and MAM (0) are very weak. This suggests that the persistent interhemispheric wind anomalies that are prevalent during the onset phase of the early-onset variety in DJF (-1,0) and MAM (0) may be sustained by external forcing. The external forcing that may trigger and sustain these interhemispheric wind anomalies is discussed in the next section. Another key difference between the early-terminating and early-onset varieties is the stronger eastward SSHA gradient along the equator in MAM (0) and JJA (0) for the early-terminating variety, which is consistent with Bjerknes feedback and the confinement of positive SSTAs to the eastern equatorial Atlantic. In contrast, the broader spatial distributions of positive SSTAs and SSHAs for the early-onset variety are suggestive of remote ENSO forcing (Chang et al., 2006), as discussed in the next section.

The late-onset variety is very distinct from the other three varieties because there is no clear preconditioning of SSTAs or surface wind anomalies in DJF (-1,0) or MAM (0). It develops spontaneously around May (0) and June (0) with no clear source of external forcing. Therefore, it appears that the late-onset variety develops through atmosphere-ocean processes internal to the equatorial Atlantic. A weak build-up of positive SSHA gradient along the equator in MAM (0) suggests

that the eastward propagation of downwelling equatorial Kelvin waves and its amplification by Bjerknes feedback play an important role in the initiation of the late-onset variety, as previously suggested by Keenlyside and Latif (2007). If that is the case, the onset mechanism of the late-onset variety is most comparable to that of canonical El Niño in the Pacific.

5.5 Potential influence of ENSO on the onsets of Atlantic Niño varieties

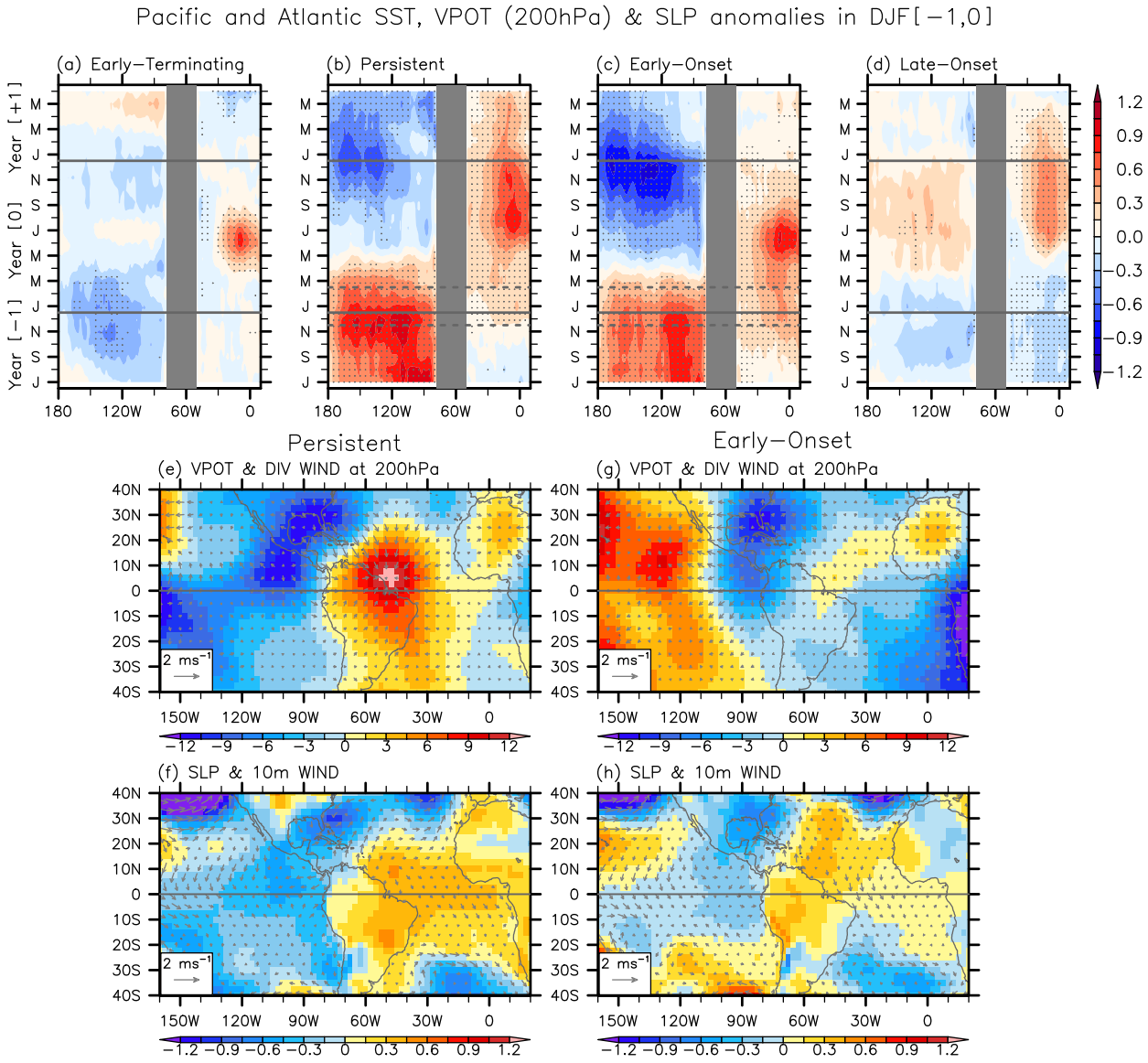

Figure 5.6: (a-d) Time-longitude SSTA plots of the tropical Pacific (averaged over 5°S-5°N) and tropical Atlantic (averaged over 3°S–3°N) for the four most frequently recurring Atlantic Niño varieties spanning from July (-1) to June (+1). Significant SSTA values at 99% or above based on a Student's t test (two tailed) are indicated by gray dots. (e, g) Velocity potential (shades) and divergent wind anomalies (vectors) at 200 hPa and (f, h) mean sea level pressure (shades) and surface (10 m) wind anomalies (vectors) in DJF (-1,0) regressed on (e, f) the persistent and (g, h) early-onset varieties. The units for SST, velocity potential, sea level pressure, and winds are in °C, 10^{-7} m^2 s^{-1}, hPa, and m s^{-1}, respectively.

Figures 5.6a-d show the four most frequently occurring Atlantic Niño varieties and the associated equatorial Pacific SSTAs between July of the preceding year and June of the following year. The early-terminating variety is linked to slightly cold SSTAs in the equatorial Pacific during the preceding boreal winter (Figure 5.6a). This means that La Niña events may occasionally precede this Atlantic Niño variety but are not necessarily required for it to develop in boreal summer. As shown in Figures 5.6b and 5.6c, it is clear that both the persistent and early-onset varieties are linked to strong El Niño events during the preceding boreal winter, suggesting that they are largely forced by El Niño events.

To better understand how some El Niño events may trigger the persistent and early-onset varieties, Figures 5.3e-h show velocity potential and divergent wind anomalies at 200 hPa, and mean sea level pressure and surface wind anomalies in DJF (-1,0) regressed onto the two varieties. In both cases, the tropical Atlantic region is characterized by anomalous subsidence, which is a typical response to El Niño-induced warming of the tropical Atlantic troposphere and associated increase in atmospheric static stability (e.g., Chiang & Sobel, 2002; Horel & Wallace, 1981; Mestas-Nuñez & Enfield, 2001; Yulaeva & Wallace, 1994). For the early-onset variety, the anomalous subsidence is largely north of the equator. Due to the anomalous sinking and increased static stability, the vertical development of convection is suppressed. Therefore, high sea level pressure anomalies are formed over TNA to sustain the interhemispheric wind anomalies. For the persistent variety, on the other hand, anomalous subsidence is stronger and covers a much broader region in the tropical Atlantic. As such, the trade winds are greatly weakened in both TNA and TSA, which in turn warms both TNA and TSA in boreal spring (MAM). However, no clear interhemispheric wind anomalies are formed across the equator. As suggested by Richter et al. (2013), the anomalously warm surface water off the coast of West Africa could be carried by ocean currents to the equatorial Atlantic region to trigger the Atlantic Niño.

Although the atmospheric flow anomalies linked to the two varieties are statistically distinctive (Figure 5.6), it is unclear why some strong El Niño events are linked to the persistent variety and others the early-onset variety. It is uncertain if this difference is due to El Nino diversity or processes internal to the Atlantic basin.

5.6 Concluding remarks

By performing a spatiotemporal EOF analysis of observed Atlantic Niño events, we identify the four most frequently recurring Atlantic Niño varieties. The first two contrast the timing of dissipation (i.e., early-terminating vs. persistent varieties), while the other two the timing of onset (i.e., early-onset vs. late-onset varieties). Largely consistent with the timings of onset and dissipation, the four varieties display remarkable differences in climate response over the surrounding continents. In particular, the persistent and late-onset varieties correspond to an extended period of increased rainfall over the West African sub-Sahel region during June-October, while the early-terminating and early-onset varieties correspond to a limited period of increased rainfall over the West African sub-Sahel region during June-August or July-August. Similarly, rainfall over northeastern South America tends to increase during the peak seasons of the early-terminating, persistent, and early-onset Atlantic Niño varieties. However, rainfall in this region is not strongly

modified during the late-onset variety. Rainfall anomalies over northeastern South America prior to or after the peak seasons are most likely driven by either the MM for the early-terminating variety (Foltz et al., 2012) or ENSO in the Pacific for the persistent and early-onset varieties (e.g., Hastenrath & Heller, 1977).

Further regression analysis suggests that each of the four Atlantic Niño varieties is subject to clearly different onset mechanisms. The early-terminating variety is preconditioned and triggered by a negative phase of the MM in boreal spring (e.g., Foltz & McPhaden, 2010). Both the persistent and early-onset varieties appear to be forced by strong El Niño events in the preceding boreal winter. The persistent variety seems to be initiated by oceanic advection of warm SSTAs off the coast of West Africa (Richter et al., 2013). The early-onset variety appears to be largely forced by interhemispheric wind anomalies that are persistently forced during DJF and MAM by El Niño-induced anomalous subsidence and increased sea level pressure over TNA. In contrast to the other three varieties, the late-onset variety is spontaneously triggered by atmosphere-ocean processes internal to the equatorial Atlantic (e.g., Keenlyside & Latif, 2007) and shows no clear source of external forcing in boreal spring, thus suggesting low seasonal predictability compared to the other three varieties.

Chapter 6

General conclusions

The interhemispheric exchange of mass and heat in the Atlantic Ocean takes place in the unique ocean-atmosphere system of the tropical Atlantic. The western boundary NBC, which is largely fed by AMOC waters, retroflects east at the equator forced by local and remote variations in the trade winds. The EUC emerges from this retroflection as a subsurface current that carries relatively cool, salty and oxygen-rich waters to the central and eastern equatorial regions. Seasonal and inter-annual variations in local and remote forcing drive both the NBC-EUC retroflection and the central-eastern thermocline upwelling, with associate changes of SST. This diversity of SSTA in the central and eastern equatorial Atlantic in turn modulate the climatic conditions in West Africa and South America.

In **chapter 2** we have explored the connections between the subtropical and tropical gyres in the South Atlantic from the surface to the intermediate layers. The predominant pathways of mass and heat exchange between both gyres have been inferred by performing two particle back-track simulations, using the GLORYS2v4 hydrographic and velocity data. The results show that nearly all water masses in the central South Atlantic eventually flow northwards along the western boundary, as the combination of NBUC and NBC, into the equatorial region. Despite this predominant northward mass and heat transfer, the recirculation of surface tropical and subtropical waters is of a significant mass and heat southward transport.

As it crosses the equator, the northward western boundary NBC is largely diverted eastward as a result of the vanishing Coriolis force and the influence of the eastward pressure-gradient force. The outcome is the EUC, which has been carefully described in **chapter 3** through a combination of field and reanalysis data. Using observations from a cruise carried out in April 2010, we have calculated the water mass balance in the NBC-EUC retroflection area. The total equatorward flow composed by the NBUC and NBC transports 22.8 Sv, which is in good agreement with the Lagrangian northward transport of 20.6 Sv at 5°S, as estimated in **chapter 2**.

The equatorial observations compare satisfactorily with data from the GLORYS2v4 reanalysis. Hence, we have used these data to again carry out Lagrangian simulations in order to characterize the main water sources and retroflection latitudinal pathways that originate the EUC. Four main water sources in the subtropics and tropics of both hemispheres ventilate the EUC through the NBC retroflection. The predominant water contribution changes as we shift between density classes and each one is dominated by a distinct retroflection latitudinal pathway. Additionally, in **chapter 3** we describe the seasonal-to-interannual transport fluctuations within the context of the coupled ocean-atmosphere tropical Atlantic system.

In **chapter 4** we identified a potential source of these fluctuations as a result of the emergence of the Neridional Mode (MM) and Equatorial Modes. The equatorial and north tropical zonal circulation is affected by changes in SSH zonal gradients due to the RW-reflected mechanism associated with the MM-EM connection. Concretely, the NECC and EUC, as well as the surface nSEC. The subsurface response to the EM is less predictable. The mechanisms over the EUC during the development of EM can be masked by additional external forcing or the same intrinsic EM variability as we show in **chapter 5**.

In order to explore the diversity of warm phase of EM, here referred as Atlantic Niño, in **chapter 5** we have used observational and reanalysis SST data-sets to identify 22 Atlantic Niño events between 1948 and 2019. Interestingly, there are no two events that closely resemble each other or that can be described by the composite mean. Thus, a spatio-temporal EOF analysis has been applied to this sample of 22 Atlantic Niño events to retain the more persistent structures. In this way, we have described four principal Atlantic Niño configurations (early-onset, late-onset, persistent and early-termination), which arise from a combination of multiple mechanisms and lead to different climatic response in critical areas such as sub-Sahel and Brazil Nordeste. In particular, we have found that either the boreal-spring preconditioning a MM of opposite sign, in the tropical North Atlantic or the remote ENSO influence can determine the onset and dissipation of most of these AN varieties.

6.1 Main scientific contributions

- The combination of numerical ocean models or reanalysis with Lagrangian modelling is a powerful tool to resolve the large-scale connections, resolving the time-dependent (or Lagrangian) streamfunctions and deciphering the water mass transformations, including changes in heat content and transport.

- In the South Atlantic, the western-boundary returning limb of the AMOC into the tropical regions arises through 14.9 Sv that come from the eastern subtropical margin and 7.4 Sv that follow interior pathways, transporting a total 0.90 PW. Adding the tropical contribution, the resulting total northward transport of mass and heat at 5°S is 20.6 Sv and 1 PW.

- Also in the South Atlantic, there is a minor yet significant southward heat transport, which results from the contribution of 0.14 PW in shallow tropical waters plus 0.04 PW in the heated subtropical recirculation waters.

- The ocean reanalysis GLORYS2v4 reproduces correctly the surface-thermocline current structure ($\sigma < 26.4$ kg m^{-3}) in the western equatorial Atlantic but some inconsistencies appear in deeper layers ($\sigma > 26.4$ kg m^{-3}). In contrast, the thermohaline structure is well captured at central ($26.4 < \sigma < 27.1$ kg m^{-3}) and intermediate layers ($27.1 < \sigma < 27.6$ kg m^{-3}).

- Observational estimations in April 2010 show equatorward NBUC and NBC transports of 8.4 ± 1.5 Sv and 14.4 ± 0.4 Sv, respectively. Most of these transports retroflect to feed the EUC, which shows a total transport of 15.4 ± 0.4 Sv at 32°W (a section from 1.5°S to 1.5°N).

- The predominant water contribution into the EUC changes as we shift between density classes. SAW is the major water contribution to the EUC, taking place within the lower-thermocline layer ($25.5 < \sigma < 26.4$ kg m^{-3}). Instead, waters of tropical origin, SEAW and NEAW are mostly present in the surface ($\sigma < 24.5$ kg m^{-3}) and upper-thermocline layers ($24.5 < \sigma < 25.5$ kg m^{-3}).

- The major water contribution to the NBC-EUC retroflection is SAW with an annual-mean transport of 6.3 ± 0.5 Sv followed by tropical SEAW with 5.1 ± 0.8 Sv. Outstandingly, SEAW increments its transport from 2008 onwards which is consistent with the recently reported STCs intensification (Brandt et al., 2021).

- There is a preferential connection between the water origin areas and the NBC latitudinal retroflection pathways. The equatorial (0° to 3°N) and north equatorial (north of 3°N) retroflections are dominated by SEAW and SAW waters. NEAW joins the north-equatorial retroflection through the nSEC, and a small portion of NAW (< 1 Sv) enters into the EUC through the NECC (northern retroflection).

- The NBC retroflection system responds to the emergence of the two main modes of variability in the tropical Atlantic. Changes in surface and subsurface equatorial zonal currents are strongly associated with the MM evolution. During the development of positive MM the zonal SSH gradient reinforces the nSEC, NECC and EUC. Conversely, the associated RW-reflection mechanism is responsible to revert the equatorial zonal SSH gradient causing an AN-like pattern. The linear response of nSEC or surface NECC to the AN contrasts with the inconsistency in the sub-surface layers.

- The transport connectivity between western north-equatorial and eastern equatorial Atlantic is influenced by the RW-reflected mechanism which can provide an equatorial transport predictability up to 3-4 months in advance.

- The transport fluctuations as a result of RW-reflected mechanism together with intrinsic variability of the EM may explain the non-linear EUC response to a warm EM event (Atlantic Niño).

- The different timings in the onset and dissipation of anomalous SSTA in the equatorial Atlantic set four principal varieties of Atlantic Niño, with remarkable differences in rainfall response over the surrounding continents. The persistent and late-onset Atlantic Niño varieties extend the period of increased rainfall over West Africa (June to October) while the early-terminating and early-onset varieties correspond to a limited period (June/July to August). In contrast, the response over north-eastern South America is similar except for the late-onset variety.

- The onset and dissipation of the early-terminating variety are driven by the negative MM. The cross-equatorial wind builds up a negative SSTA in the eastern equatorial Atlantic which is dissipated by a westward Rossby - eastward downwelling Kelvin wave propagation mechanism.

- The persistent and early-onset varieties are influenced by ENSO. Anomalous subsidence north of the equator is linked with strong El Niño conditions in the Pacific during the previous winter, causing high sea-level pressure over tropical North Atlantic and driving the early-onset of negative inter-hemispheric wind anomalies. For the persistent variety, subsidence affects the tropical North and South Atlantic, which reduces the trade winds in both hemispheres and builds up positive SSTA.

6.2 Future lines of research

- The results of this thesis have advanced our knowledge of the upper circulation and water mass characteristics in the tropical Atlantic, with special attention to the NBC-EUC retroflection. In particular, in chapter 3 we have contextualized the seasonal and interannual variability of source transports with other results in recent literature. However, further research is still necessary in order to better understand the atmosphere-ocean dynamic processes linked with these transport fluctuations. The observed linkage between the STC intensification and a positive trend of the EUC flow points at a true role of the remote wind field in EUC transport variability. Brandt et al. (2021) and Tuchen et al. (2020) show how an increase in the poleward Ekman transport, as a result of an intensification of zonal wind stress in north tropical Atlantic, is compensated by westward surface flow from the central equatorial Atlantic. Mass conservation suggests that this increase in the equatorial westward surface flows will lead to an increase in the EUC eastward transport. Indeed, our results suggest that this STC intensification drives an increase of tropical waters into the EUC. Nevertheless, it would be necessary to carry out a time-lag regression analysis of the EUC transports with the off-equatorial wind field or wind-stress curl in order to verify this hypothesis.

- Other sources of variability in the NBC-EUC retroflection deserve further consideration. Recent observational studies have shown that large intraseasonal variations in the EUC transport (Brandt et al., 2014; Johns et al., 2014) are associated with tropical instability waves (TIW). A recent study in the Pacific has shown that sub-surface TIW explains about 20% of the zonal-current variance at the equator (Liu et al., 2019). This source of variability may also be one of the causes why the EUC transport does not experience substantial changes during EM phases (chapter 4).

- The eastward NECC and EUC are the major currents fed by the NBC retroflection, but other zonal flows that depart from the NBC play a crucial role on the water mass composition of the thermocline layers in the tropical Atlantic. Concretely, the EUC is bound by its northern (NEUC) and southern (SEUC) eastward branches, centred at about 4-5° of latitude. The NEUC supplies oxygen into the oxygen minimum zone in the eastern tropical North Atlantic (e.g., Burmeister et al., 2016; Peña-Izquierdo et al., 2015), with high interannual variability (Hüttl-Kabus & Böning, 2008). Concretely, Goes et al. (2013) observed a negative correlation between NEUC transport and the MM. They suggested that changes in the meridional density gradient during the MM phases are a possible mechanism for NEUC variability at

interannual scale. On the southern side of the equator, the SEUC is partly supplied by interior recirculations from the SEC, displaying large meanders near the western boundary (Fischer et al., 2008). Fischer et al. (2008) estimated a SEUC transport increase of almost 5 Sv between the western and eastern tropical Atlantic. Our Lagrangian analysis may be expanded in future research to better understand the sources of variability of the NEUC and SEUC and their role in the water recirculation pathways that control the water mass composition in the tropical Atlantic.

- Special attention is required with our definition of the warm EM events (Atlantic Niño) in **chapter 5**. Our methodology uses a 30-year climatology but averaged every 5 years. This method defines the Atlantic Niño events by their contemporary climatology, following the methodology used to define El Niño in the Pacific by the Climate Prediction Center of the National Oceanic and Atmospheric Administration. Thus, the mean state changes along the time of analysis so we need to be careful in order to compare our findings with other results. The changing mean state may influence the amplitude and mechanisms of the identified Atlantic Niño events. Martín-Rey et al. (2018) and Richter et al. (2013), for example, subtract the climatological seasonal cycle for the entire period of study. A detailed analysis on how these different methodologies affect the results may be useful for future TAV research.

Appendix A

Supporing information for chapter 5

The supporting information provides Figures A.1 to A.6 and detailed descriptions of the threshold used to identify Atlantic Niño and additional analysis and discussion on the spatiotemporal diversity of Atlantic Niña. Figures A.1 and A.2 are same as Figure 5.3 but derived from the COBE SST, and ERSSST5 datasets, respectively. Figure A.3 show time-longitude plots of tropical Atlantic SSTAs, South American land precipitation anomalies, and West African land precipitation anomalies for the four most frequently recurring Atlantic Niña varieties. Figures A.4 and A.5 are same as Figure A.3 but derived from the COBE SST and ERSSST5 datasets, respectively. Figure A.6 show velocity potential and divergent wind anomalies at 200 hPa, and mean sea level pressure and surface wind anomalies regressed on the persistent variety minus those regressed on the early-onset variety.

A.1 Detailed descriptions of the threshold used to identify Atlantic Niño and Atlantic Niña events

To identify the Atlantic Niño events, we use a threshold that the 3 month averaged SSTAs in ATL3 are equal to or higher than 0.5°C for at least two consecutive overlapping seasons. Warm events identified based on only one or two SST datasets are discarded. Using this method, we identify 22 Atlantic Niño events in 1949, 1951, 1963, 1966, 1968, 1973, 1974, 1981, 1984, 1987, 1988, 1991, 1993, 1995, 1996, 1998, 1999, 2008, 2010, 2016, 2018, and 2019. Note that 1964 is not selected because the strong Atlantic Niño event of 1963 continued throughout the early 1964. For the same reason, 1969 and 1972 are not selected. According to the HADISST1 dataset, the warm event in 2018 started very late (September-October) and continued to 2019. However, according to the COBE SST and ERSST5 datasets, the 2018 warm event started as early as June – August. Therefore, the 2018 warm event is selected as one of the 22 Atlantic Niño events.

A.2 Spatiotemporal diversity of Atlantic Niña

It is important to note that our results specific to Atlantic-Niño diversity cannot be directly applied to Atlantic Niña diversity with reversed sign. We identify 14 Atlantic Niña events using the threshold that the 3 month averaged SSTAs in ATL3 is equal to or lower than -0.5°C for at least two consecutive overlapping seasons. Cold events identified based on only one or two datasets are discarded. The 14 Atlantic Niña events are in 1950, 1954, 1958, 1964, 1967, 1976, 1978, 1982,

1983, 1991, 1992, 1997, 2005 and 2012. The cold event in early 1951 is excluded because the Atlantic Niña event of 1950 continued throughout the early 1951. As shown in Figures A.3 to A.5, our results specific to Atlantic-Niño diversity cannot be directly applied to Atlantic Niña diversity with reversed sign. Specifically, while the persistent, early-onset and late-onset varieties (with reversed sign) still prevail, the early-terminating variety disappears and is replaced by warm-to-cold transition variety. The four Atlantic Niña varieties also show distinct patterns of rainfall response over West Africa and South America. Future studies may further examine the Atlantic Niña diversity and the associated onset mechanisms.

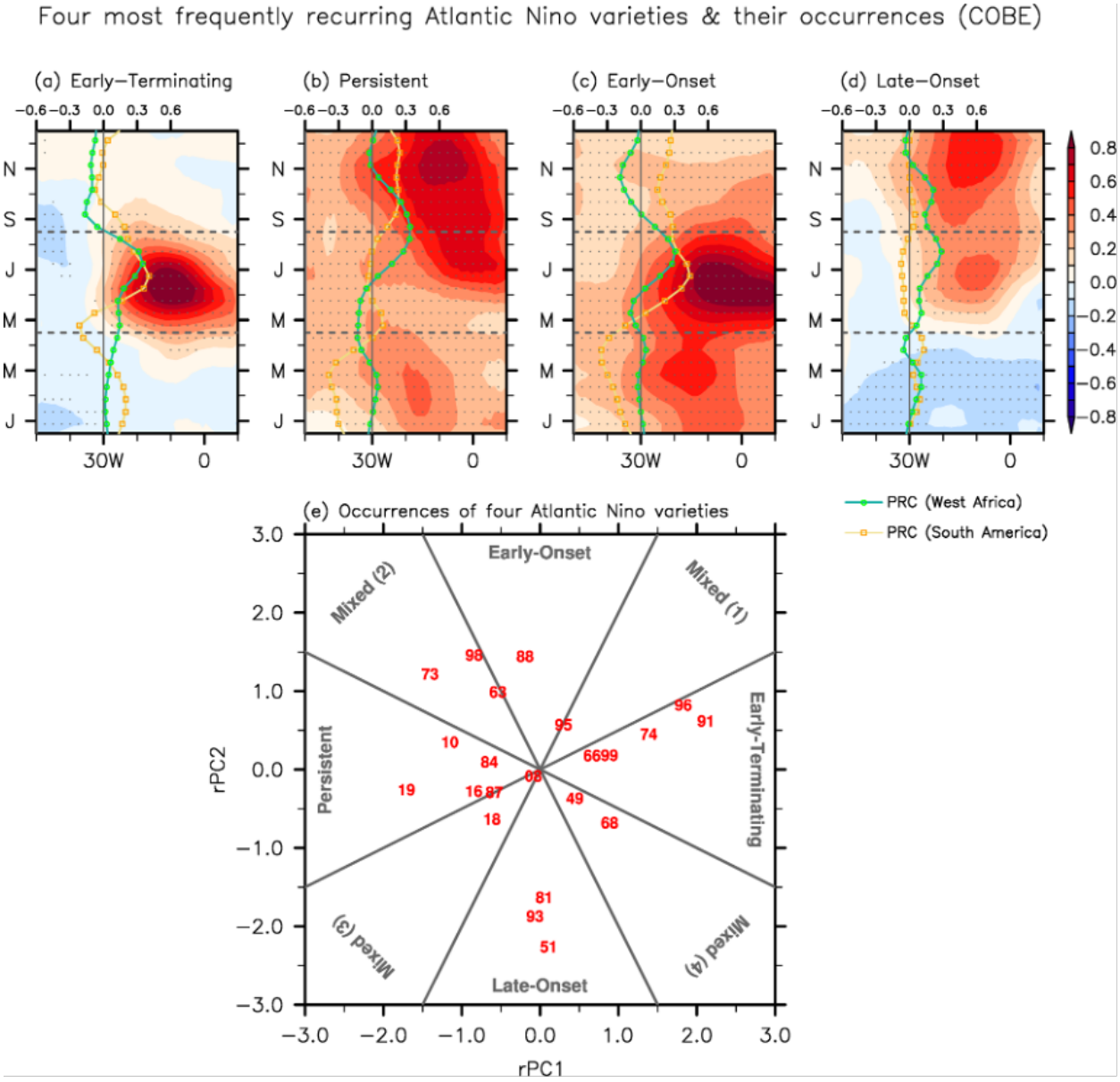

Figure A.1: Same as Figure 5.3 but derived from the COBE SST dataset

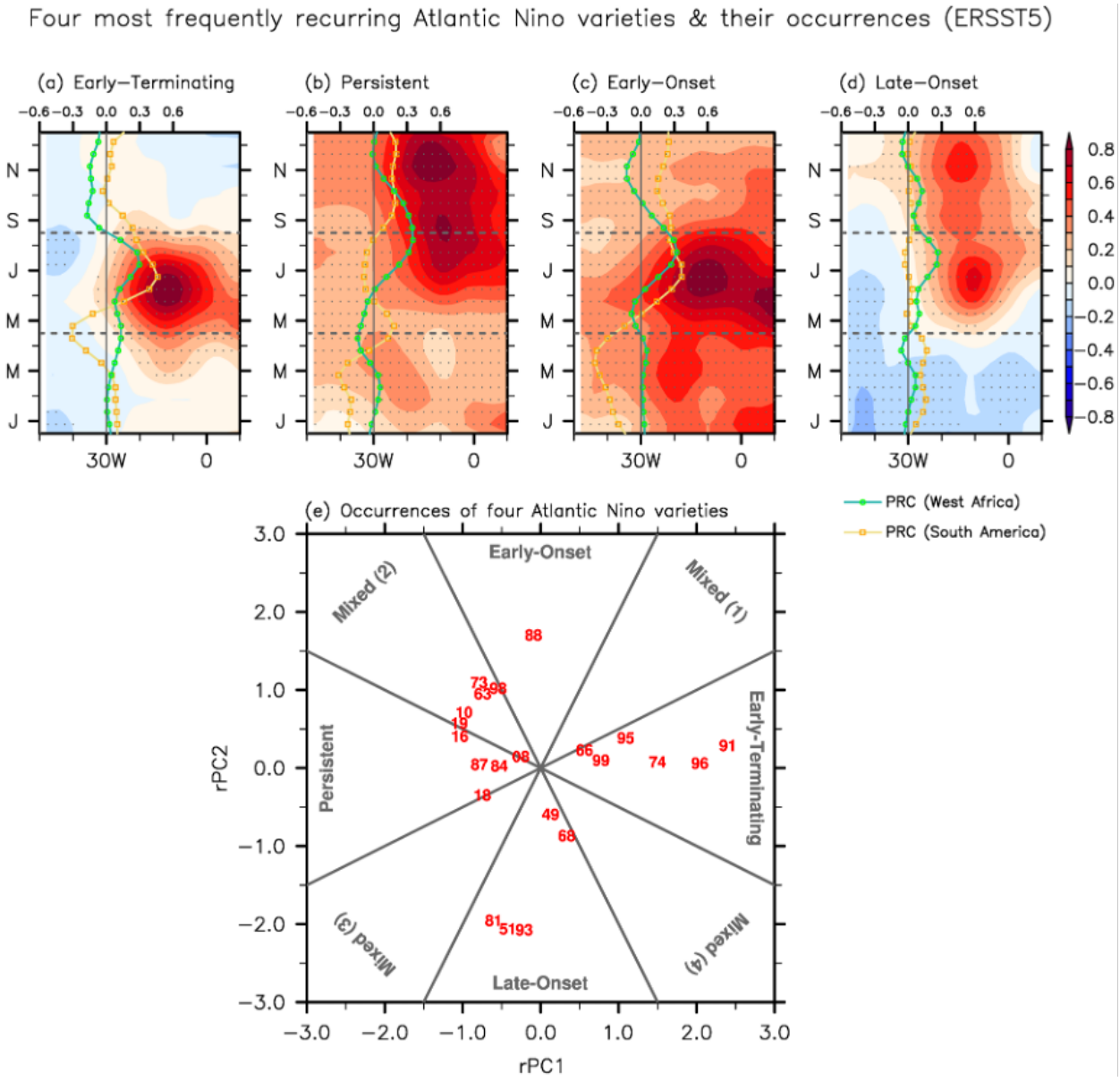

Figure A.2: Same as Figure 5.3 but derived from the ERSST5 SST dataset

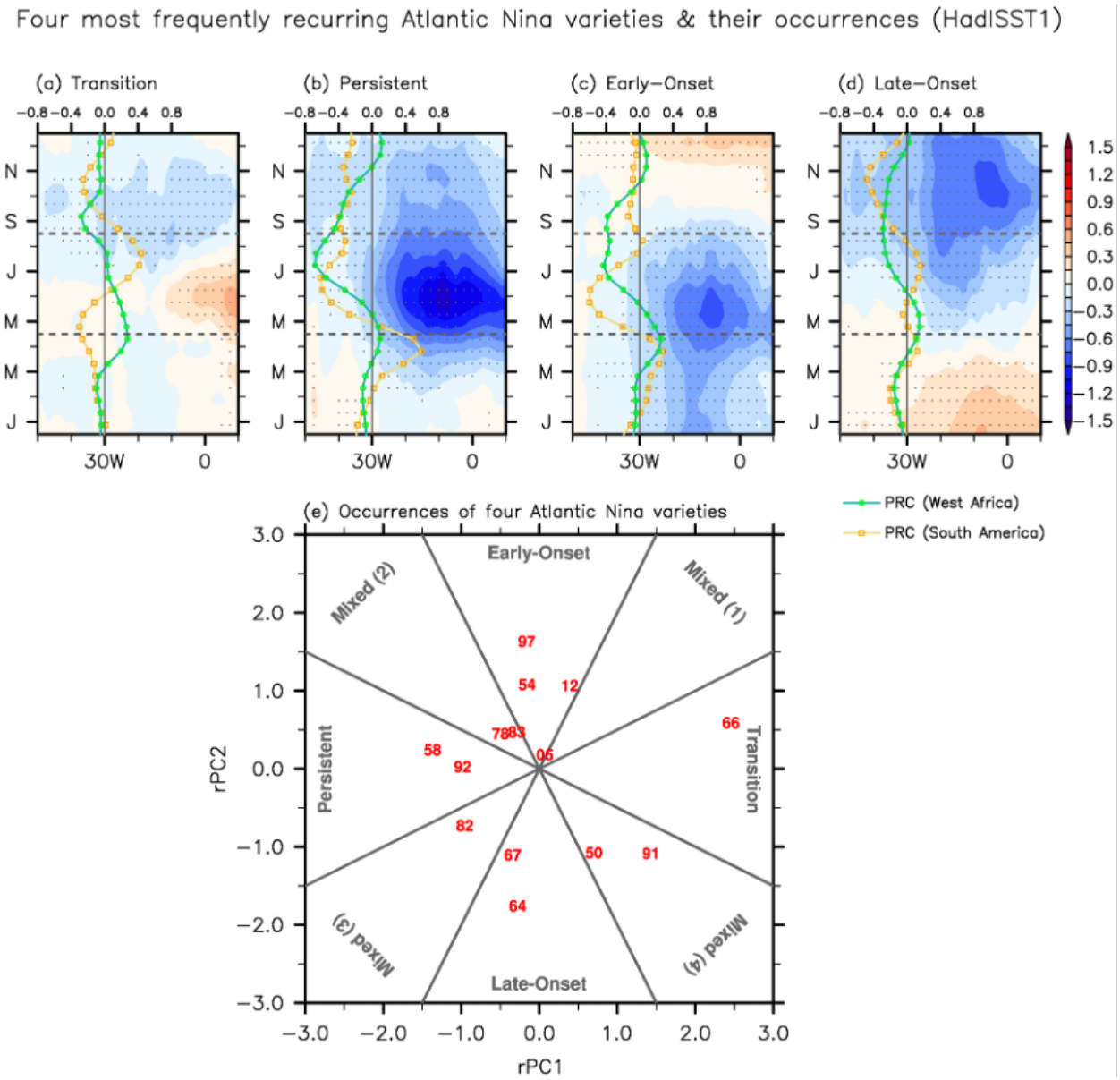

Figure A.3: (a–d) Time-longitude plots of the tropical Atlantic SSTAs derived from HadiSST (averaged over 3°S-3°N; shades) illustrate the four most frequently recurring Atlantic Niña varieties during 1948–2019, namely, (a) the transition, (b) persistent, (c) early-onset, and (d) late-onset varieties. Significant values at 99% or above based on a Student's t-test (two tailed) are indicated by gray dots. Land precipitation anomalies over South America (averaged over 0°-10°N and 70°W-50°W; orange lines) and West African sub-Sahel region (averaged over 0°-10°N and 20°W-20°E; green lines) are also shown for each of the four Atlantic Niña varieties. (e) Normalized rotated PC1 versus rotated PC2 values for all 14 events. The two-digit numbers indicate the Atlantic Niña years. The dashed gray lines in Figures S5a–5c indicate 1 May and 31 August. The thick gray lines in (e) are the boundaries (i.e., rPC1 = ±2 × rPC2 and rPC2 = ±2 × rPC1) that separate the four varieties from the mixed varieties. The units for SST and precipitation are in °C and mm day$_{-1}$, respectively.

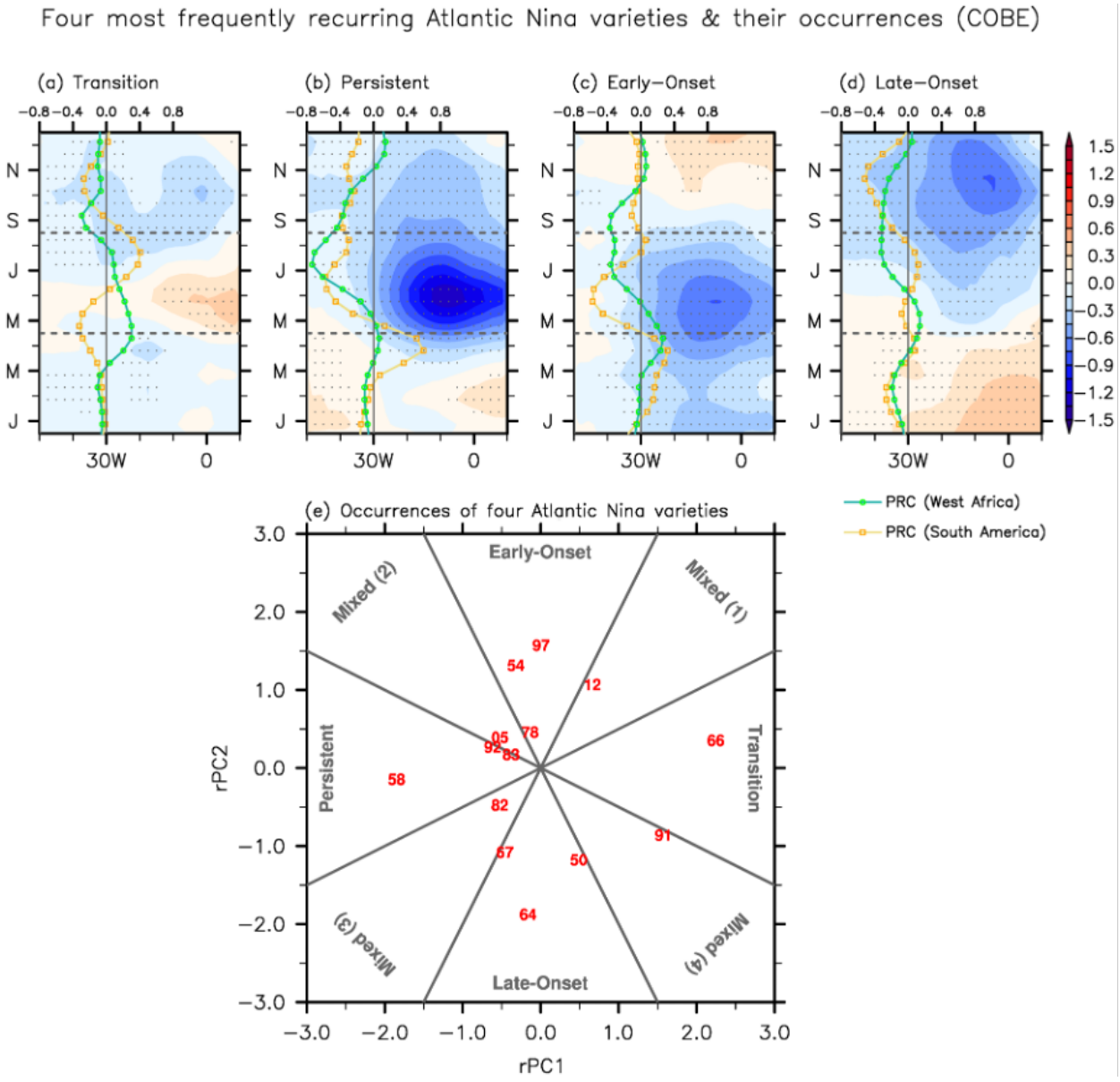

Figure A.4: Same as **??** but derived from the COBE SST dataset

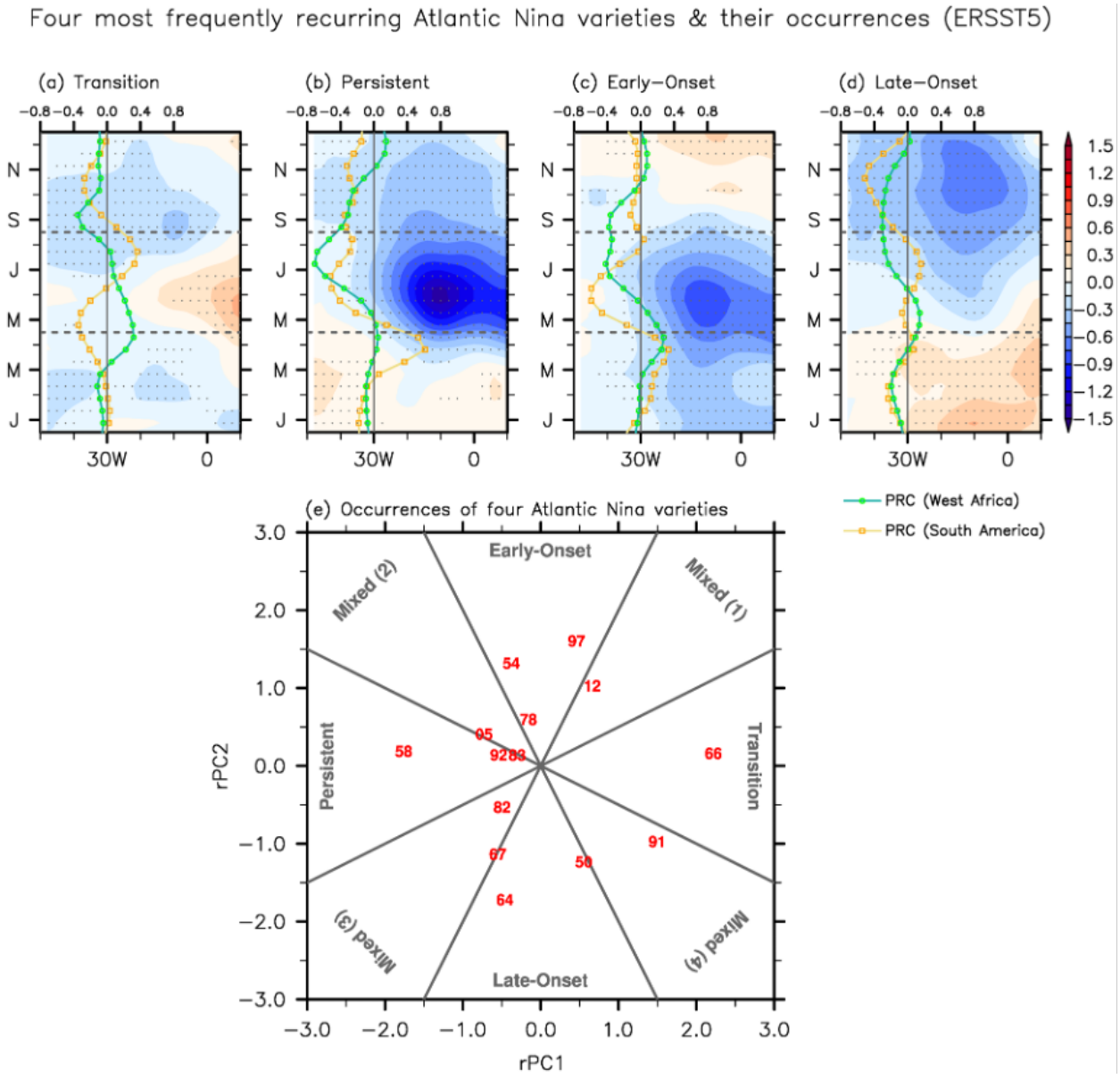

Figure A.5: Same as **??** but derived from the ERSST5 SST dataset

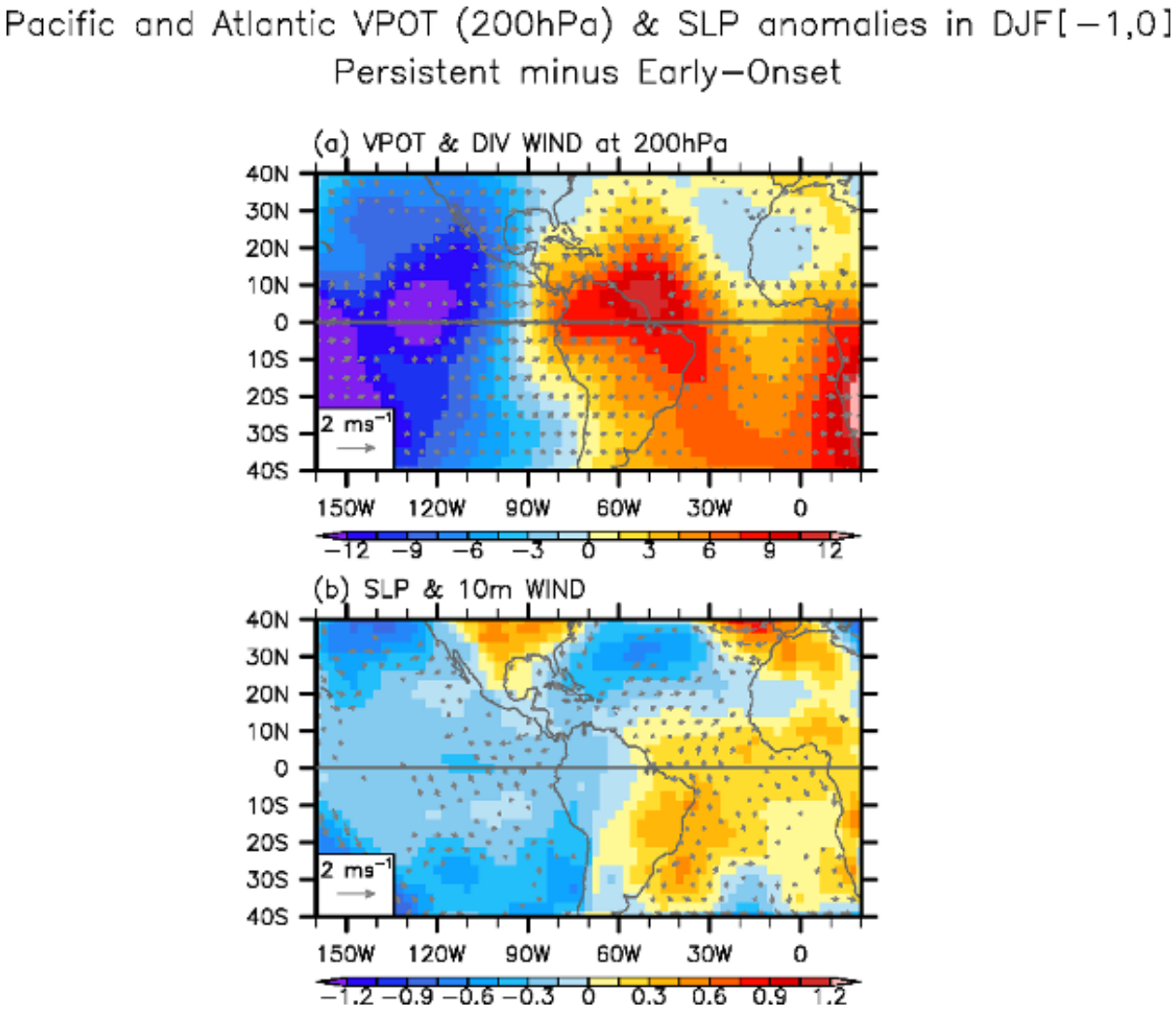

Figure A.6: (a) Velocity potential (shades) and divergent wind anomalies (vectors) at 200 hPa and (b) mean sea level pressure (shades) and surface (10 m) wind anomalies (vectors) in DJF (-1,0) regressed on the persistent variety minus those regressed on the early-onset variety. Divergent and surface wind anomalies below 95% significance level based on a Student's t-test (two tailed) are not shown. The units for velocity potential, sea level pressure and winds are in 10-7 m2 s_{-1}, hPa and m s_{-1}, respectively.

Bibliography

Alexander, M., & Scott, J. (2002). The influence of ENSO on air-sea interaction in the Atlantic. *Geophys. Res. Lett.*, *29*(14). https://doi.org/10.1029/2001GL014347

Amaya, D. J., DeFlorio, M. J., Miller, A. J., & Xie, S. P. (2017). WES feedback and the Atlantic Meridional Mode: observations and CMIP5 comparisons. *Clim. Dyn.*, *49*(5-6). https://doi.org/10.1007/s00382-016-3411-1

Arhan, M., Treguier, A. M., Bourlès, B., & Michel, S. (2006). Diagnosing the annual cycle of the equatorial undercurrent in the Atlantic Ocean from a general circulation model. *J. Phys. Oceanogr.*, *36*(8). https://doi.org/10.1175/JPO2929.1

Aristotle, & Webster, E. (2006). *Meteorology*. Neeland Media. https://books.google.es/books?id=FiVxmAEACAAJ

Arnault, S., Bourlès, B., Gouriou, Y., & Chuchla, R. (1999). Intercomparison of the upper layer circulation of the western equatorial Atlantic Ocean: In situ and satellite data. https://doi.org/10.1029/1999jc900124

Balmaseda, M. A., Mogensen, K., & Weaver, A. T. (2013). Evaluation of the ECMWF ocean reanalysis system ORAS4. *Q. J. R. Meteorol. Soc.*, *139*(674). https://doi.org/10.1002/qj.2063

Baringer, M. O., & Garzoli, S. L. (2007). Meridional heat transport determined with expendable bathythermographs-Part I: Error estimates from model and hydrographic data. *Deep. Res. Part I Oceanogr. Res. Pap.*, *54*(8). https://doi.org/10.1016/j.dsr.2007.03.011

Bjerknes, J. (1969). Atmospheric teleconnections from the equatorial pacific. *Mon. Weather Rev.*, *97*(3). https://doi.org/10.1175/1520-0493(1969)097<0163:atftep>2.3.co;2

Blanke, B., Arhan, M., Madec, G., & Roche, S. (1999). Warm water paths in the equatorial Atlantic as diagnosed with a general circulation model. *J. Phys. Oceanogr.*, *29*(11). https://doi.org/10.1175/1520-0485(1999)029<2753:WWPITE>2.0.CO;2

Boebel, O., Davis, R. E., Ollitrault, M., Peterson, R. G., Richardson, P. L., Schmid, C., & Zenk, W. (1999). The intermediate depth circulation of the western South Atlantic. *Geophys. Res. Lett.*, *26*(21). https://doi.org/10.1029/1999GL002355

Bourlès, B., D'Orgeville, M., Eldin, G., Gouriou, Y., Chuchla, R., DuPenhoat, Y., & Arnault, S. (2002). On the evolution of the thermocline and subthermocline eastward currents in the Equatorial Atlantic. *Geophys. Res. Lett.*, *29*(16). https://doi.org/10.1029/2002gl015098

Bourles, B., Molinari, R. L., Johns, E., Wilson, W. D., & Leaman, K. D. (1999). Upper layer currents in the western tropical North Atlantic (1989-1991). *J. Geophys. Res. Ocean.*, *104*(C1). https://doi.org/10.1029/1998jc900025

Bourlès, B., Lumpkin, R., McPhaden, M. J., Hernandez, F., Nobre, P., Campos, E., Yu, L., Planton, S., Busalacchi, A., Moura, A. D., Servain, J., & Trotte, J. (2008). The Pirata Program: History,

accomplishments, and future directions. *Bull. Am. Meteorol. Soc.*, *89*(8). https://doi.org/10.1175/2008BAMS2462.1

Brandt, P., Funk, A., Hormann, V., Dengler, M., Greatbatch, R. J., & Toole, J. M. (2011). Interannual atmospheric variability forced by the deep equatorial Atlantic Ocean. *Nature*, *473*(7348). https://doi.org/10.1038/nature10013

Brandt, P., Funk, A., Tantet, A., Johns, W. E., & Fischer, J. (2014). The Equatorial Undercurrent in the central Atlantic and its relation to tropical Atlantic variability. *Clim. Dyn.*, *43*(11). https://doi.org/10.1007/s00382-014-2061-4

Brandt, P., Greatbatch, R. J., Claus, M., Didwischus, S. H., Hormann, V., Funk, A., Hahn, J., Krahmann, G., Fischer, J., & Krtzinger, A. (2012). Ventilation of the equatorial Atlantic by the equatorial deep jets. *J. Geophys. Res. Ocean.*, *117*(12). https://doi.org/10.1029/2012JC008118

Brandt, P., Hahn, J., Schmidtko, S., Tuchen, F. P., Kopte, R., Kiko, R., Bourlès, B., Czeschel, R., & Dengler, M. (2021). Atlantic Equatorial Undercurrent intensification counteracts warming-induced deoxygenation. *Nat. Geosci.*, *14*(5). https://doi.org/10.1038/s41561-021-00716-1

Brandt, P., Hormann, V., Bourlès, B., Fischer, J., Schott, F. A., Stramma, L., & Dengler, M. (2008). Oxygen tongues and zonal currents in the equatorial Atlantic. *J. Geophys. Res. Ocean.*, *113*(4). https://doi.org/10.1029/2007JC004435

Brandt, P., Schott, F. A., Provost, C., Kartavtseff, A., Hormann, V., Bourlès, B., & Fischer, J. (2006). Circulation in the central equatorial Atlantic: Mean and intraseasonal to seasonal variability. *Geophys. Res. Lett.*, *33*(7). https://doi.org/10.1029/2005GL025498

Brodeau, L., Barnier, B., Treguier, A. M., Penduff, T., & Gulev, S. (2010). An ERA40-based atmospheric forcing for global ocean circulation models. *Ocean Model.*, *31*(3-4). https://doi.org/10.1016/j.ocemod.2009.10.005

Burmeister, K., Brandt, P., & Lübbecke, J. F. (2016). Revisiting the cause of the eastern equatorial Atlantic cold event in 2009. *J. Geophys. Res. Ocean.*, *121*(7). https://doi.org/10.1002/2016JC011719

Butterworth, S. et al. (1930). On the theory of filter amplifiers. *Wireless Engineer*, *7*(6), 536–541.

Carton, J. A., & Huang, B. (1994). Warm events in the tropical Atlantic. *J. Phys. Oceanogr.*, *24*(5). https://doi.org/10.1175/1520-0485(1994)024<0888:WEITTA>2.0.CO;2

Carton, J. A., Chepurin, G. A., & Chen, L. (2018). SODA3: A new ocean climate reanalysis. *J. Clim.*, *31*(17). https://doi.org/10.1175/jcli-d-18-0149.1

Castellanos, P., Pelegrí, J. L., Campos, E. J., Rosell-Fieschi, M., & Gasser, M. (2015). Response of the surface tropical Atlantic Ocean to wind forcing. *Prog. Oceanogr.*, *134*. https://doi.org/10.1016/j.pocean.2015.02.005

Chang, P., Fang, Y., Saravanan, R., Ji, L., & Seidel, H. (2006). The cause of the fragile relationship between the Pacific El Niño and the Atlantic Niño. *Nature*, *443*(7109), 324–328. https://doi.org/10.1038/nature05053

Chang, P., Ji, L., & Li, H. (1997). A decadal climate variation in the tropical Atlantic Ocean from thermodynamic air-sea interactions. *Nature*, *385*(6616). https://doi.org/10.1038/385516a0

Chen, M., Xie, P., & Janowiak, J. E. (2002). Global land precipitation: A 50-yr monthly analysis based on gauge observations. *J. Hydrometeorol.*, *3*(3). https://doi.org/10.1175/1525-7541(2002)003<0249:GLPAYM>2.0.CO;2

Chiang, J. C., Kushnir, Y., & Giannini, A. (2002). Deconstructing Atlantic Intertropical Convergence Zone variability: Influence of the local cross-equatorial sea surface temperature gradient and remote forcing from the Eastern Equatorial Pacific. *J. Geophys. Res. Atmos.*, *107*(1-2). https://doi.org/10.1029/2000jd000307

Chiang, J. C., & Sobel, A. H. (2002). Tropical tropospheric temperature variations caused by ENSO and their influence on the remote tropical climate. *J. Clim.*, *15*(18). https://doi.org/10.1175/1520-0442(2002)015<2616:TTTVCB>2.0.CO;2

Claret, M., Rodríguez, R., & Pelegrí, J. L. (2012). Salinity intrusion and convective mixing in the Atlantic Equatorial Undercurrent. *Sci. Mar.*, *76*(S1). https://doi.org/10.3989/scimar.03611.19b

Cromwell, T., Montgomery, R. B., & Stroup, E. D. (1954). Equatorial undercurrent in Pacific Ocean revealed by new methods. *Science (80-.).*, *119*(3097). https://doi.org/10.1126/science.119.3097.648

Czaja, A., van der Vaart, P., & Marshall, J. (2002). A diagnostic study of the role of remote forcing in tropical Atlantic variability. *J. Clim.*, *15*(22). https://doi.org/10.1175/1520-0442(2002)015<3280:ADSOTR>2.0.CO;2

Da Silveira, I. C., De Miranda, L. B., & Brown, W. S. (1994). On the origins of the North Brazil Current. *J. Geophys. Res.*, *99*(C11). https://doi.org/10.1029/94jc01776

Dee, D. P., Uppala, S. M., Simmons, A. J., Berrisford, P., Poli, P., Kobayashi, S., Andrae, U., Balmaseda, M. A., Balsamo, G., Bauer, P., Bechtold, P., Beljaars, A. C., van de Berg, L., Bidlot, J., Bormann, N., Delsol, C., Dragani, R., Fuentes, M., Geer, A. J., … Vitart, F. (2011). The ERA-Interim reanalysis: Configuration and performance of the data assimilation system. *Q. J. R. Meteorol. Soc.*, *137*(656). https://doi.org/10.1002/qj.828

Delandmeter, P., & Van Sebille, E. (2019). The Parcels v2.0 Lagrangian framework: New field interpolation schemes. *Geosci. Model Dev.*, *12*(8). https://doi.org/10.5194/gmd-12-3571-2019

Delworth, T. L., Rosati, A., Anderson, W., Adcroft, A. J., Balaji, V., Benson, R., Dixon, K., Griffies, S. M., Lee, H. C., Pacanowski, R. C., Vecchi, G. A., Wittenberg, A. T., Zeng, F., & Zhang, R. (2012). Simulated climate and climate change in the GFDL CM2.5 high-resolution coupled climate model. *J. Clim.*, *25*(8). https://doi.org/10.1175/JCLI-D-11-00316.1

Ding, H., Keenlyside, N. S., & Latif, M. (2009). Seasonal cycle in the upper equatorial Atlantic Ocean. *J. Geophys. Res. Ocean.*, *114*(9). https://doi.org/10.1029/2009JC005418

Dippe, T., Greatbatch, R. J., & Ding, H. (2018). On the relationship between Atlantic Niño variability and ocean dynamics. *Clim. Dyn.*, *51*(1-2). https://doi.org/10.1007/s00382-017-3943-z

Donners, J., & Drijfhout, S. S. (2004). The Lagrangian view of South Atlantic interocean exchange in a global ocean model compared with inverse model results. *J. Phys. Oceanogr.*, *34*(5). https://doi.org/10.1175/1520-0485(2004)034<1019:TLVOSA>2.0.CO;2

Döös, K., Nycander, J., & Coward, A. C. (2008). Lagrangian decomposition of the Deacon Cell. *J. Geophys. Res. Ocean.*, *113*(7). https://doi.org/10.1029/2007JC004351

Döös, K., Nilsson, J., Nycander, J., Brodeau, L., & Ballarotta, M. (2012). The World Ocean thermohaline circulation. *J. Phys. Oceanogr.*, *42*(9). https://doi.org/10.1175/JPO-D-11-0163.1

Drijfhout, S. S., de Vries, P., Döös, K., & Coward, A. C. (2003). Impact of eddy-induced transport on the Lagrangian structure of the Upper Branch of the thermohaline circulation. *J. Phys. Oceanogr.*, *33*(10). https://doi.org/10.1175/1520-0485(2003)033<2141:IOETOT>2.0.CO;2

Egbert, G. D., Bennett, A. F., & Foreman, M. G. (1994). TOPEX/POSEIDON tides estimated using a global inverse model. *J. Geophys. Res.*, *99*(C12). https://doi.org/10.1029/94jc01894

Enfield, D. B., Mestas-Nuñez, A. M., & Trimble, P. J. (2001). The Atlantic multidecadal oscillation and its relation to rainfall and river flows in the continental U.S. *Geophys. Res. Lett.*, *28*(10). https://doi.org/10.1029/2000GL012745

Eyring, V., Bony, S., Meehl, G. A., Senior, C. A., Stevens, B., Stouffer, R. J., & Taylor, K. E. (2016). Overview of the Coupled Model Intercomparison Project Phase 6 (CMIP6) experimental design and organization. *Geosci. Model Dev.*, *9*(5). https://doi.org/10.5194/gmd-9-1937-2016

Faye, S., Lazar, A., Sow, B. A., & Gaye, A. T. (2015). A model study of the seasonality of sea surface temperature and circulation in the Atlantic North-eastern Tropical Upwelling System. *Front. Phys.*, *3*(SEP). https://doi.org/10.3389/fphy.2015.00076

Ferry, N, Parent, L, Garric, G, Bricaud, C, Testut, C. E., Galloudec, O. L., Lellouche, J. M., Drevillon, M, Greiner, E, Barnier, B, Molines, J. M., Jourdain, N, Guinehut, S, Cabanes, C, & Zawadzki, L. (2012). GLORYS2V1 global ocean reanalysis of the altimetric era (1992–2009) at meso scale. *Mercat. Ocean. Newsl.*, *44*(March 2011).

Fischer, J., Hormann, V., Brandt, P., Schott, F. A., Rabe, B., & Funk, A. (2008). South Equatorial Undercurrent in the western to central tropical Atlantic. *Geophys. Res. Lett.*, *35*(21). https://doi.org/10.1029/2008GL035753

Flament, P. (2002). A state variable for characterizing water masses and their diffusive stability: Spiciness. *Prog. Oceanogr.*, *54*(1-4). https://doi.org/10.1016/S0079-6611(02)00065-4

Florenchie, P., Reason, C. J., Lutjeharms, J. R., Rouault, M., Roy, C., & Masson, S. (2004). Evolution of interannual warm and cold events in the Southeast Atlantic Ocean. *J. Clim.*, *17*(12). https://doi.org/10.1175/1520-0442(2004)017<2318:EOIWAC>2.0.CO;2

Folland, C. K., Colman, A. W., Rowell, D. P., & Davey, M. K. (2001). Predictability of northeast Brazil rainfall and real-time forecast skill, 1987-98. *J. Clim.*, *14*(9). https://doi.org/10.1175/1520-0442(2001)014<1937:PONBRA>2.0.CO;2

Folland, C. K., Palmer, T. N., & Parker, D. E. (1986). Sahel rainfall and worldwide sea temperatures, 1901-85. *Nature*, *320*(6063). https://doi.org/10.1038/320602a0

Foltz, G. R., Brandt, P., Richter, I., Rodriguez-fonseca, B., Hernandez, F., Dengler, M., Rodrigues, R. R., Schmidt, J. O., Yu, L., Lefevre, N., Da Cunha, L. C., McPhaden, M. J., Araujo Filho, M. C., Karstensen, J., Hahn, J., Martín-Rey, M., Patricola, C. M., Poli, P., Zuidema, P., … Duha, J. T. (2019). The tropical atlantic observing system. https://doi.org/10.3389/fmars.2019.00206

Foltz, G. R., & McPhaden, M. J. (2010). Interaction between the Atlantic meridional and Nio modes. *Geophys. Res. Lett.*, *37*(18). https://doi.org/10.1029/2010GL044001

Foltz, G. R., McPhaden, M. J., & Lumpkin, R. (2012). A strong atlantic meridional mode event in 2009: The role of mixed: Layer dynamics. *J. Clim.*, *25*(1). https://doi.org/10.1175/JCLI-D-11-00150.1

Fonseca, C. A., Goni, G. J., Johns, W. E., & Campos, E. J. (2004). Investigation of the North Brazil Current retroflection and North Equatorial Countercurrent variability. *Geophys. Res. Lett.*, *31*(21). https://doi.org/10.1029/2004GL020054

Fraile-Nuez, E., & Hernández-Guerra, A. (2006). Wind-driven circulation for the eastern North Atlantic Subtropical Gyre from Argo data. *Geophys. Res. Lett.*, *33*(3). https://doi.org/10.1029/2005GL025122

Frajka-Williams, E., Ansorge, I. J., Baehr, J., Bryden, H. L., Chidichimo, M. P., Cunningham, S. A., Danabasoglu, G., Dong, S., Donohue, K. A., Elipot, S., Heimbach, P., Holliday, N. P., Hummels, R., Jackson, L. C., Karstensen, J., Lankhorst, M., Le Bras, I. A., Susan Lozier, M., McDonagh, E. L., … Wilson, C. (2019). Atlantic meridional overturning circulation: Observed transport and variability. https://doi.org/10.3389/fmars.2019.00260

Fratantoni, D. M., Johns, W. E., Townsend, T. L., & Hurlburt, H. E. (2000). Low-latitude circulation and mass transport pathways in a model of the tropical Atlantic Ocean. *J. Phys. Oceanogr.*, *30*(8). https://doi.org/10.1175/1520-0485(2000)030<1944:LLCAMT>2.0.CO;2

Ganachaud, A., & Wunsch, C. (2000). Improved estimates of global ocean circulation, heat transport and mixing from hydrographic data. *Nature*, *408*(6811). https://doi.org/10.1038/35044048

García-Serrano, J., Cassou, C., Douville, H., Giannini, A., & Doblas-Reyes, F. J. (2017). Revisiting the ENSO teleconnection to the tropical North Atlantic. *J. Clim.*, *30*(17). https://doi.org/10.1175/JCLI-D-16-0641.1

Garric, G, & Parent, L. (2018). CMEMS PRODUCT USER MANUAL For Global Ocean Reanalysis Products GLOBAL-REANALYSIS-PHY-001-025 version 4.1.

Garric, G., Parent, L., Greiner, E., Drévillon, M., Hamon, M., Lellouche, J.-M., Régnier, C., Desportes, C., Le Galloudec, O., Bricaud, C., et al. Performance and quality assessment of the global ocean eddy-permitting physical reanalysis glorys2v4. In: *Egu general assembly conference abstracts*. 2017, 18776.

Garzoli, S. L., & Gordon, A. L. (1996). Origins and variability of the Benguela Current. *J. Geophys. Res. C Ocean.*, *101*(C1). https://doi.org/10.1029/95JC03221

Garzoli, S., & Richardson, P. L. (1989). Low-frequency meandering of the Atlantic North Equatorial Countercurrent. *J. Geophys. Res.*, *94*(C2). https://doi.org/10.1029/jc094ic02p02079

Garzoli, S. L. (1993). Geostrophic velocity and transport variability in the Brazil-Malvinas Confluence. *Deep. Res. Part I*, *40*(7). https://doi.org/10.1016/0967-0637(93)90118-M

Garzoli, S. L., Baringer, M. O., Dong, S., Perez, R. C., & Yao, Q. (2013). South Atlantic meridional fluxes. *Deep. Res. Part I Oceanogr. Res. Pap.*, *71*. https://doi.org/10.1016/j.dsr.2012.09.003

Garzoli, S. L., Ffield, A., Johns, W. E., & Yao, Q. (2004). North Brazil Current retroflection and transports. *J. Geophys. Res. Ocean.*, *109*(1). https://doi.org/10.1029/2003jc001775

Garzoli, S. L., & Katz, E. J. (1983). The Forced Annual Reversal of the Atlantic North Equatorial Countercurrent. *J. Phys. Oceanogr.*, *13*(11). https://doi.org/10.1175/1520-0485(1983)013<2082:tfarot>2.0.co;2

Giannini, A., Saravanan, R., & Chang, P. (2003). Oceanic Forcing of Sahel Rainfall on Interannual to Interdecadal Time Scales. *Science (80-.).*, *302*(5647). https://doi.org/10.1126/science.1089357

Giannini, A., Biasutti, M., Held, I. M., & Sobel, A. H. (2008). A global perspective on African climate. https://doi.org/10.1007/s10584-008-9396-y

Giarolla, E., Nobre, P., Malagutti, M., & Pezzi, L. P. (2005). The Atlantic Equatorial Undercurrent: PIRATA observations and simulations with GFDL Modular Ocean Model at CPTEC. *Geophys. Res. Lett.*, *32*(10). https://doi.org/10.1029/2004GL022206

Gill, A. E. (1980). Some simple solutions for heat-induced tropical circulation. *Q. J. R. Meteorol. Soc.*, *106*(449). https://doi.org/10.1002/qj.49710644905

Goes, M., Goni, G., Hormann, V., & Perez, R. C. (2013). Variability of the Atlantic off-equatorial eastward currents during 1993-2010 using a synthetic method. *J. Geophys. Res. Ocean.*, *118*(6). https://doi.org/10.1002/jgrc.20186

Góes, M., & Wainer, I. (2003). Equatorial currents transport changes for extreme warm and cold events in the Atlantic Ocean. *Geophys. Res. Lett.*, *30*(5). https://doi.org/10.1029/2002GL015707

Gordon, A. L. (1986). Interocean exchange of thermocline water. *J. Geophys. Res.*, *91*(C4). https://doi.org/10.1029/jc091ic04p05037

Gordon, A. L. (1989). Brazil-Malvinas Confluence-1984. *Deep Sea Res. Part A, Oceanogr. Res. Pap.*, *36*(3). https://doi.org/10.1016/0198-0149(89)90042-3

Gordon, A. L., Weiss, R. F., Smethie, W. M., & Warner, M. J. (1992). Thermocline and intermediate water communication between the south Atlantic and Indian oceans. *J. Geophys. Res.*, *97*(C5). https://doi.org/10.1029/92jc00485

Haarsma, R. J., Campos, E., Hazeleger, W., & Severijns, C. (2008). Influence of the meridional overturning circulation on tropical atlantic climate and variability. *J. Clim.*, *21*(6). https://doi.org/10.1175/2007JCLI1930.1

Ham, Y. G., Kug, J. S., & Park, J. Y. (2013). Two distinct roles of Atlantic SSTs in ENSO variability: North Tropical Atlantic SST and Atlantic Niño. *Geophys. Res. Lett.*, *40*(15). https://doi.org/10.1002/grl.50729

Hastenrath, S., & Heller, L. (1977). Dynamics of climatic hazards in northeast Brazil. *Q. J. R. Meteorol. Soc.*, *103*(435). https://doi.org/10.1002/qj.49710343505

Hazeleger, W., De Vries, P., & Friocourt, Y. (2003). Sources of the equatorial undercurrent in the Atlantic in a high-resolution ocean model. *J. Phys. Oceanogr.*, *33*(4). https://doi.org/10.1175/1520-0485(2003)33<677:SOTEUI>2.0.CO;2

Hazeleger, W., & Drijfhout, S. (2006). Subtropical cells and meridional overturning circulation pathways in the tropical Atlantic. *J. Geophys. Res. Ocean.*, *111*(3). https://doi.org/10.1029/2005JC002942

Hersbach, H., Bell, B., Berrisford, P., Hirahara, S., Horányi, A., Muñoz-Sabater, J., Nicolas, J., Peubey, C., Radu, R., Schepers, D., Simmons, A., Soci, C., Abdalla, S., Abellan, X., Balsamo, G., Bechtold, P., Biavati, G., Bidlot, J., Bonavita, M., … Thépaut, J. N. (2020). The ERA5 global reanalysis. *Q. J. R. Meteorol. Soc.*, *146*(730). https://doi.org/10.1002/qj.3803

Horel, J. D., & Wallace, J. M. (1981). Planetary-scale atmospheric phenomena associated with the Southern Oscillation. *Mon. Weather Rev.*, *109*(4). https://doi.org/10.1175/1520-0493(1981)109<0813:PSAPAW>2.0.CO;2

Hormann, V., & Brandt, P. (2007). Atlantic Equatorial Undercurrent and associated cold tongue variability. *J. Geophys. Res. Ocean.*, *112*(6). https://doi.org/10.1029/2006JC003931

Hormann, V., & Brandt, P. (2009). Upper equatorial Atlantic variability during 2002 and 2005 associated with equatorial Kelvin waves. *J. Geophys. Res. Ocean.*, *114*(3). https://doi.org/10.1029/2008JC005101

Hormann, V., Lumpkin, R., & Foltz, G. R. (2012). Interannual North Equatorial Countercurrent variability and its relation to tropical Atlantic climate modes. *J. Geophys. Res. Ocean.*, *117*(4). https://doi.org/10.1029/2011JC007697

Hu, Z. Z., Kumar, A., Huang, B., & Zhu, J. (2013). Leading modes of the upper-ocean temperature interannual variability along the equatorial atlantic ocean in NCEP GODAS. *J. Clim.*, *26*(13). https://doi.org/10.1175/JCLI-D-12-00629.1

Huang, B., Thorne, P. W., Banzon, V. F., Boyer, T., Chepurin, G., Lawrimore, J. H., Menne, M. J., Smith, T. M., Vose, R. S., & Zhang, H. M. (2017). Extended reconstructed Sea surface temperature, Version 5 (ERSSTv5): Upgrades, validations, and intercomparisons. *J. Clim.*, *30*(20). https://doi.org/10.1175/JCLI-D-16-0836.1

Hummels, R., Brandt, P., Dengler, M., Fischer, J., Araujo, M., Veleda, D., & Durgadoo, J. V. (2015). Interannual to decadal changes in the western boundary circulation in the Atlantic at 11°S. *Geophys. Res. Lett.*, *42*(18). https://doi.org/10.1002/2015GL065254

Hüttl-Kabus, S., & Böning, C. W. (2008). Pathways and variability of the off-equatorial undercurrents in the Atlantic Ocean. *J. Geophys. Res. Ocean.*, *113*(10). https://doi.org/10.1029/2007JC004700

Illig, S., Dewitte, B., Ayoub, N., du Penhoat, Y., Reverdin, G., De Mey, P., Bonjean, F., & Lagerloef, G. S. (2004). Interannual long equatorial waves in the tropical Atlantic from a high-resolution ocean general circulation model experiment in 1981-2000. *J. Geophys. Res. Ocean.*, *109*(2). https://doi.org/10.1029/2003jc001771

Illig, S., & Bachèlery, M. L. (2019). Propagation of Subseasonal Equatorially-Forced Coastal Trapped Waves down to the Benguela Upwelling System. *Sci. Rep.*, *9*(1). https://doi.org/10.1038/s41598-019-41847-1

Ishii, M., Shouji, A., Sugimoto, S., & Matsumoto, T. (2005). Objective analyses of sea-surface temperature and marine meteorological variables for the 20th century using ICOADS and the Kobe Collection. *Int. J. Climatol.*, *25*(7). https://doi.org/10.1002/joc.1169

Jochumsen, K., Rhein, M., Hüttl-Kabus, S., & Böning, C. W. (2010). On the propagation and decay of North Brazil Current rings. *J. Geophys. Res. Ocean.*, *115*(10). https://doi.org/10.1029/2009JC006042

Johns, W. E., Brandt, P., Bourlès, B., Tantet, A., Papapostolou, A., & Houk, A. (2014). Zonal structure and seasonal variability of the Atlantic Equatorial Undercurrent. *Clim. Dyn.*, *43*(11). https://doi.org/10.1007/s00382-014-2136-2

Jouanno, J., Hernandez, O., & Sanchez-Gomez, E. (2017). Equatorial Atlantic interannual variability and its relation to dynamic and thermodynamic processes. *Earth Syst. Dyn.*, *8*(4). https://doi.org/10.5194/esd-8-1061-2017

Jouanno, J., Marin, F., Du Penhoat, Y., Sheinbaum, J., & Molines, J. M. (2011). Seasonal heat balance in the upper 100 m of the equatorial Atlantic Ocean. *J. Geophys. Res. Ocean.*, *116*(9). https://doi.org/10.1029/2010JC006912

Jullion, L., Heywood, K. J., Naveira Garabato, A. C., & Stevens, D. P. (2010). Circulation and water mass modification in the Brazil-Malvinas Confluence. *J. Phys. Oceanogr.*, *40*(5). https://doi.org/10.1175/2009JPO4174.1

Kalnay, E., Kanamitsu, M., Kistler, R., Collins, W., Deaven, D., Gandin, L., Iredell, M., Saha, S., White, G., Woollen, J., Zhu, Y., Chelliah, M., Ebisuzaki, W., Higgins, W., Janowiak, J., Mo, K. C., Ropelewski, C., Wang, J., Leetmaa, A., … Joseph, D. (1996). The NCEP/NCAR 40-year reanalysis project. *Bull. Am. Meteorol. Soc.*, *77*(3). https://doi.org/10.1175/1520-0477(1996)077<0437:TNYRP>2.0.CO;2

Katz, E. J. (1987). Seasonal response of the sea surface to the wind in the equatorial atlantic. *J. Geophys. Res. Ocean.*, *92*(C2). https://doi.org/10.1029/JC092iC02p01885

Keenlyside, N. S., & Latif, M. (2007). Understanding equatorial atlantic interannual variability. *J. Clim.*, *20*(1). https://doi.org/10.1175/JCLI3992.1

Kerr, R. A. (2000). A North Atlantic climate pacemaker for the centuries. https://doi.org/10.1126/science.288.5473.1984

Klein, S. A., Soden, B. J., & Lau, N. C. (1999). Remote sea surface temperature variations during ENSO: Evidence for a tropical atmospheric bridge. *J. Clim.*, *12*(4). https://doi.org/10.1175/1520-0442(1999)012<0917:RSSTVD>2.0.CO;2

Knight, J. R., Folland, C. K., & Scaife, A. A. (2006). Climate impacts of the Atlantic multidecadal oscillation. *Geophys. Res. Lett.*, *33*(17). https://doi.org/10.1029/2006GL026242

Kolodziejczyk, N., Bourlès, B., Marin, F., Grelet, J., & Chuchla, R. (2009). Seasonal variability of the equatorial undercurrent at 10°W as inferred from recent in situ observations. *J. Geophys. Res. Ocean.*, *114*(6). https://doi.org/10.1029/2008JC004976

Kolodziejczyk, N., Marin, F., Bourlès, B., Gouriou, Y., & Berger, H. (2014). Seasonal variability of the equatorial undercurrent termination and associated salinity maximum in the Gulf of Guinea. *Clim. Dyn.*, *43*(11). https://doi.org/10.1007/s00382-014-2107-7

Kucharski, F., Bracco, A., Yoo, J. H., & Molteni, F. (2008). Atlantic forced component of the Indian monsoon interannual variability. *Geophys. Res. Lett.*, *35*(4). https://doi.org/10.1029/2007GL033037

Kushnir, Y., Robinson, W. A., Chang, P., & Robertson, A. W. (2006). The physical basis for predicting Atlantic sector seasonal-to-interannual climate variability. https://doi.org/10.1175/JCLI3943.1

Latif, M., Böning, C., Willebrand, J., Biastoch, A., Dengg, J., Keenlyside, N., Schwecjendiek, U., & Madec, G. (2006). Is the thermohaline circulation changing? *J. Clim.*, *19*(18). https://doi.org/10.1175/JCLI3876.1

Latif, M., & Grötzner, A. (2000). The equatorial Atlantic oscillation and its response to ENSO. *Clim. Dyn.*, *16*(2-3). https://doi.org/10.1007/s003820050014

Laurian, A., & Drijfhout, S. S. (2011). Response of the South Atlantic circulation to an abrupt collapse of the Atlantic meridional overturning circulation. *Clim. Dyn.*, *37*(3). https://doi.org/10.1007/s00382-010-0890-3

Lazar, A., Murtugudde, R., & Busalacchi, J. (2001). A model study of temperature anomaly propagation from the subtropics to tropics within the South Atlantic thermocline. *Geophys. Res. Lett.*, *28*(7). https://doi.org/10.1029/2000GL011418

Lee, S. K., Dinezio, P. N., Chung, E. S., Yeh, S. W., Wittenberg, A. T., & Wang, C. (2014). Spring persistence, transition, and resurgence of El Niño. *Geophys. Res. Lett.*, *41*(23). https://doi.org/10.1002/2014GL062484

Lee, S. K., Lopez, H., Chung, E. S., DiNezio, P., Yeh, S. W., & Wittenberg, A. T. (2018). On the Fragile Relationship Between El Niño and California Rainfall. *Geophys. Res. Lett.*, *45*(2). https://doi.org/10.1002/2017GL076197

Legeais, J. F., Ollitrault, M., & Arhan, M. (2013). Lagrangian observations in the Intermediate Western Boundary Current of the South Atlantic. *Deep. Res. Part II Top. Stud. Oceanogr.*, *85*. https://doi.org/10.1016/j.dsr2.2012.07.028

Liu, C., Fang, L., Köhl, A., Liu, Z., Smyth, W. D., & Wang, F. (2019). The Subsurface Mode Tropical Instability Waves in the Equatorial Pacific Ocean and Their Impacts on Shear and Mixing. *Geophys. Res. Lett.*, *46*(21). https://doi.org/10.1029/2019GL085123

Losada, T., & Rodríguez-Fonseca, B. (2016). Tropical atmospheric response to decadal changes in the Atlantic Equatorial Mode. *Clim. Dyn.*, *47*(3-4). https://doi.org/10.1007/s00382-015-2897-2

Losada, T., Rodríguez-Fonseca, B., Janicot, S., Gervois, S., Chauvin, F., & Ruti, P. (2010). A multi-model approach to the Atlantic Equatorial mode: Impact on the West African monsoon. *Clim. Dyn.*, *35*(1). https://doi.org/10.1007/s00382-009-0625-5

Losada, T., Rodríguez-Fonseca, B., & Kucharski, F. (2012a). Tropical influence on the summer Mediterranean climate. *Atmos. Sci. Lett.*, *13*(1). https://doi.org/10.1002/asl.359

Losada, T., Rodriguez-Fonseca, B., Mohino, E., Bader, J., Janicot, S., & Mechoso, C. R. (2012b). Tropical SST and Sahel rainfall: A non-stationary relationship. *Geophys. Res. Lett.*, *39*(12). https://doi.org/10.1029/2012GL052423

Lübbecke, J. F., Böning, C. W., Keenlyside, N. S., & Xie, S. P. (2010). On the connection between Benguela and equatorial Atlantic Nios and the role of the South Atlantic Anticyclone. *J. Geophys. Res. Ocean.*, *115*(9). https://doi.org/10.1029/2009JC005964

Lübbecke, J. F., Burls, N. J., Reason, C. J., & Mcphaden, M. J. (2014). Variability in the South Atlantic anticyclone and the Atlantic Niño mode. *J. Clim.*, *27*(21). https://doi.org/10.1175/JCLI-D-14-00202.1

Lübbecke, J. F., & McPhaden, M. J. (2012). On the inconsistent relationship between Pacific and Atlantic Niños. *J. Clim.*, *25*(12). https://doi.org/10.1175/JCLI-D-11-00553.1

Lübbecke, J. F., & Mcphaden, M. J. (2013). A comparative stability analysis of atlantic and pacific niño modes. *J. Clim.*, *26*(16). https://doi.org/10.1175/JCLI-D-12-00758.1

Lübbecke, J. F., Rodríguez-Fonseca, B., Richter, I., Martín-Rey, M., Losada, T., Polo, I., & Keenlyside, N. S. (2018). Equatorial Atlantic variability—Modes, mechanisms, and global teleconnections. https://doi.org/10.1002/wcc.527

Lumpkin, R., & Garzoli, S. L. (2005). Near-surface circulation in the Tropical Atlantic Ocean. *Deep. Res. Part I Oceanogr. Res. Pap.*, *52*(3). https://doi.org/10.1016/j.dsr.2004.09.001

Lumpkin, R., & Speer, K. (2003). Large-scale vertical and horizontal circulation in the North Atlantic Ocean. *J. Phys. Oceanogr.*, *33*(9). https://doi.org/10.1175/1520-0485(2003)033<1902:LVAHCI>2.0.CO;2

Madec, G., & the NEMO Team. (2016). NEMO ocean engine. *Note du Pôle modélisation*, (27).

Majumder, S., Schmid, C., & Halliwell, G. (2016). An observations and model-based analysis of meridional transports in the South Atlantic. *J. Geophys. Res. Ocean.*, *121*(8). https://doi.org/10.1002/2016JC011693

Martín-Rey, M., & Lazar, A. (2019). Is the boreal spring tropical Atlantic variability a precursor of the Equatorial Mode? *Clim. Dyn.*, *53*(3-4). https://doi.org/10.1007/s00382-019-04851-9

Martín-Rey, M., Polo, I., Rodríguez-Fonseca, B., Lazar, A., & Losada, T. (2019). Ocean dynamics shapes the structure and timing of Atlantic Equatorial Modes. *J. Geophys. Res. Ocean.*, *124*(11). https://doi.org/10.1029/2019JC015030

Martín-Rey, M., Polo, I., Rodríguez-Fonseca, B., Losada, T., & Lazar, A. (2018). Is there evidence of changes in tropical Atlantic variability modes under AMO phases in the observational record? *J. Clim.*, *31*(2). https://doi.org/10.1175/JCLI-D-16-0459.1

Martín-Rey, M., Rodríguez-Fonseca, B., Polo, I., & Kucharski, F. (2014). On the Atlantic–Pacific Niños connection: a multidecadal modulated mode. *Clim. Dyn.*, *43*(11). https://doi.org/10.1007/s00382-014-2305-3

McCreary, J. P., & Peng Lu. (1994). Interaction between the subtropical and equatorial ocean circulations: the subtropical cell. *J. Phys. Oceanogr.*, *24*(2). https://doi.org/10.1175/1520-0485(1994)024<0466:IBTSAE>2.0.CO;2

Mémery, L., Arhan, M., Alvarez-Salgado, X. A., Messias, M. J., Mercier, H., Castro, C. G., & Rios, A. F. (2000). The water masses along the western boundary of the south and equatorial Atlantic. https://doi.org/10.1016/S0079-6611(00)00032-X

Mercier, H., Arhan, M., & Lutjeharms, J. R. (2003). Upper-layer circulation in the eastern Equatorial and South Atlantic Ocean in January-March 1995. *Deep. Res. Part I Oceanogr. Res. Pap.*, *50*(7). https://doi.org/10.1016/S0967-0637(03)00071-2

Mestas-Nuñez, A. M., & Enfield, D. B. (2001). Eastern equatorial pacific SST variability: ENSO and non-ENSO components and their climatic associations. *J. Clim.*, *14*(3). https://doi.org/10.1175/1520-0442(2001)014<0391:EEPSVE>2.0.CO;2

Metcalf, W. G., & Stalcup, M. C. (1967). Origin of the Atlantic Equatorial Undercurrent. *J. Geophys. Res.*, *72*(20). https://doi.org/10.1029/jz072i020p04959

Mignac, D., Ferreira, D., & Haines, K. (2018). South Atlantic meridional transports from NEMO-based simulations and reanalyses. *Ocean Sci.*, *14*(1). https://doi.org/10.5194/os-14-53-2018

Murtugudde, R. G., Ballabrera-Poy, J., Beauchamp, J., & Busalacchi, A. J. (2001). Relationship between zonal and meridional modes in the tropical Atlantic. *Geophys. Res. Lett.*, *28*(23). https://doi.org/10.1029/2001GL013407

Nnamchi, H. C., Li, J., Kucharski, F., Kang, I. S., Keenlyside, N. S., Chang, P., & Farneti, R. (2015). Thermodynamic controls of the Atlantic Niño. *Nat. Commun.*, *6*. https://doi.org/10.1038/ncomms9895

Nnamchi, H. C., Li, J., Kucharski, F., Kang, I. S., Keenlyside, N. S., Chang, P., & Farneti, R. (2016). An equatorial-extratropical dipole structure of the Atlantic Niño. *J. Clim.*, *29*(20). https://doi.org/10.1175/JCLI-D-15-0894.1

Nobre, P., & Shukla, J. (1996). Variations of sea surface temperature, wind stress, and rainfall over the tropical Atlantic and South America. *J. Clim.*, *9*(10). https://doi.org/10.1175/1520-0442(1996)009<2464:VOSSTW>2.0.CO;2

North, G. R., Bell, T. L., Cahalan, R. F., & Moeng, F. J. (1982). Sampling Errors in the Estimation of Empirical Orthogonal Functions. *Mon. Weather Rev.*, *110*(7). https://doi.org/10.1175/1520-0493(1982)110<0699:seiteo>2.0.co;2

Oettli, P., Morioka, Y., & Yamagata, T. (2016). A Regional Climate Mode Discovered in the North Atlantic: Dakar Niño/Niña. *Sci. Rep.*, *6*. https://doi.org/10.1038/srep18782

Okumura, Y., & Xie, S. P. (2004). Interaction of the Atlantic equatorial cold tongue and the African monsoon. *J. Clim.*, *17*(18). https://doi.org/10.1175/1520-0442(2004)017<3589:IOTAEC>2.0.CO;2

Okumura, Y., & Xie, S. P. (2006). Some overlooked features of tropical atlantic climate leading to a new Niño-like phenomenon. *J. Clim.*, *19*(22). https://doi.org/10.1175/JCLI3928.1

Ollitrault, M., Lankhorst, M., Fratantoni, D., Richardson, P., & Zenk, W. (2006). Zonal intermediate currents in the equatorial Atlantic Ocean. *Geophys. Res. Lett.*, *33*(5). https://doi.org/10.1029/2005GL025368

Orúe-Echevarría, D., Pelegrí, J. L., Machín, F., Hernández-Guerra, A., & Emelianov, M. (2019). Inverse Modeling the Brazil-Malvinas Confluence. *J. Geophys. Res. Ocean.*, *124*(1). https://doi.org/10.1029/2018JC014733

Paris, C. B., Helgers, J., van Sebille, E., & Srinivasan, A. (2013). Connectivity Modeling System: A probabilistic modeling tool for the multi-scale tracking of biotic and abiotic variability in the ocean. *Environ. Model. Softw.*, *42*. https://doi.org/10.1016/j.envsoft.2012.12.006

Patricola, C. M., Saravanan, R., & Chang, P. (2014). The impact of the El Niño-Southern oscillation and Atlantic meridional mode on seasonal Atlantic tropical cyclone activity. *J. Clim.*, *27*(14). https://doi.org/10.1175/JCLI-D-13-00687.1

Peña-Izquierdo, J., Van Sebille, E., Pelegrí, J. L., Sprintall, J., Mason, E., Llanillo, P. J., & Machín, F. (2015). Water mass pathways to the North Atlantic oxygen minimum zone. *J. Geophys. Res. Ocean.*, *120*(5). https://doi.org/10.1002/2014JC010557

Penny, A., Templeman, S, McKenzie, M, Toral, T., D., & Hunt, E. (2020). *State of the tropics 2020 report*. James Cook University, Townsville, Australia.

Perez, R. C., Lumpkin, R., Johns, W. E., Foltz, G. R., & Hormann, V. (2012). Interannual variations of Atlantic tropical instability waves. *J. Geophys. Res. Ocean.*, *117*(3). https://doi.org/10.1029/2011JC007584

Peterson, R. G., & Stramma, L. (1991). Upper-level circulation in the South Atlantic Ocean. https://doi.org/10.1016/0079-6611(91)90006-8

Philander, S. G. (1986). Unusual conditions in the tropical Atlantic Ocean in 1984. *Nature*, *322*(6076). https://doi.org/10.1038/322236a0

Philander, S. G., Gu, D., Halpern, D., Lambert, G., Lau, N. C., Li, T., & Pacanowski, R. C. (1996). Why the ITCZ is mostly north of the equator. *J. Clim.*, *9*(12). https://doi.org/10.1175/1520-0442(1996)009<2958:WTIIMN>2.0.CO;2

Planton, Y., Voldoire, A., Giordani, H., & Caniaux, G. (2018). Main processes of the Atlantic cold tongue interannual variability. *Clim. Dyn.*, *50*(5-6). https://doi.org/10.1007/s00382-017-3701-2

Polo, I., Dong, B. W., & Sutton, R. T. (2013). Changes in tropical Atlantic interannual variability from a substantial weakening of the meridional overturning circulation. *Clim. Dyn.*, *41*(9-10). https://doi.org/10.1007/s00382-013-1716-x

Polo, I., Lazar, A., Rodriguez-Fonseca, B., & Mignot, J. (2015). Growth and decay of the equatorial atlantic SST mode by means of closed heat budget in a coupled general circulation model. *Front. Earth Sci.*, *3*. https://doi.org/10.3389/feart.2015.00037

Polo, I., Rodríguez-Fonseca, B., Losada, T., & García-Serrano, J. (2008). Tropical atlantic variability modes (1979-2002). Part I: Time-evolving SST modes related to West African rainfall. *J. Clim.*, *21*(24). https://doi.org/10.1175/2008JCLI2607.1

Polonsky, A. B., & Artamonov, Y. V. (1997). North equatorial countercurrent in the tropical Atlantic: Multi- jet structure and seasonal variability. *Dtsch. Hydrogr. Zeitschrift*, *49*(4). https://doi.org/10.1007/bf02764342

Poole, R., & Tomczak, M. (1999). Optimum multiparameter analysis of the water mass structure in the Atlantic Ocean thermocline. *Deep. Res. Part I Oceanogr. Res. Pap.*, *46*(11). https://doi.org/10.1016/S0967-0637(99)00025-4

Pottapinjara, V., Girishkumar, M. S., Murtugudde, R., Ashok, K., & Ravichandran, M. (2019). On the relation between the boreal spring position of the atlantic intertropical convergence zone and atlantic zonal mode. *Journal of Climate*, *32*(15), 4767 –4781. https://doi.org/10.1175/JCLI-D-18-0614.1

Provost, C., Arnault, S., Chouaib, N., Kartavtseff, A., Bunge, L., & Sultan, E. (2004). TOPEX/Poseidon and Jason equatorial sea surface slope anomaly in the Atlantic in 2002: Comparison with wind and current measurements at 23W. *Mar. Geod.*, *27*(1-2). https://doi.org/10.1080/01490410490465274

Rayner, N. A., Parker, D. E., Horton, E. B., Folland, C. K., Alexander, L. V., Rowell, D. P., Kent, E. C., & Kaplan, A. (2003). Global analyses of sea surface temperature, sea ice, and night marine air temperature since the late nineteenth century. *J. Geophys. Res. Atmos.*, *108*(14). https://doi.org/10.1029/2002jd002670

Reynolds, R. W., Rayner, N. A., Smith, T. M., Stokes, D. C., & Wang, W. (2002). An improved in situ and satellite SST analysis for climate. *J. Clim.*, *15*(13). https://doi.org/10.1175/1520-0442(2002)015<1609:AIISAS>2.0.CO;2

Reynolds, R. W., Smith, T. M., Liu, C., Chelton, D. B., Casey, K. S., & Schlax, M. G. (2007). Daily high-resolution-blended analyses for sea surface temperature. *J. Clim.*, *20*(22). https://doi.org/10.1175/2007JCLI1824.1

Richter, I., Behera, S. K., Masumoto, Y., Taguchi, B., Sasaki, H., & Yamagata, T. (2013). Multiple causes of interannual sea surface temperature variability in the equatorial Atlantic Ocean. *Nat. Geosci.*, *6*(1). https://doi.org/10.1038/ngeo1660

Richter, I., & Tokinaga, H. (2020). An overview of the performance of CMIP6 models in the tropical Atlantic: mean state, variability, and remote impacts. *Clim. Dyn.*, *55*(9-10). https://doi.org/10.1007/s00382-020-05409-w

Richter, I., & Xie, S. P. (2008). On the origin of equatorial Atlantic biases in coupled general circulation models. *Clim. Dyn.*, *31*(5). https://doi.org/10.1007/s00382-008-0364-z

Rintoul, S. R. (1991). South Atlantic interbasin exchange. *J. Geophys. Res. Ocean.*, *96*(C2). https://doi.org/10.1029/90jc02422

Rocha, C. B., Da Silveira, I. C., Castro, B. M., & Lima, J. A. M. (2014). Vertical structure, energetics, and dynamics of the Brazil Current System at 22°S-28°S. *J. Geophys. Res. Ocean.*, *119*(1). https://doi.org/10.1002/2013JC009143

Rodrigues, R. R., Rothstein, L. M., & Wimbush, M. (2007). Seasonal variability of the South Equatorial Current bifurcation in the Atlantic Ocean: A numerical study. *J. Phys. Oceanogr.*, *37*(1). https://doi.org/10.1175/JPO2983.1

Rodríguez-Fonseca, B., Mohino, E., Mechoso, C. R., Caminade, C., Biasutti, M., Gaetani, M., Garcia-Serrano, J., Vizy, E. K., Cook, K., Xue, Y., Polo, I., Losada, T., Druyan, L., Fontaine, B., Bader, J., Doblas-Reyes, F. J., Goddard, L., Janicot, S., Arribas, A., … Voldoire, A. (2015). Variability and predictability of west African droughts: A review on the role of sea surface temperature anomalies. *J. Clim.*, *28*(10). https://doi.org/10.1175/JCLI-D-14-00130.1

Rodríguez-Fonseca, B., Polo, I., García-Serrano, J., Losada, T., Mohino, E., Mechoso, C. R., & Kucharski, F. (2009). Are Atlantic Niños enhancing Pacific ENSO events in recent decades? *Geophys. Res. Lett.*, *36*(20). https://doi.org/10.1029/2009GL040048

Rosell-Fieschi, M., Pelegrí, J. L., & Gourrion, J. (2015). Zonal jets in the equatorial Atlantic Ocean. *Prog. Oceanogr.*, *130*. https://doi.org/10.1016/j.pocean.2014.08.008

Rühs, S., Schwarzkopf, F. U., Speich, S., & Biastoch, A. (2019). Cold vs. warm water route-sources for the upper limb of the Atlantic Meridional Overturning Circulation revisited in a high-resolution ocean model. *Ocean Sci.*, *15*(3). https://doi.org/10.5194/os-15-489-2019

Schlundt, M., Brandt, P., Dengler, M., Hummels, R., Fischer, T., Bumke, K., Krahmann, G., & Karstensen, J. (2014). Mixed layer heat and salinity budgets during the onset of the 2011 Atlantic cold tongue. *J. Geophys. Res. Ocean.*, *119*(11). https://doi.org/10.1002/2014JC010021

Schmid, C., Siedler, G., & Zenk, W. (2000). Dynamics of intermediate water circulation in the subtropical South Atlantic. *J. Phys. Oceanogr.*, *30*(12). https://doi.org/10.1175/1520-0485(2000)030<3191:DOIWCI>2.0.CO;2

Schmid, C. (2014). Mean vertical and horizontal structure of the subtropical circulation in the South Atlantic from three-dimensional observed velocity fields. *Deep. Res. Part I Oceanogr. Res. Pap.*, *91*. https://doi.org/10.1016/j.dsr.2014.04.015

Schneider, T., Bischoff, T., & Haug, G. H. (2014). Migrations and dynamics of the intertropical convergence zone. https://doi.org/10.1038/nature13636

Schott, F. A., & Böning, C. W. (1991). The WOCE model in the western equatorial Atlantic: Upper layer circulation. *J. Geophys. Res.*, *96*(C4). https://doi.org/10.1029/90jc02683

Schott, F. A., Dengler, M., Brandt, P., Affler, K., Fischer, J., Bourlès, B., Gouriou, Y., Molinari, R. L., & Rhein, M. (2003). The zonal currents and transports at 35°W in the tropical Atlantic. *Geophys. Res. Lett.*, *30*(7). https://doi.org/10.1029/2002GL016849

Schott, F. A., Dengler, M., Zantopp, R., Stramma, L., Fischer, J., & Brandt, P. (2005). The shallow and deep western boundary circulation of the South Atlantic at 5°-11°S. *J. Phys. Oceanogr.*, *35*(11). https://doi.org/10.1175/JPO2813.1

Schott, F. A., McCreary, J. P., & Johnson, G. C. Shallow overturning circulations of the tropical-subtropical oceans. In: *Geophys. monogr. ser.* Vol. 147. 2004. https://doi.org/10.1029/147GM15.

Servain, J., Wainer, L., McCreary, J. P., & Dessier, A. (1999). Relationship between the equatorial and meridional modes of climatic variability in the tropical Atlantic. *Geophys. Res. Lett.*, *26*(4). https://doi.org/10.1029/1999GL900014

Shannon, L. V., Boyd, A. J., Brundrit, G. B., & Taunton-Clark, J. (1986). ON THE EXISTENCE OF AN EL NINO-TYPE PHENOMENON IN THE BENGUELA SYSTEM. *J. Mar. Res.*, *44*(3). https://doi.org/10.1357/002224086788403105

Soutelino, R. G., Gangopadhyay, A., & da Silveira, I. C. (2013). The roles of vertical shear and topography on the eddy formation near the site of origin of the Brazil Current. *Cont. Shelf Res.*, *70*. https://doi.org/10.1016/j.csr.2013.10.001

Speich, S., Blanke, B., & Cai, W. (2007). Atlantic meridional overturning circulation and the Southern Hemisphere supergyre. *Geophys. Res. Lett.*, *34*(23). https://doi.org/10.1029/2007GL031583

Speich, S., Blanke, B., & Madec, G. (2001). Warm and cold water routes of an O.G.C.M. thermohaline conveyor belt. *Geophys. Res. Lett.*, *28*(2). https://doi.org/10.1029/2000GL011748

Stramma, L., & England, M. (1999). On the water masses and mean circulation of the South Atlantic Ocean. *J. Geophys. Res. Ocean.*, *104*(C9). https://doi.org/10.1029/1999jc900139

Stramma, L., Fischer, J., Brandt, P., & Schott, F. (2003). Circulation, variability and near-equatorial meridional flow in the central tropical Atlantic. *Elsevier Oceanogr. Ser.*, *68*(100). https://doi.org/10.1016/S0422-9894(03)80141-1

Stramma, L., Fischer, J., & Reppin, J. (1995). The North Brazil Undercurrent. *Deep. Res. Part I*, *42*(5). https://doi.org/10.1016/0967-0637(95)00014-W

Stramma, L., Rhein, M., Brandt, P., Dengler, M., Böning, C., & Walter, M. (2005). Upper ocean circulation in the western tropical Atlantic in boreal fall 2000. *Deep. Res. Part I Oceanogr. Res. Pap.*, *52*(2). https://doi.org/10.1016/j.dsr.2004.07.021

Svendsen, L., Kvamstø, N. G., & Keenlyside, N. (2014). Weakening AMOC connects Equatorial Atlantic and Pacific interannual variability. *Clim. Dyn.*, *43*(11). https://doi.org/10.1007/s00382-013-1904-8

Talley, L. D. (2003). Shallow, intermediate, and deep overturning components of the global heat budget. *J. Phys. Oceanogr.*, *33*(3). https://doi.org/10.1175/1520-0485(2003)033<0530:SIADOC>2.0.CO;2

Talley, L. D. (2008). Freshwater transport estimates and the global overturning circulation: Shallow, deep and throughflow components. *Prog. Oceanogr.*, *78*(4), 257–303. https://doi.org/10.1016/j.pocean.2008.05.001

Tamsitt, V., Abernathey, R. P., Mazloff, M. R., Wang, J., & Talley, L. D. (2018). Transformation of Deep Water Masses Along Lagrangian Upwelling Pathways in the Southern Ocean. *J. Geophys. Res. Ocean.*, *123*(3). https://doi.org/10.1002/2017JC013409

Tokinaga, H., Richter, I., & Kosaka, Y. (2019). ENSO influence on the Atlantic Niño, revisited: Multi-year versus single-year ENSO events. *J. Clim.*, *32*(14). https://doi.org/10.1175/JCLI-D-18-0683.1

Tschakert, P., Sagoe, R., Ofori-Darko, G., & Codjoe, S. N. (2010). Floods in the Sahel: An analysis of anomalies, memory, and anticipatory learning. *Clim. Change*, *103*(3). https://doi.org/10.1007/s10584-009-9776-y

Tuchen, F. P., Lübbecke, J. F., Brandt, P., & Fu, Y. (2020). Observed Transport Variability of the Atlantic Subtropical Cells and Their Connection to Tropical Sea Surface Temperature Variability. *J. Geophys. Res. Ocean.*, *125*(12). https://doi.org/10.1029/2020JC016592

Uppala, S. M., Kållberg, P. W., Simmons, A. J., Andrae, U., da Costa Bechtold, V., Fiorino, M., Gibson, J. K., Haseler, J., Hernandez, A., Kelly, G. A., Li, X., Onogi, K., Saarinen, S., Sokka, N., Allan, R. P., Andersson, E., Arpe, K., Balmaseda, M. A., Beljaars, A. C., … Woollen, J. (2005). The ERA-40 re-analysis. https://doi.org/10.1256/qj.04.176

Urbano, D. F., De Almeida, R. A., & Nobre, P. (2008). Equatorial undercurrent and North equatorial countercurrent at 38°W: A new perspective from direct velocity data. *J. Geophys. Res. Ocean.*, *113*(4). https://doi.org/10.1029/2007JC004215

Vallès-Casanova, I., Lee, S. K., Foltz, G. R., & Pelegrí, J. L. (2020). On the Spatiotemporal Diversity of Atlantic Niño and Associated Rainfall Variability Over West Africa and South America. *Geophys. Res. Lett.*, *47*(8). https://doi.org/10.1029/2020GL087108

van Sebille, E., Griffies, S. M., Abernathey, R., Adams, T. P., Berloff, P., Biastoch, A., Blanke, B., Chassignet, E. P., Cheng, Y., Cotter, C. J., Deleersnijder, E., Döös, K., Drake, H. F., Drijfhout, S., Gary, S. F., Heemink, A. W., Kjellsson, J., Koszalka, I. M., Lange, M., … Zika, J. D. (2018). Lagrangian ocean analysis: Fundamentals and practices. https://doi.org/10.1016/j.ocemod.2017.11.008

Van Sebille, E., Sprintall, J., Schwarzkopf, F. U., Sen Gupta, A., Santoso, A., England, M. H., Biastoch, A., & Böning, C. W. (2014). Pacific-to-Indian Ocean connectivity: Tasman leakage, Indonesian Throughflow, and the role of ENSO. *J. Geophys. Res. Ocean.*, *119*(2). https://doi.org/10.1002/2013JC009525

Verbrugge, N., Mulet, S., Guinehut, S., & Buongiorno-Nardelli, B. Armor3d: A 3d multi-observations t, s, u, v product of the ocean. In: *Egu general assembly conference abstracts*. 2017, 17579.

Vimont, D. J., & Kossin, J. P. (2007). The Atlantic Meridional Mode and hurricane activity. *Geophys. Res. Lett.*, *34*(7). https://doi.org/10.1029/2007GL029683

Visbeck, M. (2002). Deep velocity profiling using lowered acoustic Doppler current profilers: Bottom track and inverse solutions. *J. Atmos. Ocean. Technol.*, *19*(5). https://doi.org/10.1175/1520-0426(2002)019<0794:DVPULA>2.0.CO;2

Vizy, E. K., & Cook, K. H. (2002). Development and application of a mesoscale climate model for the tropics: Influence of sea surface temperature anomalies on the West African monsoon. *J. Geophys. Res. Atmos.*, *107*(3). https://doi.org/10.1029/2001jd000686

von Schuckmann, K., Brandt, P., & Eden, C. (2008). Generation of tropical instability waves in the Atlantic Ocean. *J. Geophys. Res. Ocean.*, *113*(8). https://doi.org/10.1029/2007JC004712

von Schuckmann, K., Le Traon, P. Y., Alvarez-Fanjul, E., Axell, L., Balmaseda, M., Breivik, L. A., Brewin, R. J., Bricaud, C., Drevillon, M., Drillet, Y., Dubois, C., Embury, O., Etienne, H., Sotillo, M. G., Garric, G., Gasparin, F., Gutknecht, E., Guinehut, S., Hernandez, F., … Verbrugge, N. (2016). The Copernicus Marine Environment Monitoring Service Ocean State Report. *J. Oper. Oceanogr.*, *9*. https://doi.org/10.1080/1755876X.2016.1273446

von Storch, H., & Zwiers, F. W. (1984). *Statistical Analysis in Climate Research*. https://doi.org/10.1017/cbo9780511612336

Waliser, D. E., & Gautier, C. (1993). A satellite-derived climatology of the ITCZ. *J. Clim.*, *6*(11). https://doi.org/10.1175/1520-0442(1993)006<2162:ASDCOT>2.0.CO;2

Wang, C., Kucharski, F., Barimalala, R., & Bracco, A. (2009). Teleconnections of the tropical Atlantic to the tropical Indian and Pacific Oceans: A review of recent findings. *Meteorol. Zeitschrift*, *18*(4). https://doi.org/10.1127/0941-2948/2009/0394

Wang, C., & Zhang, L. (2013). Multidecadal ocean temperature and salinity variability in the tropical north atlantic: Linking with the AMO, AMOC, and subtropical cell. *J. Clim.*, *26*(16). https://doi.org/10.1175/JCLI-D-12-00721.1

Wang, L., Yu, J. Y., & Paek, H. (2017). Enhanced biennial variability in the Pacific due to Atlantic capacitor effect. *Nat. Commun.*, *8*. https://doi.org/10.1038/ncomms14887

Wang, W., Anderson, B. T., Kaufmann, R. K., & Myneni, R. B. (2004). The relation between the North Atlantic Oscillation and SSTs in the North Atlantic Basin. *J. Clim.*, *17*(24). https://doi.org/10.1175/JCLI-3186.1

White, R. H. (2015). Using multiple passive tracers to identify the importance of the North Brazil undercurrent for Atlantic cold tongue variability. *Q. J. R. Meteorol. Soc.*, *141*(692). https://doi.org/10.1002/qj.2536

Xie, S. P., & Carton, J. A. Tropical atlantic variability: Patterns, mechanisms, and impacts. In: *Geophys. monogr. ser.* Vol. 147. 2004. https://doi.org/10.1029/147GM07.

Xie, S., & Philander, S. G. H. (1994). A coupled ocean-atmosphere model of relevance to the ITCZ in the eastern Pacific. *Tellus A*, *46*(4). https://doi.org/10.1034/j.1600-0870.1994.t01-1-00001.x

Yulaeva, E., & Wallace, J. M. (1994). The signature of ENSO in global temperature and precipitation fields derived from the microwave sounding unit. *J. Clim.*, *7*(11). https://doi.org/10.1175/1520-0442(1994)007<1719:TSOEIG>2.0.CO;2

Zebiak, S. E. (1993). Air-sea interaction in the equatorial Atlantic region. *J. Clim.*, *6*(8). https://doi.org/10.1175/1520-0442(1993)006<1567:AIITEA>2.0.CO;2

Zhang, D., McPhaden, M. J., & Johns, W. E. (2003). Observational evidence for flow between the subtropical and tropical Atlantic: The Atlantic subtropical cells. *J. Phys. Oceanogr.*, *33*(8). https://doi.org/10.1175/2408.1

Zhu, J., Huang, B., & Wu, Z. (2012). The role of ocean dynamics in the interaction between the Atlantic meridional and equatorial modes. *J. Clim.*, *25*(10). https://doi.org/10.1175/JCLI-D-11-00364.1

Zuo, H., Alonso-Balmaseda, M., Mogensen, K, & Tietsche, S. (2018). OCEAN5: The ECMWF Ocean Reanalysis System and its Real-Time analysis component. *ECMWF Tech. Memo.*, (823).

Acknowledgements

This thesis would not have been possible without the valuable collaboration of the several authors present in each chapter. Concretely, I am really grateful with Sang Ki Lee who opened the doors from ocean to climate hosting me in NOAA-AOML for two months. I was completely immersed in science and just for science, something that should happen more often.

I am also grateful with Erik van Sebille who hosted me for three months in Utrecht University where I developed my skills in Lagrangian modelling, an incredible world of creativity with just being in front of a screen, lost between lines of code.

I would also like to thank Anna Cabré, who is always ready to cooperate and help you with whatever you need, always with a smile.

I specially want to thank Marta Martín Rey who has been my co-supervisor during the last year and a half. She did the final push that this thesis needed.

Finally, none of this would happen without Josep Lluís Pelegrí, to ask him to do a master thesis some years ago was one of the best decisions I probably made. I'm used to doubt for absolutely all decisions I make, but this one was an incredible exception.

The development of this thesis have been funded by:

- FPI contract BES2015-071314 as part of VADERETRO project. *Ministerio de Economia y Competitividad*
- VADERETRO. Western boundary retroflections. Ref.: CTM2014-56987-P. *Ministerio de Economia y Competitividad*.
- Pati Científic. Development of a citizen monitoring program for the Barcelona coastal waters, www.paticientific.org. Ref. 19S01645-006. *Institut de cultura de Barcelona. Ajuntament de Barcelona*.
- SAGA. South Atlantic Gate-Away. Ref.: RTI2018-100844-B-C33. *Ministerio de Economia y Competitividad*.
- CLIMATE-COVID19. Ref.: PIM-E-202030E222.

More acknowledgments in the printed version.